Durham E-Theses

Enhanced Crystallisation Control Using Structured Ternary Fluids

MAUNDER, JENNIFER,JULIET

ENHANCED CRYSTALLISATION CONTROL USING STRUCTURED TERNARY FLUIDS

Jennifer Juliet Maunder

A thesis submitted for the degree of Doctor of Philosophy at the University of Durham

September 22, 2023

ABSTRACT

A theory of thermodynamic control over crystallisation has been established for both organic and inorganic materials, allowing the most stable polymorphs to be synthesised under ambient conditions. This control arises from the use of surfactant microemulsions, where nanoscale droplets of one phase are suspended in another. Through this, solute may be confined, slowing crystal growth to allow only the most stable nuclei of the most stable polymorph to persist and grow.

Structured ternary fluids (STFs) are complex mixtures that, at certain compositions, contain nanostructures similar to those of surfactant microemulsions, often leading to them being described as surfactant-free, or ultra-flexible microemulsions. This thesis reveals that STF nanostructures may be used to achieve a similar degree of thermodynamic control, where STFs comprised of water, octanol and ethanol could selectively grow the most stable polymorph of glycine, γ-glycine, at supersaturations, $\frac{c}{c_{sat}}$, of $1.30 - 1.40$. These systems were also used to seed bulk crystallisations, exhibiting an excellent correlation between the polymorphic outcome of the STF and seeded products.

Moreover, this work shows that STFs have potential for use in polymorph screening. All three ambient temperature polymorphs of glycine were selectively targeted from a single STF by tailoring the glycine supersaturation. Additionally, all four clinically relevant polymorphs of 5-methyl-2-[(2-nitrophenyl)amino]-3-thiophenecarbonitrile (ROY) were nucleated concomitantly in an STF of toluene, isopropanol and water, using a high supersaturation of $\frac{c}{c_{sat}}$ = 5.5. This demonstrated that STF-formed nuclei remain spatially separated for extended periods. This allows multiple polymorphs to nucleate and survive even if there are more stable, faster growing polymorphs present elsewhere.

Crucially, in bulk solution, crystallisation is governed by a slow nucleation rate and fast crystal growth mechanism that leads to a lack of polymorphic control and can promote amorphous product precipitation. Conversely, in STFs it has been shown that a fast nucleation rate and a slow crystal growth mechanism were exhibited, promoting crystallisation control.

ACKNOWLEDGEMENTS

STATEMENT OF COPYRIGHT

PUBLICATION LIST

The following publication has arisen from the work presented in this thesis:

1. J. J. Maunder, J. A. Aguilar, P. Hodgkinson and S. J. Cooper, Structured ternary fluids as nanocrystal incubators for enhanced crystallization control, *Chem. Sci.*, 2022, **13**, 13132–13140.

   Web Access: https://pubs.rsc.org/en/content/articlehtml/2022/sc/d2sc04413g

LIST OF TABLES

LIST OF FIGURES

TABLE OF CONTENTS

1 INTRODUCTION AND BACKGROUND

Crystallisation is prevalent throughout nature. Most obviously, it is responsible for the formation of rocks and gemstones, but it also creates the coral reefs in our oceans, and snowflakes in the sky. Many industrial processes harness this process, including ceramics, polymers, pharmaceuticals, agriculture, and food production. Due to its ubiquity, it is extremely important to understand the mechanisms behind this process, especially if we are to optimise it for industrial application. However, this is a controversial topic. There have been multiple contrasting theories put forward to explain crystallisation, and consequently it is poorly defined.

Here, we propose that by crystallising materials in confined domains, such as within droplet microemulsions or structured ternary fluids (STFs), it is possible to investigate crystallisation in its earliest stages and use this to control the polymorphic outcome.

1.1 SOLUTE CONFINEMENT IN MICROEMULSION STRUCTURES

1.1.1 Surfactants

Figure 1.1: Structure of a general non-ionic, C_nE_m, surfactant.

Surface active agents (surfactants) are amphiphilic molecules comprised of a hydrocarbon chain and a polar, or ionic head group. Hydrocarbons interact only very weakly with water. This means that strong dispersion forces and hydrogen bonding between water molecules act to 'push' the hydrocarbon chains out, and so they are referred to as hydrophobic. Conversely, head groups are known as hydrophilic as they have strong dipole-dipole or ion-dipole interactions with water and are

therefore solvated.[1] This action can be exploited to adsorb surfactants onto oil/water interfaces, altering the interfacial free energy.

1.1.1.1   Classification

Surfactants can be characterised as anionic, cationic, zwitterionic, or non-ionic according to the charge of their head group. It is also possible to alter the surfactant by adapting the tail group. This can be achieved by the addition of functional groups, or by varying the chain length and chain saturation/unsaturation. The main consequence of this is to change how molecules may pack together, either at an interface or in aggregated structures.

1.1.1.2   Interfacial Behaviour

Due to their amphiphilic nature, surfactant molecules spontaneously accumulate at an oil/water interface. This is thermodynamically favourable as it lowers the system's free energy by lowering the interfacial tension between the oil and water phases.

Interfacial tension arises due to an imbalance of intermolecular forces at the oil/water interface compared with those in the bulk. Consequently, work must be done to break some of the intermolecular interactions in order to bring molecules from the bulk to the interface.

The interfacial tension is the work done in creating a unit area of the interface, as described by the change in the Gibbs free energy (Equation 1.1)

$$dG = Vdp - SdT + \gamma dA + \sum \mu_i dn_i \qquad (1.1)$$

where G is the Gibbs free energy, γ is the interfacial tension, μ_i and n_i are the chemical potential and number of moles of component i, respectively, A is the interfacial area, and p, V, and T are the pressure, volume, and temperature of the system, respectively. At constant pressure, temperature, and composition, this can be simplified to Equation 1.2 defining interfacial tension.[2]

$$\gamma = \frac{dG}{dA}_{T,p,n_i} \qquad (1.2)$$

2

The surfactant molecules adsorb at the interface in order to have their hydrophilic head groups in the water phase and their hydrophobic tail groups in the oil phase. These interactions are more favourable than those between the two immiscible phases, meaning the interfacial tension is lowered.

1.1.1.3   Micellisation

When surfactants are at low concentration in aqueous solution, they will behave monomerically, forming a uniform dispersion, albeit with a surface excess. As the surfactant concentration is increased above a threshold value known as the critical micelle concentration (CMC), the molecules aggregate into a range of micelle structures (Figure 1.2) depending on the concentration and the physical properties of the surfactant molecules.[3,4]
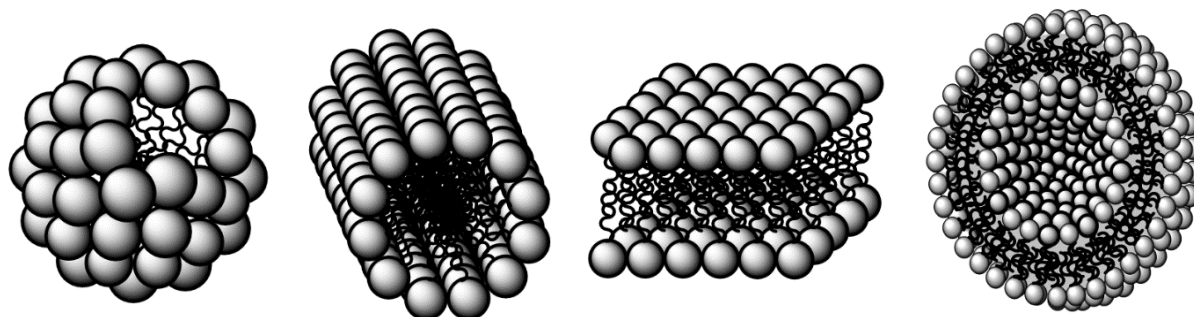
Figure 1.2: Representations of spherical micelles, worm-like micelles, bilayer sheets and vesicles, from left to right, respectively.

Micelle formation in aqueous solution is an entropic effect driven by the favourable entropy associated with removing hydrophobic chains from water at the CMC. Whilst the surfactant molecules are constrained in micelles, resulting in an entropic penalty owing to the loss of translational entropy of the individual monomers, it is the effect on the surrounding water molecules that dominates. When a surfactant enters this system, the ordinarily strong hydrogen bonds between water molecules become restricted to specific water molecule orientations since water cannot hydrogen bond to the hydrophobic surfactant chain, and hence cage-like water structures form around the alkyl chains. This is known as the hydrophobic effect and reduces the number of configurations that the water molecules can take. Upon micellisation, water molecules are released and there is an associated

increase in entropy. This effect is greater than the entropic penalty of creating ordered surfactant structures due to the much larger concentration of water molecules.[5,6]

As surfactant concentration increases further, micelles organise into hierarchical structures with long-range order, such as lamellar phases, as depicted in Figure 1.3. However, it is not only the concentration but also the shape of the surfactant which determines the structures that may form. This is quantified using the packing parameter, a dimensionless quantity that uses the geometry of the surfactant molecules to predict the phase that will form.[3]
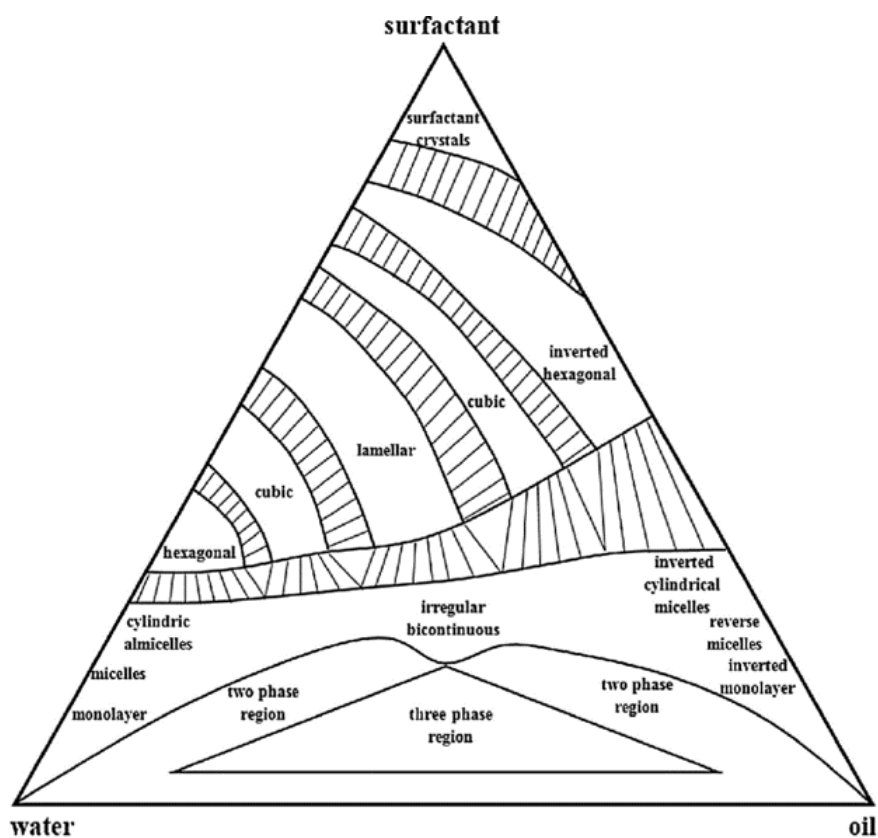
Figure 1.3: Phase diagram for a typical oil/water/surfactant system.[7]

The packing parameter is dependent on three terms, l_c, a_0, and V, as illustrated in Figure 1.4. l_c is the maximum critical radius of the micelle, and a_0 and V are the optimum head group surface area of the molecule necessary for bilayer self-assembly to occur, and the tail group volume of the molecule, respectively. This theory assumes that the surface area of the head group is close to that required to produce a bilayer, and that l_c, a_0, and V are constants for a given surfactant. This is not strictly true as

variables such as temperature and salinity can change the effective values of a_0 and V, and therefore

the packing parameter should be used only as an approximate measure.
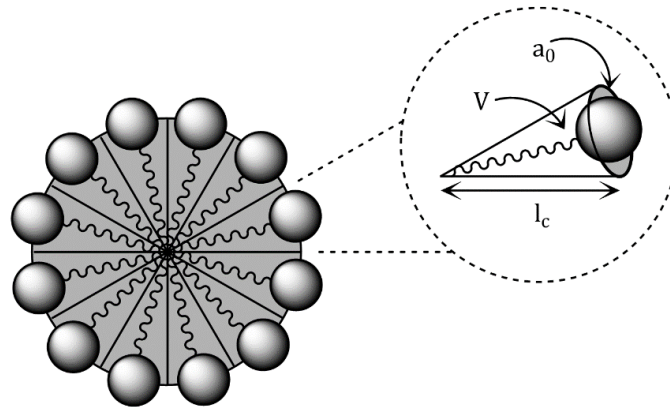
Figure 1.4: Diagram to show the values described in the packing parameter.

For a micelle of radius, R,[7]

$$\frac{V}{Ra_0} = \frac{1}{3}$$

(1.3)

As the maximum critical radius of the micelle has been previously defined as l_c, then $R < l_c$ and the

equation may be written as follows:

$$P_c = \frac{V}{a_0 l_c} < \frac{1}{3}$$

(1.4)

where P_c is the packing parameter. This equation is known as the packing condition for spherical

micelle formation. The conditions for other micellar phases can also be determined using similar

arguments, which are listed in Table 1.1.[3,8]

Table 1.1: Packing parameter conditions required for different micellar structures.[7]

Micellar phase	Packing condition
Spherical micelles	$P_c < \frac{1}{3}$
Cylindrical (Worm-like) micelles	$\frac{1}{3} < P_c < \frac{1}{2}$
Bilayers (Vesicles)	$\frac{1}{2} < P_c < 1$
Inverted structures	$1 < P_c$

1.1.2 Emulsions

Two immiscible liquids, when mixed, tend to form two separate phases to minimise their interfacial contact, and consequently the Gibbs free energy. As previously discussed, using surfactants reduces the interfacial tension between the two phases, so turbid emulsions form upon vigorous stirring.[1] Emulsions typically consist of oil droplets in water (o/w) or water droplets in oil (w/o). However, they are not thermodynamically stable and phase separation will occur given enough time.

Emulsions may destabilise via different mechanisms. For example, creaming and sedimentation, where droplets less dense than the continuous phase rise to the top and those denser sink to the bottom. This phenomenon can be quantified by Equation 1.5.[9,10]

$$v = \frac{R^2 \Delta \rho g}{18 \eta} \tag{1.5}$$

where v is the velocity at which the droplets cream/settle, R is the droplet radius, $\Delta \rho$ is the difference in density between the droplet phase and the continuous phase (positive for settling, negative for creaming), η is the viscosity of the continuous phase, and g is the acceleration due to gravity. We can deduce from this that droplets of smaller radius will cream/sediment at much slower rates compared with larger droplets. In addition, due to thermal fluctuations, droplets will often collide. If collisions occur with sufficient energy, droplets will coalesce and consequently form a single, larger droplet, which will cream/sediment at a faster rate.[10]

Another mechanism for the phase separation of an emulsion is via Ostwald ripening. This presents as the growth of large droplets at the expense of smaller ones. It occurs as the solubility of a spherical droplet of radius r in the bulk continuous phase, $C(r)$, will increase as the droplet radius decreases, according to the Kelvin equation.[9]

$$C(r) = C(\infty) \, \exp \left[\frac{2 \gamma V_m}{r R T} \right] \tag{1.6}$$

where, $C(\infty)$ is the saturation solubility, i.e. the solubility of the droplet species in the continuous phase when in equilibrium with a phase-separated layer of that species, γ is the interfacial tension, V_m

is the molar volume of the confined phase, and R and T are the molar gas constant and temperature, respectively. Consequently, smaller droplets will more readily dissolve back into the continuous phase. This arises because smaller droplets have a higher Laplace pressure than larger droplets, and therefore a larger chemical potential, μ. Molecules spontaneously diffuse from areas of high to low μ, facilitating the growth of larger droplets.[11,12]

As emulsions are widely used in large industries such as agrochemicals and pharmaceuticals, much effort has been invested into trying to stabilise these systems. The focus is often on preventing coalescence and Ostwald ripening to reduce the creaming/sedimentation rate. One method is to use amphiphilic block copolymers that migrate to oil/water interfaces, acting in a similar way to surfactants. The portion of the polymer chain that protrudes out of the droplet and into the continuous phase provides steric stabilisation. As droplets approach each other, the polymer chains become confined to a smaller region and this limits the number of conformations that they can adopt, which is entropically unfavourable (Figure 1.5). In addition, the increase in concentration of polymer in the region between the droplets leads to the exclusion of the continuous phase molecules, lowering their concentration. This creates an osmotic pressure difference, where the continuous phase molecules will migrate from the areas of high concentration, into the inter-droplet region where there is a low concentration, again, pushing the droplets apart.[13]
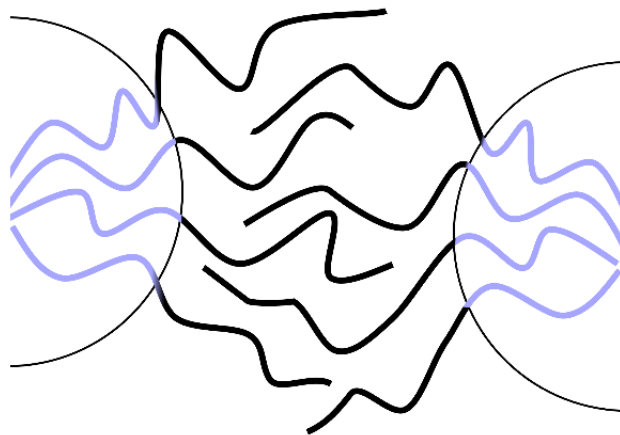
Figure 1.5: Diagram of two polymer grafted droplets approaching each other.

1.1.3 Nanoemulsions

Nanoemulsions are metastable systems with emulsion droplets in the size range of approximately $20 - 500$ nm. They appear blue in colour due to the scattering of blue light preferentially by the dispersed phase as light passes through the system.[14]

1.1.4 Microemulsions

Microemulsions have smaller droplet sizes (approximately $1 - 100$ nm) compared with regular emulsions, leading to lower turbidity and, more importantly, thermodynamic stability. Visually they appear as transparent, single-phase liquids as the droplet sizes are too small to scatter visible light.

As surfactant molecules lower the interfacial tension, γ, spontaneous emulsification will occur when γ is low enough that it is overcompensated by the entropy change, ΔS, associated with dispersing droplets throughout the continuous phase.[9]

$$\Delta G_f = \gamma \Delta A - T \Delta S \tag{1.7}$$

where ΔG_f is the Gibbs free energy of formation, ΔA is the change in the interfacial area (note that this will also increase as droplets are created), and T is temperature. From this, it may be observed that if $\gamma \Delta A < T \Delta S$ then ΔG_f will be negative and droplet formation will be spontaneous.

1.1.4.1 Winsor Classification

The Winsor classification refers to systems that can arise when a surfactant is present at concentrations above its CMC in combination with both oil and aqueous phases (Figure 1.6).[13]
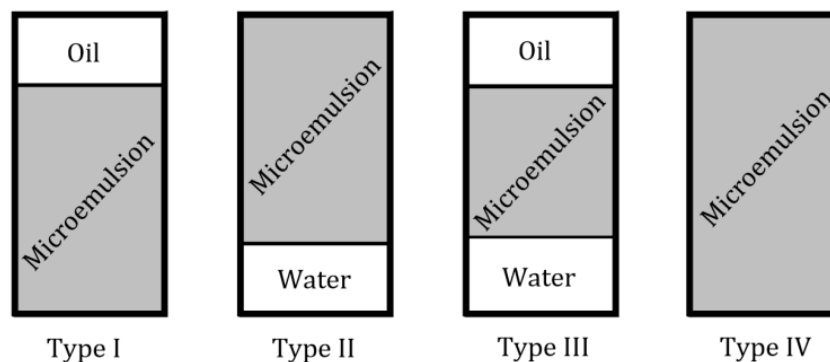
Figure 1.6: Winsor classification of microemulsions.

The Winsor I classification refers to a phase separated system with an o/w microemulsion below a layer of excess oil. Similarly, Winsor II refers to a phase separated system with a w/o microemulsion above a layer of excess water. Winsor III has three phases, an excess oil above and a water layer below a bicontinuous microemulsion phase, which contains continuous domains of oil and water, as shown in Figure 1.7. Bicontinuous microemulsions often arise when a surfactant has an equal affinity for both oil and water. Winsor IV is a completely homogeneous system made up of either an o/w, w/o, or bicontinuous microemulsion.
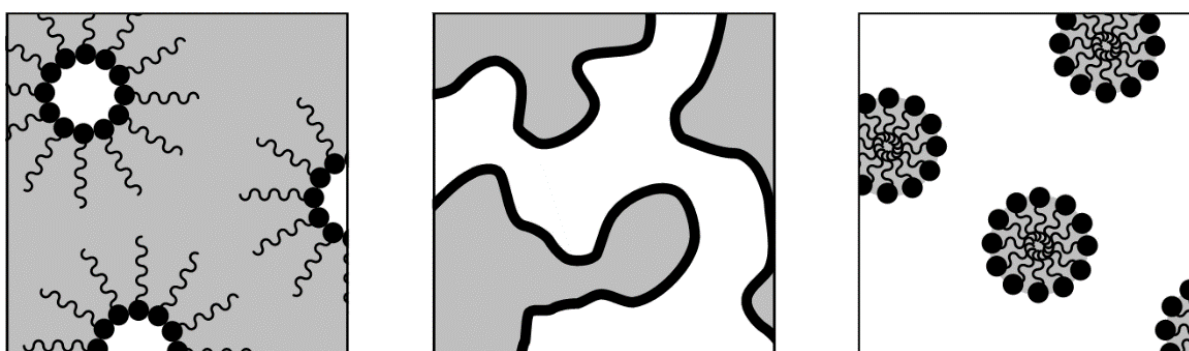
Figure 1.7: Depictions of a w/o emulsion, bicontinuous structure, and o/w emulsion, left to right, respectively. Grey and white areas represent the oil and water phases, respectively, and black lines represent surfactants.

1.1.4.2 Co-surfactants

In some cases (typically for ionic surfactants), the CMC of a surfactant or the solubility limit will be achieved before the interfacial tension is low enough to form a microemulsion and in these cases a co-surfactant can be employed.[1]

Co-surfactants are surface active and therefore can be considered surfactants; however, they do not form micelles above their solubility limit. Instead, they will simply form a new phase. Common co-surfactants include short chain alcohols or amines, which have small head groups, which can aid in packing of the molecules at the interface, allowing the interfacial tension to drop even lower than it would with only the surfactant.[16]

1.1.5   Structured Ternary Fluids (STFs)

1.1.5.1   Background

Ternary mixtures of two virtually immiscible solvents, combined with a hydrotrope that can solubilise both, enables emulsions with extraordinary stability to form.[22] This phenomenon is called the 'Ouzo effect', named after the popular liquor in which it is observed. While the first example of such a mixture was first reported by Smith *et al.*[17] in 1977, this 'Ouzo effect' was only officially named in 2003.[30] It then wasn't until 2012 when Klossek *et al.*[18] confirmed the presence of well-defined aggregates in the area of the phase diagram known as 'the pre-Ouzo' region, defined as the monophasic, transparent domain close to the phase separation boundary. In this region, there is insufficient water to cause the phase separation and hence visible clouding that is indicative of the Ouzo effect. Scattering experiments, backed up with molecular modelling studies[18-28] have determined three structures within this region: pre-Ouzo aggregates, bicontinuous phases, and reverse micelle-like morphologies (Figure 1.8) and hence a structured ternary fluid (STF) exists within this pre-Ouzo region. Structuring within this entire pre-Ouzo region, which borders the biphasic region, may help to explain the unexpected stability of ouzo emulsion droplets. In particular, there is X-ray and neutron scattering evidence that a dynamic equilibrium exists between STF and the larger ouzo emulsion droplets, similar to processes observed within nanoemulsions.[28,29]

In the 1970s, 'detergentless microemulsions' (or surfactant-free microemulsions), were reported by Smith *et al.*[17] when it was observed that three optically transparent phases (an oil, aqueous and alcohol-rich phase) formed upon centrifugation. This is akin to the Winsor III classification of traditional microemulsions, though here the three phases consisted of an oil layer, alcohol-rich layer and an aqueous layer. It was determined recently that the formation of these 'detergentless microemulsions' requires some polarity within the oil phase, and that the stabilisation is not due to film bending energies or film entropies, as is the case in traditional (rigid or flexible) microemulsions. Instead, stability arises due to the balance of hydration forces vs entropy of mixing in the system and

so the term 'ultra-flexible microemulsion' (UFME) was coined.[21-23] In this work, the term STFs is used

preferentially over UFMEs as this facilitates discussion of the whole ternary phase diagram.
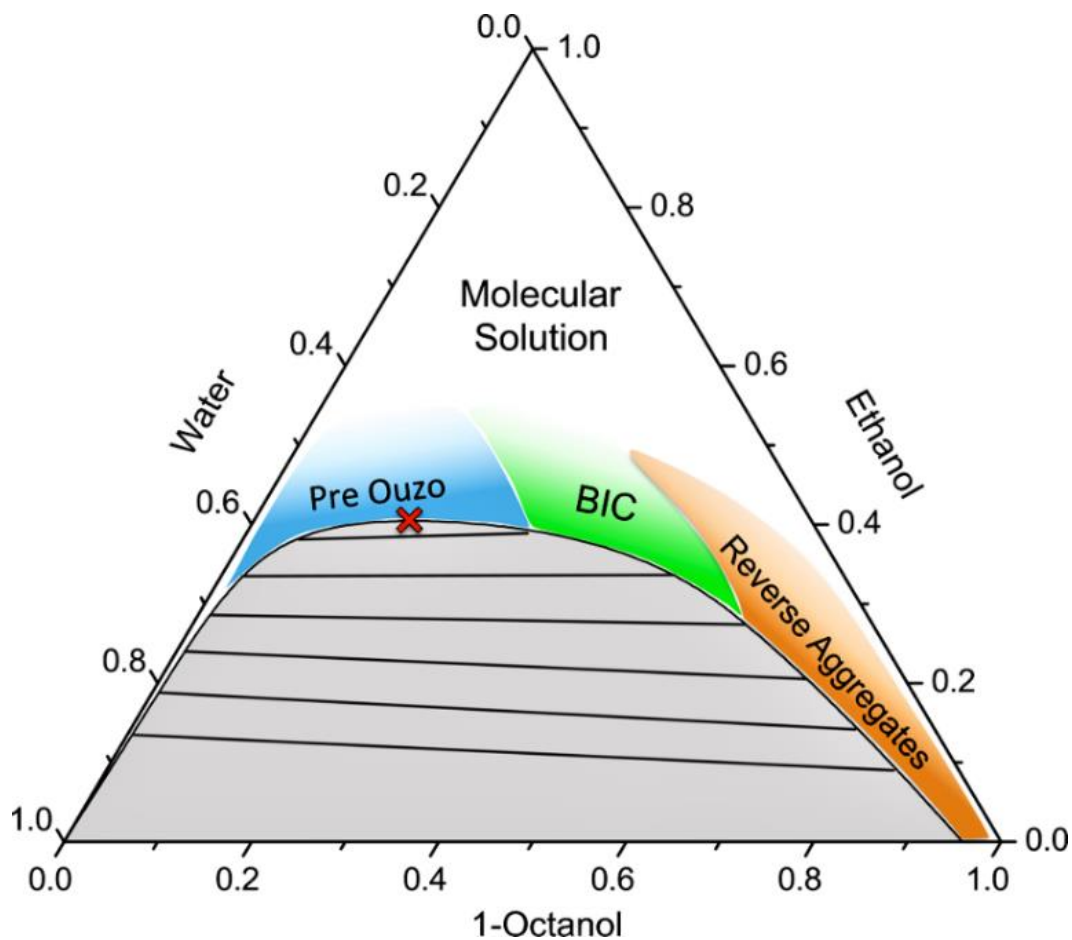
Figure 1.8: Schematic representation of the structuring in the monophasic region above the phase separation border, the colour gradient in the domains represents the structuring becoming less pronounced at higher concentrations of ethanol. Black lines represent tie lines in the biphasic region.[23]

1.1.5.2   Formation

In the last decade, researchers including Zemb, Schöttl, Kunz, Prévost, Klossek, Diat, Marcus, Lopian,

and Horinek (amongst others) have been collaborating on innovative research of STF systems,

particularly that of 1-octanol, ethanol, and water mixtures.[18-28] They have provided much evidence

using molecular modelling, as well as X-ray and neutron scattering techniques, to elucidate a detailed

phase diagram and a theory behind the structuring found. While the following studies were performed

with an STF comprising octanol/ethanol/water, this theory should apply ubiquitously to other systems

in which the Ouzo effect is evident.

11

It has been identified that in the pre-Ouzo region of the phase diagram where nano-structuring occurs, the polar and non-polar phases (water and 1-octanol, respectively) are spatially separated into different domains. This is depicted in Figure 1.9.
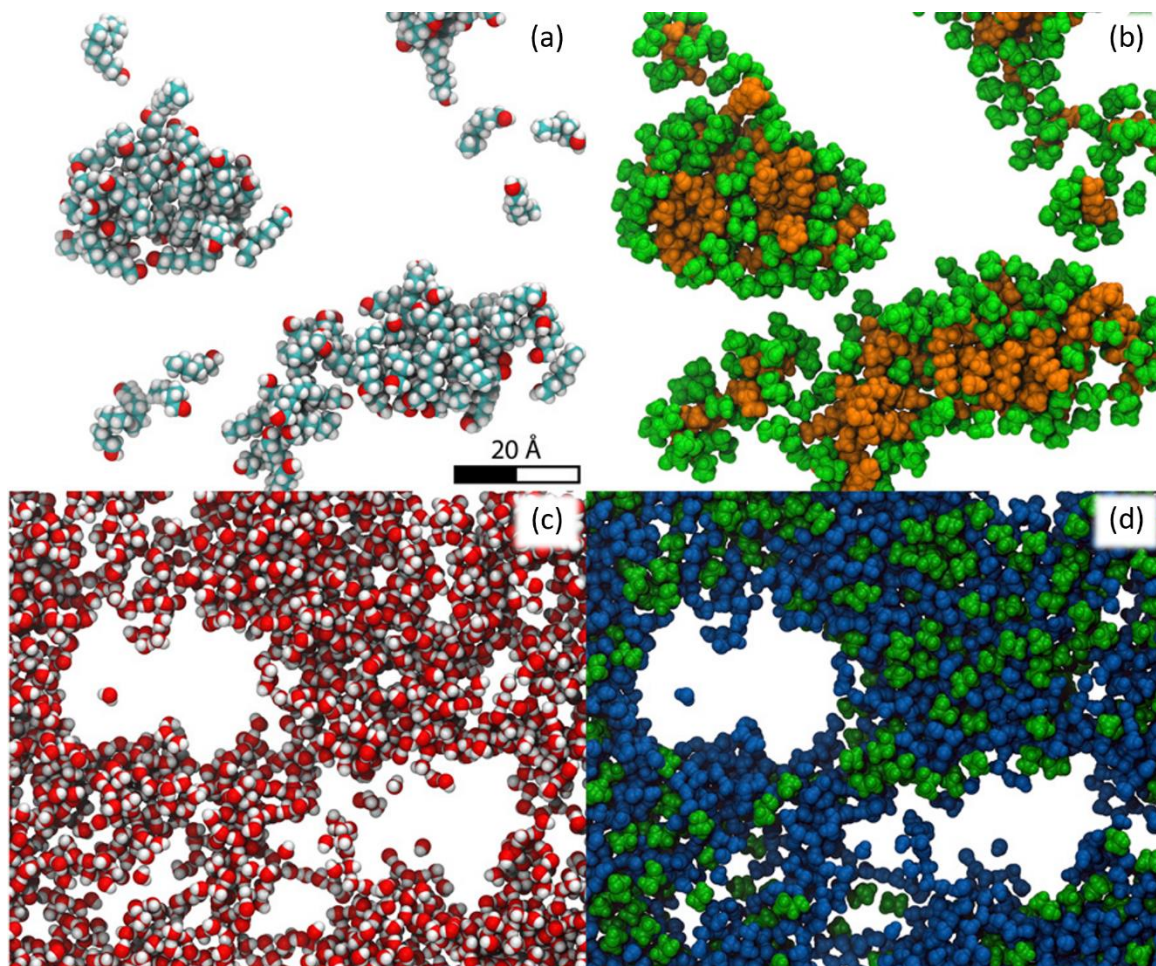
Figure 1.9: Snapshots from molecular dynamic simulations performed by Zemb et al. showing the single-phase pre-Ouzo system comprising octanol and water weight fractions of 0.2 and 0.8, respectively (a) Octanol molecules only, (b) ethanol molecules (green) bound to octanol (orange), (c) water molecules only and (d) ethanol molecules (green) bound to water (blue),.[22]

Here the hydrotrope (ethanol) can solubilise both octanol and water, and therefore tends to accumulate into a diffuse interface between the two domains. It should be noted that octanol does not act as a surfactant in this system.[22]

For this structure to be stabilised, there must be a corresponding minimum in the free energy of the system. In contrast to traditional microemulsions, this system contains neither electrostatic repulsions

to prevent coalescence of nanodomains, nor bound surfactant molecules to significantly lower interfacial tensions and influence size and shape of micellar aggregates.[22]

This problem was addressed through investigation of the three main contributions to the free energy of these complex solutions: entropy of mixing, free energy of hydration, and van der Waals forces. Firstly, the entropy associated with dispersing one immiscible phase in another will always tend to drive a system towards smaller dispersed domains in order to increase mixing between the two phases as this increases the system's configurational entropy.

Secondly, the hydration force is a typically repulsive force that acts between two surfaces separated by water layers at short surface separation distances of a few nanometres. This arises due to the interaction between the surfaces and the water molecules, which may induce dipole orientation and/or water packing into quasi-layers. Taking octanol-in-water STFs as an example, the ethanol-rich interfaces of the octanol aggregates may induce such orientation of water molecules, meaning the hydration force is significant at this interface. This produces a net repulsion of the octanol aggregates due to the energy required for perturbation of the ordered, bound water layers. Thus, the hydration force favours larger aggregate structures that reduce the total interfacial area. This was modelled as an exponentially decreasing function with surface separation (Figure 1.10).

Finally van der Waals terms associated with attractive dispersion forces between aggregates were considered. However, in comparison to the entropy and hydration effects, the van der Waals term was found to be negligibly small. The non-negligible hydration and entropy contributions to the total free energy of the system are illustrated in Figure 1.10.[22] This is plotted against the correlation length, ξ, related to the separation between aggregate surfaces. A broad, shallow minimum is present here at a correlation length of approximately 2 nm, allowing for the formation of the polydisperse domains observed experimentally.
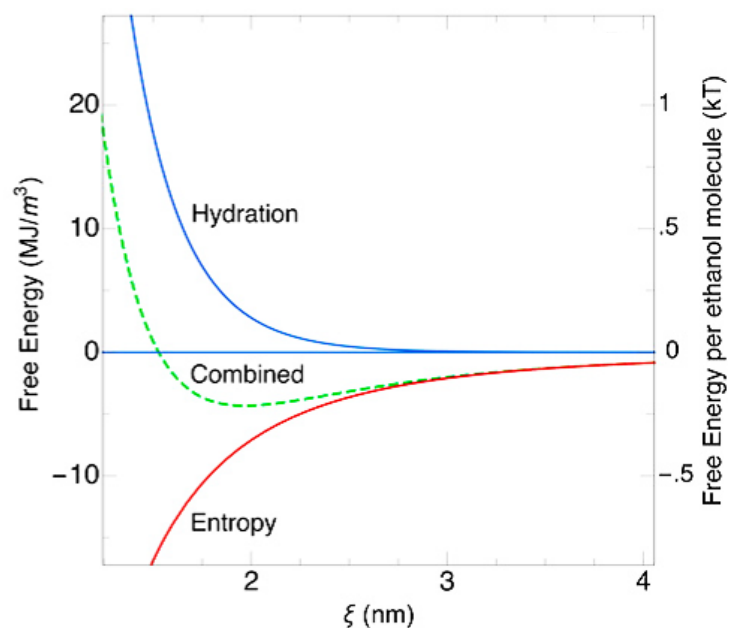
Figure 1.10: A graph showing the contributions of entropy and hydration forces to the free energy of the UFME system (per unit volume of sample, left scale, and per ethanol molecule, right scale) against the correlation length, ξ.[22]

When the concentration of ethanol is then increased further, moving out of the pre-Ouzo region and up the phase diagram to the ethanol apex (Figure 1.8), it was found that microstructuring disappeared and simple molecular solutions formed.[22]

1.1.5.3   Characterisation

Studies have been performed to understand the morphology and behaviour of STF nano-structures, moving from the octanol-rich to the water-rich areas of the pre-Ouzo region (Figure 1.11). In the water-rich domain, the scattering curves of both water and octanol were near identical, as well as being large in scattering intensity. This suggests the presence of two distinct domains with relatively large clusters of octanol. For octanol-rich STFs, the spectra closely resemble the binary case of octanol/ethanol which suggests a homogeneous distribution of the two alcohols.[28]

When considering the ethanol spectra across the series, there is little variance in their appearance, suggestive of an even affinity between water and octanol domains. In water-rich STFs, scattering does differ greatly from the octanol and water curves, meaning it does not relate directly to either domain. This supports the theory that an excess of ethanol exists at the boundary between the two immiscible domains.[28]
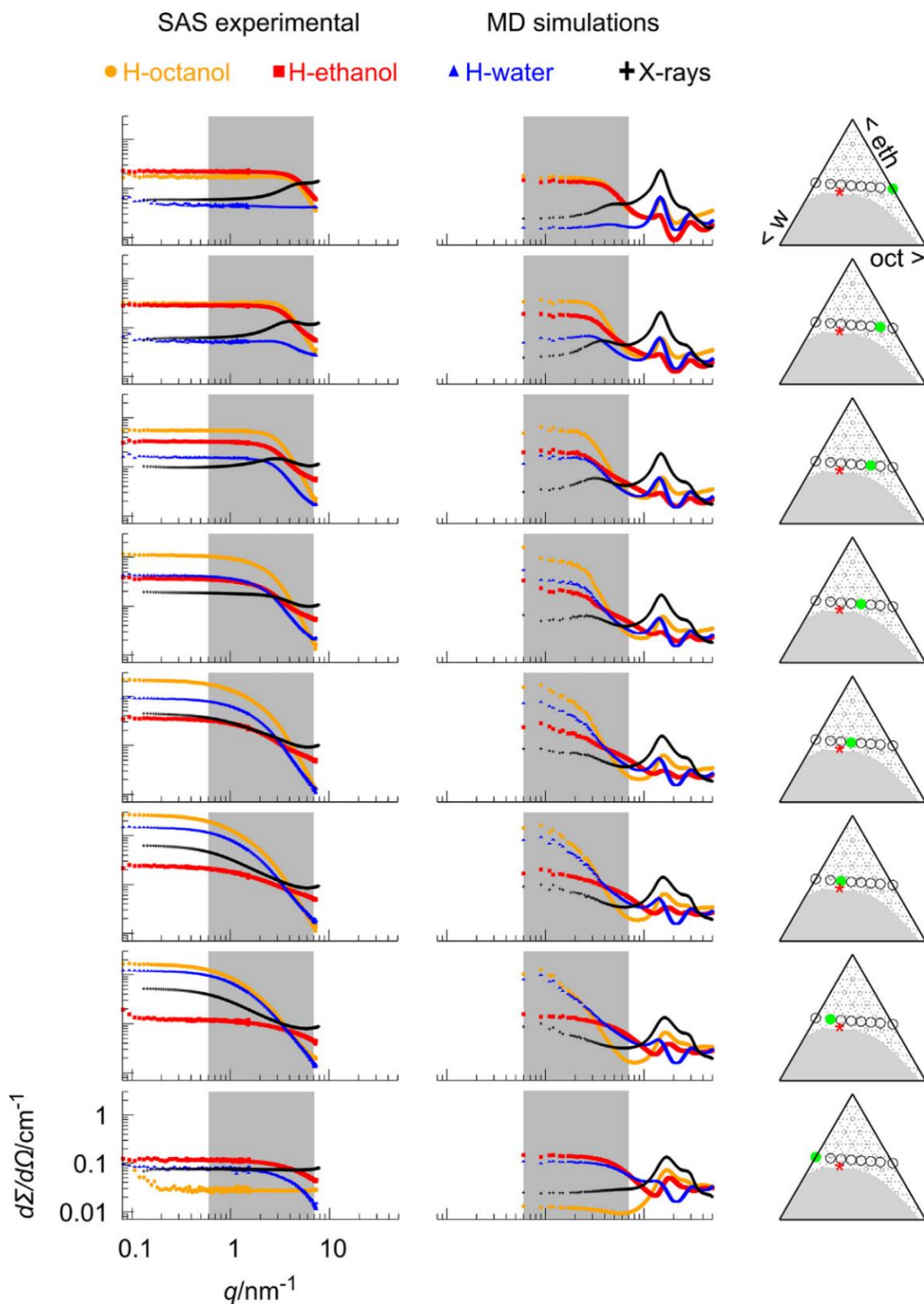
Figure 1.11: Experimental and simulated small angle scattering (SAS) curves for eight samples along a dilution line from high octanol content (top) to high water content (bottom), maintaining a constant mass fraction of ethanol. Grey areas indicate common q-ranges for each set of data, where q is the scattering vector related to the difference between in the incident and scattered waves. The hydrogenated (H) octanol, ethanol and water curves refer to neutron studies where the other two components are deuterated, allowing the scattering from the hydrogenated species to be elucidated. The X-ray curves reveal scattering from regions with electron density contrast.[28]

15

Molecular dynamics simulation snapshots have been taken within the water-rich and octanol-rich domains. In the water-rich sample (left, Figure 1.12) large octanol aggregates surrounded by bound ethanol molecules are present. The continuous phase in this case is a molecular solution of water with the remaining ethanol. There are water-free regions within this continuous phase, implying the existence of entirely separated octanol domains.
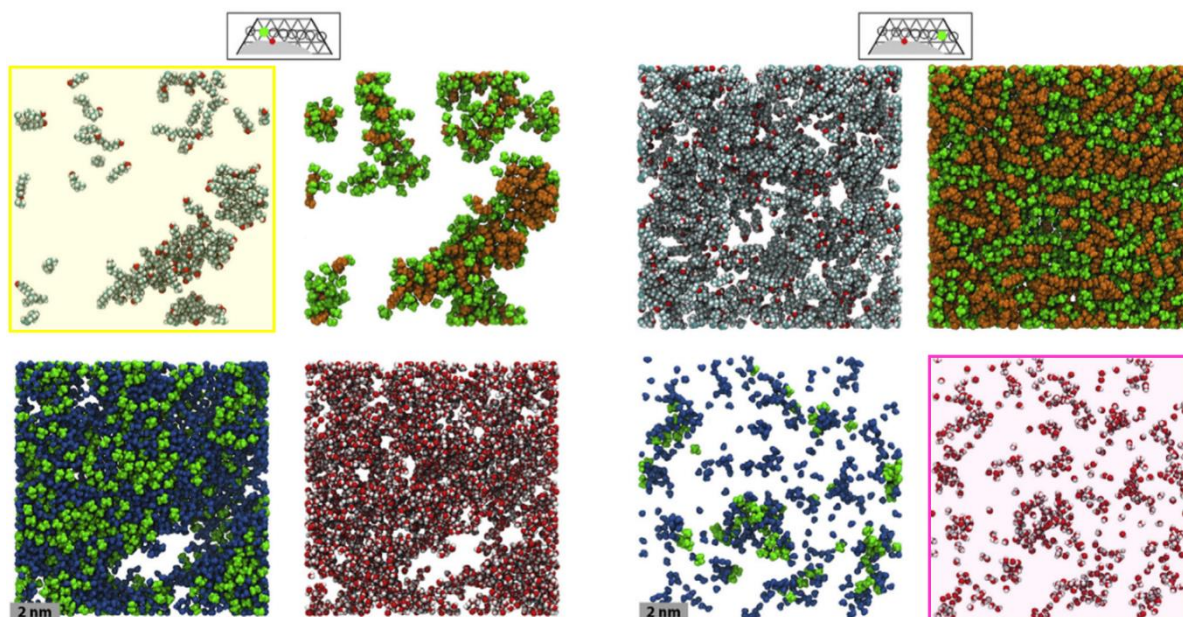
Figure 1.12: Snapshots of molecular simulations run by Schöttl et al..[28] For each sample on the phase diagram the boxes moving clockwise contain: n-octanol molecules only, ethanol (green) bound to n-octanol (orange), water molecules only, and ethanol (green) bound to water (blue). Octanol and water dispersed-phase aggregates are highlighted in yellow and pink, respectively.

In the octanol-rich sample (right, Figure 1.12), the water molecules appear to form more diffuse aggregates, with monomeric water still present. In this case, the ethanol molecules do not form a consistent interface around water aggregates. The continuous phase does not contain any regions in which discrete water pockets may exist, suggesting that the water molecules may be involved in more of a three-dimensional random network. It appears that the hydroxyl groups of the octanol molecules form a network that is extended by ethanol. Water is incorporated into this hydrophilic network through local aqueous swelling (Figure 1.13). This has been described as reverse micellar aggregates in previous papers, as the swollen aqueous regions still appear to form some pockets, albeit smaller and less distinct than the octanol aggregates.[23,24,28]
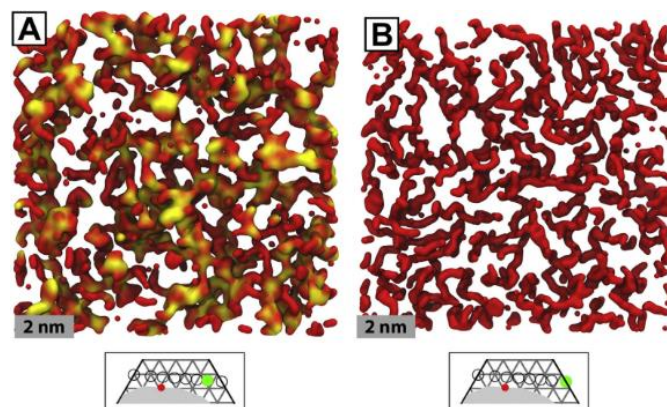
16

It should be noted that in the intermediate region between the water-rich and octanol-rich phases, the samples still behaved as a bicontinuous microemulsion of two distinct water and octanol domains separated by an ethanol boundary region.[24,28]

1.1.6   Response to additives and temperature

It has been shown that pre-Ouzo aggregates are sensitive to salts.[23] Upon addition of electrolytes to the water-rich phase, a salting-out effect towards ethanol takes place. This has the effect of driving the ethanol molecules towards the interface of, and even inside, the octanol aggregates, so increasing the size of these domains. This is not always the case, however. Antagonistic salts consist of chaotropic (structure-breaking) and kosmotropic (structure-making) ionic components, meaning they weakly or strongly interact with water, respectively (essentially hydrophobic and hydrophilic in this case). Upon addition to UFME structures, these salts partially adsorb to the interface and cause a charge separation, creating an additional electrostatic repulsion term, stabilising the aggregates and transforming them into micelles more closely resembling those formed using surfactant/co-surfactant with an excess of anionic surfactant.[23]

Additionally, the effect of introducing sulfuric acid has been investigated. Upon increasing the concentration of acid in the aqueous domain, the maximum of the binodal (closer to the water-rich area) decreases, increasing the monophasic area. This may be due to the presence of a second hydration force, or through an increased accumulation of ethanol in the interfacial region. Sulfuric

acid present in the water phase reduces the solubility of water in octanol at equilibrium even further, and the clustered networks described by Figure 1.13 will be less energetically favourable to form.[26] It was also observed that it was only in concentrations above 2 mol dm^{-3} that a significant change in the behaviour of these systems was recorded. Below this threshold concentration, scattering experiments confirmed the persistence of the aggregated structures.[26]

Finally, Zhang *et al.* investigated the effect of temperature on the phase boundary of the ternary phase diagram, recorded using conductivity and dynamic light scattering (DLS) experiments. It was found that upon increasing temperature, the area describing the monophasic region increased linearly due to the greater free energy weighting of entropy at higher temperatures (Figure 1.14). The effect specifically on the pre-Ouzo aggregated region was also determined, taking the upper boundary as the point at which aggregates were no longer detectable using DLS. It was observed here that the area describing the pre-Ouzo region decreased as a function of temperature.[31]
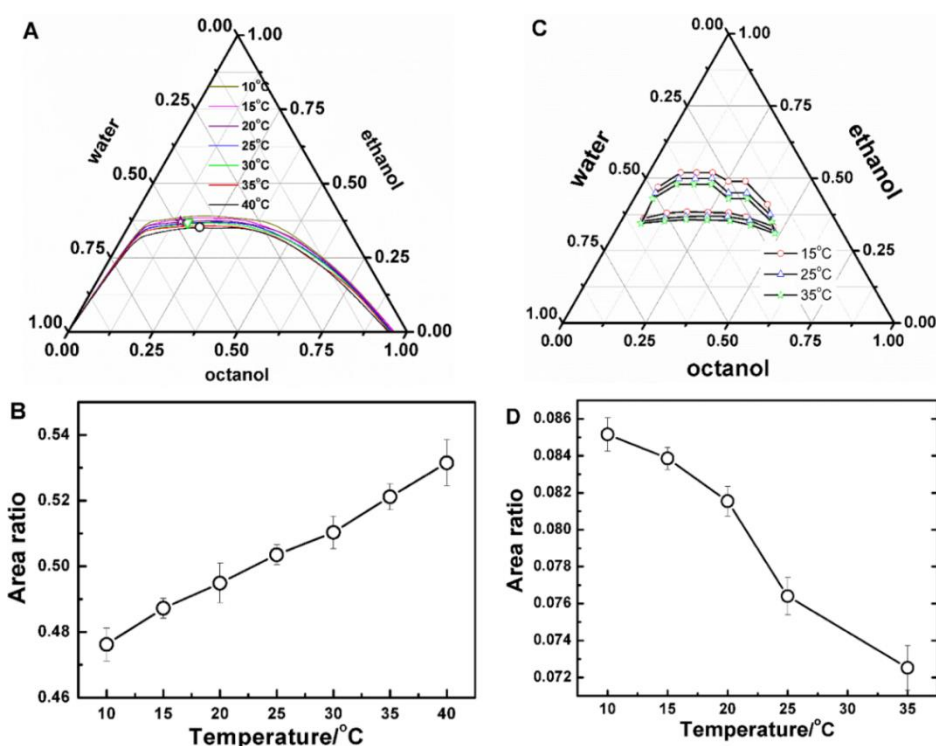
Figure 1.14: The effect of temperature on the ternary phase diagram. (A) shows the change in the phase boundary, (B) the change in relative area of the monophasic region, (C) the change of the pre-Ouzo region, and (D) the change in relative area of the pre-Ouzo region.[31]

1.1.7 Current STF research and use

STFs have proved to be effective solubilisers for many common household products, such as in mouthwash[20] or mosquito repellent.[31,32] Even perfumes often contain similar systems, whereby the nano-structuring may have influence over the vapour pressures of various components, affecting the performance of fragrances.[34,35]

STF systems may overcome several industrial limitations imposed by traditional surfactant-based systems. In particular, surfactants are small and not very volatile and therefore cannot be removed from a mixture by using filtration or evaporation methods during extraction processes.[24] Furthermore, surfactant molecules act as physical barriers around droplet surfaces which is problematic when considering applications where access in/out of the confined domains is required. As an exemplifier, Zoumpanioti *et al.*[36] established that lipase enzymes maintained catalytic activity at 30 °C while contained within a STF with the enzyme stability increased relative to analogous surfactant microemulsion systems.

There is a growing list of systems that can be characterised as STF systems. Some examples are listed in Table 1.2. Here, the majority of STF research has been based upon water as the polar phase. This is commonly found in surfactant-based microemulsions and so it is unsurprising that this class of STF has been the focus of research. However, there may be applications in which a non-aqueous alternative is required. While sparse, there are a few non-aqueous STFs that have been discovered, and this area of research is set to develop. To date, these investigations have focussed on understanding the structures formed in these systems, but there is no reason to suggest they may not be used in the same processes as their aqueous counterparts. Consequently, depending on its use, an STF may be selected to tailor an experiment to a wide range of conditions.

Table 1.2: Non-exhaustive list of STFs reported to date and the focus of current research.

First phase	Second phase	Hydrotrope	Characterisation techniques	Investigated Uses	Reference
Water	Hexane	Propanol	Visual inspection, Ultracentrifugation, Conductivity, ^{1}H NMR	Structural investigations, Nanoparticle synthesis, enzymatic and chemical reactions	[17,36-39]
	Toluene		Visual inspection, Ultracentrifugation, Conductivity, ^{1}H NMR	Structural investigations	[40]
	Oleic acid		Visual inspection, Conductivity, UV-vis, Surface tension, DLS, Cryo-TEM	Structural investigations, Stimuli responsive microemulsions	[41,42]
	Isopentyl acetate		Visual inspection, Cyclic Voltammetry, Fluorescence, UV-vis, DLS, Cryo-TEM	Structural investigations	[43]
	HDES		Visual inspection, Conductivity	Stimuli responsive microemulsions	[44]
	Ethyl Acetate		Visual inspection, Conductivity, UV-vis	Nanoparticle synthesis	[45]
	1-octanol	Ethanol	Visual inspection, SAXS, Neutron Scattering, MD-Simulation, Fluorescence, UV-vis, Conductivity	Structural investigations, Stimuli responsive microemulsions	[18-28,46]
	DCM		Visual inspection, Conductivity, UV-vis	Nanoparticle synthesis	[47,48]
	Tertiary amine		Visual inspection, Conductivity, DLS	Stimuli responsive microemulsions, Oil removal	[49]
	Diethyl malonate		Visual inspection, Conductivity, UV-vis, DLS, TEM	Solubilisation technology	[50]
	HDES		Visual inspection, Conductivity, UV-vis	Stimuli responsive microemulsions, Nanoparticle synthesis	[51]
	MMA	1-butanol	Visual inspection, Conductivity, UV-vis, Surface tension, DLS	Nanoparticle synthesis	[52]
bmimBF$_4$	Toluene	Ethanol	Visual inspection, Conductivity, dielectric relaxation spectroscopy	Structural investigations	[53]
Glycerol	Octanol		Visual inspection, DLS, SAXS	Structural investigations	[54]

To prove the existence of structuring within the ternary fluids, many techniques such as small angle X-ray and neutron scattering,[19,22-24,28] and static and dynamic light scattering.[18,49,50] NMR, conductivity, UV-vis spectrometry of probe molecules and molecular dynamics have been used.[20,21,55-57] Most commonly, the procedure for analysing an STF will first involve the development of a phase diagram using visual observations, through mixing components titrimetrically and observing the turbidity of the resulting fluid. Then, the pre-Ouzo region will be investigated through conductivity measurements. However, to form a clearer understanding of the properties of the STFs, additional spectroscopic and scattering techniques should be used. For example, many of the studies outlined in Table 1.2 also utilise UV-vis spectroscopy and light scattering techniques for relatively quick results. When selecting an STF for an application, it is suggested that at least a combination of visual inspection, conductivity and UV-vis should be used to confirm the presence of structuring. For more rigorous structural studies, more complex techniques such as dynamic light scattering, cryo-TEM, X-ray and neutron scattering, as well as computational methods should also be used to confirm the nanostructures present and provide a much clearer picture.

Initially, the focus of research into these systems was on determining the structures present and understanding the mechanism of their formation and stability.[17,40] In the last decade, research has begun to move towards potential applications.[45-52] In theory, STFs should be directly analogous to traditional surfactant microemulsions and so could find application in areas such as food technology, drug delivery, and nanoparticle synthesis. So far, there has been the most effort in the latter application. Nanoparticles such as silica,[47] Ag_2CO_3,[38] BaF_2[51] have been successfully synthesised, using the nanodomains as templates to precipitate the materials with uniform spherical morphologies. Additionally, there has been interest in developing stimuli responsive STFs, which may undergo demulsification with changes in temperature, pH, and by introducing CO_2 into the system.[44,46,49,51] This is again useful in nanoparticle synthesis as it may be helpful in the extraction of the suspended nanoparticles by simply 'turning off' the microemulsion structures.

To-date, studies on particle formation have focused on the particle morphologies obtained, rather than the crystallization kinetics.[47,52,58-61] Consequently, the effect of STF nanoconfinement on crystallisation has not been considered. In this work, we reveal the unique crystallization kinetics in these systems and demonstrate the extensive potential these systems have for understanding and controlling crystallisation.

1.2 CRYSTALLISATION

A crystal is a solid material in which the constituent components are arranged in a highly ordered, repeating structure, called the crystal lattice. The process in which these materials are formed is known as crystallisation, which occurs in two stages, nucleation, and growth. For this to occur the system must be supersaturated, where the crystallising solute must be in concentrations higher than the saturation limit of the system.

Nucleation is the creation of a new phase inside another. Classical crystallisation theory describes this as the formation of small solid clusters of repeat units, otherwise known as crystal nuclei, out of a solution, or gas phase. After stable nuclei are produced, they will continue to grow until the supersaturation is relieved. In non-classical crystallisation, multiple nucleation events take place, forming nanoparticles which aggregate into a close-packed crystalline superstructure. In some cases, this may occur from an initial amorphous cluster capable of reorganising into an ordered structure.

If a crystal grows from a single nucleus continuously with no grain boundaries and therefore has infinite long-range order it is known as a single crystal. Polycrystalline materials still have an ordered structure, but it is local as there are multiple different orientations. Conversely, if a material contains no long-range order it is known as amorphous.

1.2.1 Supersaturation

Crystallisation is driven by the supersaturation of the system. This may be described as the difference in chemical potential, $\Delta\mu$, between the bulk crystal and the solute.[17]

$$\Delta\mu = k_B T \ln(S) \qquad (1.8)$$

where k_B is the Boltzmann constant, T is the temperature, and S is the supersaturation ratio, i.e. the solute concentration, c, divided by the concentration at saturation, c_{sat}.[52,66]

The supersaturation ratio is often the parameter used to quantify the level of supersaturation, where a value greater than one describes a system that is above the saturation limit. This is typically regarded as a "supersaturated solution".

Supersaturation can be controlled by changing the concentration or the temperature of the system, as demonstrated by the solubility curve in Figure 1.15. Here, three regions can be described:

1. The undersaturated zone, where the amount of solute in solution is below the solubility of the system and it is therefore stabilised with respect to crystallisation. Any existing nuclei will dissolve.

2. The metastable zone, where the system is supersaturated, but the system is metastable with respect to crystallisation and nucleation will not be immediate.

3. The labile zone, where the system is more supersaturated than the metastable zone, so the system is unstable with respect to crystallisation, and nucleation will be immediate.
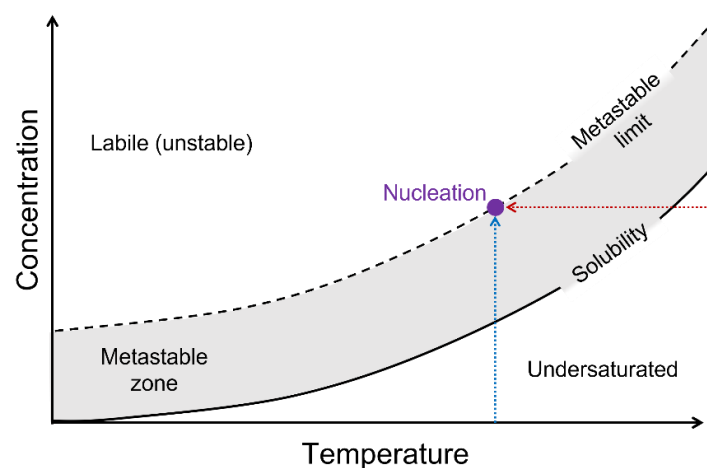
Figure 1.15: Solubility curve schematic.

For example, at a fixed concentration (red line, Figure 1.15), if the solution is cooled from a high temperature where the solute is fully dissolved, the system will pass through the metastable zone

until the metastable zone limit is reached and the solute will crystallise. The same result can be achieved by increasing the concentration of a solution at a fixed temperature (blue line, Figure 1.15), or a combination of both.

1.2.2 Classical nucleation theory

1.2.2.1 Homogeneous nucleation

The foundations of classical nucleation theory were laid out in work by Gibbs in the 1870s[62] and later built upon by Volmer and Weber,[63] Becker and Döring,[64] and Frenkel.[65] Classical nucleation theory describes the formation process whereby single molecules may come together to form clusters. These clusters, or nuclei, will exist in equilibrium with the surrounding solution and can also shrink, or redissolve by the removal of single molecules. Most nuclei will initially be made of only a few molecules and will break back up into their individual units. However, there is some chance that a cluster, now known as a critical nucleus, will contain a large enough number of molecules to have equal probability of growing or dissolving.

During homogeneous nucleation, individual molecules will come together in the interior of a solution (i.e. away from the surface or walls of the container) to form a nucleus of radius, r. This results in the formation of a solid interface within the liquid solution which relates to a change in the Gibbs free energy, ΔF, for the system.[62] This can be separated into contributions from surface area and volume changes, ΔF_S and ΔF_V, respectively. ΔF_V relates to the bulk free energy, and ΔF_S to the work required to create a solid/liquid interface.

$$\Delta F_V = -i(\Delta \mu) \tag{1.9}$$

$$\Delta F_S = \gamma \Delta A \tag{1.10}$$

where i is the number of molecules in the cluster, γ is the surface tension, A is the surface area, and $\Delta \mu$ is the change in the chemical potential and relates to the supersaturation, $\Delta \mu = k_B T \ln S$. Assuming a spherical nucleus, the free energy terms become:

$$\Delta F_V = -\frac{4\pi r^3}{3v} k_B T \, lnS \tag{1.11}$$

$$\Delta F_S = 4\pi r^2 \gamma \tag{1.12}$$

where v is the volume of a single molecule. Therefore, the final expression for the homogeneous nucleation free energy is:[66]

$$\Delta F_{homo} = -\frac{4\pi r^3}{3v} k_B T lnS + 4\pi r^2 \gamma \tag{1.13}$$

For small nuclei, with a low value of r, the two terms may be competitive. However, ΔF_V scales with r^3 as opposed to ΔF_S which scales with only r^2, and therefore the ΔF_V term will dominate as r increases. This is depicted by the free energy curves depicted in Figure 1.16.[68]
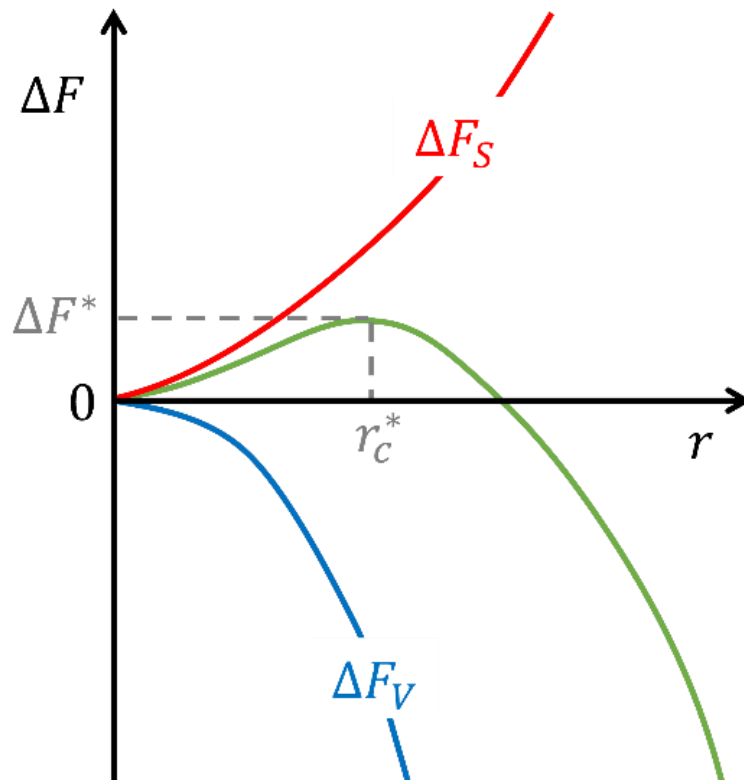
Figure 1.16: Depiction of a free energy curve to describe the change in free energy as a function of nuclear radius. Note, the green curve will reach some minimum in free energy at larger r, due to the depletion of supersaturation in the system.

The green curve represents the resultant free energy profile for a typical crystallisation, which has a maximum at a radius corresponding to the critical nucleus, r_c^*, and relates to the activation energy required for nucleation to occur, ΔF^*. The (subcritical) nucleus will likely redissolve back into solution

if it does not match or exceed r_c^*, whereas post-critical nuclei are more likely to grow than dissolve. The relationship between the size of the nucleus and its solubility is given by the Gibbs-Thompson equation:

(1.14)

$$lnS = \frac{2\gamma v}{k_B T r_c^*}$$

This equation is obtained by calculating the derivative of Equation 1.13 and setting it to zero to find an expression for r_c^*, which then gives ΔF^* as:[70]

$$\Delta F^* = \frac{16\pi\gamma^3 v^2}{3(k_B T lnS)^2} = \frac{4\pi\gamma r_c^{*2}}{3} \qquad (1.15)$$

The rate of nucleation, J, depends on the rate of impingement of the individual solute molecules onto the nuclei, W^*, and the equilibrium concentration of critical nuclei, $n(i^*)$.

$$J = W \times n(i^*) \qquad (1.16)$$

$$n(i^*) = n \exp\left(-\frac{\Delta F^*}{k_B T}\right) \qquad (1.17)$$

where n is the concentration of solute molecules. In any system, although the total energy will remain constant at a constant pressure and temperature, there will likely be localised fluctuations in supersaturation. The areas with the highest localised supersaturation will carry the largest amount of energy, which will promote nucleation.

Combining Equations 1.15, 1.16 and 1.17 gives the expression for the rate of homogeneous nucleation:[68,71,72]

(1.18)

$$J = Wn \exp\left(-\frac{16\pi\gamma^3 v^2}{3k_B{}^3 T^3 (lnS)^2}\right)$$

1.2.2.2 Heterogeneous nucleation

While homogeneous nucleation occurs away from any surface or interface, heterogeneous nucleation involves a foreign surface or interface for the crystal to grow on. Due to solid impurities or container walls/defects, this is often experimentally more likely. These foreign species catalyse nucleation by providing an alternative, lower activation energy route to nucleation compared with homogeneous

26

nucleation because the critical nucleus volume is decreased by an amount that depends upon the contact angle, θ, between the critical nucleus and surface.[70,72]

$$\Delta F^*(Heterogeneous) = f(\theta) \times \Delta F^*(Homogeneous) \qquad (1.19)$$

where $f(\theta)$ is the wetting factor:

$$f(\theta) = \frac{1}{2} - \frac{3}{4}\cos(\theta) + \frac{1}{4}\cos^3(\theta) \qquad (1.20)$$

which is equal to the ratio of the heterogeneous critical nucleus volume to the homogeneous critical nucleus volume, with θ given by Equation 1.21.

$$\cos\theta = \frac{\gamma_{c,s} - \gamma_{s,l}}{\gamma_{l,c}} \qquad (1.21)$$

where $\gamma_{c,s}$, $\gamma_{s,l}$, and $\gamma_{l,c}$ are the interfacial tensions between the crystal and surface, the surface and liquid, and the liquid and crystal, respectively (Figure 1.17).[73,74]
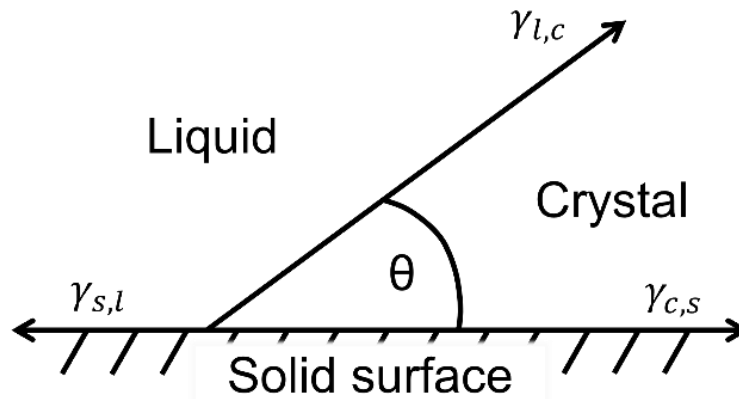
Figure 1.17: Depiction of the contact angle between three different phases during heterogeneous nucleation.

When $\theta = 180°$, $f(\theta) = 1$, and the crystal will detach from the surface, becoming independent, which simplifies to a case of homogeneous nucleation. At the other extreme, when $\theta = 0°$, $f(\theta) = 0$, and the free energy barrier is reduced to zero. The solution will completely wet the surface and the critical nuclei will form a strongly adsorbed monolayer on the surface.

1.2.2.3 Non-classical nucleation

Classical nucleation theory describes a case where crystal nuclei form from individual solute molecules coming together in a cluster. However, it has been argued that this is an oversimplified model, which gave rise to alternative crystallisation mechanisms, which are termed non-classical routes.[68] One of these involves a mechanism whereby multiple nucleation events take place, forming nanoparticles which aggregate into a close-packed crystalline superstructure, called a mesocrystal (Figure 1.18). Mesocrystals are typically short-lived intermediates as they are thermodynamically unstable due to their large interfacial areas, and so undergo mesoscopic transformations to form larger single crystals.[75]
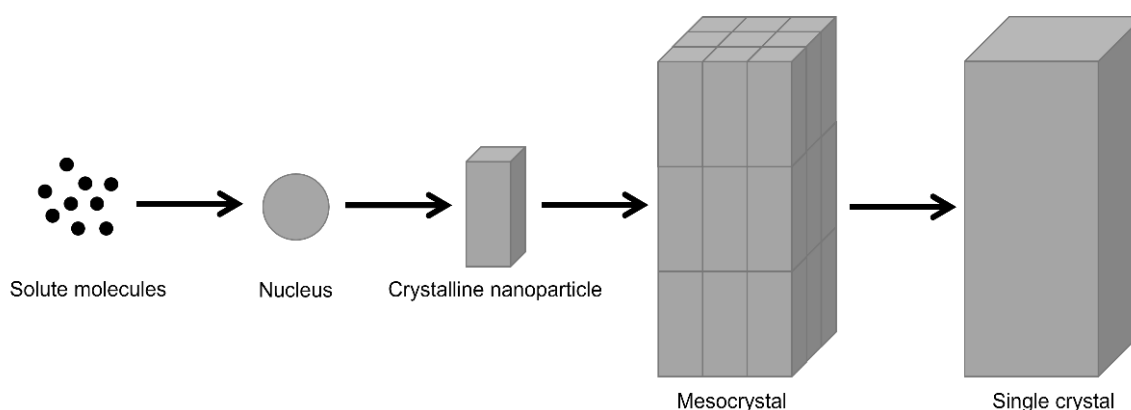
Figure 1.18: Depiction of mesocrystal formation in a non-classical nucleation process.

Another non-classical approach to nucleation, the two-step model, was first suggested by Wolde and Frenkel in 1997.[76] Here, it was suggested that by choosing a composition close to a liquid-liquid critical point, the free-energy barrier for nucleation is strongly reduced and critical concentration fluctuations may increase. These result in the formation of liquid-like clusters of individual solute molecules, followed by a molecular reorganisation within this amorphous phase into a more ordered structure. This was initially proposed with respect to protein crystallisation in Monte Carlo simulations, where the solute molecules have short-range interactions. It was reported that an intermediate, disordered, and highly concentrated liquid-like phase formed first. Then, beyond a critical size, crystalline nuclei may form inside these droplets with more long-range ordered structures. This has also been supported

through light and X-ray scattering studies, as well as fluorescence measurements into crystallisation of both proteins and more general colloidal systems.[68,76-81]

Further evidence for a two-step model was published in 2022 by Liao and Wynne,[82] where the laser-induced nucleation of glycine was studied, considering solutions away from a liquid-liquid critical point. Here, an amorphous phase of glycine was observed, and was found to survive for extended periods, before being "activated" using a high-power laser, or lower-power Raman excitation laser to induce nucleation. Glycine is a widely studied material with respect to crystallisation.[140-160] Previous studies, that did not involve laser-induced nucleation, did not record this initial amorphous phase prior to nucleation, indicating that the crystallisation route may depend on the conditions applied. For example, the use of D_2O as a solvent has been shown to direct the polymorphic outcome of glycine crystallisation,[184] and high supersaturations may aid in the initial formation of an amorphous phase, which may not necessarily be observed at lower supersaturation.[83] Other factors that may influence the crystallisation route include the use of additives,[202] or the rate at which supersaturation increases in a system, for example, through solvent evaporation.[84]

1.2.3 Crystal Growth

Proceeding nucleation, the second stage of crystallisation is crystal growth whereby solute molecules attach to the crystal surface. This is a lower energy process than nucleation and therefore is much more labile. Therefore, in conventional crystallisation processes, nucleation is slow and rate determining, and growth is fast.

The surface of a crystal may have different sites to which solute molecules may attach. These surface structures were suggested by Kossel, who proposed that a crystal surface could be modelled as lattices of cubic building blocks which will form layers with flat faces upon growth.[82-88] If a layer is incomplete, it would form steps and kinks as depicted in Figure 1.19.

A building block can now be added in one of three places:

1. On top of a face, bound on one side.

2. On a step, bound on 2 sides.

3. In a kink, bound on three sides.
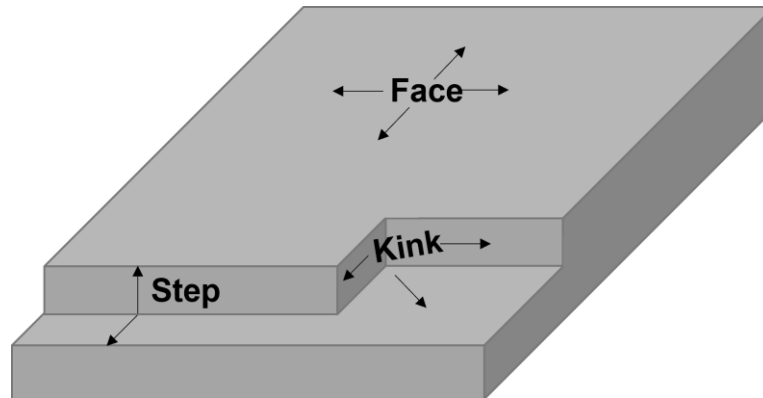
Figure 1.19: Depiction of a crystal structure, illustrating face, step and kink sites.

Additions to a kink site are energetically favourable in a supersaturated system, as a kink site defines the equilibrium position of a macroscopic crystal. This is because the detachment of a kink site molecule involves breaking three intermolecular bonds, whilst attachment to a kink site involves making three intermolecular bonds. So, at equilibrium, the rates of attachment and detachment to kink sites are equal. Blocks will therefore add at these sites until a row is complete. The next addition will then take place at the more unfavourable sites. This occurs by the formation of a 2D nucleus onto the flat surface, which is often slow (albeit faster than a new nucleation event) and therefore rate-determining.[72,88,89]

In Figure 1.19 the crystal faces are perfectly flat. However, crystals can undergo surface roughening at high temperatures and/or supersaturation.[88-91] At high supersaturation, this happens because the free energy barrier to 2D nucleation on the crystal face is so low that only a few molecules need to attach, creating multiple nucleation sites, and therefore roughening. In contrast, roughening due to temperature will only occur if the temperature is sufficiently high that the configurational entropy that increases due to the roughening outweighs the free energy cost of the reduced intermolecular bonding. Rough faces supply many more kink sites, leading to a continual growth mechanism. The rate

of growth is then proportional to the supersaturation of the system, and all crystal faces will generally grow at the same rate.[92]

The Kossel model assumes the crystal is perfect. However, in reality, it may contain defects and impurities. Screw dislocations (Figure 1.20) provide a permanent source of step sites on which the crystal may grow without the need for 2D-nucleation.[89,94] Consequently, this growth mechanism will therefore occur at low supersaturations when the free energy barrier to surface nucleation is too high.
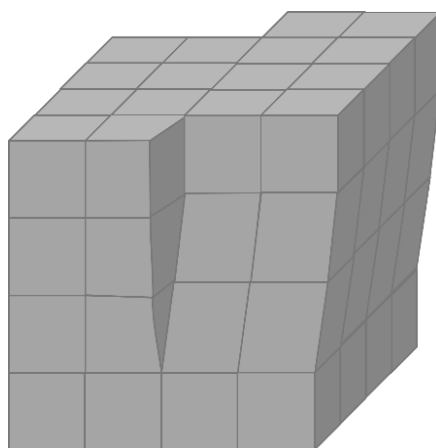
Figure 1.20: Depiction of a crystal structure containing a screw dislocation.

1.2.4   Polymorphism

Crystals with the same chemical makeup, but with different crystal structures, are termed polymorphs. They arise due to changes in the arrangement of atoms or ions in a crystal lattice.[95] Due to the differences in crystal structure, each polymorph will possess differences in physical properties such as melting point, colour, morphology, and solubility. This is of particular importance when considering drug formulations.[96]

A crystal may also undergo transitions between polymorphic forms, which can be induced through the introduction of additives,[97] mechanical grinding,[98,99] or by varying temperature or pH.[100,101] Over time, metastable polymorphs can transform to more stable ones, and this has important ramifications for drug formulations. If the most stable polymorph is not identified, the drug may transform unexpectedly, leading to complications with bioavailability and bioactivity. This was particularly

pertinent in the case of Ritonavir. This was an anti-HIV drug that was produced and administered in the 1990s. Two years post-marketing, the drug began to fail solubility quality-control measures because it had transformed into a more stable and less soluble polymorph. This had the effect of lowering the bioavailability of Ritonavir; it became ineffective and it had to be removed from the market, costing the producer hundreds of millions of dollars.[102]

Ostwald's rule of stages[103] states that metastable polymorphs will tend to form before stable ones, and consequently the nucleation barrier for the most stable polymorph is typically the largest, see Figure 1.21.[104,105]
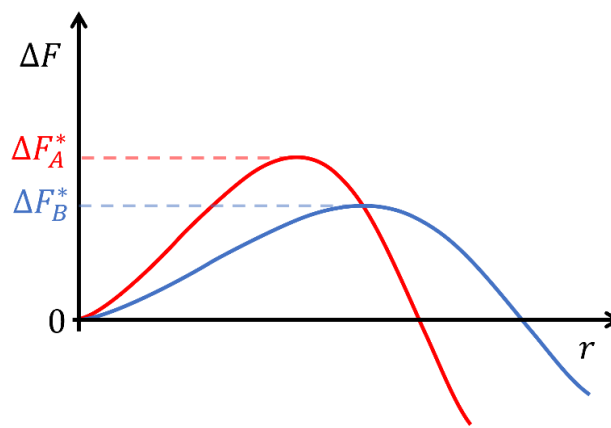
Figure 1.21: Depiction of the free energy change, ΔF, with nucleus size, r, for a bulk crystallisation.

1.3   CRYSTALLISATION IN 3D NANOCONFINED SYSTEMS

Following nucleation, as the post-critical nucleus grows, there is a decrease in supersaturation which gives rise to a minimum in the free energy when saturation is reached. In bulk solution, this typically arises when crystals are μm or mm-sized. However, in a 3D nanoconfined system, such as a droplet microemulsion or STF, this minimum can occur in the nm range, at a size denoted, r_{min}^*. The population of r_{min}^* nuclei is given by the Boltzmann factor:

$$exp\left(\frac{-\Delta F_{min}^*}{k_B T}\right) \tag{1.22}$$

where ΔF_{min}^* is the free energy change on obtaining the r_{min}^* crystal from the nanosolution. Therefore, for a bipolymorphic system, if $\Delta F_{min}^* \gg k_B T$, the population of r_{min}^* nuclei will be very low for both polymorphs (Figure 1.22(b)) and crystallisation will be greatly reduced.
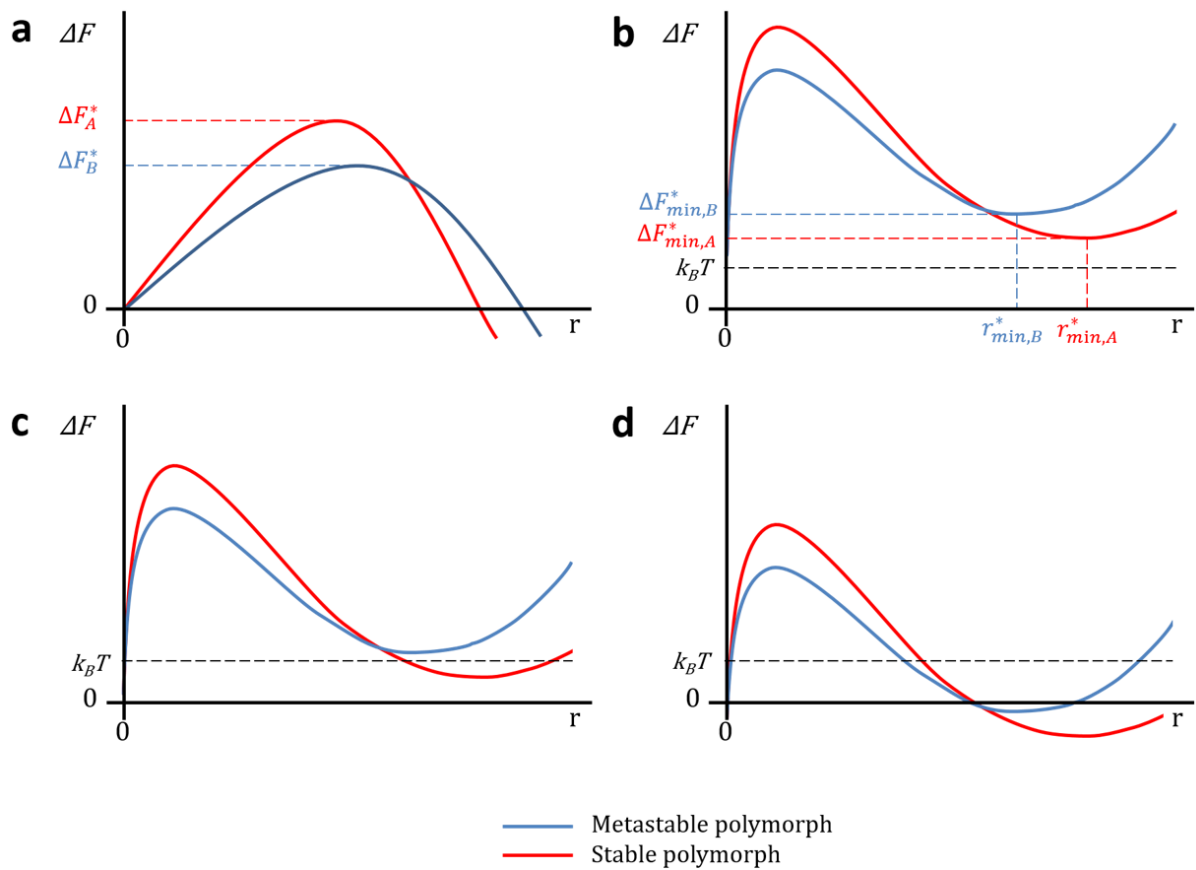
Figure 1.22: Depiction of the free energy change, ΔF, with nucleus size, r, for the crystallisation of two polymorphs, A and B (red and blue respectively) in bulk solution (a) and in 3D nanoconfined systems (b-d). (b) shows both minima are greater than k_BT. For (c), only the minimum for polymorph A is lower than k_BT, and so only A will crystallise (thermodynamic control). In (d), both minima are below k_BT (kinetic control).[66]

Conversely, if $\Delta F_{min}^* < k_B T$, the population will be much larger, meaning that a significant percentage of droplets will contain a (near) stable nucleus, particularly of the more stable polymorph, and crystallisation can progress (Figure 1.22(c)). Going further, if $\Delta F_{min}^* \ll k_B T$ (Figure 1.22(d)), then it is no longer just the stable polymorphic form that has a sizeable r_{min}^* nuclei population and hence both forms will crystallise, and kinetic control again dominates as in bulk solution.[66,107]

In droplet microemulsion systems, it is unlikely that crystals will grow in the continuous phase because the solute has very low/negligible solubility in this phase. Hence, crystallisation mainly proceeds from

collisions between microemulsion droplets. If the energy of collision is large enough, then transient dimers can form. This allows control over both nucleation and the growth rate of crystallisation, and can also help limit aggregation. If one of the colliding droplets was to contain a crystal nucleus, the concentration of solute in the surrounding solution would be depleted. Upon dimer formation, a concentration gradient would be generated, resulting in a flow of supersaturated material from the second, nucleus-free droplet into the first, allowing the nucleus to continue growing (Figure 1.23).[66]

For this process to occur, there must therefore be a pre-existing crystal nucleus in one of the colliding droplets prior to dimer formation. Consequently, the stability of the crystal nucleus becomes the limiting factor for crystallisation in microemulsions, rather than the ability to surmount the nucleation barrier, which limits crystallisation in bulk solutions. This means that thermodynamic control may be achieved in microemulsions to elicit the most stable polymorph, as only the most stable crystal nuclei of the most stable polymorph may be present during dimer formation, and hence grow.[66,109]

Compared with bulk solutions, the much greater reduction of supersaturation as the nucleus grows in microemulsion droplets means that much higher supersaturation levels are required to allow (near) stable nuclei to form. By increasing the supersaturation level, a microemulsion system can be altered from one that won't crystallise, i.e. it is stabilised due to nanoconfinement (Figure 1.22(b)), to one where only the largest and most supersaturated droplets are able to form (near) stable nuclei, usually of the most stable polymorph alone (Figure 1.22(c)). This is because the most stable polymorph typically has the lowest solubility, and therefore compared with other polymorphs, can grow into larger nuclei, r^*_{min}, prior to the depletion of supersaturation. This larger stable nucleus size and the inherent bulk stability result in the lowest value of ΔF^*_{min}. Following initial nuclei formation, growth can continue via transient dimer formation until either the supersaturation is alleviated, or the nuclei outgrow the dimensions of the host droplet and are therefore no longer confined.[66,109]
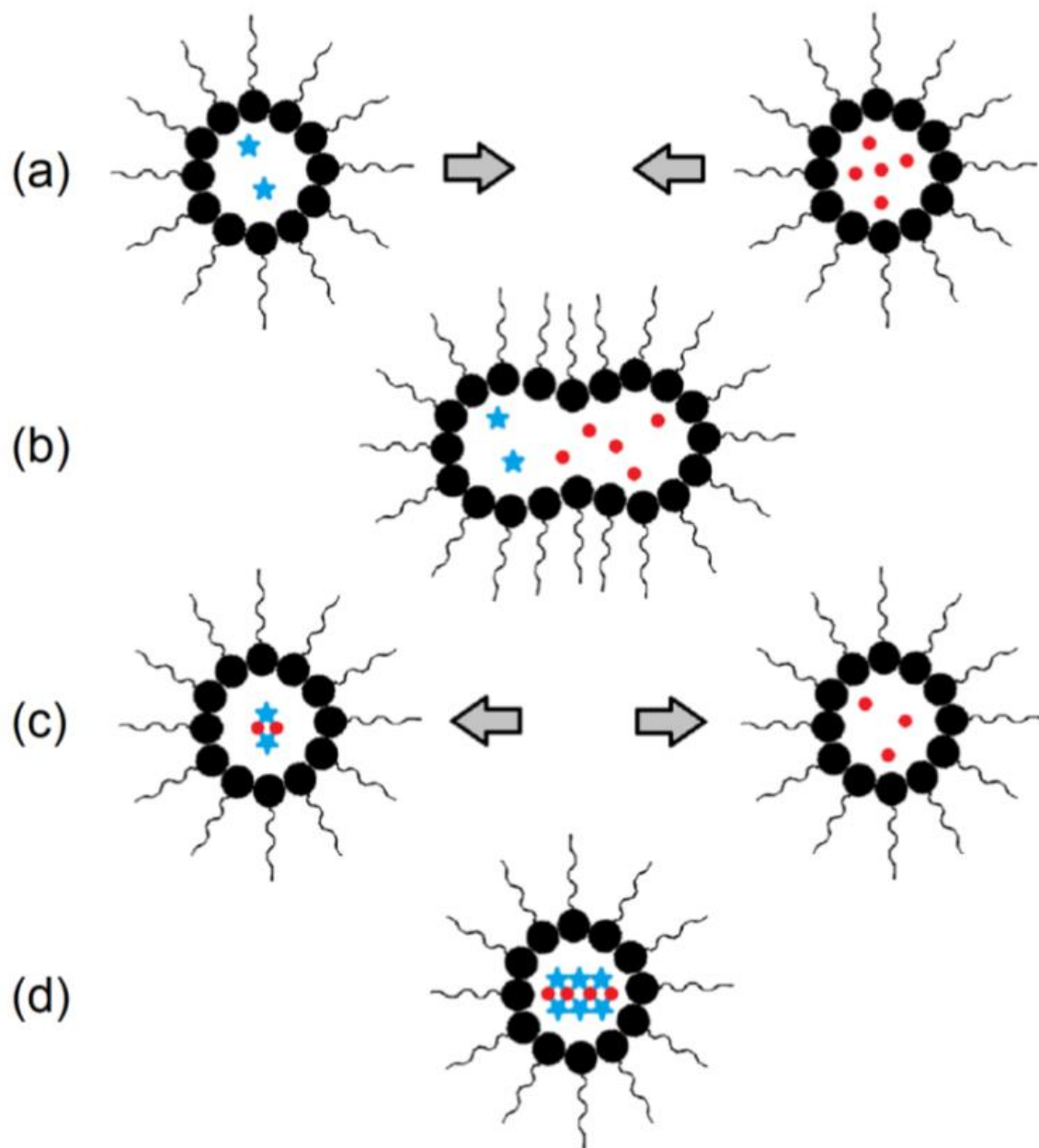
Figure 1.23: Schematic diagram illustrating the process of crystallisation within microemulsions. (a) Approach of two micelles. (b) Transient dimer formation. (c) Dimer break back into monomers. (d) Droplet containing larger crystal after repeated collisions.

Microemulsions have been successfully used in previous research to synthesise stable polymorphs of organic and inorganic materials.[104,105] This has been especially useful for materials which commonly only become crystalline under high temperature and pressure and would otherwise be amorphous. Cooper et al. have been investigating this methodology, producing the stable polymorphs of materials

such as glycine,[66,104-106] mefenamic acid,[66,104,106] dipicolinic acid,[106,108] nanographite,[109] hydroxyapatite,[105] titanium dioxide,[105] and more recently, silicon dioxide.[110]

Unfortunately, this technique is still of limited use on an industrial scale due to the small quantity of material that can be produced and the difficulty of removing residual surfactant from this small amount of material. The yield of nanomaterial is typically low in microemulsion syntheses for two main reasons. Firstly, the nanoconfined droplet phase is a small fraction of the overall microemulsion, and the solute confined within the droplets is a smaller fraction still. Secondly, the nanoconfinement of material can lead to such a slow rate of crystal growth that crystal dimensions are often limited to nm-μm sizes at the point of extraction. Hence centrifugation or ultracentrifugation is often required with subsequent clean-up further reducing yields.

The mechanism may be applied directly to any system in which the solute can be impermanently confined in an array of nm-sized pools. Therefore, STFs not only offer advantageous 3D confinement effects, enabling thermodynamic control over crystallisation, but they avoid the drawbacks of the difficulty in extracting the resulting crystals, and removing the stubborn residual surfactant from them.

1.4 PROJECT AIMS

This thesis aims to investigate the use of structured ternary fluids (STFs) in the crystallisation of glycine and other materials in confinement.

Chapter 3 investigates the use of STFs in the w/o microemulsion region to crystallise the thermodynamic polymorph of glycine selectively. The 15% water line will be characterised to show the difference between the confined and non-confined regions on the polymorphic outcome.

Chapter 4 explores STFs containing a mass fraction of 0.40 to observe the effect of different STF nanostructures on the polymorphic outcome of glycine crystallisation, moving from o/w microemulsion nanostructuring, through the bicontinuous region, and into the w/o microemulsion

region. Resulting nanocrystals will be used to seed bulk syntheses in order to ascertain the applicability of this method for larger scale, selective polymorph nucleation and growth.

Chapter 5 demonstrates the ubiquity of the crystallisation technique outlined in Chapters 3-4. The materials, ROY and quartz, will be used to exemplify this, with ROY historically being an important molecule in polymorph screening research, and quartz demonstrating the versatility as an inorganic crystalline structure, and not an organic drug/drug precursor.

Chapter 6 evaluates the theoretical work undertaken during the COVID-19 lockdowns. This will act as an introduction to molecular dynamics simulation aiming to model glycine in the STFs and looks at diffusion and motion of glycine within the systems.

Chapter 7 provides the overarching conclusions for the work presented in the thesis. This chapter will then cover other future directions for the project, including expansion of the work towards other materials, as well as other STFs.

2 EXPERIMENTAL TECHNIQUES

2.1 FOURIER TRANSFORM INFRA-RED (FT-IR) SPECTROSCOPY

FT-IR spectroscopy can be used to provide information about the chemical bonds present within a material. Light is only absorbed by a molecule if its frequency corresponds to the gap between molecular vibrational energy levels. This means that the wavenumbers at which light is transmitted depends on the characteristic vibrational energies of the molecule(s) in question. To collect a spectrum, infrared light is passed through a sample, and the intensity of transmitted light is recorded. A spectrum can then be separated into three regions dependent on wavenumber: the near-infrared (13,000 – 4000 cm^{-1}); the mid-infrared (4000 – 400 cm^{-1}); and the far-infrared (<400 cm^{-1}). In FT-IR spectroscopy, the transmission is recorded using a Michelson interferometer. Data then undergo Fourier transform, to present the spectrum as a function of wavenumber (cm^{-1}).

For solid and liquid samples, attenuated total reflectance (ATR) is used to measure the spectra without needing complicated sample preparation methods. A sample is placed on top of a crystal with a high refractive index such as diamond. If the sample is a solid, a metal anvil can be used to compress it onto the crystal surface to ensure good contact. An infra-red beam is then shone through the crystal at the angle required for the beam to undergo total internal reflections, and an evanescent wave is produced. This wave extends into the sample and can be absorbed. When the sample absorbs this radiation, the wave will be attenuated (reduced) and will produce a reduced signal when it is passed back into the main infra-red beam path and eventually into the detector (Figure 2.1).

The data in this report were obtained using a PerkinElmer Spectrum FT-IR spectrometer. A small amount of powdered sample was placed on the diamond surface of the main instrument platform before being compressed using a metal anvil. The sample was then scanned over a range of 4000 - 380 cm^{-1}.
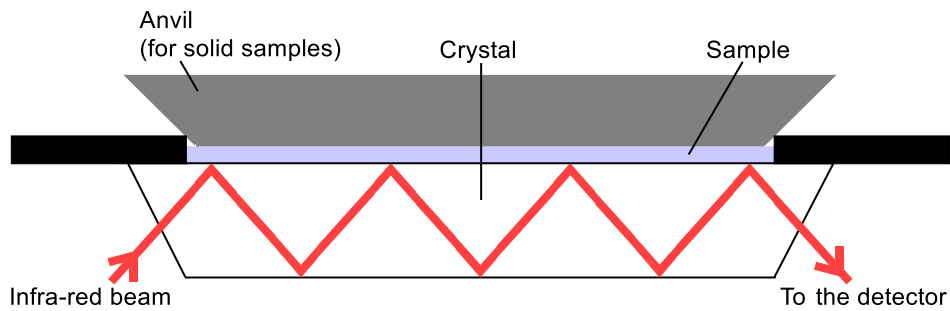
Figure 2.1: Diagram depicting the process of attenuated total reflection in FT-IR spectroscopy.

2.2 X-RAY SCATTERING AND DIFFRACTION

Upon collisions with an atom, incident X-ray beams can either be absorbed, resulting in electron excitation and ionisation, or the beam may be scattered which can be considered elastic; there is no loss of energy upon deflection. As a result, X-ray scattering experiments can be used as a relatively non-destructive method of providing information on the electron density and, by extension, on the structure of materials.[111,112] In a structure such as a crystal with a regular distribution of electron density on a length scale similar to the wavelength of the incident X-ray radiation, the diffracted radiation may interfere, causing destructive or constructive interference. This results in regular diffraction peaks, mirroring the symmetry of the electron density distribution. The resultant diffraction patterns will inversely relate to the crystal lattice structure. The condition for constructive interference of the diffraction beams, and hence diffraction peaks, is given by Bragg's law:[113,114]

$$n\lambda = 2dsin\theta$$

where n is the order of diffraction (integer value), λ is the wavelength of the radiation, d is the perpendicular distance between crystal lattice planes, and θ is the complement of the angle of (2.1) incidence, depicted in Figure 2.2. This equation applies not only to crystalline materials, but also to any system in which there is a periodic distribution in electron density.
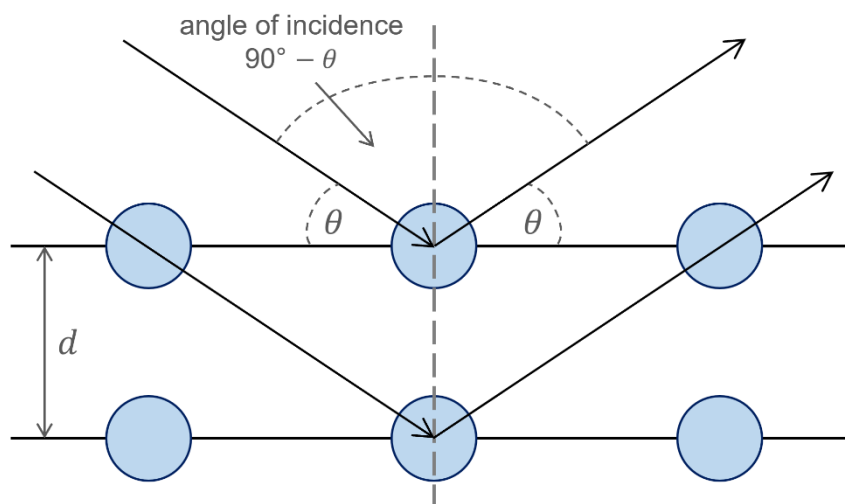
Figure 2.2: Diagram of the Bragg scattering of X-rays by planes through points in a crystal lattice.

2.2.1   Powder X-ray Diffraction (PXRD)

In PXRD, a powdered sample is placed on a flat disk, before being irradiated with monochromatic X-rays of a known wavelength. The diffracted X-rays are then recorded. Most commonly, an electronic detector will digitally record intensity as a function of the diffraction angle, θ. The detector and sample rotate with angular velocities of 2θ, and θ, respectively, meaning that for an incident angle, θ, the lattice planes parallel to the surface with an interplanar distance, d, given by Bragg's law, will be diffracting. The d-spacings can then be calculated from the collected θ angles. Since d-spacings are a function of a crystal's unit cell, and the intensity of a signal depends on the arrangement of atoms within a unit cell, PXRD can identify unknown crystalline materials through matching against a database of known patterns. Additionally, it may be used to determine whether or not a material displays crystallinity. Well-defined peaks appear for crystals, with peak broadening for smaller particle sizes, whereas no sharp peaks are evident for amorphous substances.[115]

To prepare each sample used for the research described in this thesis, the powder was ground to make it fine and to reduce preferred orientation effects, whilst being careful not to input too much energy, which may induce polymorphic transitions. The ground powder was then used to fill a silicon dioxide hole-chip sample holder, ensuring the sample completely filled the holder, and was compacted and flattened to provide a smooth surface. Data was then collected using a Bruker D8 Advance

diffractometer operated at 40 kV and 40 mA. This produced Cu Kα1 and Kα2 radiation at a wavelength of 1.5406 Å. DIFFRAC.MEASUREMENT.COMMANDER software (version 7.0) was used to set up and control each experimental run. The width of the incident X-ray beam was 2, 4, or 6 mm depending on the quantity of the sample. A step size of 0.02° was used to scan 2θ values between 10° and 70°, holding the beam at each angle for 1.00, 1.67, and 2.50 s for the 6, 4 and 2 mm beams, respectively.

2.3 TRANSMISSION ELECTRON MICROSCOPY (TEM)

TEM uses high energy electrons passing through a thin sample (less than 1 µm thick) to probe the structure of materials. An electron beam is focussed on a sample and is scattered due to interactions with the atomic nuclei and electrons in the material. The transmitted electron beam is then passed through a series of intermediate lenses to focus and magnify the resultant sample image before it can be viewed digitally on a phosphor screen or on photographic film. Individual rows of atoms may be resolved using a mode of TEM known as high resolution electron microscopy (HREM). This may be used to establish the crystallinity and size of nanoparticles in a material. Furthermore, selected area electron diffraction (SAED) patterns can be taken, giving information on crystal lattice parameters. Chemical composition can also be determined at high spatial resolution using energy dispersive X-ray (EDX) spectroscopy, which is typically performed alongside TEM.

To prepare samples for TEM, 20 drops of an STF containing suspended nanocrystals was transferred onto a holey carbon film on a 300-mesh copper TEM grid using a Pasteur pipette and air-dried. This volume of STF was chosen to ensure enough material was deposited onto the grid to make a measurement. The analysis was performed using a JEOL 2100F field emission gun TEM (FEG TEM) operating at 80/200 kV, with a ZrO/W (100) Schotky Field Emission analytical emission microscope, with an Oxford INCAx-Sight Si(Li) detector for EDX spectroscopy and a Gaian Orius CCD camera. Phase contrast HREM was used for imaging nanoscale crystals. The Fast Fourier Transform (FFT) function on the Gatan Digital Micrograph software could then be used to take Fourier transforms of the HREM, producing diffraction-type patterns that could be compared with selected area diffraction patterns.
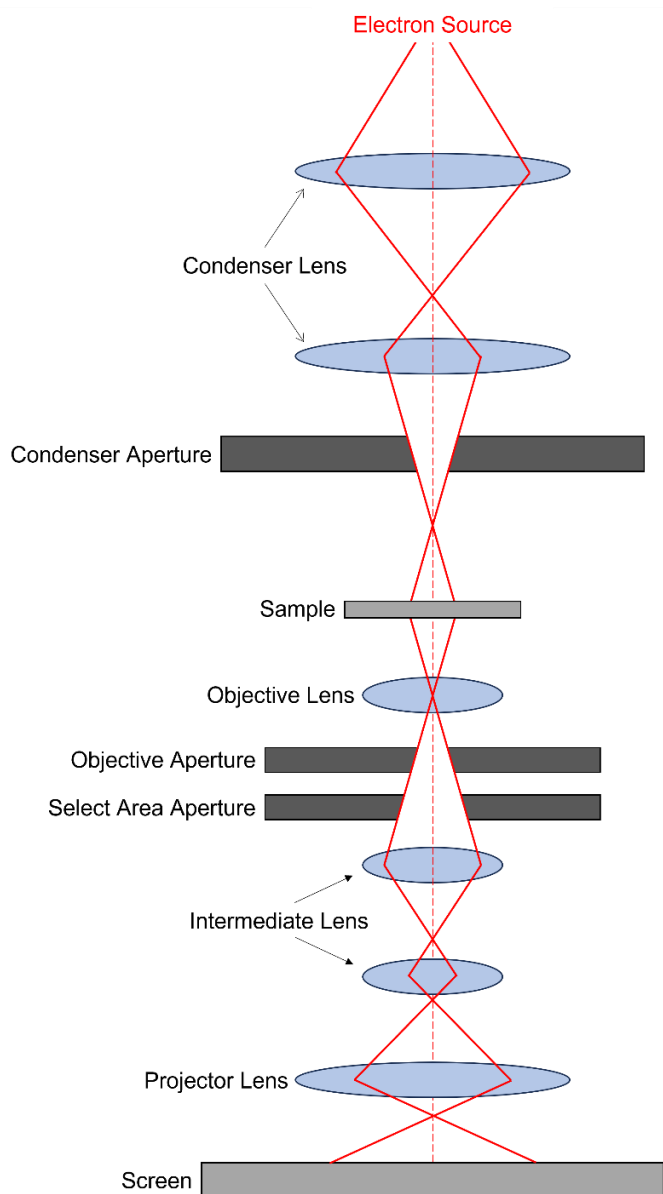
Figure 2.3: Lens diagram of a TEM microscope setup.

2.4 OPTICAL MICROSCOPY

Optical microscopy data were acquired on an Olympus BX50 microscope equipped with a digital camera. Samples were transferred to a clean glass microscope slide before images were taken. To assess crystal growth rates, glass microscope slides were cut to measure 38 x 26 mm before spreading silicone grease around the outside to form a border. 2–3 drops of fluid were then transferred to the centre of one of the prepared slides before sealing with another clean slide. The sealed sample was then placed on a Linkam heating/cooling block, fitted with a central hole to allow light transmission

through the sample. The sample was heated to 60 °C to ensure all glycine remained dissolved, before cooling to 25 °C, where the temperature was held. After the first crystal was identified, images were taken once every minute, with the length and width of the crystal(s) in each sequential image then measured. The increase in circumference per unit time was calculated, and from this, the crystal growth rate was determined.

2.5 DIFFUSION ORDERED NUCLEAR MAGNETIC RESONANCE (NMR) SPECTROSCOPY

Nuclei possess intrinsic angular momentum, known as spin, which is quantised in units of ħ. NMR active nuclei must have a non-zero spin quantum number, I, meaning that they must contain an odd number of protons and/or neutrons. Therefore ^{1}H nuclei, containing a single proton, are NMR active ($I = ½$) and can be used to understand the structure of any hydrogen containing species, which usefully includes most organic compounds. ^{12}C ($I = 0$) is not NMR active, however, the isotope ^{13}C is, and can also be used.

An external magnetic field is used to align nuclei to an equilibrium spin state, before being excited with electromagnetic radiation. The frequency required for excitation, v_x, is given by:

$$v_x = \frac{\gamma B}{2\pi} \tag{2.2}$$

where γ is the magnetogyric ratio of the nucleus, and B is the magnetic field at the nucleus. The nuclei will then resonate at characteristic frequencies, dependent on the chemical environment, giving rise to peaks in the resultant NMR spectra. By measuring the heights, areas, and shifts of the recorded peaks compared with a reference, it is possible to acquire valuable information about chemical structure.

Diffusion ordered spectroscopy is a pulsed field gradient NMR procedure which is used to separate different species in a sample based on their diffusion coefficients. A 90° radio-frequency pulse is applied to the sample in order to excite the nuclei. This pushes the magnetisation into the x-y plane where the spins will begin to precess. A gradient pulse (G) is then applied which introduces a spatial

dependency by exposing the spins to different fields at different locations, thereby causing a dephasing of the spins as shown in Figure 2.4. The sample is then left to diffuse for a chosen period of time, where the molecules will move spatially depending on their diffusion properties, before a second gradient pulse is applied to the system to refocus the signal. If there is no significant diffusion, the signal will return to the original position as seen if Figure 2.4(a). However, should the molecules diffuse significantly, spins will not realign, and the recorded signal intensity will be reduced, (Figure 2.4(b)).
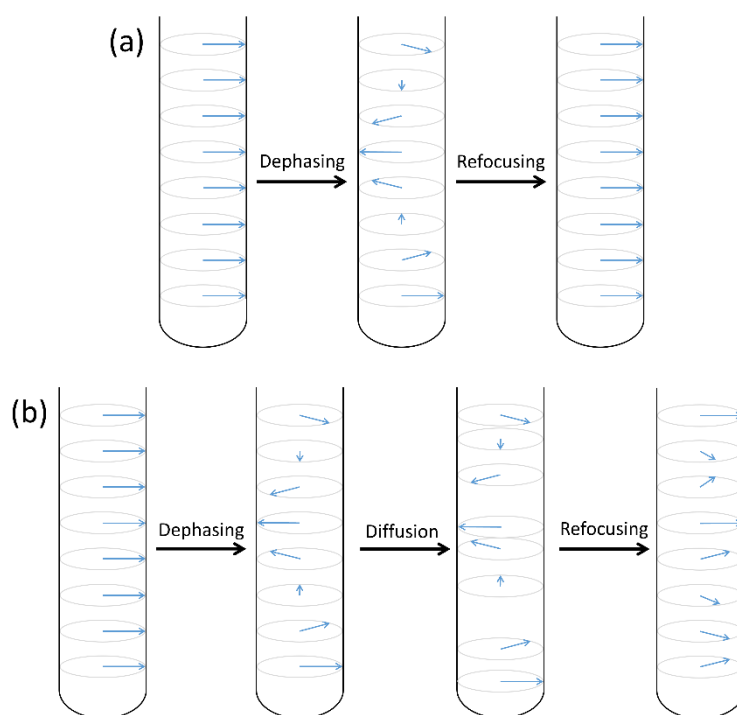
Figure 2.4: Depiction of signal dephasing and refocussing in samples that (a) do not diffuse, and (b) are allowed to diffuse.

This process will be repeated while the gradient field strength will be incremented. A plot of signal amplitude, I, against the gradient strength, g, should produce a curve that fits a Gaussian decay which can be fitted to the function:

$$I = I_0 \exp[-D\gamma^2\delta^2 g^2\Delta']$$
(2.3)

where I_0 is the signal amplitude without diffusion, D is the diffusion coefficient, δ is the diffusion delay and Δ' is the effective diffusion time.

In this work a Oneshot45 pulse sequence[116] was chosen to record diffusion data (Figure 2.5).
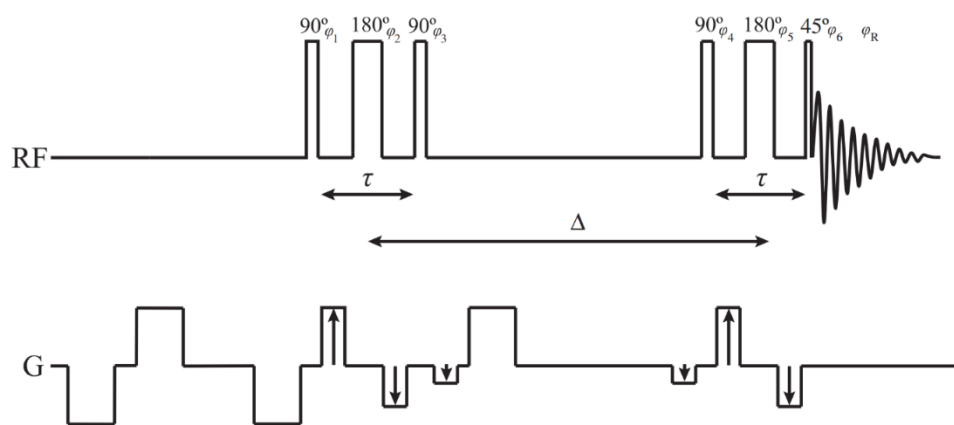
Figure 2.5: Oneshot45 pulse sequence.[116]

A factor that must be considered when measuring diffusion coefficients in solution-state samples is convection. This is particularly true in low viscosity samples, or at elevated temperatures. Convection is caused by small temperature gradients and will cause flows in the sample which will register as faster diffusion and will therefore result in anomalously rapid signal decays, masking any true diffusion and rendering the data unusable. There are pulse sequences that can take convection into consideration by assuming that it is laminar and constant with respect to time. The sequence introduces an extra stimulated echo step halfway through the experiment which phase labels the spins in the opposite direction, and therefore eliminates any ordered motion, while still recording any diffusion due to random motion. The drawback of this method is a 50% signal attenuation compared with the previously discussed sequence with no convection compensation. Consequently, if it can be confirmed that no convection is evident in the sample, then the non-compensated sequence should be selected to attain a better signal-to-noise ratio in the signal.

A 500 MHz Varian spectrometer equipped with a probe able to deliver a nominal maximum pulsed field gradient of 62 G cm^{-1} was used to acquire Diffusion-Ordered SpectroscopY (DOSY) data. The real value, i.e. the field gradient felt by the sample, was 60.95 G cm^{-1}, and was obtained by calibrating the maximum gradient strength. Standard 5 mm NMR tubes were used. A capillary containing D_2O was used to provide the lock signal. This is a signal that is tracked and can be used to compensate for any drift in the magnetic field over time.

For $^{13}C\{^1H\}$ diffusion measurements, the Oneshot45[116] spectra were acquired with a spectral width of 31250 Hz, 16 transients, four dummy scans and 93750 complex points before Fourier transformation. The diffusion delay (Δ) was set to 800 ms and the diffusion gradient length (δ) was 3 ms. Gradient strength was incremented in 15 steps from 5.58 G cm^{-1} to 46.5 G cm^{-1} in equal steps of gradient squared. The unbalancing factor (a) was 0.2. The gradient stabilisation delay was 2 ms. The repetition time was 34.0 s, of which 3.0 s comprised the acquisition time. The results were analysed using mono-exponential fittings. The ^{13}C T_1 were measured using the inversion recovery method.

For ^1H diffusion measurements, the Oneshot45[116] spectra were acquired with a spectral width of 8013 Hz, 16 transients, four dummy scans and 32768 complex points before Fourier transformation. The diffusion delay (Δ) was set to 400 ms and the diffusion gradient length (δ) was 2 ms. Gradient strength was incremented in 15 steps from 5.58 G cm^{-1} to 46.5 G cm^{-1} in equal steps of gradient squared. The unbalancing factor (a) was 0.2. The gradient stabilisation delay was 2 ms. The repetition time was 6 s, of which 4.0 s comprised the acquisition time. The results were analysed using mono-exponential fittings.

The convection test was carried out at 298.1 K using the ^1H convection compensated double-stimulated echo DBPPSTE_cc pulse sequence[117,118] using different unbalancing factors. Spectra were acquired with a spectral width of 8013 Hz, 32 transients, four dummy scans and 32768 complex points before Fourier transformation. The diffusion delay (Δ) was set to 200 ms and the diffusion gradient length (δ) was 2 ms. The diffusion-encoding gradient pulses were set to 27.9 G cm^{-1}. The unbalancing factor (a) was 0.15. The gradient stabilisation delay was 2 ms. The repetition time was 6.0 s, of which 4.0 s comprised the acquisition time.

2.6   VISCOSITY MEASUREMENT

Viscosity, η, is a measure of a fluid's resistance to flow. There are two measures of this physical property, the dynamic viscosity, and the kinematic viscosity. Dynamic viscosity is the proportionality between the rate of shear, $\frac{du}{dy}$, and the shear stress, τ, of a sample.

$$\tau = \eta \frac{du}{dy} \qquad\qquad (2.4)$$

Kinematic viscosity is related to the dynamic viscosity by dividing it by the fluid density. Kinematic viscosity can be measured by using an Ubbelohde viscometer as shown in Figure 2.6. Here, a sample is loaded into tube 1, and is slowly drawn up through tube 2 until it fills both bulbs. The viscometer is then left upright and the time taken for the fluid meniscus to pass between points A and B can be recorded with a stopwatch. The kinematic viscosity for a Newtonian fluid is then calculated from the product of the measured flow time, t, and the viscometer constant, C, which in this work was 0.005272 cSt s^{-1}.
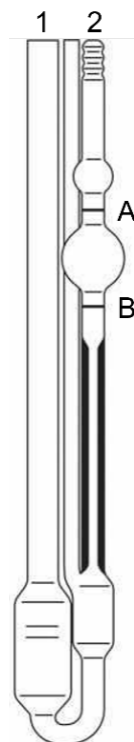
Figure 2.6: Diagram of an Ubbelohde viscometer.

2.7 UV-VIS SPECTROSCOPY

UV-vis spectroscopy is a technique that is used to measure the amount of incident electromagnetic radiation in the UV, visible and near-IR regions that are absorbed by a sample. This is achieved by comparing the intensity of light that passes through a non-absorbing reference, I_0, with the intensity of light that passes through the sample, I.

$$A = log_{10}\left(\frac{I_0}{I}\right)$$
(2.5)

where A is the absorbance of light by the sample. This can also be related to the concentration of the absorbing species in the sample through the Beer-Lambert law:

$$A = \varepsilon c l$$
(2.6)

where ε is the extinction coefficient of the species, and l is the path length of the sample. In a UV-vis experiment, the absorbance will be measured by the spectrometer and can be plotted as a function of the wavelength of incident light. From this, information about the electronic structure of the absorbing species can be obtained, as the wavelength(s) absorbed relate to the electronic transitions in the material. The position of the maximum absorbance can also provide information about the local environment of the absorbing species. For example, the excited state of a material is more polar than the ground state and is therefore more stable in more polar solvents. This leads to a lower excitation energy and a shift in the maximum absorbed wavelength; this phenomenon is known as solvatochromism.

In this work, 3 ml of each STF sample was made up twice, once without the presence of dye (for the reference) and once containing 5.5 mM disperse orange (DO1) in the octanol and ethanol phases. DO1 is insoluble in water and therefore will remain confined only to the non-aqueous regions. Figure 2.7 shows the water and dye-containing octanol phases prior to ethanol addition, to demonstrate that there is no transfer of dye into the water phase. A Unicam UV2 UV-vis spectrometer was used, scanning between 450 – 500 nm at a scan rate of 240 nm min^{-1} at 0.05 nm intervals.

Figure 2.7: Water (colourless) and 0.55 mM DO1 in Octanol (orange) phases with varying composition.

2.8 CONDUCTIVITY

Conductivity measures the ability of a material to transport an electric current. A conductivity meter is used to measure this property. In solution, a probe containing positive and negative electrodes with a fixed surface area and separation is submerged in the fluid and an electrical current applied. A probe will first be calibrated against a non-conducting fluid such as deionised water before being submerged in the sample fluid. Any cations and anions in solution will migrate towards the negative and positive electrodes, respectively (Figure 2.8). This allows charge to be carried between them. Consequently, the more ions, or the greater their charge, the larger the conductivity measurement will be. Other factors that may influence the conductivity of a solute in solution are the temperature and the viscosity of the solvent, as they impact the rate of ion diffusion.
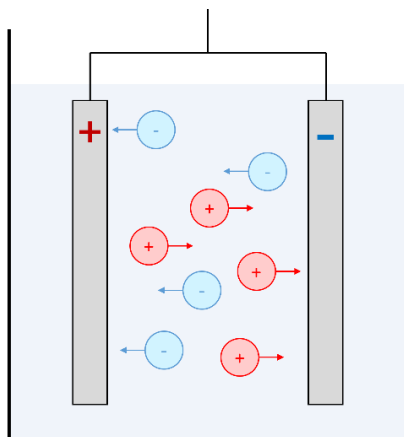
Figure 2.8: Diagram demonstrating the operation of a conductivity meter.

In this work, a Jenway 4510 conductivity meter was used with a cell constant, K, of 10 and a voltage of 9 V AC ± 10 at 50/60 Hz. A temperature of 25.0 ± 0.4 °C was used to measure STFs containing 3 mg of dissolved glycine zwitterions. This low mass was chosen to measure the conductivity of STFs, regardless of their composition, owing to the low solubility of glycine in ethanol and octanol.

3 THERMODYNAMIC CONTROL IN STFS

3.1 INTRODUCTION

The aim of the work described in this chapter was to investigate the use of STFs in the w/o microemulsion region to crystallise the most thermodynamically stable polymorph of glycine, γ-glycine, selectively. Compositions containing 15% water by mass have been characterised to show the difference between the confined and non-confined regions on the polymorphic outcome, indicating thermodynamic control in the confined region.

3.2 GLYCINE

Glycine is the simplest amino acid, with the chemical formula NH_2CH_2COOH, and exists in zwitterionic form in solution (Figure 3.1). It is commonly found in proteins and has application to several important industries such as pharmaceuticals,[119-126] food,[127-130] and agriculture.[131-136]
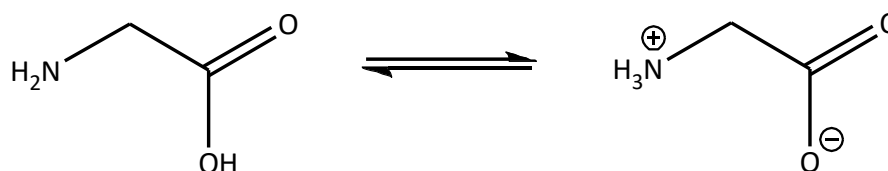
Figure 3.1: Structure of glycine and its zwitterionic form.

Under ambient conditions, glycine may exist as one of three major polymorphs, labelled α, β, and γ, where α-glycine is the most prevalent, and γ-glycine is the most stable and therefore the least soluble.[137] Owing to the difficulty in crystallising the most stable polymorph, it has been the focus of much research that aims to illustrate the process of thermodynamic control over crystallisation.[141,142,104]

3.2.1 Uses

As amino acids are the building blocks of proteins, glycine is prevalent in protein-rich foods and can be used as a food additive, seasoning or preservative. It is also often used in food supplements such

as protein powders. This is not only relevant to humans, but also to agriculture, where it functions as an additive to livestock feed[135] and, due to its nitrogen content, a plant fertiliser.[131,132]

Glycine is a nonessential amino acid, meaning that it is synthesised in the human body, making it inherently biocompatible. It comprises 11.5% of the body's amino acid content, where it acts as a neurotransmitter in the central nervous system,[137] and as a precursor for important biological molecules such as haem, creatine, DNA, glutathione, and collagen.[138] While it is formed in the body through interorgan metabolism, with modern diets it is often not produced in sufficient quantity. A small deficit is not harmful, but significant deficits can lead to issues with immune response, growth, and metabolism.[139] Consequently, in proper doses, glycine supplementation has been proven to be effective in treating some metabolic disorders,[119,126] inflammatory diseases,[122] cases of obesity,[139] diabetes,[123] and liver disease;[125] it is also used in a wide range of therapies for ailments including insomnia,[121] stroke and schizophrenia.[120,124]

When synthesising a crystalline compound to be used *in vivo*, it is important to understand the polymorphic form of that drug material. Different polymorphs will have different physical properties, such as solubility, which will affect the bioavailability and bioactivity of the drug.

3.2.2   Polymorphism

To date, five non-solvated polymorphs of glycine have been discovered, labelled α, β, γ, δ, and ε. Of these, only the α, β, and γ forms will nucleate under ambient conditions, whereas the δ, and ε forms may only be obtained under high pressure.[143] Table 3.1 outlines the crystal properties of each of the three ambient polymorphs that will be considered in this work.

Figure 3.2 depicts the crystal structure of each polymorph, with the unit cells indicated by the black boxes. The α-form exists as two dimers connected by hydrogen bonding (pink). These dimers then connect through further hydrogen bonds (orange) to form layers that are not connected to other layers in the structure. In β-glycine, the molecules arrange to form layers of single molecules connected by hydrogen bonded (pink), these then also form hydrogen bonds to the other layers

(orange). In γ-glycine, hydrogen bonds form trimeric structures (pink), which can then go on to bond to other trimers in layers (orange).[145,146]

Table 3.1: Crystallographic parameters for the α, β, and γ polymorphs of glycine.[142]

Polymorph	Stability	Crystal Structure	Molecules in unit cell	Morphology	Space Group
α	Metastable	Monoclinic	4	Bipyramidal	$P2_1/n$
β	Metastable	Monoclinic	2	Acicular (needle-like)	$P2_1$
γ	Stable	Hexagonal	3	Prismatic	$P3_2$
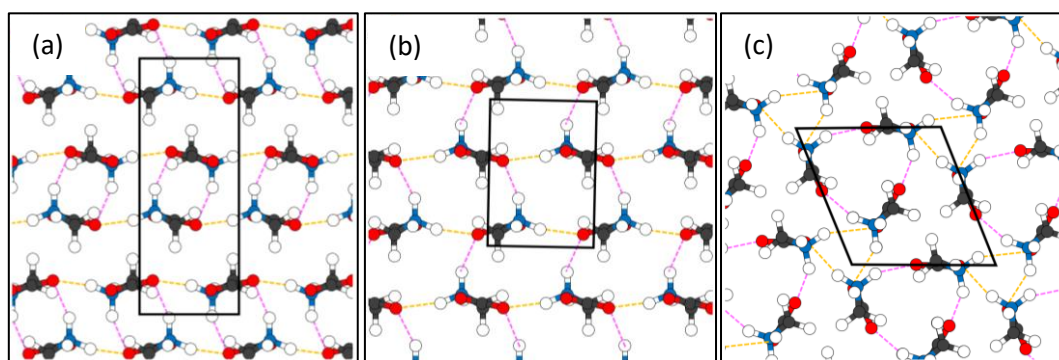
Figure 3.2: Depiction of the crystal structures of (a) α-glycine, (b) β-glcyine, and (c) γ-glycine. Unit cells are indicated by the black boxes, pink dashed lines represent the main monomer, dimer, or trimer connections, and the orange dashed lines represent additional hydrogen bonding present in order to form layered structures.

The growth behaviour of each polymorph from solution can be evaluated by considering the solvent interactions that may occur with the crystal nuclei. There are three different sites on the glycine (gly) molecule that can form hydrogen bonds with solvent (sol), $N-H_{gly}---O_{sol}$, $C-O_{gly}---H_{sol}$ and $C-H_{gly}---O_{sol}$. In order for an additional glycine molecule to form bonds with the growing crystal nucleus, these solvent interactions must first be broken. Of the three glycine-solvent hydrogen bonds, the $C-H_{gly}---O_{sol}$ bond is the weakest, and consequently the growth of the crystal will be more facile should there be more C-H bonds in surface sites on the crystal. It has been suggested that α-glycine grows through the addition of dimeric glycine units in a layered structure.[146] Due to the dimeric nature of α-glycine, the structure has non-polar faces, with exposed C-H bonds on either side (Figure 3.3(a)). Provided that there is sufficient solute concentration, growth will proceed quickly, due to the relative ease in

replacing solute interactions with the crystal faces. This could, however, be a competitive effect, due to the poisoning of the other polymorphs, or due to solute monomers attaching in the incorrect orientation more readily in different polymorphs, requiring energy to reorientate, and slowing growth.
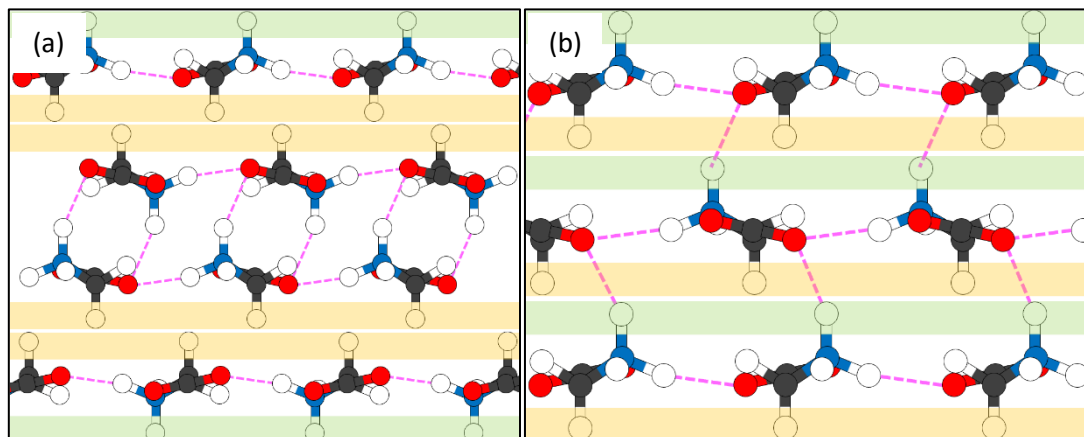
Figure 3.3: Depiction of the crystal structuring in (a) α-glycine, and (b) β-glycine. Yellow and green highlighted areas indicate crystal faces which would expose C-H, and N-H bonds on the surface, respectively.

It is well known that β-glycine is typically nucleated in the prescence of alcohols such as methanol and ethanol.[146,147] These alcohols act as anti-solvents for glycine and therefore lower its solubility when added to aqueous solutions. It has been reasoned that this decrease in solubility causes the dimerisation of glycine to become less prevalent, and more monomer units will attach to the α-glcyine surfaces, exposing N-H bonds which form stronger intermolecular hydrogen bonds with the solvent that are more difficult to overcome, and slows the rate of growth as the faces become saturated with exposed N-H sites. β-glycine, on the other hand, has different crystal faces, with exposed N-H sites on one face, and C-H sites on the opposite face (Figure 3.3(b)). As the structure is built from monomer units instead of dimers, this will not restrict the growth because, although there will be preferential growth on only one face as opposed to two, there will always be one face with exposed C-H groups to allow growth to proceed, so growth will be unimpeded.[146]

γ-glycine rarely grows in alcohol-containing solutions. Although it is similar to β-glcyine in that its structure is built of monomer units as opposed to dimers, the polar structures formed expose the COO^- groups on the opposite face to the NH_3^+ functional groups and so the consideration of

C-H$_{gly}$---O$_{sol}$ interactions no longer defines growth. The COO$^-$ rich face will appear 'corrugated', with ridges in which solvent molecules may be contained. Water will only weakly bind to these sites due to electrostatic repulsion between oxygen lone-pairs on the solvent and glycine carboxylate groups, countering any hydrogen bond formation. This means that glycine NH$_3^+$ groups may readily fill this vacancy instead of water to grow the crystal face. Alcohols such as methanol and ethanol may form additional hydrogen bonds to the carboxylate groups in these recesses, which means that it will take more energy to displace. This effectively poisons the addition of further molecules via the carboxylate face, which is the usual mechanism of γ-glycine growth.[146] Resultantly, a 'crystal growth dead zone' induced by this poisoning mechanism for crystals such as γ-glycine that contain a corrugated surface has been reported by Liu *et al*. For glycine solutions, this occurred below a supersaturation of 0.32. It was found that at high supersaturations above this value, the corrugated carboxylate-rich face then became the fastest growing, leading to the conclusion that a high driving force is required to overcome the poisoning effect.[146]

In solution, α-glycine grows up to ~500 times faster than γ-glycine.[146,149] Therefore, it will quickly outgrow the γ-polymorph upon nucleation. Due to Ostwald's rule of stages, it is likely the metastable polymorph will nucleate first, and if it grows quickly enough, any more stable γ-glycine nuclei that do form will be too small and will shrink at the expense of the much larger and so more stable α-polymorph. As there is more solute available, the nucleation and growth rates will be enhanced, exacerbating this effect at higher supersaturations.

Chew et al.[149] calculated that the difference in the activation energy for growth in solution between the two polymorphs was ~15 kJ mol^{-1} (approximately $6k_BT$ at room temperature), which is consistent with the dissociation of glycine dimers. This suggests that, in the growth mechanism of γ-glycine, an additional step is required to break up dimers. It has been suggested by Weissbuch *et al.* that these dimers may arise in solution where they must break up to add to the structure monomerically.[146] More likely, zwitterions may attach to the growing γ-glycine to form surface dimers in the incorrect

orientation. These then require breaking so that the zwitterions may reorient and adopt the proper γ-glycine crystal structure. This step is unnecessary for α-glycine due to its already layered dimeric structure (Figure 3.3(a)). Enthalpies of solution in water were recorded as 14523 ± 76 J mol^{-1}, 14198 ± 73 J mol^{-1}, 14791 ± 84 J mol^{-1}, for α, β, and γ- glycine, respectively, meaning that γ-glycine is the most thermodynamically stable polymorph.[150] However, there is only a small difference in energy (0.2 kJ mol^{-1}) between α-glycine and γ-glycine.[149] Consequently, the thermodynamic driving force for a phase transition from α→γ is low. This, combined with the rapid growth rate, makes α-glycine the dominant polymorph under ambient conditions.

Similarly, β-glycine has a small thermodynamic driving force for phase transition to the α-form. This can be driven forwards through the use of high temperatures or predominantly humidity. In solution, the β-form can readily transform due to its higher solubility, and will undergo dissolution to help supply the growth of more stable and less soluble α-nuclei. Due to this, ethanolic conditions as well as an increased supersaturation of solute will slow the dissolution rate, and hence promote β-glycine persistence.[159]

Selective γ-polymorph formation has been reported by altering the conditions under which glycine is nucleated and/or grown. For example seeding solutions with γ-glycine nuclei,[151] applying electric fields,[152] nonphotochemical lasers,[153] and through the addition of α-form inhibitors such as aspartic and malonic acids.[151,154]

While STFs have been studied to understand their physical properties, behaviours, and analogy to surfactant microemulsions, little work has been published on their use in particle formation.[47,52,58-61] Recent studies have involved inorganic or metal nanoparticles, and focused on the particle morphologies obtained through templating effects, rather than the crystallisation kinetics. Due to the difficulty in selectively crystallising each polymorphic form, glycine has been used in many investigations into polymorphism.[143-154] Successful nucleation of the most stable polymorph of crystalline materials using confined domains found in surfactant microemulsion systems has been well

documented including, but not limited to, the nucleation and growth of γ-glycine.[66,104,107-110] We hypothesise that STFs may afford the same thermodynamic control using nanoconfined domains to overcome Ostwald's rule of stages. This is provided that nanoconfinement exists for longer timescales than the nucleation time despite the nanoconfined domains being more transient and less well-structured than in microemulsions.

3.3 EXPERIMENTAL

3.3.1 Materials

The chemicals used were as follows: octan-1-ol (99%, Fisher Scientific), ethanol (≥99.8%, Fisher Scientific), α-glycine (≥99%, SigmaAldrich) and glycine-1-13C (99 atom% 13C, Sigma-Aldrich). Ultra-high purity water (18.2 MΩ cm) was obtained from a Sartorius arium® comfort water purifier.

3.3.2 Solubility Assessment

STFs containing ethanol, water and octanol were prepared for the required compositions on a 10 g scale. Excess α-glycine was then weighed and added to each sample vial, which were then sealed using PTFE tape. Each STF composition was made twice, with each duplicate being stored in an oven set at 36 °C and 50 °C, respectively, for four months over the first national lockdown due to the COVID-19 pandemic. After this time, the samples underwent hot filtration, residual glycine (which remained exclusively α-glycine) was weighed and its mass was recorded. From this, the amount of α-glycine that dissolved, and therefore the solubility of α-glycine in each sample, could be calculated. Consequently, the saturation values found relate to α-glycine, and not the stable polymorph γ-glycine which would have a lower saturation value by ~9% according to solubility data presented by Little *et al.,* Yang *et al.,* and Azhagan *et al.* for α- and γ-glycine dissolved in water.[155-157]

3.3.3 Bulk Solution Crystallisation

As control experiments, crystallisations were performed in both bulk water and a binary water/ethanol solution to confirm the majority polymorph formed when there was no microemulsion-like structuring present. In these cases, 200 ml of water (or a mixture of 60:40 wt% water and ethanol,

respectively) were made before dissolving glycine to produce samples with relative supersaturations of $\frac{c}{c_{sat}}$ = 1.4 using gentle heating, where c_{sat} and c are the α-glycine saturation point and the actual concentrations, respectively. Samples were then cooled to 25 °C and allowed to crystallise for one week prior to extraction from solution via Büchner filtration and washing with a small amount of ethanol. Samples were then left to dry at 60 °C and analysed using FT-IR and optical microscopy.

3.3.4   STF Preparation and Crystallisation

Prevost et al.[24] have previously reported X-ray and neutron scattering data which identified that a composition containing 15, 50, and 35 wt% water, octanol, and ethanol, respectively contained nano-structures of approximately 4.7 nm, comparable to those found in traditional surfactant microemulsions. This composition was then tested in order to optimise the system with respect to γ-glycine crystallisation.

Table 3.2: Composition of STF used to mimic surfactant-based microemulsion w/o droplet nanostructuring.

	Water	Octanol	Ethanol
Mass fraction	0.15	0.50	0.35
Volume in 220 ml of STF / ml	27.5	111.2	81.3

Firstly, STFs were made up to contain the composition outlined in Table 3.2 with a total volume of 220 ml and a $\frac{c}{c_{sat}}$ of 1.4 with respect to the STF (0.38 g glycine in 220 ml). This was chosen to enable crystallisation to occur within 24 hours while maintaining a relatively low supersaturation to encourage γ-glycine nucleation and growth. Eight solutions were made to this specification at a temperature of 60 °C, before being cooled at a rate of 10 °C hour⁻¹. The first indication of glycine crystallisation occurred in one of the samples when the temperature reached 36 °C. Any crystals in this system were extracted via filtration *in vacuo* to identify which polymorph appeared first in the STF. The other seven solutions were cooled further to 30 °C and allowed to crystallised, remaining at that temperature to avoid material crystallising too rapidly due to the supersaturation becoming too high. One solutions was then selected after 1, 2, 5, 6, and 7 days, as well as two weeks of growth time,

respectively, and the crystals from it extracted via filtration *in vacuo.* These were analysed using FT-IR and optical microscopy in order to identify any changes in the polymorphs produced over time.

Subsequently, experiments were performed to understand the effect of supersaturation on the polymorphic outcome. STFs with the same composition as described in Table 3.2 were produced and masses of glycine corresponding to supersaturations in the range of $\frac{c}{c_{sat}}$ = 1.2 – 1.6 were dissolved.

Consequently, a general protocol for crystallisations was determined and was as follows:

1. An STF was made with the desired composition.

2. Glycine was dissolved in the STF to achieve a selected $\frac{c}{c_{sat}}$ value. These systems were stirred with a magnetic stirrer bar at 50 – 60 °C for one hour, or until all glycine was fully dissolved. For crystallisations at supersaturations corresponding to $\frac{c}{c_{sat}}$ of 2.00 or higher, samples were sonicated in an ultrasound water bath for two hours, or until all glycine had dissolved.

3. The STF was stored for at least one hour at a temperature of at least 10 °C above the temperature at which $\frac{c}{c_{sat}}$ = 1.00 to ensure full dissolution.

4. The STF was cooled at a controlled rate of 10 °C hour⁻¹ in an oven to a chosen temperature to achieve the correct $\frac{c}{c_{sat}}$ value.

5. STFs were stored at that temperature for one week to ensure that, should multiple polymorphs nucleate, the stable but slower growing γ polymorph could compete with the faster growing metastable polymorphs.

6. Resulting crystals were then extracted via Büchner filtration and washed with a small amount of the corresponding non-glycine containing STF, followed by a small amount of ethanol to remove residual octanol.

7. Crystals were left to dry at 60 °C.

Once this was determined, an investigation of the structural dependence of the polymorphic outcome was performed. STFs containing ethanol, water and octanol at constant water mass fraction of 0.15

were prepared on a 200 ml scale according to the masses in Table 3.3. The ethanol mass fraction was varied from 0.30 to 0.85 to encompass the w/o nanostructured region, as well as the unstructured region of the phase diagram, see Figure 3.4.

Table 3.3: Compositions of STFs used to assess the effect of confinement on crystallisation.

Water mass fraction	Octanol mass fraction	Ethanol mass fraction	Water / g	Octanol / g	Ethanol / g	Glycine / g
0.15	0.55	0.30	25.15	92.21	50.30	0.4889
0.15	0.50	0.35	25.08	83.61	58.53	0.4200
0.15	0.45	0.40	25.02	75.05	66.71	0.3642
0.15	0.40	0.45	24.95	66.54	74.86	0.3199
0.15	0.35	0.50	24.89	58.07	82.96	0.2857
0.15	0.30	0.55	24.82	49.65	91.02	0.2601
0.15	0.25	0.60	24.76	41.27	99.04	0.2416
0.15	0.20	0.65	24.70	32.93	107.01	0.2287
0.15	0.15	0.70	24.63	24.63	114.95	0.2199
0.15	0.10	0.75	24.57	16.38	122.84	0.2136
0.15	0.05	0.80	24.51	8.17	130.70	0.2084
0.15	0.00	0.85	24.44	0.00	138.51	0.2027
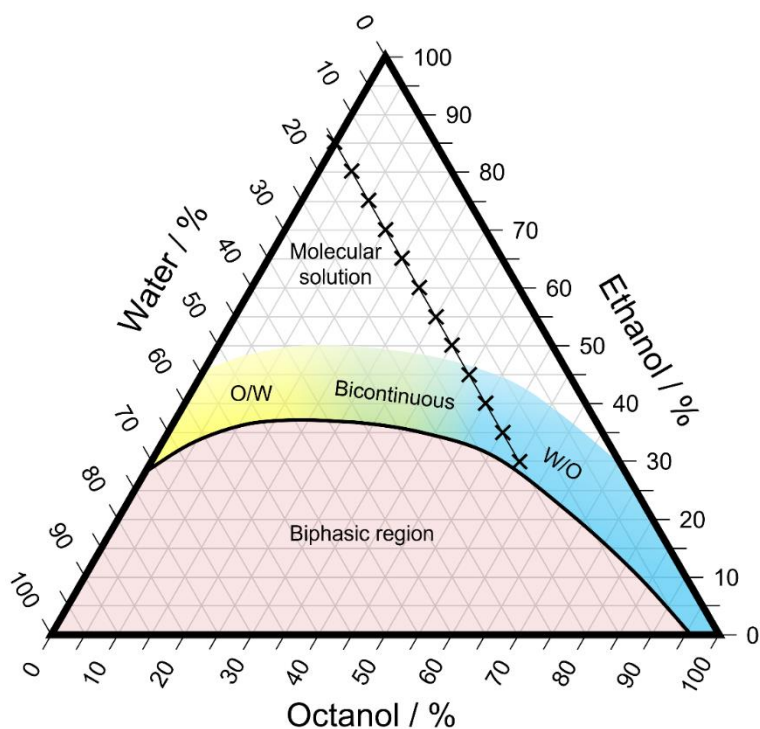
Figure 3.4: Water, octanol and ethanol phase diagram, with the STFs tested along the line of 0.15 mass fraction of water.

3.3.5   Seeding Studies

Separate 250 ml STFs were prepared that with the aim to make suspended nanocrystals of γ- and α-glycine according to the general protocol outlined above. These STFs contained a water mass fraction of 0.15 and had a relative glycine concentration, $\frac{c}{c_{sat}}$, of 1.40. However, the STFs were stored at 25 °C for only 16 hours (as opposed to one week) for the nanocrystals to form. At this time, it was visually observed that the STFs contained 1–5 sedimented crystals of size ≤ 0.1 mm, but the majority of the glycine was still in the STF, either in solution or in the form of suspended nanocrystals.

For the seeding experiments, a 5.0 ml aliquot of the nanocrystal-containing STF was added to 15.0 ml of a binary solution of 0.40 mass fraction water and 0.60 mass fraction ethanol, which contained glycine at a supersaturation corresponding to $\frac{c}{c_{sat}}$ of 1.30. Crystals were extracted for ATR-FT-IR analysis from the seeded experiments, and also from the STFs used for the seeding, after one week.

3.3.6   Characterisation

3.3.6.1   UV-vis Measurements

UV-vis characterisation was performed using Disperse Orange 1 dye (DO1), which was dissolved in both the ethanol and octanol phases at a concentration of 5.50×10^{-4} mol dm^{-3}. This was chosen because DO1 is insoluble in water and will produce a shift in the absorbance maximum upon changes in the solvent environment, such as the presence of any nano-structuring.

The maximum absorbance of DO1 is centred between 431-485 nm depending on its environment[165] (Figure 3.5). This wavelength value was extracted from the recorded spectrum for each STF composition in order to assess the impact of changing the ethanol/octanol mass fraction with a constant water mass fraction of 0.15 used throughout.
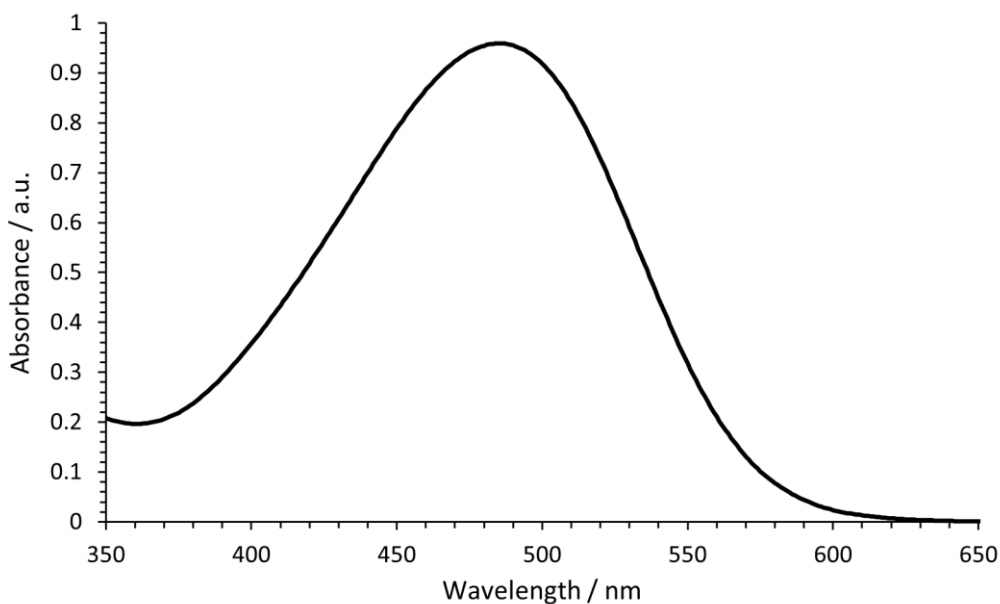
Figure 3.5: Example UV-vis spectrum of DO1 in octanol.

3.3.6.2   FT-IR Spectroscopy

A typical FT-IR spectrum for α-glycine is shown in Figure 3.6, with the wavenumber of characteristic FT-IR peaks and their corresponding molecular vibration for glycine polymorphs summarised in Table 3.4. It should be noted that these values have been taken from papers by the groups of Chernobai, Ferrari, Lee and Ahamed[158-161] and are used in this work as a guide only, as experimental set up and environment may differ leading to small discrepancies up to an average of ± 4 cm^{-1}.
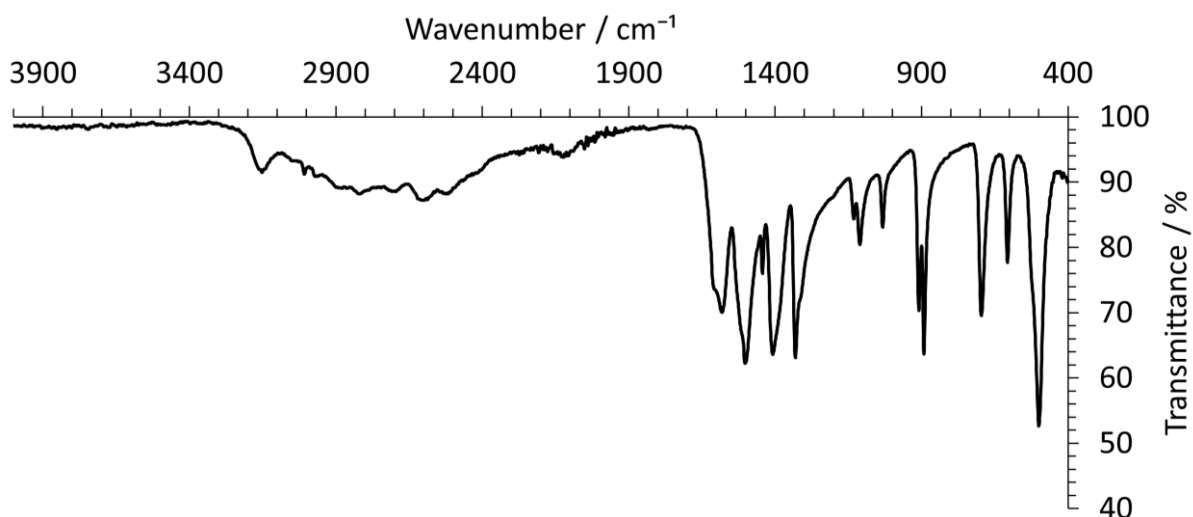
Figure 3.6: Example FITR spectrum of α-glycine.

Table 3.4: Summary of the major signals found in the FT-IR spectrum of α, β, and γ glycine.[158-161]

Vibration	Literature			Experimental		
	α / cm^{-1}	β / cm^{-1}	γ / cm^{-1}	α / cm^{-1}	β / cm^{-1}	γ / cm^{-1}
NH_3^+ antisymmetric stretch	3165	3176	3104	3156	3177	3093
NH_3^+ symmetric stretch	2614		2602	2607		2601
COO^- antisymmetric stretch	1605	1662	1596	1585	1662	1573
NH_3^+ deformation	1507	1515	1497	1500	1518	1494
CH_2 bend	1444	1445	1436	1443	1445	1435
COO^- symmetric stretch	1413	1409	1391	1408	1410	1387
CH_2 wag	1333	1334	1335	1331	1332	1333
NH_3^+ rock	1133	1134	1135	1132	1133	1127
CCN asymmetric stretch	1033	1042	1043	1033	1040	1043
CH_2 rock	910	915	929	909	914	928
CCN symmetric stretch	893	893	890	892	892	888
COO^- bend	694	701	685	695	700	683
COO^- wag	607		607	607		608
COO^- rock	504		504	499		499

The two peaks of importance in this work are highlighted in yellow in Table 3.4 and are due to a CH_2 rock and C-C stretch. They were chosen as they are isolated from any other interfering signals and are easily identifiable by the signature double peak. Moreover, the difference in wavenumber for the CH_2 rock vibration between each polymorph is sufficiently large that they appear as distinct peaks in the spectra.

In all further FT-IR spectra, raw transmittance data were converted to absorbance using Equation 3.1.

$$A \ = \ 2 \ - \ log_{10}(\%T) \tag{3.1}$$

where A and $\%T$ are the absorbance and percentage transmittance, respectively. Each spectrum was normalised relative to the peak at 890 cm^{-1} in order to draw meaningful comparisons, as this peak was consistent regardless of the polymorphic form(s) present. Example spectra for the α, β, and γ polymorphs are shown in Figure 3.7.
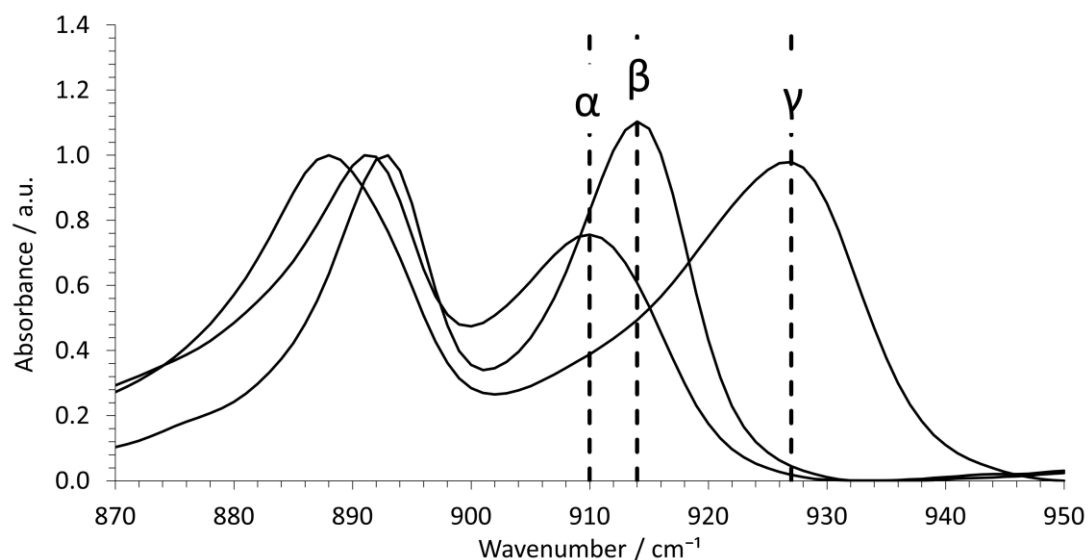
Figure 3.7: Example FT-IR spectra of α, β, and γ-glycine polymorphs in terms of absorbance. Only the characteristic signals in the range of 870 – 950 cm⁻¹ are shown for clarity.

3.3.6.3   NMR Diffusiometry

NMR samples were made using the same composition ratios outlined in Table 3.3, albeit scaled down to a total volume of 0.7 ml. These solutions were transferred to an NMR tube before a clean, sealed capillary tube containing D_2O was inserted in the centre. The NMR tube was then sealed with a cap prior to analysis to ensure no loss of material due to evaporation. Samples were recorded at 25 °C.

3.3.6.4   Viscosity Measurements

Kinematic viscosity measurements were taken using an Ubbelohde capillary viscometer at 25 °C. STF solutions along the 15 wt% water line of the phase diagram (Table 3.3) were made up to a total volume of 15 ml before being analysed on the viscometer. Each measurement was repeated five times and an average taken before converting to dynamic viscosity by dividing by the density of each sample. The density was calculated by recording the change in mass when 1 ml of STF was removed from a 10 ml sample.

3.3.6.5   Optical Microscopy

Optical microscopy data were acquired on an Olympus BX50 microscope equipped with a digital camera. Samples were transferred to a clean glass microscope slide before images were taken. Optical

microscopy was also used on samples to assess crystal growth rates. The sample was heated to 60 °C to ensure all glycine remained dissolved, before cooling to 25 °C, where the temperature was held. After the first crystal was identified, images were taken once every minute, with the length and width of the crystal(s) in each sequential image then measured. The increase in circumference per unit time was calculated and, from this, the crystal growth rate was determined.

3.3.6.6   Conductivity Measurements

Samples for conductivity measurements were made up to a total volume of 27 ml, with each containing 3 mg of dissolved glycine, thus providing zwitterions to allow the current to flow. All measurements were taken at 25.0 ± 0.4 °C. Each measurement was repeated five times, and the mean value calculated.

3.4   RESULTS AND DISCUSSION

3.4.1   Viscosity Measurement

3.4.1.1   Binary systems

Figure 3.8 shows the change in dynamic viscosity as a function of the change in ethanol mass fraction in binary systems of ethanol and water. The black data points depict the values obtained experimentally, whereas the orange data points show the theoretical values if the mixture behaved ideally. According to the Kendall-Munroe relation, the theoretical viscosity for ideal binary and ternary mixtures is given by Equation 3.2.

$$\ln(\eta_m) = \sum_i x_i \ln(\eta_i) \qquad (3.2)$$

where x_i is the mole fraction of component i, and η_i and η_m are the viscosities of component i and the mixture, respectively. From Figure 3.8, it can be seen that water/ethanol binary mixtures deviate significantly from ideality, where a distinct maximum is observed at approximately 50 wt% ethanol, showing that the viscosity of any binary mixture of ethanol and water is greater than the sum of the

individual viscosities. Like surfactants, alcohols contain a hydrophobic hydrocarbon chain, with a hydrophilic -OH functional group. This means that short-chain alcohols, like ethanol, may develop transient structures when mixed with water. The -OH groups will form hydrogen bonds with the surrounding water molecules, creating hydration layers which have a higher viscosity than bulk water.
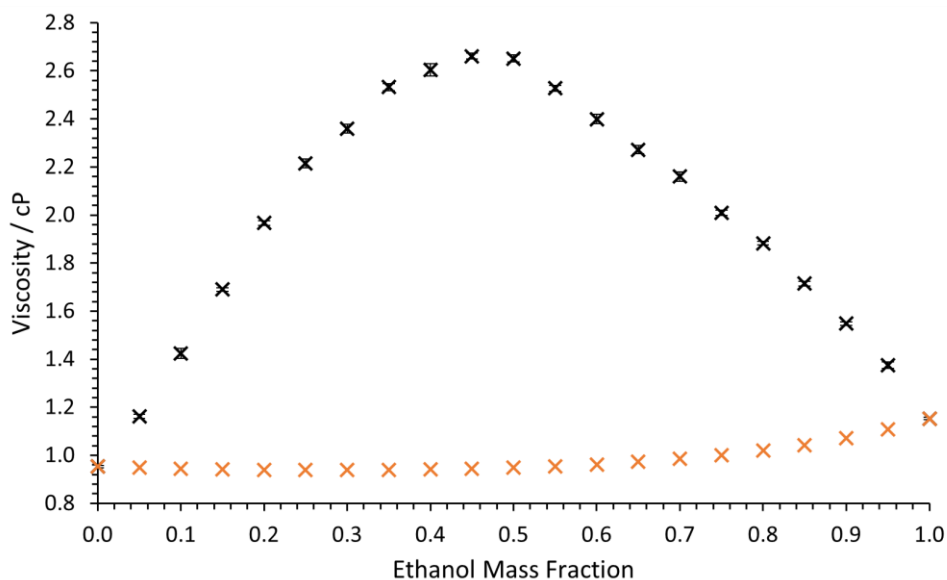
Figure 3.8: Viscosity change with ethanol mass fraction for real (black) and ideal (orange) ethanol/water mixtures.

This structuring is evident in practice as ethanol-water mixing is exothermic. In pure ethanol, molecules are capable of an average of one hydrogen bond per molecule, as, while each ethanol has two hydrogen bond accepting oxygen lone pairs, ethanol has only one hydrogen atom with sufficient $\delta+$ charge to donate to the bond. Water, on the other hand, has both two acceptor and two donor sites, and therefore will be able to form additional hydrogen bonds more efficiently when added to ethanol. Consequently, when mixed, more hydrogen bonds will be formed than broken and the process will be exothermic.

The viscosity of binary octanol/ethanol mixtures is shown by Figure 3.9. In contrast to Figure 3.8, this shows close agreement between the measured viscosity and the calculated ideal viscosity. 1-octanol is significantly more viscous than ethanol due to its longer hydrocarbon chain. Both alcohols contain hydrogen bonding through their single -OH groups, however, there will also be attractive Van der Waals intermolecular interactions which will be stronger for the larger octanol molecules. As the

ethanol content increases, these interactions become weaker, and the viscosity decreases. Due to the much larger mass of octanol, this appears as a sharp decrease as ethanol mass fraction increases, as the same mass of ethanol will contribute a larger absolute number of molecules to the system.
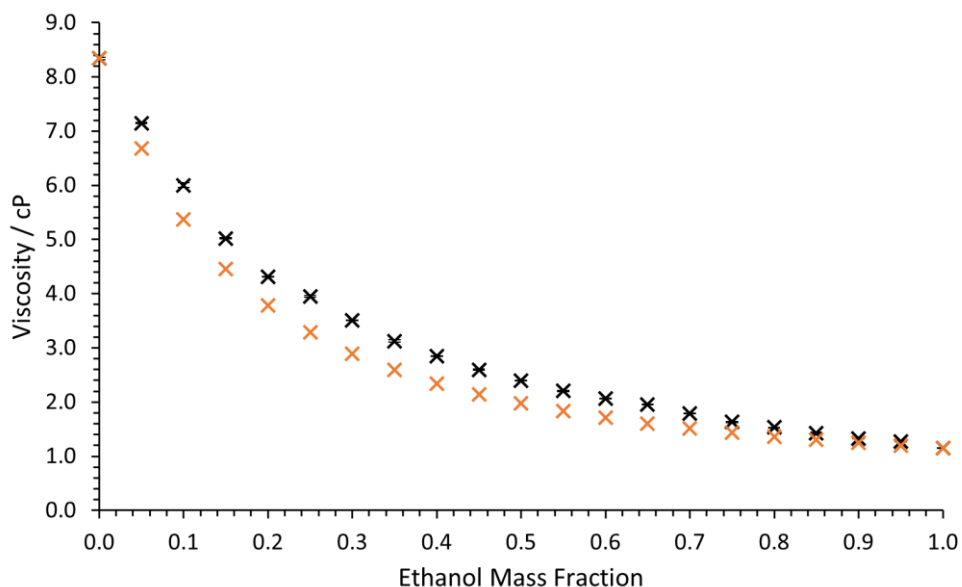
Figure 3.9: Viscosity change with ethanol mass fraction for real (black) and ideal (orange) ethanol/octanol mixtures.

No data have been collected for the binary octanol/water systems as the two solvents are virtually immiscible and will phase separate upon mixing. It should be noted that water is sparingly soluble in octanol, but only up to a water mass fraction of ~0.05 at 25 °C.

3.4.1.2   15 wt% Water

Figure 3.10 shows the change in viscosity in STFs with a water mass fraction of 0.15. At low ethanol mass fraction, the viscosity is highest because octanol is the most viscous component and makes up the continuous phase. As discussed in Section 1.1.5, water and ethanol will form swollen hydrogen-bonded networks throughout the octanol phase. However, as the water mass fraction is constant, the viscosity contribution of the water forming hydrogen bonds in hydration layers is approximately constant. Thus, the trend follows that as the octanol content decreases so too does the viscosity, much like in the binary octanol/ethanol systems.
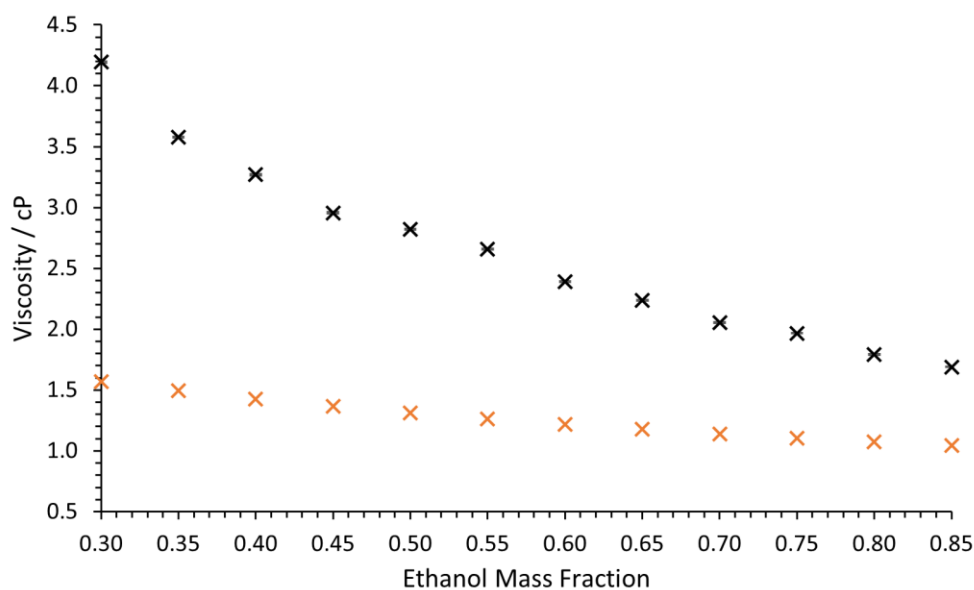
Figure 3.10: Viscosity change with ethanol mass fraction for STFs containing a constant water mass fraction of 0.15 (black) compared to the ideal values calculated using equation 3.2 (orange).

Importantly, each composition deviates from ideality as given by the orange data points. It is expected that, even in the binary system, the solution will not behave ideally due to the hydrogen bonding between ethanol and water as previously discussed. However, this deviation becomes greater at lower mass fractions of ethanol, consistent with the increasing amount of nanostructuring predicted.

3.4.2   NMR Diffusiometry

Theoretically, when glycine is dissolved in the STF systems, it should be contained within the aqueous domains, owing to its lack of solubility in the ethanol and octanol components. Here, it will diffuse via Brownian motion into whatever volume it has available to it. If the glycine zwitterion encounters a boundary, such as the walls of the container, or the softer interface of a nanoconfined domain, it will rebound back on itself (Figure 3.11). The measured diffusion coefficient will then be smaller than the value obtained in an unrestricted solution, as the distance that the molecules appear to have travelled is shorter.
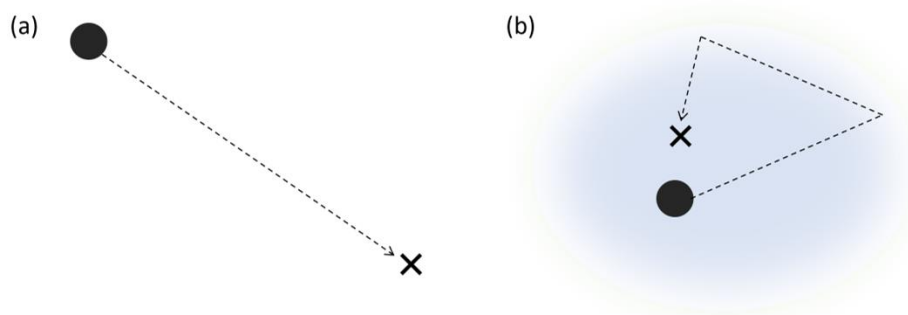
Figure 3.11: Schematic diagram of diffusion paths for a molecule in (a) bulk solution, and (b) confined nanodroplet.

The relationship between the diffusion coefficient, the area over which the zwitterions diffuse in a given time, D, and the dynamic viscosity of the sample, η, is given by the Stokes-Einstein equation,

$$D = \frac{k_B T}{6\pi r \eta}$$

(3.3)

where r is the Stokes radius, the radius of a hard sphere that diffuses at the same rate as the component particle. Consequently, assuming the Stokes radius does not change significantly for glycine in the STF formulations, the product $D\eta$ should remain constant in the absence of confinement, and will decrease upon confinement, due to the reduced apparent diffusion coefficient.

Figure 3.12(a) shows that for binary systems of octanol in ethanol, the viscosity independent diffusion coefficient as measured by NMR diffusiometry, $D\eta$, remained reasonably constant with values of (9.6 ± 0.5) x 10^{-13} m² Pa and (14.1 ± 0.9) x 10^{-13} m² Pa, respectively, irrespective of composition. This reflects the almost ideal nature of mixing between octanol and ethanol, as seen in Figure 3.9, as the diffusion of neither solvent is affected by intermolecular interaction. For systems of water, ethanol and glycine (Figure 3.12(b)), the $D\eta$ values for dissolved glycine were also relatively constant at (8.4± 0.7) x 10^{-13} m² Pa. In contrast, those of the solvents varied more, with mean $D\eta$ values of (20 ± 3) x 10^{-13} m² Pa and (13 ± 1) x 10^{-13} m² Pa, respectively. This variation can be attributed to the highly non-ideal nature of ethanol/water mixtures. At high ethanol mass fractions, the water may be somewhat restricted by the hydrogen bonded networks and structures formed in ethanol, and this may be the cause of the decrease in the $D\eta$ values of water above an ethanol mass fraction of 0.5.
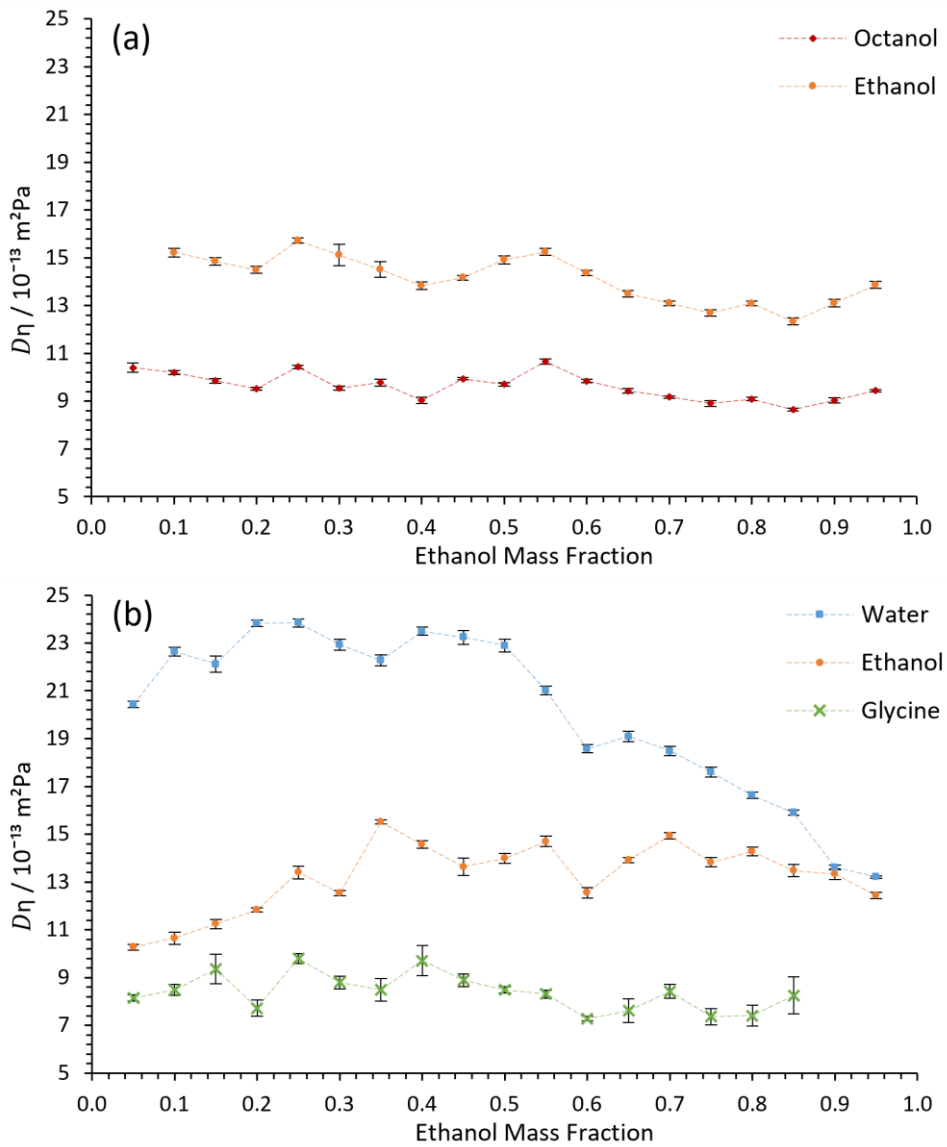
Figure 3.12: Changes in the viscosity independent diffusion coefficients, Dη, with increasing ethanol mass fraction for octanol, ethanol, water and glycine molecules in solutions of (a) octanol and ethanol and (b) water, glycine and ethanol. Dη was calculated through multiplication of the solution viscosity with the NMR-measured diffusion coefficients.

Figure 3.13 shows the relative $D\eta$ value of each component for STFs containing a constant water mass fraction of 0.15. The relative $D\eta$ value is given by the following equation:

$$relative\ D\eta = \frac{D\eta\ (STF)}{D\eta\ (binary)} \tag{3.4}$$

where $D\eta\ (STF)$ is the $D\eta$ value for the STF and $D\eta\ (binary)$ is the $D\eta$ value of the binary solution with the same ethanol mass fraction. The resultant data will therefore have a value of 1 if the component is unrestricted (as in a binary solution) and will be decreased as the component becomes more restricted relative to the binary system.
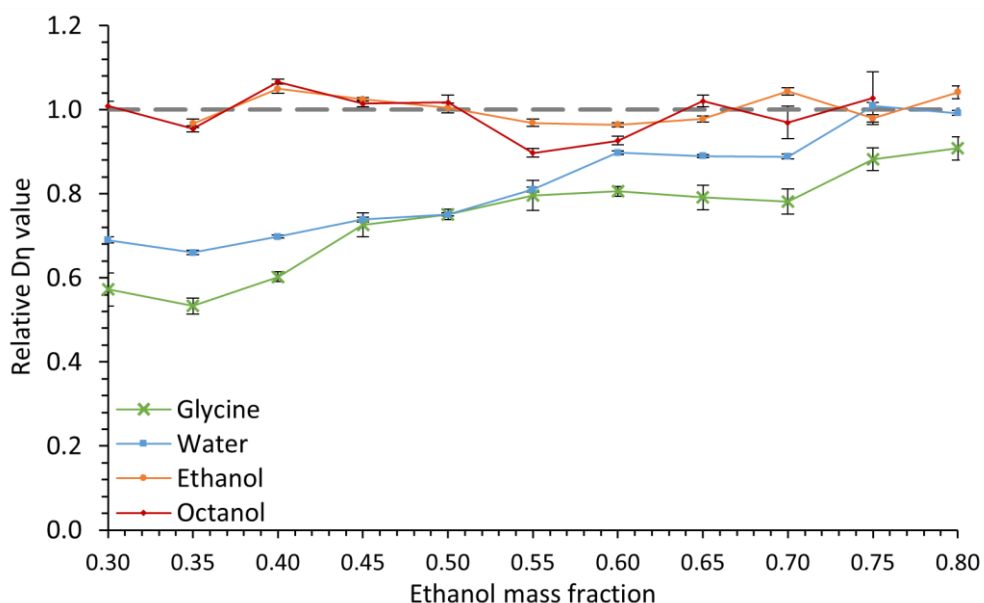
Figure 3.13: Relative Dη values (compared with binary ethanol/water, and ethanol/octanol mixtures) for glycine, water, ethanol, and octanol in STF mixtures containing a constant water mass fraction of 0.15 and different mass fractions of ethanol and therefore octanol.

Here it can be seen that ethanol remains relatively unconfined throughout, with an average relative $D\eta$ value of 1.00 ± 0.03. Octanol only displays a slight deviation from this with an average relative $D\eta$ value of 0.96 ± 0.07 and a maximum decrease of 15% of the unconfined value. These values are consistent with octanol remaining largely unconfined in these formulations.

Owing to the more flexible and transient nature of the nanostructuring in the ternary systems compared with their surfactant microemulsion counterparts, the transition between the w/o structured region and unstructured molecular solutions as ethanol content increases will be gradual. As the ethanol-rich boundary layers between the domains swell, they will solvate increasing amounts of both the octanol and water phases. The STFs will still contain hydrogen-bonded networks, but now with fewer, less well-defined aqueous "droplets", and more solvated octanol, which slightly decreases the relative $D\eta$ value of octanol. This is observed at an ethanol mass fraction of approximately 0.55, until a value of 0.65, above which the relative $D\eta$ value returns to approximately 1 as the fluid becomes more like an unstructured molecular solution.

The most significant changes in the relative $D\eta$ values are seen for the water and glycine molecules as the ethanol mass fraction changes. For a component confined within a nanostructured domain, we would expect a significant reduction in the relative $D\eta$ values (Figure 3.13) and this is what is observed for water and glycine at low ethanol mass fraction, with a reduction of up to 35% and 50%, respectively, consistent with water nanodomains with glycine confined inside.

In conclusion, the relative diffusion coefficients of octanol, water and glycine can be used to predict the level of structuring present within STFs containing 15 wt% water. In STFs with an ethanol mass fraction of less than 0.55, w/o microemulsion-like structures should be present as octanol is unconfined, with water and glycine becoming increasingly restricted at lower ethanol mass fractions, x_{eth}. Between 0.55 $\leq$ x_{eth} $\leq$ 0.70, there is a transitional region between w/o structures, and a molecular solution, where octanol and water become increasingly solvated within ethanol domains. Above an ethanol mass fraction of 0.70, the system behaves as a molecular solution, and nanostructuring is lost.

From these data, as ethanol content decreases and w/o microemulsion structures form, glycine should become confined in the small domains of water, decreasing the observed diffusion coefficients, and allowing thermodynamic control over crystallisation.

3.4.3   UV-vis Measurements

DO1 is an azo dye, meaning its molecular structure contains a N=N functional group, referred to as an azo bridge (Figure 3.14). It displays a strong maximum at a wavelength of approximately 400 – 550 nm due to a $\pi - \pi^*$ electronic transition in the amino-4-nitroazobenzene chromophore. Shifts in UV-vis spectral maxima may be observed when the dye molecules are placed in different solvent environments.[162-164]
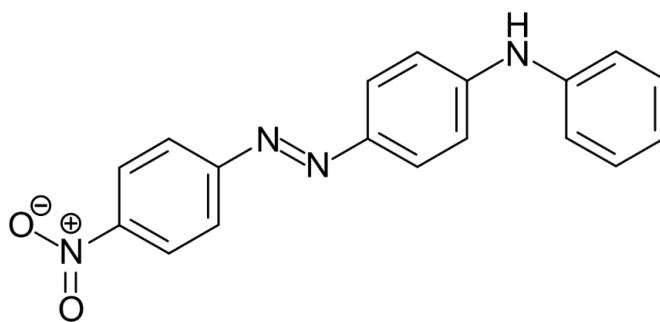
Figure 3.14: Structure of the azo dye Disperse Orange 1 (DO1).

In order to describe the behaviour of such solvatochromatic probes in different solvents, Kamlet and Taft proposed a set of three parameters, known as the Kamlet-Taft solvent parameters.[165,167] These are the hydrogen bond donating ability, α, the hydrogen bond accepting ability, β, and the dipolarity/polarisability, π*. In work performed by Airinei *et al.* it was determined that for azo dyes, the most important contributions to the solvatochromic shifts observed in UV-vis spectra were from the α and π* terms.[162] For azo dyes, increasing the dipolarity/polarisability of the solvent results in a red shift of the absorption maximum. This is due to solute-solvent interactions that will stabilise the π* orbitals. It was found that the polarisability of the solvent has been shown to display a dominant impact on the solvatochromic shift observed for azo dyes in general. However, all but one of the azo dyes tested did not contain a N–H group through which hydrogen bonding may occur, and for the one that did, (Disperse Orange 3) DO3, the α term became more impactful of the solvatochromic shift. Therefore, it is hereby predicted that, while DO1 contains fewer N–H groups than DO3, both the polarisability and hydrogen bond donating ability will be a factor in the DO1 absorbance shift due to some hydrogen bonding to the solvent through the single N–H group.

In this chapter, STFs tested contain the same low water mass fraction (0.15). DO1 dye is immiscible in water and should therefore be excluded from any water domains within the STFs. It should, however, be dissolved in both the ethanol-rich and octanol-rich regions so it is these solvent environments that will be primarily considered. Both ethanol and octanol contain terminal -OH groups, the same number of hydrogen atoms through which they can act as a hydrogen bond donor, and therefore a similar hydrogen bond donor ability. It is therefore predicted that the much larger differences in polarisability,

owing to the large differences in mass between ethanol and octanol, will play the dominant role over differences in solvatochromic shift in these formulations.

Polarisability is a measure of a molecule's ability to induce a dipole moment in another molecule. In the case of water and ethanol, which are already polar molecules as shown by the electrostatic potential surfaces in Figure 3.15, this is achieved as the electron density of the solute molecule will form attractive electrostatic interactions with the positive dipole of the polar molecule. In octanol, which is considered non-polar despite the -OH head group due to its long hydrocarbon chain, polarisability is instead attributed to induced dipole – induced dipole interactions. Dispersion forces arise from transient dipole moments found in non-polar molecules as electrons move, which may attract each other. Larger molecules have greater dispersion forces, and therefore polarisability, than smaller ones due to the larger number of electrons they possess.
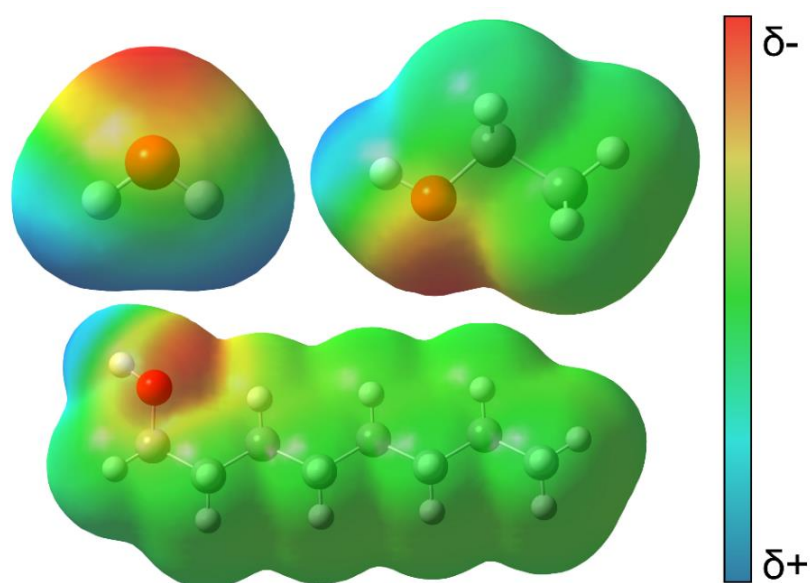
Figure 3.15: Electrostatic potential surface maps generated using the self-consistent field (SCF) method, showing the electron density across molecules of water (top left), ethanol (top right) and 1-octanol (bottom).

Figure 3.16 shows the change in the maximum absorbed wavelength, with the increase in ethanol mass fraction in the STFs. It is predicted that as the ethanol content increases, the fluid should move from containing nanostructuring, to a molecular solution in which the nanostructuring is lost.

While nanostructuring is present, the ethanol molecules have been shown to form a hydrogen-bonded networks in a continuous phase of octanol.[28] This network will be swell with water molecules to provide a diffuse boundary between the immiscible water and octanol. The water-rich side of the ethanol boundary will contain a lower concentration of DO1 solute, owing to its much lower solubility in water. In STFs where structuring is present, the largest solvent contribution will be from the continuous octanol phase. Here, the DO1 solute molecules should behave similarly to the way in which they would behave if they were in a bulk solution.
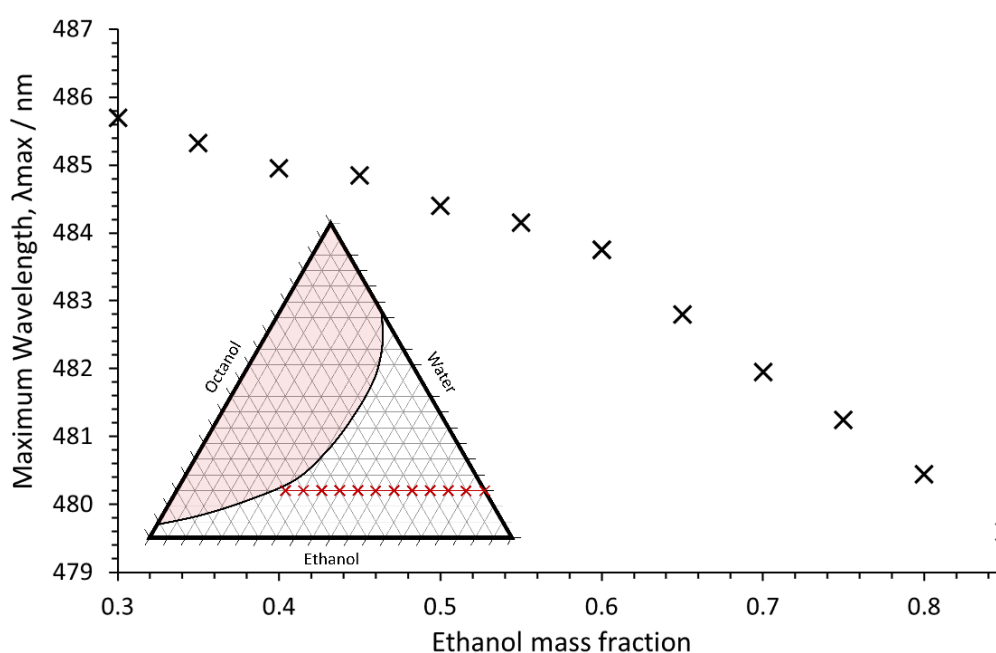
Figure 3.16: Change in maximum wavelength with ethanol mass fraction in STFs containing a constant water mass fraction of 0.15.

The molecular weights of water, ethanol, and octanol are 18.02 g mol^{-1}, 46.07 g mol^{-1}, and 130.23 g mol^{-1}, respectively. Consequently, octanol is much larger in size than the other two components, contains a greater number of electrons, and therefore has a higher polarisability. This appears to be reflected in the observed maxima in samples of pure octanol and ethanol, where the value of λ_{max} for DO1 were found to be 484.6 nm and 474.1 nm, respectively, suggesting that octanol could stabilise the π* orbital (LUMO) to a greater degree than ethanol, leading to a red shift in the wavelength. As the ethanol mass fraction increases, the diffuse boundary region will swell even further, particularly as the number of ethanol molecules per unit mass is greater than the number of octanol molecules

per unit mass. Consequently, more of the octanol and water phases will be solvated into the boundary region. This should disrupt the octanol-dye interactions and increase the number of ethanol-dye interactions, resulting in a shift to shorter absorbance maxima. At an ethanol mass fraction of 0.60 there appears to be a change in the solvent environment in which the dye is situated, moving from one in which the octanol phase is dominant as the bulk phase to one where ethanol begins to dominate. It is therefore predicted that, in terms of polymorphic outcome, the thermodynamic product may be dominant below an ethanol mass fraction of 0.60, and the kinetic product dominant above this point.

As ethanol content increases and solvates more octanol and water, a molecular solution will begin to form. At this point, there should be no locally enriched and depleted aqueous domains, and the small ethanol and water molecules will be randomly dispersed with the octanol. This would cause a greater disruption to the polarization of the dye, as there is a higher proportion of ethanol that is "unlocked" from the water domains that will be capable of interacting with the dye. This may be responsible for the sharper decrease in the maximum wavelength observed at 0.60 mass fraction of ethanol.

3.4.4   Conductivity Measurements

The data shown in Figure 3.17, describing the change in conductivity with increasing ethanol mass fraction, closely follow the same trends observed in the diffusion studies. Below a threshold value of 0.55 for the ethanol mass fraction, the conductivity is at a minimum. Between $0.55 \leq x_{eth} \leq 0.70$, the conductivity sharply increases, before plateauing at a maximum conductivity of approximately 3 μS. This result is expected due to the close relationship between diffusion of ions and conductivity as described by the Nernst-Einstein equation.

$$\Lambda_{eq} = \frac{zF^2}{RT}(D_+ + D_-) \tag{3.5}$$

where Λ_{eq}, z, F, R and T are the equivalent conductivity, ion valency, Faraday constant, molar gas constant and temperature, respectively, and D_+ and D_- are the diffusion coefficients for cations and anions, respectively.
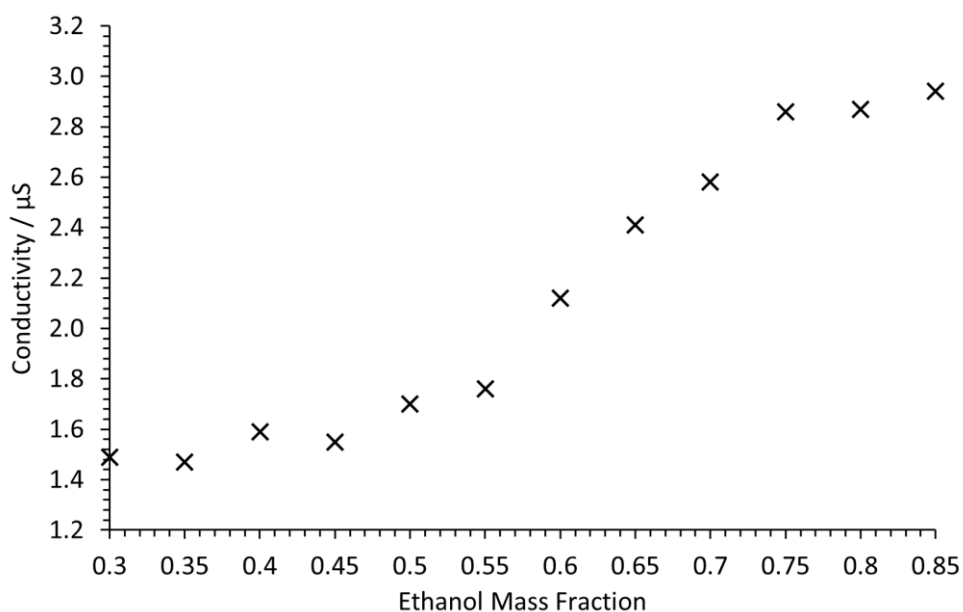
Figure 3.17: Conductivity change with ethanol mass fraction for STFs containing a water mass fraction of 0.15 and a constant mass of glycine.

In the STF solutions, the only ionic component of the systems will be the solvated glycine zwitterions. Therefore, the conductivity is expected to be directly proportional to the glycine diffusion observed, i.e. as diffusion becomes restricted, the systems will have a reduced conductivity. As the system loses its nanostructuring, glycine will diffuse more freely through the system, carrying charge and therefore increasing the conductivity. This trend continues until the system becomes a molecular solution, where ions have maximum freedom and a corresponding maximum conductivity with be reached.

3.4.5   Crystallisation

3.4.5.1   *Optimising Crystallisation*

According to Neutron scattering data recorded by Prevost *et al.*, an STF system comprised of water, octanol, and ethanol in a ratio by mass of approximately 15:50:35 was the most promising system, with similar scattering behaviour to that seen in surfactant-based microemulsions. For example, this

composition led to the identification of w/o structures with a characteristic size of approximately 4.7 nm by X-ray scattering. For surfactant-based microemulsions used by Chen *et al.* to selectively crystallise γ-glycine, small angle X-ray scattering data revealed w/o droplets with a core size of (1.7–4.2) ± 0.2 nm. This system was therefore used as a starting point, in order to optimise the crystallisation methodology.

This is corroborated by the measured diffusion data, as this composition is the point at which the diffusion of glycine and water were most restricted and therefore represents the composition with the most promising nanoconfined domains.

3.4.5.2   Growth time

Figure 3.18 summarises the changes in polymorphic form that were produced after different growth times. After six hours had elapsed, the first crystals became visible and were extracted. Upon analysis using FT-IR spectroscopy, they were identified as γ-glycine. This indicates that thermodynamic control is governing the initial polymorphic outcome. However, between one and five days, α-glycine nucleated and grew at a faster rate compared with γ-glycine, quickly becoming the dominant polymorph. This should in fact be the case, as it is known that upon nucleation, α-glycine grows ~500 times faster than γ-glycine. However, from day six onward the only polymorph remaining in the samples was γ-glycine. This suggests that the supersaturation may have decreased sufficiently so that the γ-glycine saturation point was reached, and that the system was at a minimum in free energy. At this point the system would be undersaturated with respect to α-glycine and so α-glycine will continuously dissolve, to produce a system supersaturated with respect to γ-glycine, so that γ-glycine crystal growth occurs. This Ostwald ripening mechanism will continue until all the α-glycine has dissolved, leaving just γ-glycine remaining. This process would be facile due to the presence of pre-existing γ-glycine nuclei in solution.
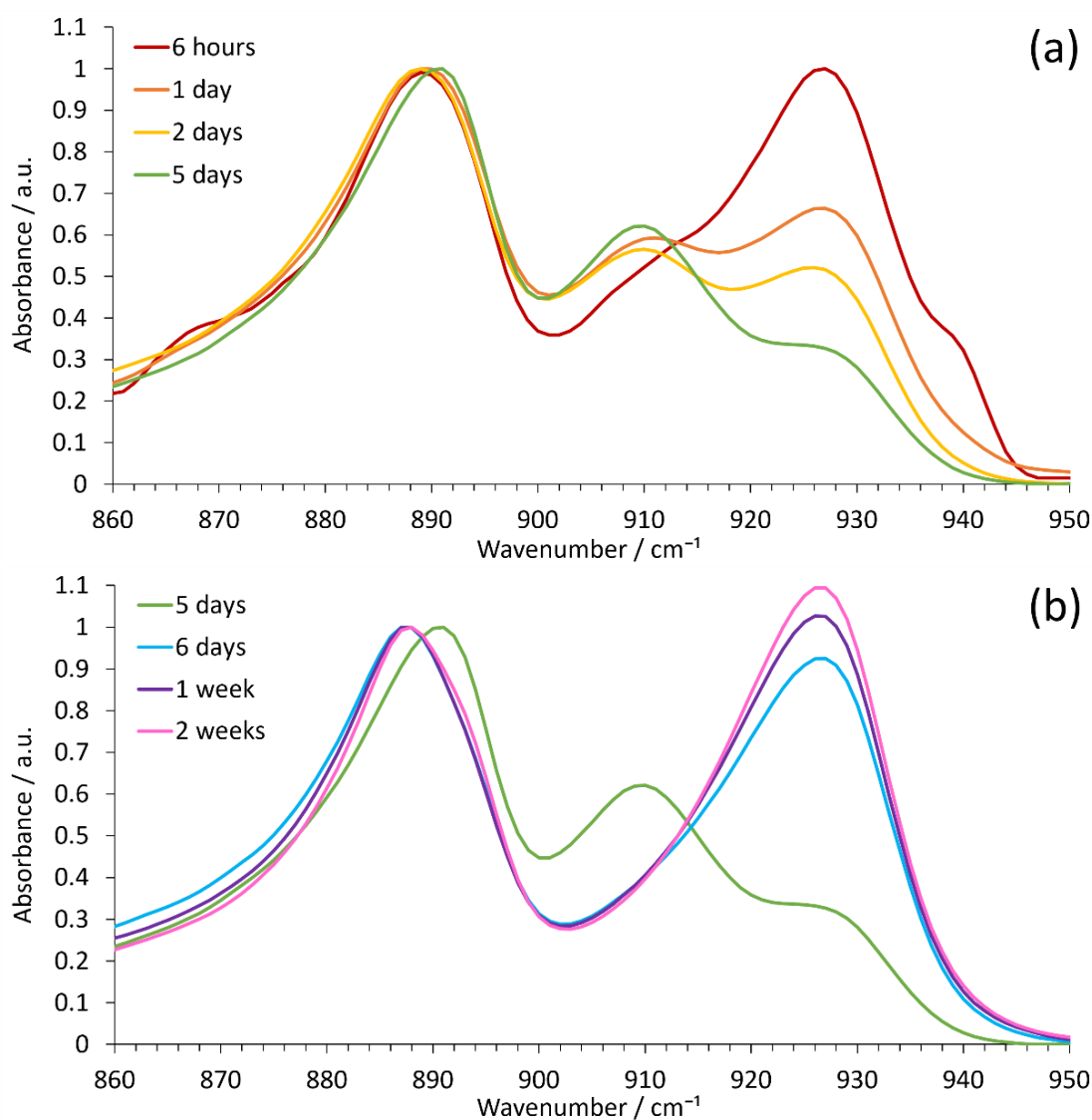
Figure 3.18: Normalised FT-IR data for the crystallisation products extracted after different growth times for STFs containing a water:octanol:ethanol mass ratio of 15:50:35, and a relative glycine supersaturation, $\frac{c}{c_{sat}}$ of 1.4. Absorbance maxima at 909 cm^{-1} and 928 cm^{-1} identify material as containing α-glycine and γ-glycine, respectively.

3.4.5.3   Supersaturation

To further understand the effect that the relative concentration has on the polymorphic outcome, STFs containing a range of different glycine masses (0.38 – 0.47 g) relating to relative supersaturations between $\frac{c}{c_{sat}}$ = 1.2 – 1.6 were made. Crystals were harvested after one week to allow any α-glycine to transform into γ-glycine should any γ-glycine have been competitively nucleated. The outcome is summarised in Figure 3.19.

Figure 3.19 shows that for STFs with $\frac{c}{c_{sat}}$ = 1.2 − 1.6, some γ-glycine was nucleated, although the α-form was the majority polymorph in samples with higher glycine concentrations of $\frac{c}{c_{sat}}$ > 1.5. At a relative supersaturation of $\frac{c}{c_{sat}}$ < 1.5, the γ-form was the main polymorph present after one week of growth. A relative supersaturation of $\frac{c}{c_{sat}}$ = 1.44 was the highest glycine concentration tested that contained γ-glycine as the sole polymorphic product, and this was therefore identified as the threshold concentration for thermodynamic control. As yield decreased with concentration, for future crystallisations a maximum supersaturation of $\frac{c}{c_{sat}}$ = 1.4 was used in order to maximise yield while maintaining reliable thermodynamic product formation.
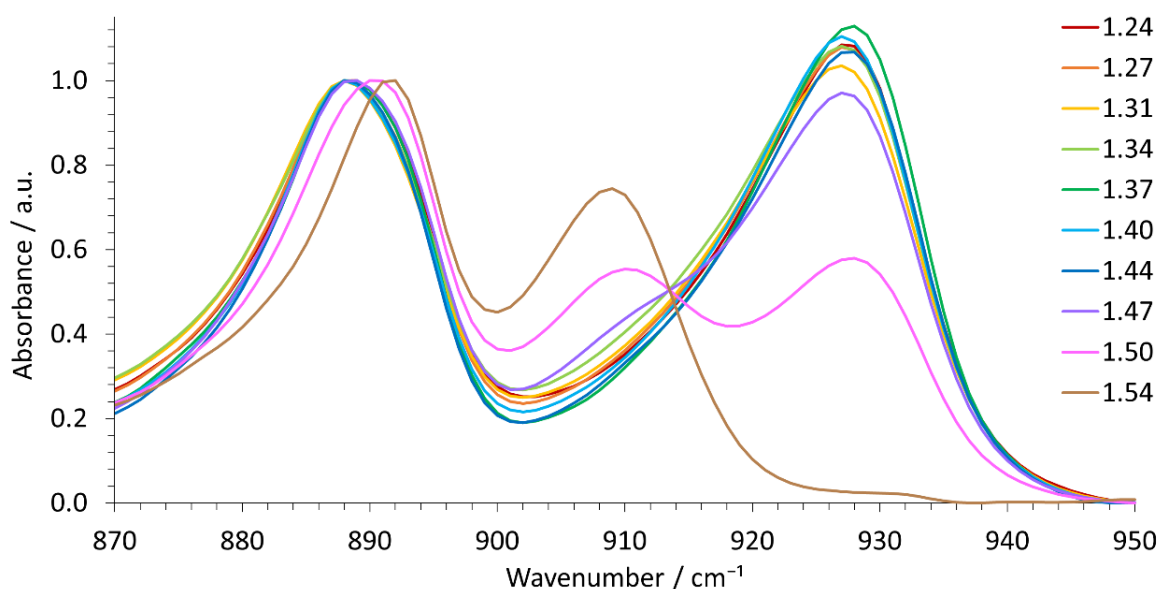
Figure 3.19: Normalised FT-IR data recorded for the crystallisation products extracted after one week for STFs containing a water:octanol:ethanol mass ratio of 15:50:35, at different glycine supersaturations $\left(\frac{c}{c_{sat}}\right)$. Absorbance maxima at 909 cm^{-1} and 928 cm^{-1} identify material as containing α-glycine and γ-glycine, respectively.

These results have been visually corroborated using optical microscopy to observe the morphologies of the crystalline products. This also provided information of the size on the crystals produced, which fell in a range of 0.14-2.1 mm (measured along the longest dimension of the crystal). Some examples are given in Figure 3.20.
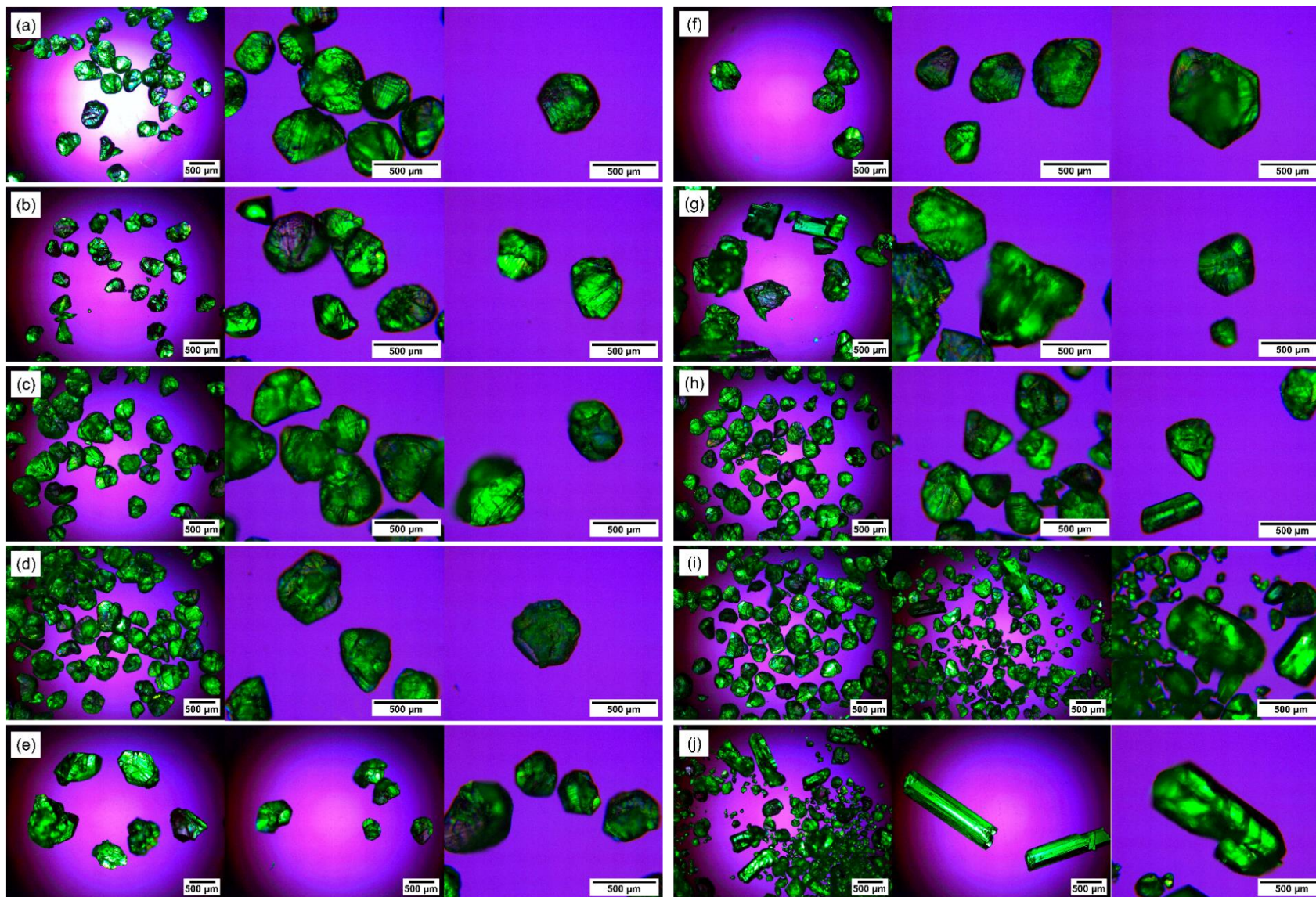
Figure 3.20: Optical microscopy images of glycine crystals extracted from STFs containing a water:octanol:ethanol mass ratio of 15:50:35 with an initial $\frac{c}{c_{sat}}$ of (a) 1.24, (b) 1.27, (c)1.31, (d) 1.34, (e) 1.37, (f) 1.40, (g) 1.44, (h) 1.47, (i) 1.50, (j) 1.54. Triangular/hexagonal crystals are γ-glycine, whereas elongated bipyramidal crystals, seen predominantly in (j), are α-glycine.

3.4.5.4 Confinement Effects

UV-vis, conductivity, and NMR diffusiometry data corroboratively suggest that there are two regimes present as the systems move along a constant line of 0.15 water mass fraction in the phase diagram. At a lower ethanol mass fraction (approximately 0.3 – 0.6), the water phase appears to be in confinement, suggestive of w/o nanostructuring. As the ethanol mass fraction increases above 0.60, this confinement is lost as nanostructuring is lost, and the fluids become more like molecular solutions in character. To investigate the effect of this apparent confinement on the outcome of the crystallisation of glycine, crystallisations were completed along this line using a relative supersaturation of $\frac{c}{c_{sat}}$ = 1.4. The STFs were prepared as outlined in Section 3.3.4 and allowed to crystallise at 25 °C over one week. Figure 3.21 shows that in STFs with an ethanol mass fraction of 0.50 or less, γ-glycine grew selectively, suggesting that, within this range, glycine is still confined within pockets of water, and nanostructuring is still effective in providing nanoreactors in which crystallisation can occur.
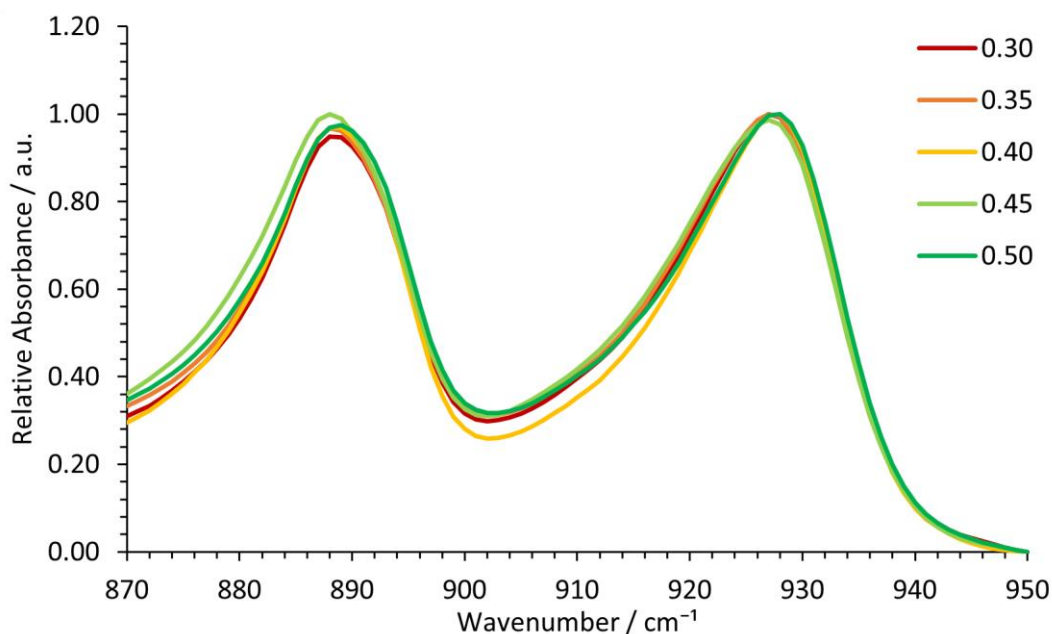
Figure 3.21: Normalised FT-IR data recorded for the crystallisation products extracted after one week for STFs with a water mass fraction of 0.15, a relative glycine supersaturation of $\frac{c}{c_{sat}}$ = 1.4 and different ethanol mass fractions of 0.30 – 0.50 as outlined in the figure legend. Absorbance maxima at 928 cm^{-1} identify material as γ-glycine.

Figure 3.22 shows the crystallisation product in STFs with an ethanol mass fraction between 0.50 – 0.75. This is the region identified in the conductivity data where the systems transitioned between the confined and unconfined regimes. As the ethanol content increased, the γ-glycine content of the product decreased, becoming the minority polymorph above an ethanol mass fraction of 0.60. Consequently, it can be concluded that above 50 wt% ethanol, the nanostructuring begins to break down and becomes increasingly ineffective in controlling the polymorphic outcome.
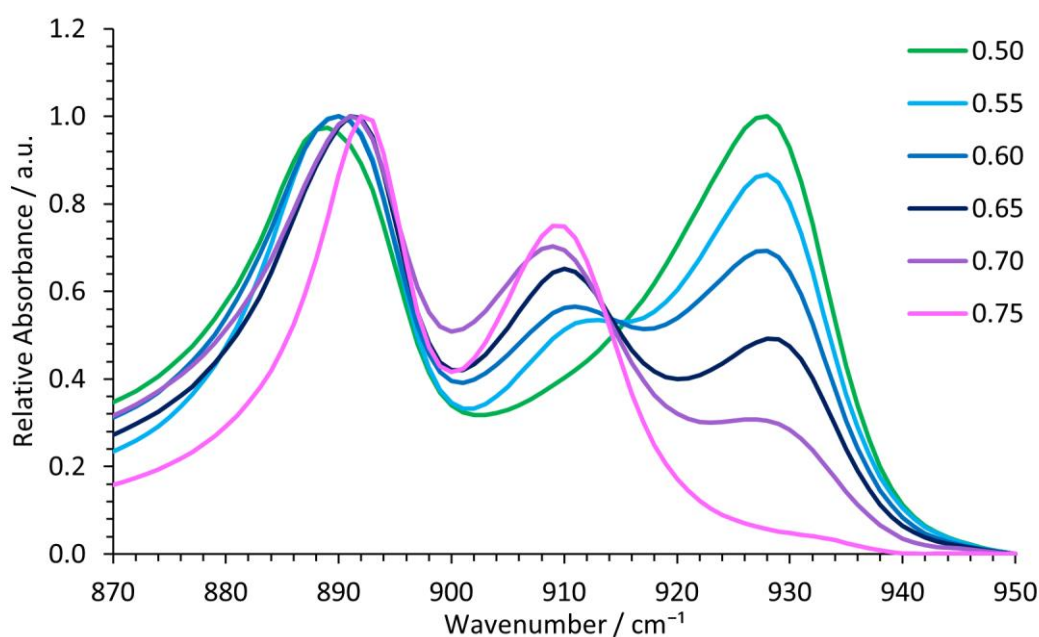
Figure 3.22: Normalised FT-IR data recorded for the crystallisation products extracted after one week for STFs with a water mass fraction of 0.15, a relative glycine supersaturation of $\frac{c}{c_{sat}}$ = 1.4 and different ethanol mass fractions of 0.50 – 0.75 as outlined in the figure legend. Absorbance maxima at 909 cm^{-1} and 928 cm^{-1} identify material as containing α-glycine and γ-glycine, respectively.

When nanostructuring occurs, it is due to the accumulation of ethanol into diffuse boundary layers between the water and octanol domains since ethanol may equally solubilise both fluids. As the ethanol content increases, more water and octanol may be solubilised until the domains are no longer separated, and a molecular solution is formed. Figure 3.23 depicts this, where the green region symbolises the area in which ethanol has solubilised water and octanol. The yellow and blue regions represent the octanol and water phases, respectively. If glycine is confined in a blue region, γ-glycine is more likely to nucleate, whereas if it is unconfined, or in a region of high antisolvent concentration,

the metastable forms tend to nucleate. As the ethanol content increases, the water pockets will decrease in number and will become less well-defined so that the γ-form will no longer form preferentially, indicating that kinetic control over crystallisation dominates as in bulk solution crystallisation.
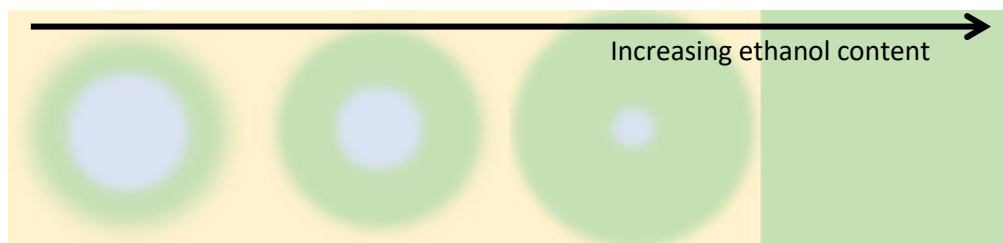
Figure 3.23: Diagram representing the predicted structural changes upon increasing ethanol content in STFs with w/o nanostructures. Water and octanol phase are represed by the blue and yellow regions, repsectively, and the ethanolic boundary region is depicted in green.

Figure 3.24 shows that in fluids made with an ethanol mass fraction of 0.75 − 0.85, α-glycine is the sole polymorphic form produced. This is consistent with the conductivity and diffusion data collected, summarised in Figure 3.25, and suggests that at this point, the water and octanol became fully solubilised, with no defined aqueous nanodomains.
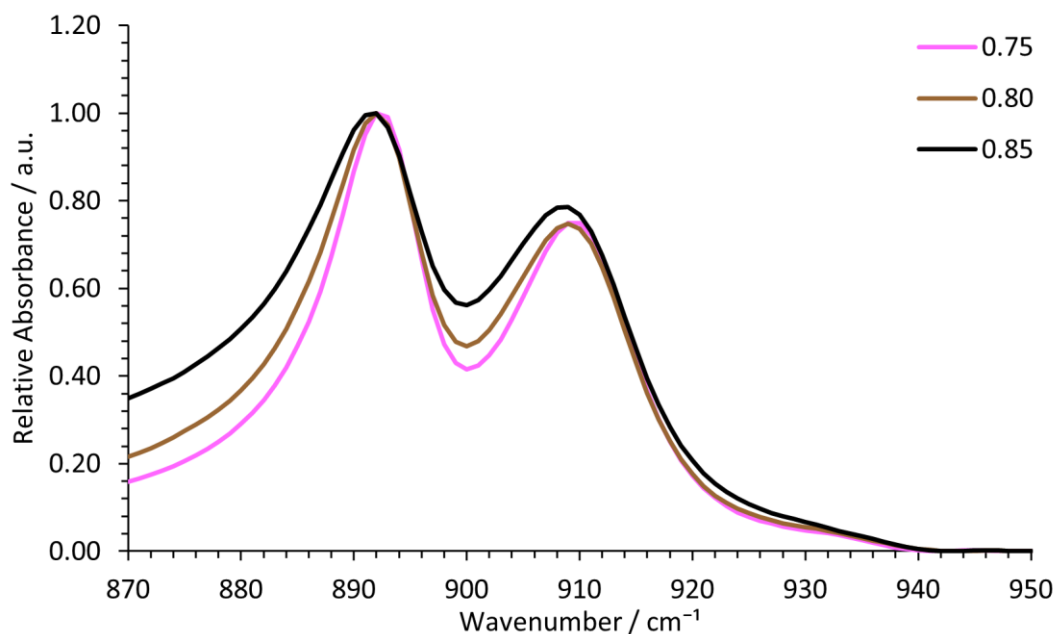
Figure 3.24: Normalised FT-IR data recorded for the crystallisation products extracted after one week for STFs with a water mass fraction of 0.15, a relative glycine supersaturation of $\frac{c}{c_{sat}}$ = 1.4 and different ethanol mass fractions of 0.75 − 0.85 as outlined in the figure legend. Absorbance maxima at 909 cm^{-1} identify material as α-glycine.

Collectively, these results suggest that to promote thermodynamic control over crystallisation to crystallise the most stable polymorph of a crystalline material, STFs with an ethanol mass fraction of less than 0.50 should be used. This ensures the presence of water nanodomains in which solute molecules can remain confined. Without these nanostructures, thermodynamic control is lost, and the kinetic form will dominate.
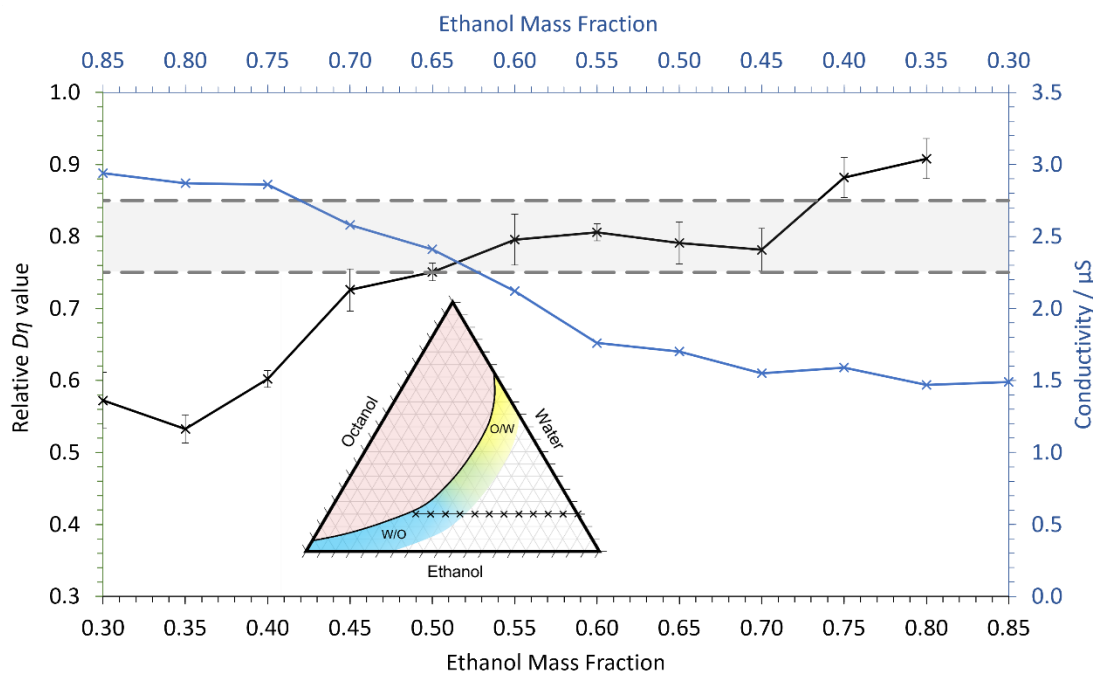
Figure 3.25: Relative Dη values (compared with binary ethanol/water, and ethanol/octanol mixtures) for glycine (black), and conductivity measurements (blue) for STF mixtures containing a constant water mass fraction of 0.15. The shaded region, bounded by dashed lines, indicates the diffusion values above and below which kinetic and thermodynamic control over crystallisation maybe be observed, respectively.

The observed polymorphic outcome agrees with the theoretical predictions made from diffusion, UV-vis, and conductivity measurements. Consequently, these techniques could be powerful tools for determining whether future STF systems will act as nanocrystal reactors for producing the most stable polymorph of crystalline systems or not. For example, Figure 3.25 highlights the regions in which each polymorph was observed relative to the diffusion and conductivity of glycine in the STFs. Above a relative diffusion value of ≥ 0.85 the systems only produced the kinetic product, α-glycine, between $0.75 <$ relative $Dη < 0.85$ a combination of polymorphs will form, and when the relative $Dη \leq 0.75$, only the thermodynamic product is formed. As previously discussed, this is supported by simple

conductivity measurements, which could therefore be used as quick, initial guidance, in order to avoid more complicated and expensive DOSY-NMR techniques. NMR could then be used to confirm the degree of restriction and likely success over crystallisation when promising systems have been identified. Scattering and computational techniques could also then be used as a final study to fully comprehend and model the size and behaviours of the nanodomains present.

Note that UV-vis measurements identified only two regimes, not the three observed by conductivity and NMR diffusiometry. This is likely because the DO1 dye was essentially absent from the nanoconfined aqueous domains and so was only sensitive to the compositions of the predominantly octanol/ethanol regions. Here was a distinct change in the wavelength with STF composition around an ethanol mass fraction of 0.60. This is interesting, as it is the point at which the dominant polymorph formed transitions from the thermodynamic product at low mass fractions, and kinetic product at high mass fractions. Consequently, this technique may also be used in conjunction with conductivity measurements as a predictor of polymorph formation, as well as the degree of nanostructuring in STFs.

3.4.6   Seeding Capabilities

To assess the ability of the STFs to seed bulk solutions, aliquots of the nanocrystal-containing fluids were transferred to metastable water/ethanol binary solutions that were supersaturated with glycine. The resultant crystals formed at short timeframes of one to two hours, and were then extracted after one week, at the same time as the STFs from which the seed containing aliquots were taken. The results of the seeded experiments are given in Figure 3.26 – Figure 3.28.

Figure 3.26 shows that after seeding with the STF samples containing solely γ-glycine, γ-glycine was the product formed from the seeded binary ethanol/water solutions. If left undisturbed, only α-glycine was formed in the metastable binary solutions without the addition of STF aliquots. Consequently, it may be concluded that seeding with the nanocrystals suspended in the STF systems is successful in

the growth of the seed polymorph in unstructured, bulk solution, with the polymorph appearing as macroscopic crystals in a shorter timeframe compared with the STF system.
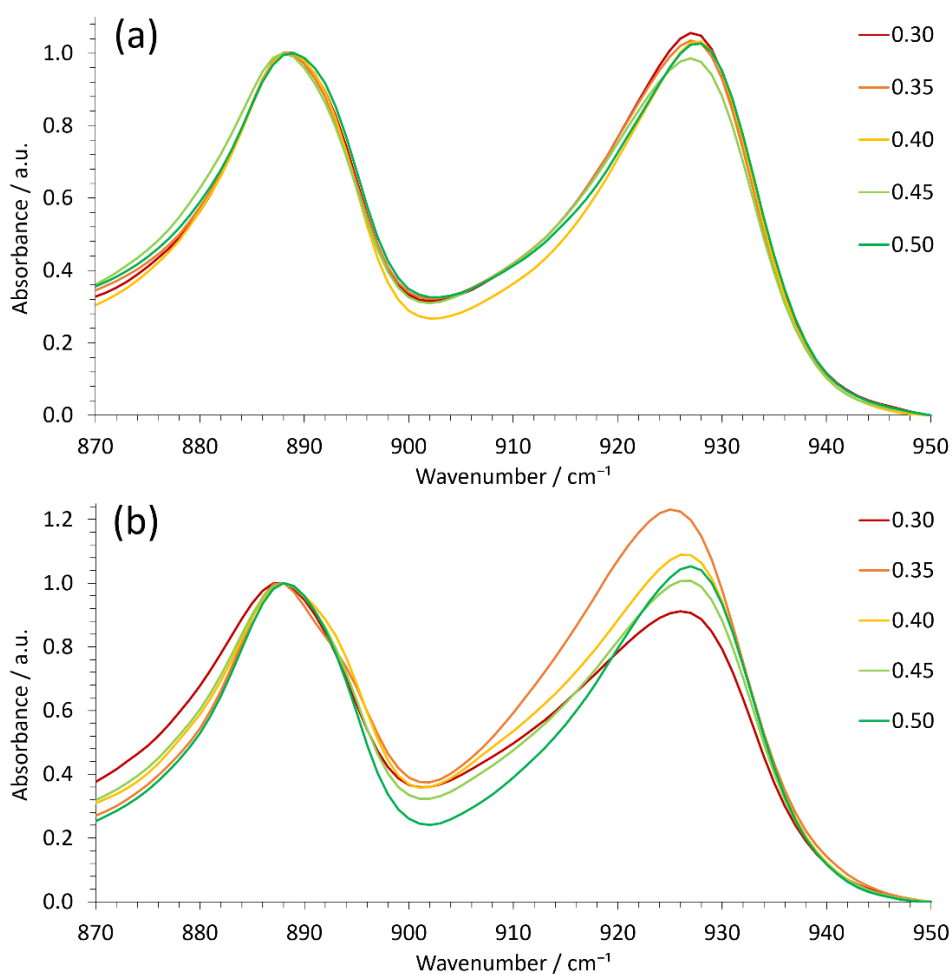
Figure 3.26: Normalised FT-IR data recorded for (a) the crystallisation products extracted after one week for STFs with a water mass fraction of 0.15, a relative glycine supersaturation of $\frac{c}{c_{sat}}$ = 1.4 and different ethanol mass fractions, (b) the crystallisation products extracted after one week for bulk solutions seeded with aliquots of the STFs in (a). Absorbance maxima at 909 cm^{-1} and 928 cm^{-1} identify material as containing α-glycine and γ-glycine, respectively.

In the STFs in which there is a transition between the structured and unstructured region, it was observed that there was a mixture of the kinetic and thermodynamic products formed (Figure 3.27(a)). Upon seeding, a similar mixture of polymorphs was produced, albeit less well-correlated. In each case where a mixture of polymorphs was obtained from the STF, the corresponding seeded product would contain a large, often dominant proportion of α-glycine. As only 5 ml was taken from each solution, the number of seeds produced would be limited and will contain a random distribution of seeds. In the case of samples in which only one polymorph is present, only that polymorph will be extracted

and grown. When there are different polymorphs present in the same STF, there is a chance that the aliquot taken may not fully represent the same ratio of products found in the final STF product due to the random distribution of nuclei in the fluids.
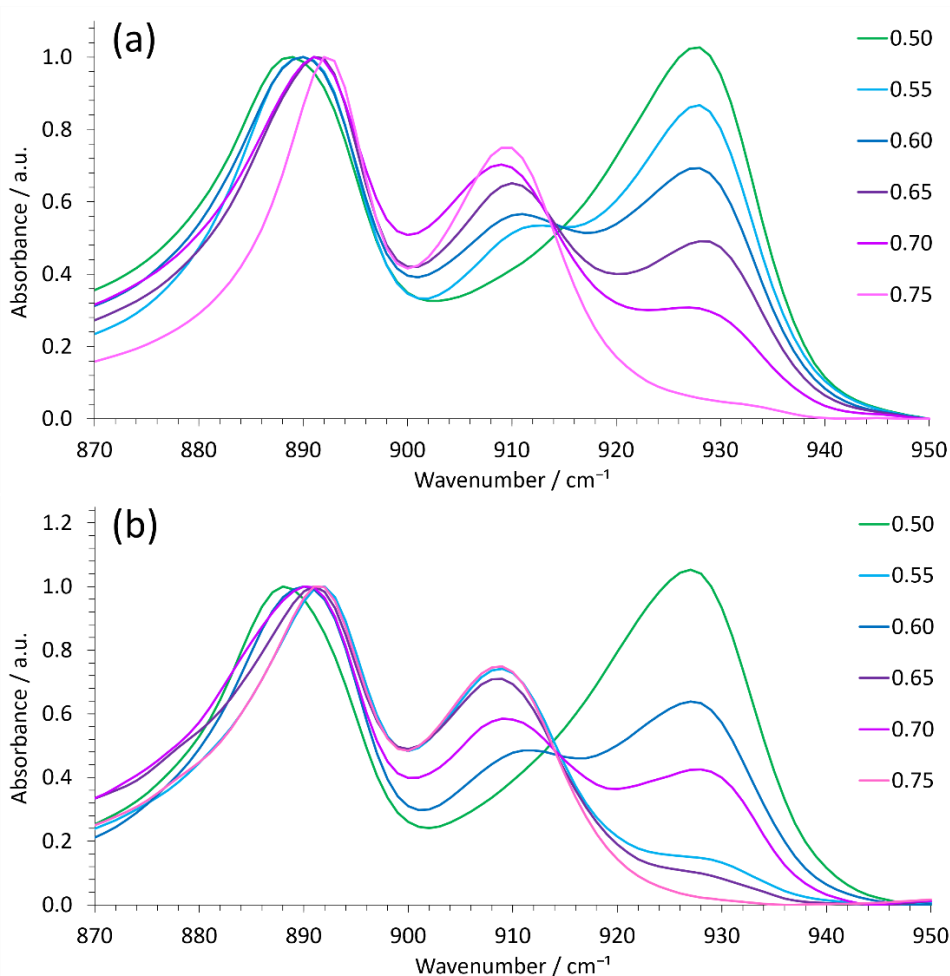
Figure 3.27: Normalised FT-IR data recorded for (a) the crystallisation products extracted after one week for STFs with a water mass fraction of 0.15, a relative glycine supersaturation of $\frac{c}{c_{sat}}$ = 1.4 and different ethanol mass fractions, (b) the crystallisation products extracted after one week for bulk solutions seeded with aliquots of the STFs in (a). Absorbance maxima at 909 cm^{-1} and 928 cm^{-1} identify material as containing α-glycine and γ-glycine, respectively.

Additionally, as evidenced in the growth tests, if both α and γ glycine are nucleated concomitantly, then the α-polymorph will become dominant in short growth times. The growth time used in these experiments was 16 hours before aliquots were taken. In some solutions, α-glycine may have been dominant at the time of seeding and then this is reflected in the higher proportions of α-glycine observed in the seeded product compared with the STFs. It is important to note that, regardless of the

ratio of products, in STFs containing both polymorphs, both polymorphs were also detectable in the seeded binary solutions.

Finally, the unstructured fluids (ethanol mass fractions >0.70) were used, and the results summarised in Figure 3.28. Here, the unstructured solutions only produced α-glycine, which was again directly reflected in only α-glycine crystallising in the seeded products.
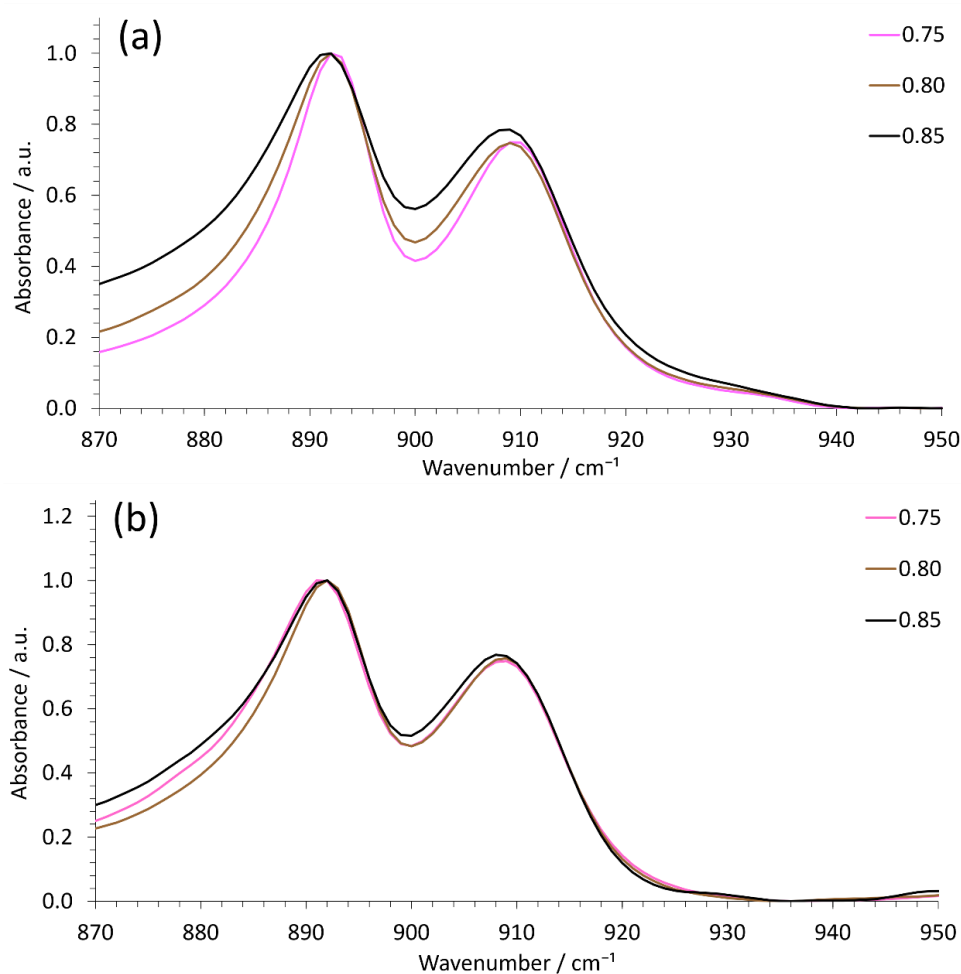
Figure 3.28: Normalised FT-IR data recorded for (a) the crystallisation products extracted after one week for STFs with a water mass fraction of 0.15, a relative glycine supersaturation of $\frac{c}{c_{sat}}$ = 1.4 and different ethanol mass fractions, (b) the crystallisation products extracted after one week for bulk solutions seeded with aliquots of the STFs in (a). Absorbance maxima at 909 cm^{-1} and 928 cm^{-1} identify material as containing α-glycine and γ-glycine, respectively.

3.5 CONCLUSIONS

In summary, the presence of aqueous nanodomains in STFs containing water, octanol and ethanol, as presented by Prevost *et al.* in small-angle scattering studies,[24] has been corroborated through the

use of simple conductivity and UV-vis measurements, as well as NMR diffusiometry. Furthermore, these data have confirmed that dissolved glycine does not significantly impact this nanostructuring and may be confined within the aqueous domains, leading to restricted diffusion. For relative diffusion values ≥ 0.85 and ≤ 0.75, STFs selectively produced α-glycine and γ-glycine, respectively, with those compositions at intermediate values producing a combination of polymorphs. This result mirrors the ability of surfactant microemulsions to control the polymorphic outcome of crystallisation, leapfrogging Ostwald's rule of stages to crystallise the most thermodynamically stable polymorph of glycine.[104] However, STFs provide a promising alternative as surfactants can be problematic during crystallisation due to difficulties in product extraction, as well as their expense compared with the simple solvents used in this work.

Moreover, due to the less rigid nature of STFs, they can be used to seed larger bulk systems without the need to first extract the nanocrystals. Aliquots of STFs were taken prior to crystal sedimentation, while nanocrystals remained suspended in the fluids. The aliquots were transferred to binary ethanol/water solutions, breaking up any STF nanostructures present and providing more dissolved glycine from which the seeds could grow. This led to the selective growth of both α-, γ-glycine, or combinations of both depending on the STF from which seeds were taken.

4 INVESTIGATING THE EFFECT OF NANOSTRUCTURING

4.1 INTRODUCTION

Selective polymorph formation has been well-studied in nm-confined systems.[66,104-110,168-173] The advantages of this methodology compared with bulk crystallisations include the high supersaturations that may be achieved, and the large number of nanoreactors that can be present in a single system, with the same/similar environments and volumes. Nucleation is a stochastic process meaning that the nucleation of a certain polymorph is based on a random probability. Statistically, nucleation of the desired polymorph is more likely to occur when there are more nanoreactors present and the nucleation energy barrier is lower.

Additional factors, when considering the difference between bulk and confined systems, are the influence of temperature gradients across the reactor, as well as the impact of inhomogeneous mixing and impurities in the solution.

4.1.1 Crystallisation of glycine in nanoconfinement

Droplet microemulsions[66,104-110] and nanoporous systems[168-173] have previously been used for selective polymorph and allotrope formation, as well as to control the physical properties of crystals such as morphology and melting point.

Nanopores result in a physical constraint to crystal growth, meaning that the size of the nanocrystals formed is restricted to the size of the pores. They have been used extensively as templates to induce both preferred orientation as well as size in the crystals. For example, it has been demonstrated that when confined to polymer (PS-PDMA) pores, nanocrystals of β-glycine grew parallel to the direction of the pores.[171] As well as allowing morphology to be tailored, it is commonly known that the melting point of crystals confined in nanoporous media is reduced when compared to the same material in bulk, with an inverse relationship between the pore size and melting point depression.[174-178] The

surface of most solids will melt at a lower temperature compared to the bulk of the material. As particle size decreases and the surface area-to-volume ratio increases, this will result in a melting point depression, below the equilibrium melting temperature of the material. This is often modelled by the Gibbs-Thompson equation.[178,179] The term 'surface pre-melting', has been coined to describe a mechanism that may lead to such melting point depressions. This proceeds in two stages: firstly, the formation of a liquid-like amorphous phase from the melting of surface sites that surrounds the nanocrystal core; then secondly the growth of this liquid phase into the core, until the crystal is completely melted.[70,175,176]

This pre-melting has been observed for many materials, including a study into glycine nanocrystals inside controlled-pore glass powders and porous polymers (p-PS-PDMA) by Hamilton *et al.*[171] Interestingly, as well as a melting point depression, it was observed that the metastable β-polymorph was formed preferentially, and persisted for several days. This contrasts with bulk crystallisations in which β-glycine is highly metastable and will transform to α-glycine within a few minutes. This kinetic stabilisation effect has been observed not just in glycine,[168-171] but in other polymorphic materials such as glutaric acid,[179] acetaminophen,[180,181] benzyl alcohol,[182] carbamazepine,[183] and ROY.[172,183]

Typically, in studies examining the crystallisation of glycine in nanoconfinement, the focus has been on this kinetic product stabilisation. Recently, *in situ* NMR spectroscopy has been used as a strategy for probing the mechanism of crystallisation. Juramy *et al.* used Dynamic Nuclear Polarization (DNP) NMR spectroscopy to observe the evolution of glycine crystallisation when confined in mesoporous silica materials.[168] It was concluded that crystallisation proceeded more slowly in confinement, and as a result, the early stages of crystallisation may be directly observed, including the initial formation of transient phases prior to transformation into more stable forms as predicted by the two-stage nucleation model previously discussed. This is important as typically crystal growth is rapid in bulk crystallisations and hence it is not possible to assess the crystallisation behaviour in the earlier nucleation and growth stages. Additionally, this methodology has allowed a higher degree of

sensitivity in measuring detectable signals, which is important in nanoconfined systems, as there is intrinsically a smaller amount of solid that will be in a system at the nucleation stage. There are some drawbacks to this technique, however, as often polarizing agents and deuterated solvents are added to the crystallising systems, and this may alter the crystallisation pathway. For example, in experiments performed by Vioglio *et al.*, it was reported that the use of D_2O promoted the formation of γ-glycine, the most stable polymorph, as opposed to the metastable forms that would otherwise crystallise.[184]

4.1.2   Crystallisation in droplets

The use of droplet nanoreactors for nanoparticle crystallisation has been, again, typically focussed on investigations into crystallisation kinetics. Systems can be broadly categorised into droplets deposited onto solid surfaces,[185] droplets suspended in gas,[186,187,190] or in a second liquid.[66,104-110] In general, the two former methods use solvent evaporation to control droplet supersaturation.

For example, inkjet printing technology has been used to selectively nucleate the highly metastable β-glycine polymorph from printing pL-sized droplets and allowing them to evaporate on various surfaces.[185,191] The use of different solid substrates on which the droplets were deposited ruled out the impact of the surface on the crystallisation outcome, and led to the conclusion that it was the droplet size that led to polymorphic control, as smaller droplets (<0.1 μL) resulted in only β-glycine growth, whereas larger droplets deposited by micropipette (≥0.1 μL) also nucleated α-glycine.[185] Similar results have also been observed when using a spray drying technique to control crystallisation of the metastable carbamazepine IV polymorph.[190] Here the atomising gas flow rate was adjusted to produce droplets with sizes between 5.39 – 38.55 μm, in which, again, the smallest droplets produced the most control over the selective nucleation of the carbamazepine IV polymorph. Here, the higher evaporation rates of smaller droplets enable higher supersaturations to be attained and this favours nucleation of more metastable polymorphs.

Another method through which polymorph control may be achieved in droplet suspensions is through electrostatic levitation.[186,187] Here, an undersaturated droplet can be injected using a syringe in between two electrodes such that it levitates. Conditions such as the temperature and relative humidity in which the droplet is situated can be changed to promote evaporation of the droplet solvent by a predetermined amount, increasing the supersaturation of the remaining solution to a desired value. Raman spectroscopy and X-ray diffraction can then be performed on this suspended droplet to assess the crystallisation process *in-situ*.

Moving away from droplet drying, microfluidic systems allow the formation of µm-sized droplets of one phase in another, largely immiscible phase. These devices enable the injection of droplets directly into the suspension medium, forming identical droplets much faster and at much larger scales than can be achieved through manual processes such as using micropipettes. As a result, they have found use in studies on protein crystallisation,[188] and on materials such as calcium carbonate.[189] In this case, supersaturation was controlled by making up solutions containing different solute concentrations, rather than tuning the concentration through evaporation. The solution was then passed through the microfluidic system, which would form droplets that moved through the device at a constant linear velocity. By changing the input concentration from 4 mM to 8 mM, Yashina *et al.* selectively nucleated both calcite and vaterite, respectively. Then, upon increasing solute concentration further to 10 mM, this selectivity was lost and combinations of both polymorphs once again nucleated, similar to the results observed in bulk crystallisations. This suggests that different supersaturation ranges may be used in order to tailor the polymorphic outcome of crystallisations, in which lower supersaturations may favour the nucleation of single polymorphs, and higher supersaturations will favour the nucleation of polymorphic mixtures.[189]

As previously discussed, surfactant microemulsions have been successfully used in the crystallisation of polymorphic materials, providing an array of nanodroplets suspended in a continuous phase of immiscible fluid.[66,104-110] This has been shown to "leapfrog Ostwald's rule of stages" and selectively

nucleate only the most thermodynamically stable polymorphs of both organic and inorganic materials such as glycine,[66,104] ROY,[66] mefanemic acid,[66] graphite,[109] and quartz[110] when lower supersaturations are employed. This is an important development, as it is not the metastable forms that are favoured in this case as seen in other nanoconfined systems. This methodology relies on the fact that individual droplets, or nanoreactors, are independent at long enough timescales for only the most stable nuclei to persist at these lower supersaturations, but not so independent as to disallow crystal growth of these stable nuclei through occasional collisions with other droplets, leading to droplets merging and a provision of more solute to the nuclei. In more rigid systems, crystal growth is slowed not due to a restriction of solute molecules, but due to the physical constraints of the nanodomains, such as pore walls.

STFs provide significant advantages over nanoporous and microemulsion systems for crystallisation. Application of nanoporous media is limited due to challenges in extracting crystals from the surrounding solid matrix, while crystals are often limited to sub-mm sizes due to slow growth and are contaminated with surfactant which is difficult to remove. In contrast, crystals grow at a slowed but reasonable rate in the STFs, and so crystals may reach sedimentable dimensions for easy extraction or may be restricted to the nm-scale and suspended in solution by using lower initial supersaturations. The experimental procedure for crystallisation in STFs is similar to that of bulk solution crystallisation, but with the advantage of higher nucleation rates and slower growth profiles that aid selectivity and early-stage crystallisation analysis. Furthermore, polymorphs with vastly different stabilities and growth rates may be targeted and nucleated from the same formulation; an ability that would be beneficial in areas such as polymorph screening.

The problem of crystallizing a desired polymorph in many systems is well established.[192,193] In the case of glycine, it is difficult to crystallise the stable, but slow-growing, γ-form from aqueous solutions.[149,154,194] Instead, the metastable α-polymorph typically crystallises.[195] The metastable β-form can crystallise in nanoconfinement, or by rapidly adding the antisolvent ethanol to bulk aqueous

glycine solutions, thereby achieving high supersaturations so as to nucleate the β-form, but in the latter case, solution-mediated transformation to the more stable α-polymorph is rapid, particularly for solutions with high water content.[159,196]

This chapter aims to demonstrate the unique crystallisation kinetics in STF systems, not only to nucleate the most thermodynamically stable polymorph, but also to tailor systems to target metastable forms, thereby demonstrating the extensive potential these systems have for understanding and controlling crystallisation.

4.2 EXPERIMENTAL

4.2.1 Materials

The chemicals used were as follows: octan-1-ol (99%, Fisher Scientific), ethanol (≥99.8%, Fisher Scientific), α-glycine (≥99%, SigmaAldrich) and glycine-1-13C (99 atom% 13C, Sigma-Aldrich). Ultra-high purity water (18.2 MΩ cm) was obtained from a Sartorius arium® comfort water purifier.

4.2.2 STF Preparation and Crystallisation

In order to assess the saturation concentration, c_{sat}, of each STF used in work described in this chapter, the same procedure as outlined in section 3.3.2 was followed. Then, the same general protocol for glycine crystallisation from STFs was followed:

1. An STF was made with the desired composition.

2. Glycine was dissolved in the STF to achieve a selected $\frac{c}{c_{sat}}$ value. These systems were stirred with a magnetic stirrer bar at 50 – 60 °C for one hour, or until all glycine was fully dissolved. For crystallisations at supersaturations corresponding to $\frac{c}{c_{sat}}$ of 2.00 or higher, samples were sonicated in an ultrasound water bath for two hours, or until all glycine had dissolved.

3. The STF was stored for at least one hour at a temperature of at least 10 °C above the temperature relating to saturation point of the solution to ensure full dissolution.

4. The STF was cooled at a controlled rate of 10 °C hour^{-1} in an oven to a chosen temperature to achieve the correct $\frac{c}{c_{sat}}$ value.

5. STFs were stored at that temperature for one week to ensure that, should multiple polymorphs nucleate, the stable but slower growing γ polymorph could compete with the faster growing metastable polymorphs.

6. Resulting crystals were then extracted via Büchner filtration and washed with the corresponding non-glycine containing STF, followed by a small amount of ethanol to remove residual octanol.

7. Crystals were left to dry at 60 °C.

STFs containing ethanol, water and octanol at constant ethanol mass fraction of 0.40 were prepared on a 250 ml scale according to the masses in Table 4.1. The water mass fraction was varied from 0.00 to 0.60 to encompass the pre-Ouzo nanostructured region of the phase diagram, see Figure 4.1. These compositions were scaled down to 25 ml for the higher supersaturation β-glycine experiments.

Table 4.1: Composition of STF used to assess the impact of nanostructuring.

Water mass fraction	Octanol mass fraction	Ethanol mass fraction	Water / g	Octanol / g	Ethanol / g
0.00	0.60	0.40	0.00	121.45	80.96
0.05	0.55	0.40	10.21	112.30	81.67
0.10	0.50	0.40	20.60	102.99	82.39
0.15	0.45	0.40	31.17	93.51	83.12
0.20	0.40	0.40	41.93	83.86	83.86
0.25	0.35	0.40	52.89	74.04	84.62
0.30	0.30	0.40	64.05	64.05	85.39
0.35	0.25	0.40	75.41	53.86	86.18
0.40	0.20	0.40	86.98	43.49	86.98
0.45	0.15	0.40	98.77	32.92	87.80
0.50	0.10	0.40	110.78	22.16	88.63
0.55	0.05	0.40	123.03	11.18	89.47
0.60	0.00	0.40	135.50	0.00	90.34

4.2.3   Variations to Chapter 3 procedure

As in Chapter 3, once all the glycine had dissolved, the samples were maintained at an elevated

temperature above the saturation temperature for a further hour before cooling to 25 °C. Cooling was

then achieved by either directly placing the samples in a water bath at 25 °C (fast-cooling method) or

cooling at a controlled rate of 10 °C hour⁻¹ in an oven (slow-cooling method). γ- and α- glycine crystals

were obtained in the STFs using both the fast- and slow-cooling methods, whereas β-glycine crystals

were obtained in the STFs using only the fast-cooling method. Crystals were extracted from solution

via Büchner filtration after one week for α- and γ- glycine, but only after 10–20 minutes for β-glycine

seeded experiments.

4.2.4   Seeding Studies

Separate 250 ml STFs were prepared that contained suspended nanocrystals of γ-, α- and β-glycine.

For the γ- and α-glycine suspended nanocrystals, STFs containing 0.25 mass fraction of water and 0.40

mass fraction of water, respectively, were used with a relative glycine concentration, $\frac{c}{c_{sat}}$, of 1.30 at

25 °C. These STFs were cooled via the slow-cooling method and were then left at 25 °C for 16 hours

for the nanocrystals to form. At this time, the STFs contained between one and five sedimented

crystals of size ≤ 0.1 mm but the majority of the glycine was still in the STF, either in solution or in the

form of suspended nanocrystals. For the β-glycine suspended nanocrystals, STFs containing 0.25 mass

fraction of water at a higher relative glycine concentration, $\frac{c}{c_{sat}}$, of 2.10 were used alongside the fast-

cooling method, with the β-nanocrystals forming within one hour at 25 °C, at which point, again, there

were between one and five sedimented crystals present.

For the seeding experiments, a 5.0 ml aliquot of the nanocrystal-containing STF was added to 15.0 ml

of a binary solution of 0.40 mass fraction water and 0.60 mass fraction ethanol, which contained

glycine at a supersaturation corresponding to $\frac{c}{c_{sat}}$ of 1.30. γ- and α-glycine crystals were extracted for

ATR-FT-IR analysis from the seeded experiments, and the STFs used for the seeding, after one week.

β-glycine crystals were extracted for ATR-FT-IR analysis from the seeded experiments 10–20 minutes

after seeding, at which point the nanocrystal-containing STFs were also extracted, with the shortened timeframes being necessary due to the rapid solution-mediated transformation of β-glycine into α-glycine in unstructured solution.

4.2.5   Characterisation

All characterisation techniques followed the same procedures explained in section 3.3.6, albeit with the STF compositions described by Table 4.1.

4.3   RESULTS AND DISCUSSION

In order to determine the effect of nanostructure of STFs on crystallisation outcome, the pre-Ouzo region of the ternary phase diagram was identified, and a line of constant ethanol mass fraction of 0.40 was chosen to encompass o/w, bicontinuous and w/o structures, transitioning from high to low water content, respectively (Figure 4.1).
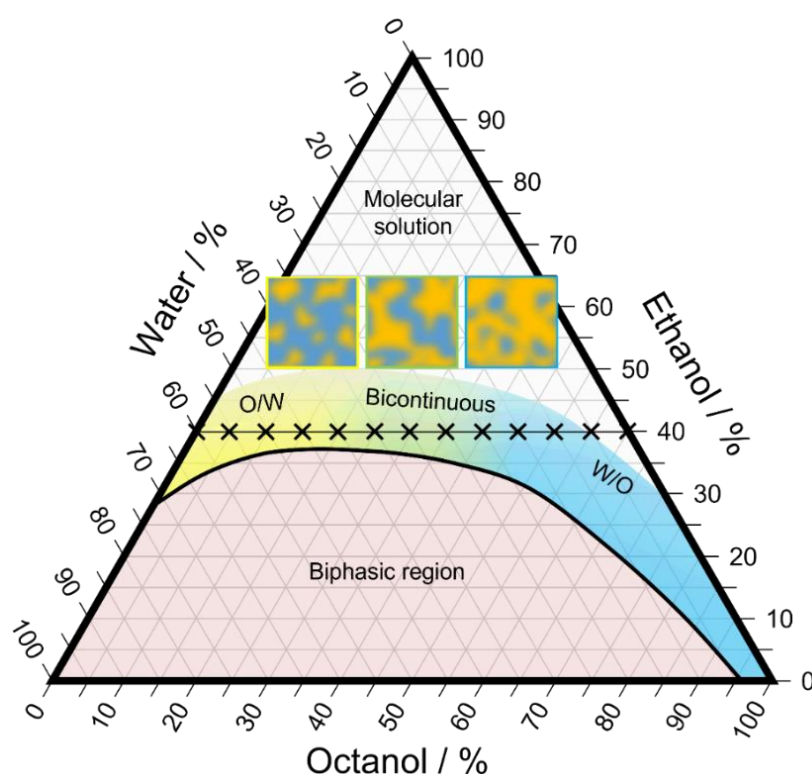
Figure 4.1: Ternary phase diagram for water, 1-octanol, and ethanol. Shaded regions indicate areas where phase separation (pink) and nanostructuring (yellow, green and blue) occurs, and crosses indicate the STF compositions tested in this chapter.

As highlighted in Chapter 3, UV-vis and conductivity measurements, followed by NMR diffusiometry, may be used in conjunction to identify compositions of an STF in which nano-structuring occurs.

4.3.1   Solubility

Initially, the solubility of glycine in each of the proposed systems was tested, and the results are outlined in Figure 4.2. This indicates two behaviours at low and high water mass fractions, as highlighted by the blue and red trendlines. At low water mass fraction, there is a very low glycine solubility in the STFs, which grows at an increasing rate with increasing water content. At higher water mass fractions between 0.30 and 0.35, the relationship between solubility and water content becomes linear. Glycine is virtually insoluble in octanol and ethanol and is therefore expected to be predominantly confined to the water domains. Hence, at a water mass fraction of 0.00, the solubility is ≈ 0 mg cm^{-3}.
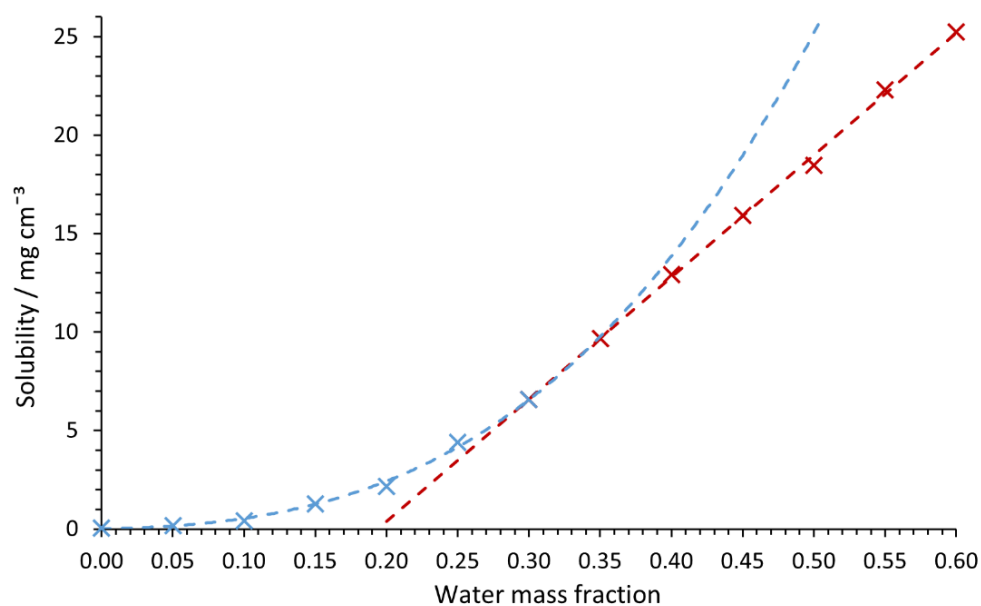
Figure 4.2: Solubility of glycine in different STF compositions, each with a constant ethanol mass fraction of 0.40. Trendlines represent the observed relationship between the solubility and the water mass fraction as cubic (blue) at low mass fractions, and linear (red) at high mass fractions, rationalised as being due to the different nanostructures present in each composition.

At low water mass fractions (e.g. 0.05), water-rich domains will exist as nanoscale droplets with a large surface area to volume ratio. As the surface of these droplets is bounded by an ethanol-rich region in which some of the water volume will be dissolved, the volume remaining in which glycine can dissolve

will be reduced even further. The greater the surface area to volume ratio of the nanodomains, the greater the effect of this volume reduction and therefore, as the water content increases, the solubility increases at an increasing rate as the surface becomes less significant. The ethanol-rich boundary region will still contain some water and consequently will have improved glycine solubility when compared to pure ethanol. However, the comparative solubility with the water domains is small enough to justify it being considered negligible in this work. For example, for 15 wt% water in ethanol, the solubility of glycine is reduced to 0.2% of that in pure water.

At 25 °C, the low water content data can be fitted with the following relationship between water mass fraction (m_w) and solubility (S) in mg cm^{-3}:

$$S = 150{m_w}^3 + 22{m_w}^2 + 1.7m_w \qquad (4.1)$$

At high water mass fractions (0.30 – 0.60), the amount of glycine that dissolves is proportional to the amount of water in the system. This is due to water becoming the majority phase, and subsequently not being confined in droplet-like structures. If no longer confined, the water will behave as a continuous, bulk phase and therefore the amount of glycine dissolved directly mirrors the amount of water in the system. For Figure 4.2, this leads to a linear data fit with the following equation for the STFs with high water content:

$$S = 62m_w - 12 \qquad (4.2)$$

Figure 4.3 describes how the solubility of each of the STFs varied with increasing temperature. Unsurprisingly, the solubility of glycine increased with temperature and followed the same trend observed at room temperature, whereby the relationship between water mass fraction, m_w, and solubility was cubic when $m_w \leq 0.30$, and linear when $m_w > 0.30$. These data allowed the saturation concentration, c_{sat}, at different temperatures to be assessed and the relative concentration of STFs to be calculated when different cooling strategies were employed.
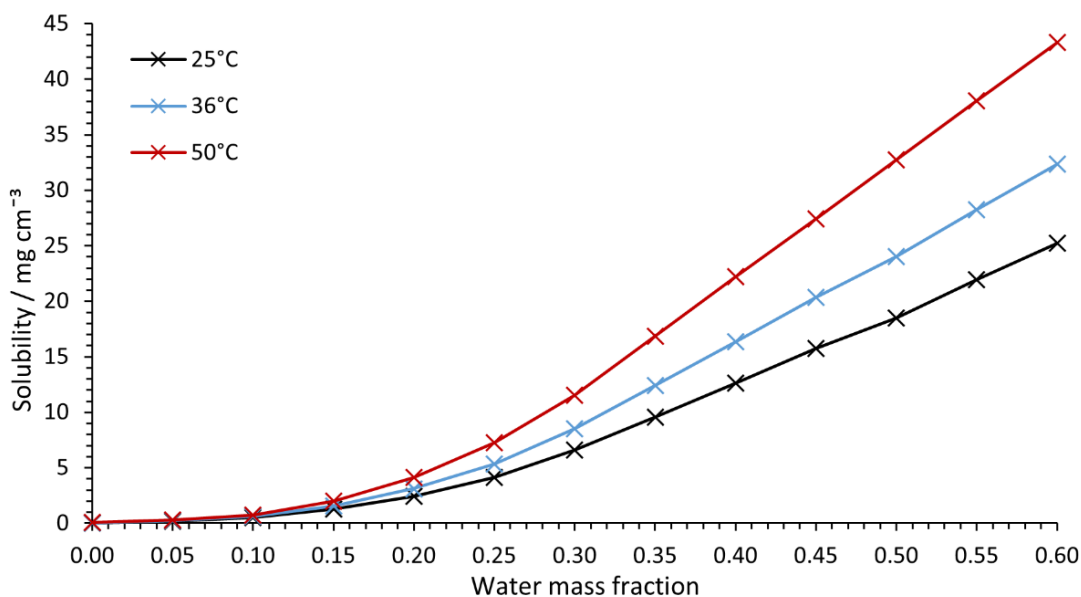
Figure 4.3: Solubility of glycine at different temperatures in different STF compositions, each with a constant ethanol mass fraction of 0.40.

4.3.2 UV-vis Measurements

In Chapter 3, work was focussed on STFs with a constant water mass fraction of 0.15, and it was only the effect of polarisability that was thought to have impacted the solvatochromic shift observed in the UV-vis spectra collected because DO1 is essentially insoluble in water and so is accessing only the ethanol- and octanol-rich regions. Here, however, it is a line of constant mass fraction of ethanol (0.40) that is assessed, and therefore it is the behaviour of all three phases (octanol, water, and octanol/water-enriched ethanol) that are considered.

First, to simplify the picture, the binary combinations of water/octanol, ethanol/water and ethanol/octanol were considered (Figure 4.4). It should be noted that water and octanol are essentially immiscible, and will form unstable suspensions that phase separate easily when mixed in compositions above water mass fractions, m_w, of 0.05 at 25 °C. For this reason, only three data points have been taken in the range of $0.00 \leq m_w \leq 0.05$. Figure 4.4(a) shows that increasing the ethanol content of both ethanol-containing systems decreased λ_{max}. For octanol/ethanol binary solutions, this was suggested to be influenced by the larger size, mass and polarisability of octanol, stabilising the π^* orbital of DO1 to a greater extent compared with ethanol. For ethanol/water binary solutions,

the hydrogen bond donating ability, α, and the dipolarity/polarisability should both contribute to the observed changes in λ_{max}. Water is a smaller molecule than ethanol and therefore less polarisable. However, more notably, as depicted in Figure 3.15 water is significantly more dipolar and should therefore stabilise the π* orbital of DO1 to a greater extent when compared to ethanol. Additionally, water has two hydrogen atoms with significant enough δ+ charge to donate towards hydrogen bonding, and therefore the hydrogen donating ability of water is also greater than ethanol, which only has one such hydrogen atom.
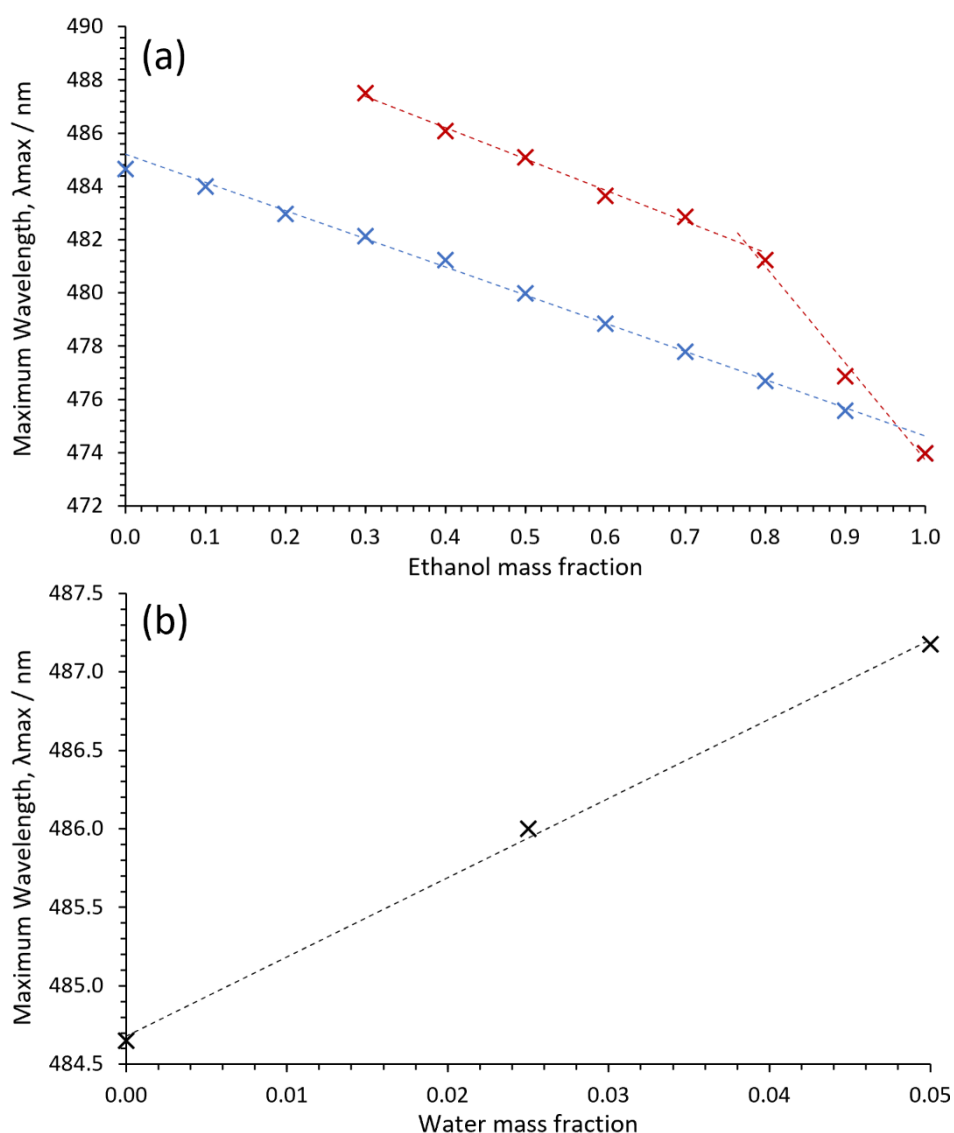
Figure 4.4: Change in maximum wavelength in the absorption spectra of DO1 in binary solutions of (a) ethanol/water (red) and ethanol/octanol (blue), and (b) water/octanol.

Instead of the linear relationship observed in the ethanol/octanol binary solutions, it can be seen that the ethanol/water binary system has at least two different regimes. There may exist a third regime at lower ethanol mass fractions (<0.3) but this could not be measured with DO1 due to its low solubility in water-rich solutions. This was attributed to the same non-ideality argument used for earlier viscosity experiments, whereby temporary micellar-type structures and hydration layers may form due to the aforementioned hydrogen bonding between ethanol and water. When comparing the two curves in Figure 4.4(a), it is evident that when added to ethanol, water leads to a larger red-shift in λ_{max} compared with octanol. This is corroborated by Figure 4.4(b) for octanol/water binary solutions. While octanol is significantly larger, and more polarisable than water, water is significantly more dipolar, and will also be a better hydrogen bond donor. Both factors appear to lead to an increased λ_{max} upon increasing the water content, similar to the trend observed in ethanol/water solutions.

It was concluded therefore that the three solvents may be ranked as follows for their ability to increase DO1 π* orbital stabilisation and therefore shift the observed λ_{max} to longer wavelengths: ethanol < octanol < water. Water will also only begin to have an effect on the UV-vis spectrum of DO1 if dissolved in ethanol (≤ 70 wt%) or octanol (≤ 5 wt%), since DO1 is essentially insoluble in water and so DO1 is largely absent from the water-rich regions. This allows DO1 to act as a probe, to gauge an idea of the solvent environments that may be found within the ternary fluids.

When water is not present in the system, the octanol and ethanol should mix essentially ideally as a molecular solution, illustrated by the linear behaviour seen in Figure 4.4(a). This led to a λ_{max} of 481 nm for the binary ethanol/octanol solution containing an ethanol mass fraction of 0.40. This is the average λ_{max} value obtained in each pure solvent (474.1 nm and 484.6 nm for ethanol and octanol, respectively), weighted to the relative mass fraction of each component.

Figure 4.5 shows that from $0 \leq m_w \leq 0.15$, there is a sharp increase in λ_{max} of 4 nm. This is unsurprising as water has been shown to increase λ_{max} by the greatest amount. As water enters the system, some should be confined to nanodomains and be effectively inaccessible to DO1 solute due

to its water insolubility. However, some water molecules should be located in the ethanol-rich boundary networks. As seen in the binary ethanol/water curve (Figure 4.4(a)), even a small increase in water content leads to a large increase in λ_{max}.
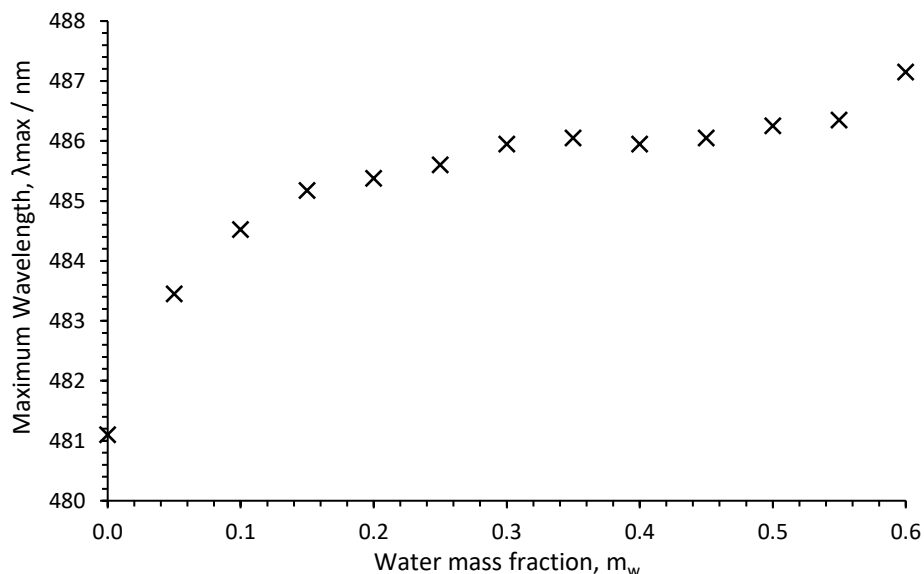
Figure 4.5: Change in maximum wavelength in the absorption spectra of DO1 in STF formulations with a constant ethanol mass fraction of 0.40.

From $0.15 \leq m_w \leq 0.55$, the value of λ_{max} only exhibits a small increase of ~1 nm over the whole range of compositions. As the ethanol-rich boundary regions have an approximately fixed mass fraction of ethanol, there is a maximum amount of water that may be solvated in these domains in order to maintain the nanostructuring. It may be concluded, therefore, that this point is reached at a water mass fraction of approximately 0.15. Any additional water content should then go into swelling the existing water domains. In these increasingly voluminous water domains, DO1 will be excluded, and therefore the changes in wavelength are minimal as the nature of the interactions within the boundary region should ultimately be invariant. There is, however, a small increase (~1 nm) in λ_{max} across this range which may be due to the decrease in octanol content. As the octanol content decreases, the proportion of dye interactions arising from the ethanol-rich boundary region compared to dye interactions from the essentially pure octanol phase will increase, meaning that the more highly dipolar and hydrogen bonded region would have a larger impact on the solvatochromic shift.

This essential plateau in λ_{max} persists until the formulation becomes a binary ethanol/water solution at a water mass fraction of 0.60. At this point, ethanol would essentially be 'unlocked' from the boundary regions between the immiscible octanol- and water-rich regions and is diluted into the entire aqueous phase due to the absence of octanol. At this point the wavelength increases sharply again, as the DO1 would now exist in a more water-rich environment.

To summarise, the UV-vis data collected in Figure 4.5 suggests that the solvatochromic behaviour of the azo dye DO1 could be rationalised by considering the effect of the ethanol-rich boundary phase in STFs across the pre-Ouzo region with fixed ethanol mass fraction. From binary solution measurements (Figure 4.4), it was observed that water has the greatest impact on the red shift of the observed DO1 absorbance peak, and as such it is suggested that it is the degree to which water is solvated in the ethanol-rich regions, and can therefore interact with the DO1 molecules, that dictates the observed shifts. At low water content, water exists in swollen networks of ethanol, so increasing the water content led to a sharp increase in λ_{max}. As water content increased further, a plateau was observed in the recorded λ_{max} values. This was rationalised as a maximum concentration of water in the ethanol being reached, with additional water then not contributing to domains in which DO1 was present. When no octanol remained in the system at a water mass fraction of 0.60, the λ_{max} sharply increased again, as ethanol, and therefore DO1 was distributed evenly throughout the aqueous solution.

When aiming to determine the presence and/or nature of nanostructures present in a potential STF, UV-vis measurements are often taken as outlined in Table 1.2.[41-52] The data collected here suggests that w/o droplet-like structures are likely to exist in formulations with $0 \leq m_w \leq 0.15$. However, the transition to bicontinuous and then to o/w droplet structures is not discernible. This is likely due to the choice of DO1 as the solvatochromic probe. In many experiments, methyl orange or methylene blue are chosen due to their solubility in only the water phase. However, unfortunately neither could be used in this case due to their additional solubility in both octanol and ethanol. DO1 was found to be insoluble in at least one phase (water) and still gave discernible solvatochromic shifts. As it was

solubilised in both ethanol and octanol phases, it could not distinguish the octanol structuring that formed in the STFs, and therefore the plateau region extended well into the area of the phase diagram in which o/w nanostructures have been predicted to arise.

4.3.3   Conductivity

To extract more information about the different nanostructures that may exist inside the pre-Ouzo region, conductivity measurements were performed across the same 0.40 mass fraction of ethanol line in the ternary phase diagram.

Figure 4.6 outlines the conductivity results. Here, three distinct regions can be seen, with transitions at water mass fractions (m_w) of 0.10 and 0.40. Below 0.10, the systems have a very low conductivity, owing to the lack of glycine solubility in ethanol and octanol, respectively. As glycine zwitterions are the only ionic component of the system, the conductivity of the STFs should depend on their ability to transfer charge through the system. As water was introduced into the systems and increased m_w from 0.05 − 0.10, the glycine dissolves within the aqueous domains and has increased mobility as the number of aqueous domains increases, leading to a rise in the conductivity, albeit the glycine zwitterions would be restricted inside the aqueous nanodroplets. This heavily limits their ability to diffuse through the solution, so the conductivity remained below 2 µS. When m_w was between 0.10 − 0.40 the conductivity increased still, but less sharply, with values ranging between approximately 2 − 3 µS across that composition range. This suggests the aqueous nanodomains increased in volume or became more connected as the water content increased, increasing the transfer of charge because glycine zwitterions diffused more freely. It is proposed that in this region, the steady increase in conductivity highlights the region in which the system begins changing from a strictly w/o droplet-type microemulsion structure to a bicontinuous structure, where solute diffusion will increase, but still be restricted relative to an unconfined system. When m_w reached 0.45, a sharp increase in conductivity was measured. This indicates a drastic change in the aqueous environment, from one with restricted nanodomains, to one in which the water is the continuous phase, allowing

the glycine to diffuse freely through the entirety of the system, provided the now confined octanol phase does not interfere with the path of the ions.
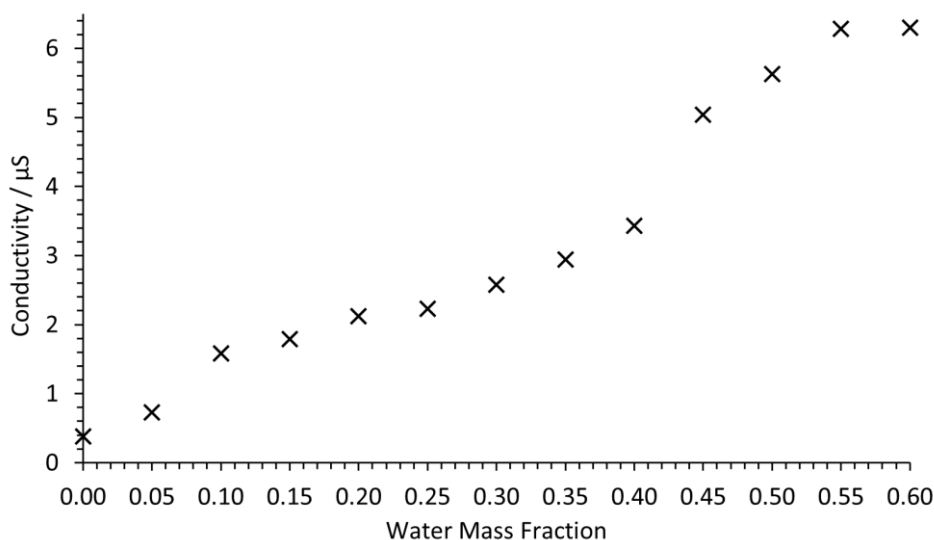
Figure 4.6: Conductivity change with water mass fraction for STFs containing an ethanol mass fraction of 0.40 and a constant mass of glycine.

When combined with the data collected from UV-vis measurements, these data indicate that there are two structural transitions occurring in the samples measured, aligning with the existence of w/o droplet-type structures when m_w is 0.15 or below, bicontinuous structures when m_w is between 0.15 − 0.40, and o/w droplet-type structures when m_w is above 0.40.

4.3.4   Viscosity

Figure 4.7 shows the viscosity change across the STF systems tested. There is a strong curvature to the dataset, with a maximum in the viscosity present when m_w is 0.30. This demonstrates the significant non-ideality of the systems, whereby the formation of hydrogen-bonded networks through the system is increasing the overall viscosity of the system. The maximum is observed when there are equal parts water and octanol in the solution (by mass). This profile resembles the results collected in the case of binary solutions of ethanol and water (Figure 3.8, inlayed in Figure 4.7). This suggests that the non-ideality of these structures arises predominantly from the hydrogen-bonded networks that develop within the STFs between the water and ethanol phases.
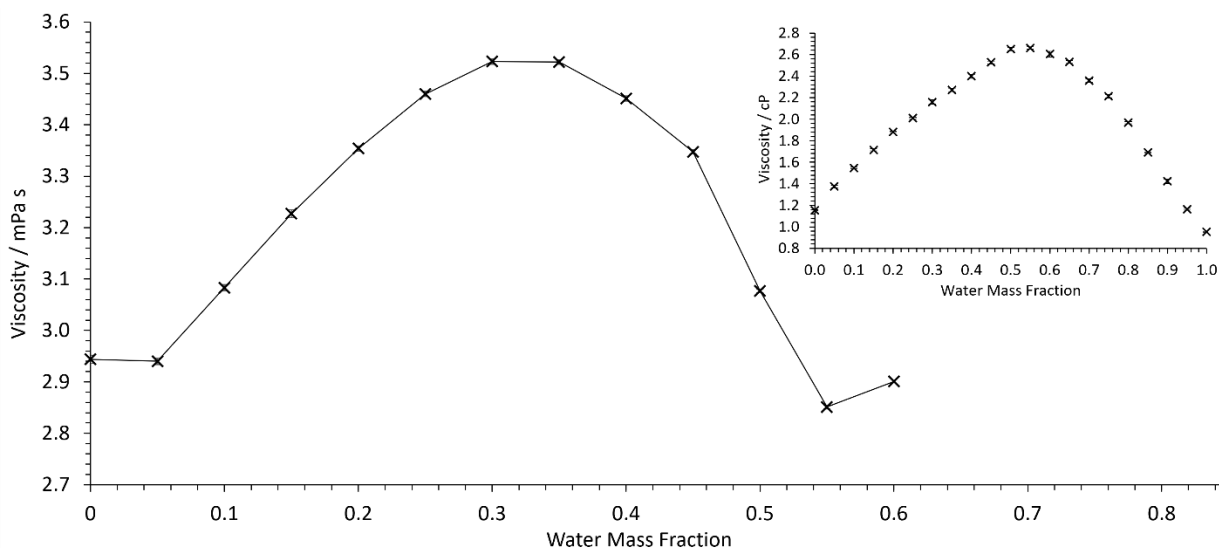
Figure 4.7: Viscosity change with water mass fraction for STFs containing a constant ethanol mass fraction of 0.40. Binary ethanol/water viscosity change with water content is included as an inlay in the top right corner.

Viscosity is a measure of the resistance to fluid flow. Consequently, the greatest viscosity should arise when there are more hydrogen bonds in the fluid which require breaking to achieve the flow. This will occur in the bicontinuous region as seen in Figure 4.7 as here there will be the largest interfacial area, which will be perturbed during viscous flow. Conversely, in the w/o and o/w microemulsion nanostructured regions, the continuous phase will constitute the majority of the sample and therefore the structures will not be perturbed in the same way, as largely the same intermolecular interactions will exist in all directions. This is particularly evident at water mass fractions of 0.05 and 0.55, as the viscosity of the fluids does not significantly vary from that of the binary fluids without the respective confined phase. As the solutions approach 30 wt% water, the solutions become more bicontinuous in nature and the amount of ethanol-octanol and ethanol-water hydrogen bonds will be maximised, which is reflected in the maximised viscosity.

4.3.5 NMR Diffusiometry

From UV-vis and conductivity data, it was expected that water should exist as a confined phase in mixtures with low water mass fraction. Therefore, when considering the diffusion of water and glycine, the apparent viscosity-independent diffusion coefficient ($D\eta$) should decrease as the water content reduces. This is what is observed (Figure 4.8): there is a ~40% decrease in the apparent $D\eta$ for

water at low water mass fractions relative to the 0.60 water/0.40 ethanol mass fraction binary system, consistent with soft nanoconfinement. Even at water mass fractions of 0.25, the values were reduced by ~20% compared to the binary system. Likewise, octanol was expected to be confined in STFs with high water content, and therefore low octanol content; again, this was observed. Ethanol, on the other hand, remains unconfined at all compositions. It should be noted that although ethanol's Dη value increases slightly in the bicontinuous region, it never decreased significantly, indicating that there is no restriction. The magnitude of these Dη changes was similar to those reported in a STF composed of an ionic liquid, ethanol and toluene.[55] Thus, in agreement with previous studies,[18-28] these findings confirm that soft nanoconfinement is present in the ternary 0.40 mass fraction ethanol systems studied.
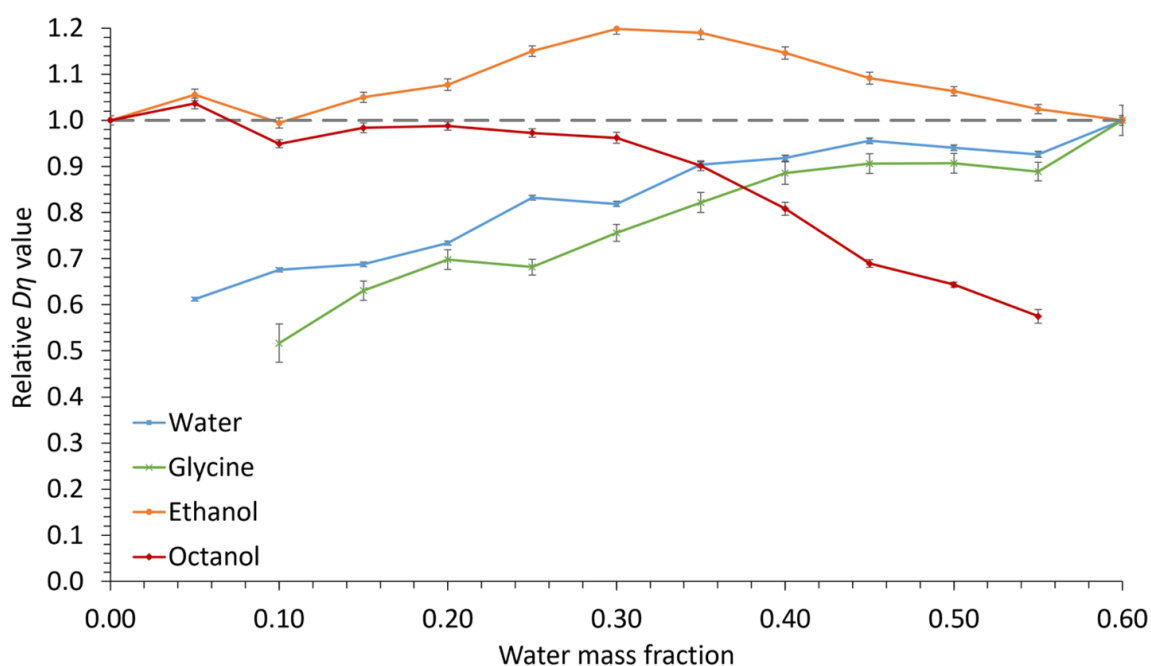
Figure 4.8: Relative Dη values (compared with binary ethanol/water, and ethanol/octanol mixtures) for glycine, water, ethanol, and octanol in STF mixtures containing a constant ethanol mass fraction of 0.40 and different mass fractions of water and therefore octanol.

As elucidated in Chapter 3, nanoconfinement is lost as ethanol content increases in the ternary mixtures. For ternary fluids with a greater ethanol mass fraction of 0.60, the relative Dη values reflect this as they remain similar for all components in all compositions (Figure 4.9).
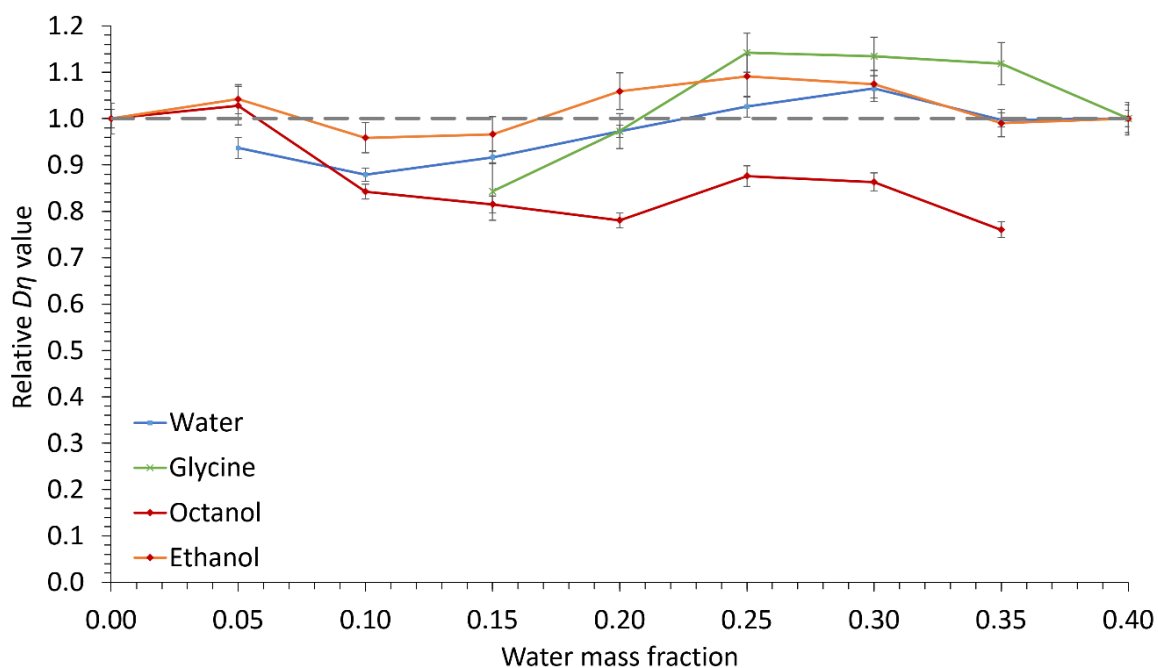
Figure 4.9: Relative Dη values (compared with binary ethanol/water, and ethanol/octanol mixtures) for glycine, water, ethanol, and octanol in STF mixtures containing a constant ethanol mass fraction of 0.60 and different mass fractions of water and therefore octanol.

Crucially, Figure 4.8 shows that the relative Dη values for glycine closely follow those of the water component, the only difference being slightly lowered relative Dη values at low water content. This is consistent with glycine diffusion being restricted because the glycine resides primarily within dynamic water pockets and is largely excluded from the interfacial regions, as expected due to the poor solubility of glycine in both ethanol and octanol (Figure 4.2). Nanoporous materials and droplet microemulsions provide considerably greater restricted diffusion compared to STFs.[197,198] For instance, in droplet microemulsions, diffusion coefficients can be reduced by 1–2 orders of magnitude.[198] Instead, the degree of restricted diffusion here is more similar to that of oils and aqueous phases in bicontinuous surfactant-based microemulsions.[199] Nevertheless, this degree of restricted diffusion has proven to be sufficient to cause transformative effects on the crystallisation behaviour in this work.

4.3.6 Crystallisation of γ-glycine

Crystallisation experiments were conducted on the 0.40 ethanol mass fraction octanol/ethanol/water formulations, since it has been demonstrated that these are in the pre-Ouzo region and hence show

nanostructuring. The glycine polymorph was principally determined by ATR-FT-IR, with characteristic peaks for α, β and γ-glycine occurring at 909, 914 and 928 cm^{-1}, respectively (Table 3.4). A slow cooling methodology was used to induce γ-glycine crystallisation. This will typically favour thermodynamically stable polymorphs because the system spends sufficient time at higher temperatures where only the stable polymorph is supersaturated. Note that this strategy fails for γ-glycine in bulk aqueous solution, because the metastable α-polymorph is only slightly less stable than the stable form,[149] and γ-glycine has a much lower growth rate.[149,154] Consequently, nanocrystals of α-glycine can grow to larger dimensions more rapidly, ultimately becoming more stable and growing at the expense of the much smaller γ-glycine nanocrystals, which then dissolve back into solution. Therefore, to selectively crystallise γ-glycine, specific additives, or a pH away from the isoelectric point, are required.[200-202] However, in our water-in-oil STF compositions containing 0.10 mass fraction of water, γ-glycine was successfully crystallised as the sole product by using slow cooling for supersaturations with $\frac{c}{c_{sat}}$ = 1.30 (Figure 4.10), where c_{sat} and c are the saturation and actual concentrations, respectively; this was also confirmed by powder X-ray diffraction (Figure 4.16).
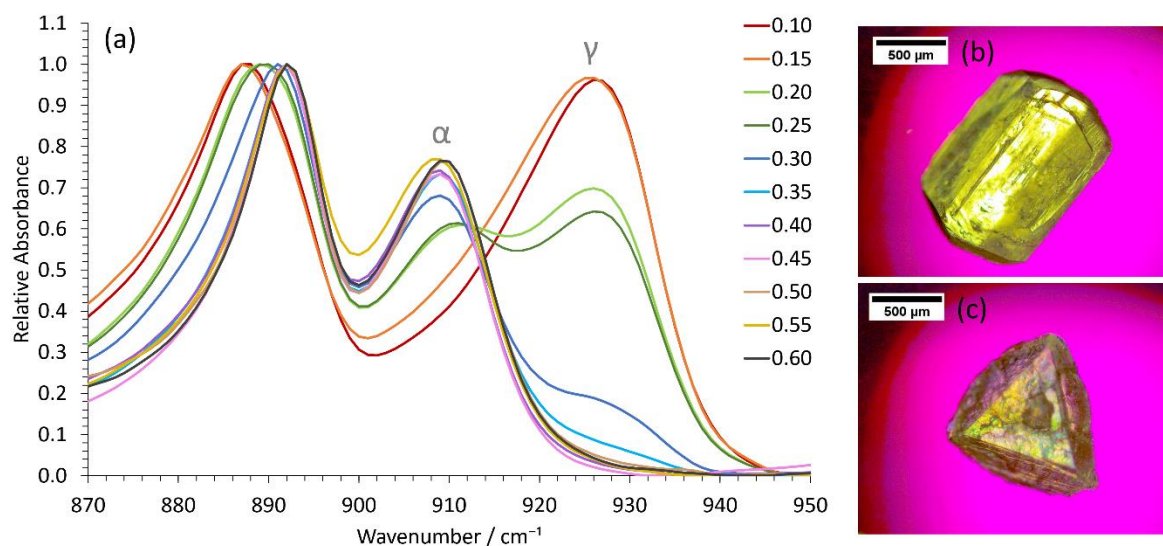
Figure 4.10: (a) Representative ATR-FT-IR spectra of extracted crystals as a function of water mass fraction in the STF. The spectra have been normalized relative to the common peak at 890 cm^{-1}. Optical micrographs showing the typical morphology of (b) α-glycine crystals obtained from the binary system and higher water mass fraction STFs, and (c) γ-glycine crystals obtained from the lower water mass fraction STFs. Absorbance maxima at 909 cm^{-1} and 928 cm^{-1} identify material as containing α-glycine and γ-glycine, respectively.

For water-in-oil STF compositions of 0.15 mass fraction of water, γ-glycine crystallised as the majority polymorph, with only a minor amount of α-glycine present. In bicontinuous STF compositions of 0.20 and 0.25 mass fraction of water, both α- and γ-glycine typically crystallised concomitantly, with γ-glycine usually being the predominant polymorph at supersaturations with $\frac{c}{c_{sat}}$ = 1.30.

At higher water mass fractions, where octanol replaced water as the nanoconfined phase to give oil-in-water structures (Figure 4.1), the ability to crystallise γ-glycine was markedly reduced, as expected. In particular, in formulations containing 0.30 and 0.35 mass fraction of water, where structuring was still more bicontinuous is nature, α-glycine was the majority polymorph, with some γ-glycine still evident, whilst for mass fractions of water ~0.40, only α-glycine was evident at $\frac{c}{c_{sat}}$ values of 1.30.

In contrast, when octanol/ ethanol/water unstructured solutions containing 0.60 mass fraction of ethanol were used, only α-glycine crystallised (Figure 4.11).
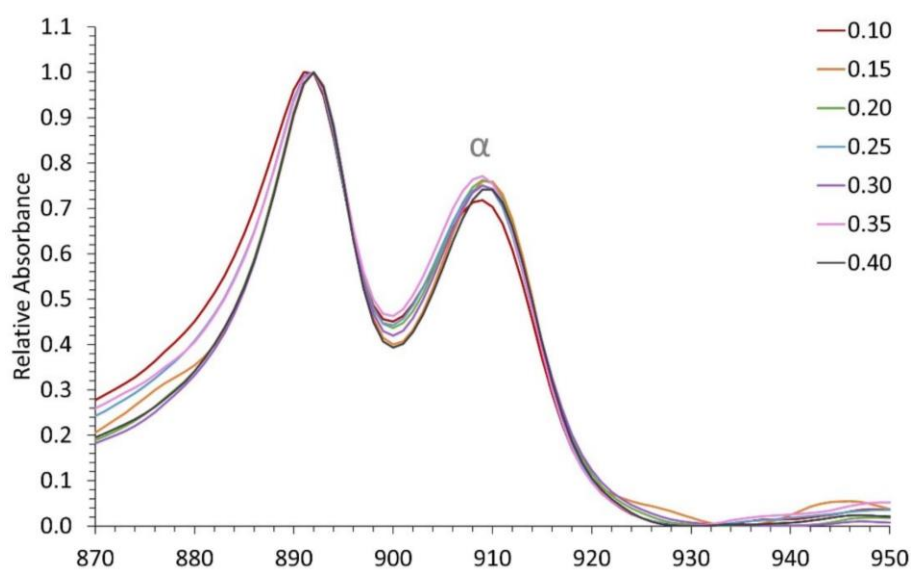
Figure 4.11: Representative FT-IR data for extracted glycine crystals produced in unstructured octanol/ethanol/water solutions with varying water mass fractions at a fixed ethanol mass fraction of 0.60 and a glycine $\frac{c}{c_{sat}}$ = 1.30. The spectra have been normalized relative to the common peak at 890 cm^{-1}. Absorbance maxima at 909 cm^{-1} identify material as α-glycine.

4.3.7   25 wt% Water STF

As previously discussed, the bicontinuous STF with 0.25 mass fraction of water was the system with the largest proportion of water in which γ-glycine could be nucleated as the predominant polymorph

at supersaturations with $\frac{c}{c_{sat}}$ = 1.30. The ability of this system to nucleate both the thermodynamic product, γ-glycine, and the main kinetic product, α-glycine, concomitantly suggests that this system could prove a powerful tool in polymorph screening, whereby multiple polymorphs may nucleate and persist for extended periods in a single vessel. This STF composition was therefore studied further to understand the growth behaviour of glycine, and ultimately tailor the polymorphic outcome of crystallisation.

4.3.8   Fast cooling methodology

A faster-cooling method was employed to compare the effect of the cooling strategy on the polymorphic outcome of crystallisation. It was found that this strategy was also able to crystallise γ-glycine, provided STFs with water mass fractions of 0.25 were used at $\frac{c}{c_{sat}}$ values of 1.30 (Figure 4.12). This is consistent with the nanocrystals growing more independently from one another in the same STF due to the restricted diffusion, enabling smaller, less stable nanocrystals to persist.
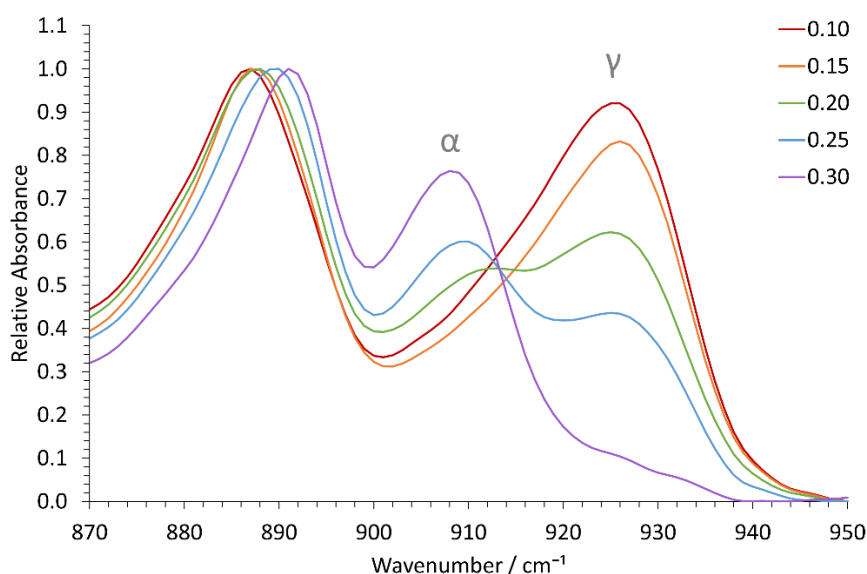
Figure 4.12: Representative ATR-FT-IR spectra for extracted glycine crystals produced from STFs with varying water mass fractions and a glycine $\frac{c}{c_{sat}}$ = 1.30 using a fast-cooling crystallization methodology. The spectra have been normalized relative to the common peak at 890 cm^{-1}. Absorbance maxima at 909 cm^{-1} and 928 cm^{-1} identify material as containing α-glycine and γ-glycine, respectively.

It should be noted that the control exhibited by this methodology was not as strict as that observed by the previous, slow-cool strategy. Comparing Figure 4.10 and Figure 4.12 reveals that, in the fast-

cooled samples, there is a higher proportion of α-glycine present in the samples for which a mixture of polymorphs was present. There appears to be a minor quantity of the metastable polymorph in even the STF with the lowest mass fraction of water (0.10). This demonstrates that though it is still possible to achieve the crystallisation of the most stable polymorph, the degree of selectivity and control is somewhat reduced. This is because the STFs will not spend sufficient time at a higher temperature whereby only the most stable polymorphs will be supersaturated and are therefore able to nucleate, persist and grow. Subsequently, should the fast-growing α-glycine polymorph nucleate, it will be less likely to dissolve back into solution, and will be able to grow competitively, even dominating the extracted product. It is evident that both methods give near-pure samples of γ-glycine at a water mass fraction of 0.15, however it should be noted that the yield of these samples was low due to the low glycine solubility in the STF.

The fast-cooling method may provide some benefit however, particularly if it were to be used on an industrial scale. For example, fewer energy costs will be incurred due to their only being one heating stage of approximately 1-2 hours to dissolve the material, as opposed to 4-5 hours required for the slow-cooling method. It will also produce less demand on equipment as the ovens used to dissolve the material will only be in use for half of the time, meaning sample turnover may theoretically be doubled. A balance therefore must be struck between the demands of the methodology, the degree of polymorph selectivity, and the yield of the product, depending on the intended application. For this work, a slow-cooling method was employed, unless otherwise stated, as this was deemed the most reliable method to achieve polymorph selectivity.

4.3.9   Crystallisation of β-glycine

Whilst the stable γ-glycine polymorph could be crystallised in our STFs by using low supersaturations, the metastable β-glycine polymorph could be targeted at higher supersaturations. We focused on the 0.35 octanol/0.40 ethanol/0.25 water mass fraction formulation. This system is in the bicontinuous region, but it is sufficiently close to the water-in-oil boundary for 3D nanoconfinement effects to be

apparent, as demonstrated by its ability to crystallise γ-glycine. This formulation was preferable to lower water mass fraction water-in-oil STFs, even though these possessed greater 3D nanoconfinement, because of the significantly greater glycine amounts that could be dissolved (Figure 4.2) and the ease with which it was hereby found that the system could be tailored to produce all three ambient pressure polymorphs of glycine. β-Glycine crystals could be extracted alongside the more stable α-glycine from STFs with 0.25 mass fraction of water at supersaturations with $\frac{c}{c_{sat}}$ of ≥1.90 for up to 3.5 hours (Figure 4.13).
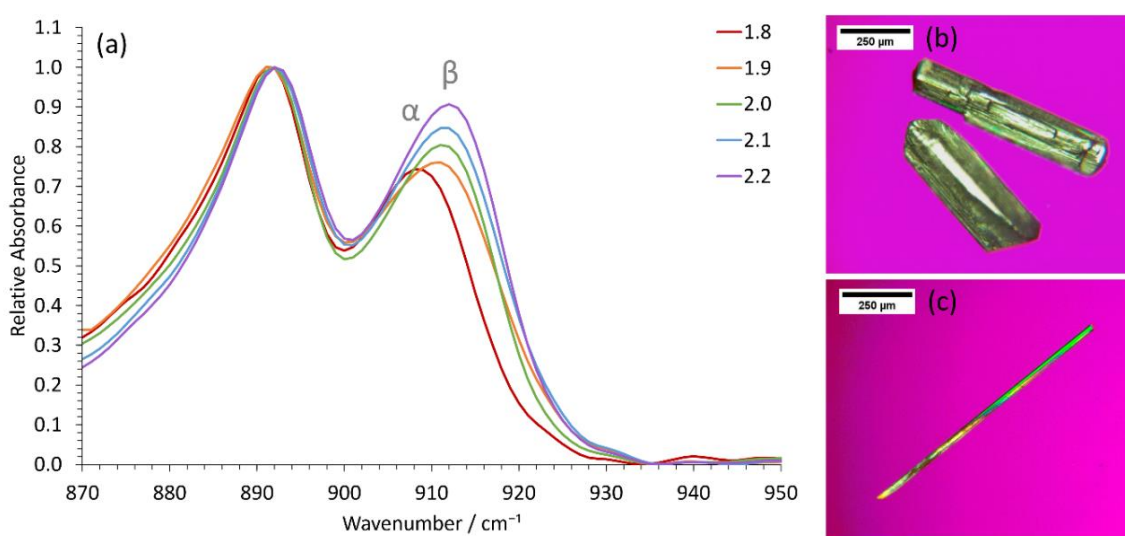
Figure 4.13: (a) Representative ATR-FT-IR spectra of extracted crystals as a function of $\frac{c}{c_{sat}}$. The spectra have been normalized relative to the common peak at 890 cm^{-1}. Optical micrographs showing the typical morphology of (b) α-glycine crystals obtained from the binary system and higher water mass fraction STFs and (c) β-glycine crystals obtained from the 0.25 water mass fraction STFs. Absorbance maxima at 909 cm^{-1} and 914 cm^{-1} identify material as containing α-glycine and β-glycine, respectively.

Here, the ability of nanocrystals within the same STF to exist more independently of one another is beneficial. In particular, the restricted diffusion in STFs hinders crystal growth and Ostwald ripening, allowing less stable forms that nucleate to survive alongside more stable, faster growing polymorphs. Furthermore, the restricted diffusion of the nanoconfined immiscible liquid and its solute means that any locally high supersaturations will be prolonged, facilitating the nucleation of polymorphs that would normally be difficult to nucleate. For instance, assuming a Poisson distribution of solute molecules amongst aqueous swollen pockets of mean size 4 nm, then for a supersaturation with $\frac{c}{c_{sat}}$

of 2, a 100 ml 0.25 water mass fraction STF would have ~0.1% of aqueous pockets with supersaturations with $\frac{c}{c_{sat}}$ in excess of 4, i.e. >10^{16} pockets that could act as sites for nucleation of high energy polymorphs (See Appendix). Consequently, even if a metastable polymorph were significantly more soluble than the stable form, locally high supersaturations sufficient for nucleation of this highly metastable form should be present within the STF. In solutions lacking this aqueous nanoconfinement, such locally high supersaturations would be transitory because they would be rapidly dissipated by the osmotic pressure arising from the concentration gradient. Hence, only α-glycine crystallised from the binary 0.60 water/ 0.40 ethanol mass fraction solution at this supersaturation level. Indeed, significantly higher supersaturations with $\frac{c}{c_{sat}}$ of ≥2.4 were required before β-glycine nucleated concomitantly with α-glycine in this binary system (Figure 4.15), and this β-glycine did not persist, as it underwent a solution-mediated phase transformation to α-glycine within 30 minutes (Figure 4.14).
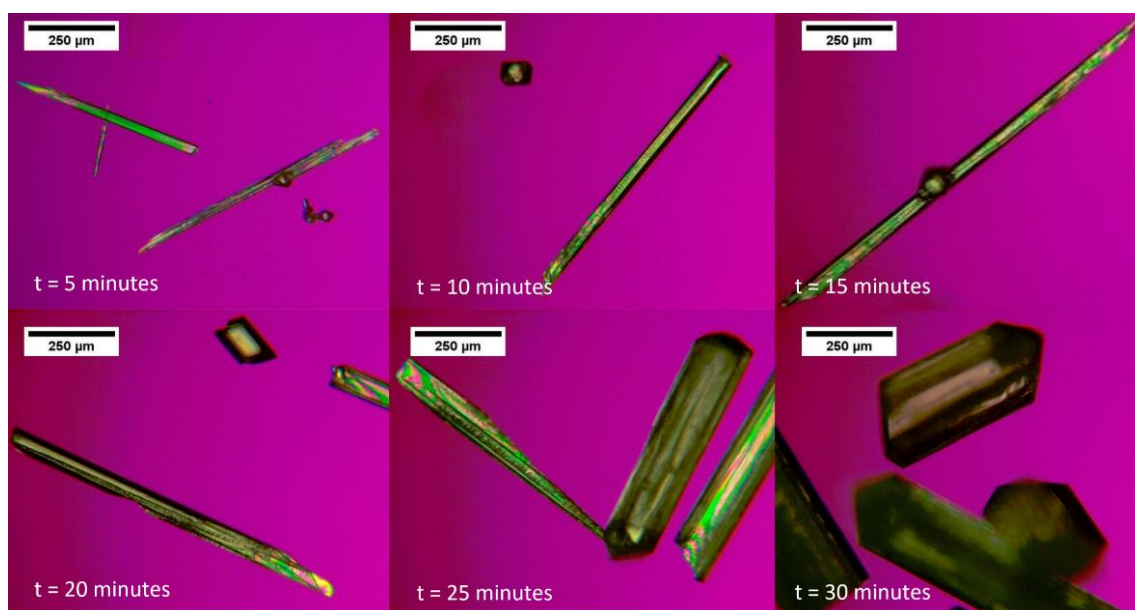
Figure 4.14: Optical micrographs showing the solution-mediated phase transformation of β-glycine to α-glycine within 30 minutes for the $\frac{c}{c_{sat}}$ = 2.4 system.
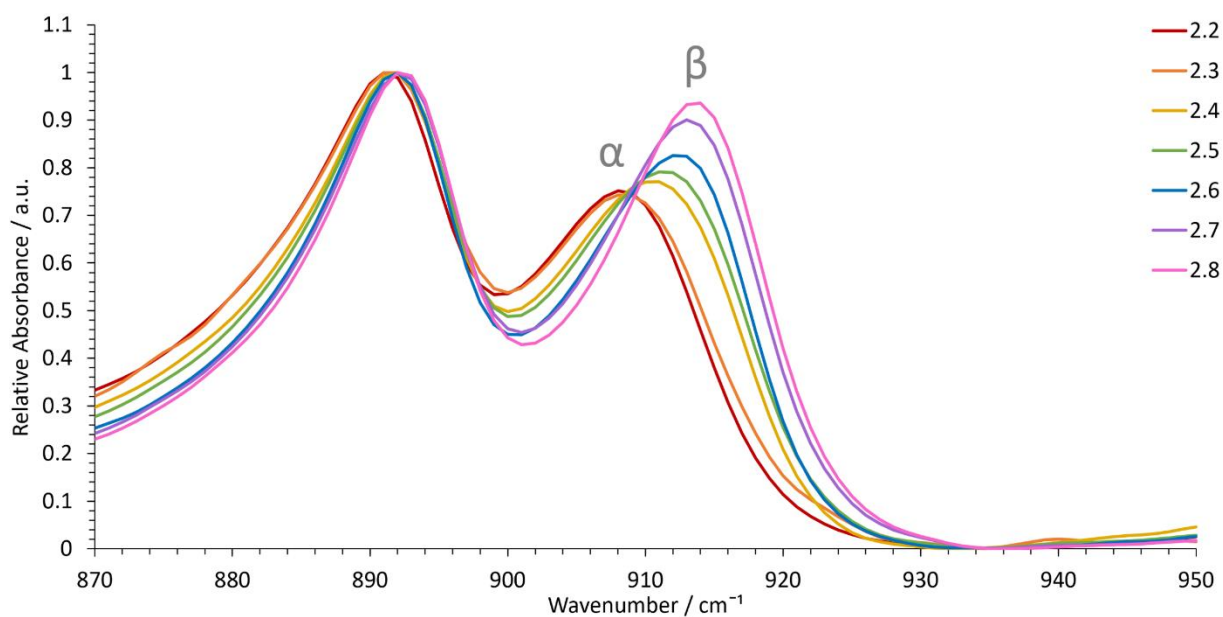
Figure 4.15: Representative ATR-FT-IR spectra for extracted glycine crystals obtained from binary ethanol and water solutions with ethanol mass fractions of 0.6 and varying supersaturations corresponding to glycine $\frac{c}{c_{sat}}$ of 2.2 – 2.8. The spectra have been normalized relative to the common peak at 890 cm^{-1}. Absorbance maxima at 909 cm^{-1} and 914 cm^{-1} identify material as containing α-glycine and β-glycine, respectively.

The crystallisation of each of the three ambient polymorphs of glycine has also been confirmed using powder X-ray diffraction (PXRD). The recorded patterns for each polymorph are shown in Figure 4.16, alongside the corresponding FT-IR spectra. The PXRD patterns can be compared to the International Center for Diffraction Data (ICDD) files 00-032-1702, 00-002-0171 and 02-088-4306 for α-, β- and γ-glycine, respectively. Note that the characteristic diffraction peaks for each polymorph are indicated by asterisks and are summarised in Table 4.2.[158,159 ,202,205] The β-glycine PXRD spectrum contains trace amounts of the α-glycine polymorph, which can be most easily discerned by the tiny α-glycine peaks at 14.8° and 19.5°.

Table 4.2: Characteristic pXRD peaks for α-, β- and γ-glycine.[158,159 ,202,205]

Polymorph	Characteristic pXRD peak / °
α-glycine	19.5
	29.7

Polymorph	Characteristic pXRD peak / °
β-glycine	18

Polymorph	Characteristic pXRD peak / °
γ-glycine	25.3
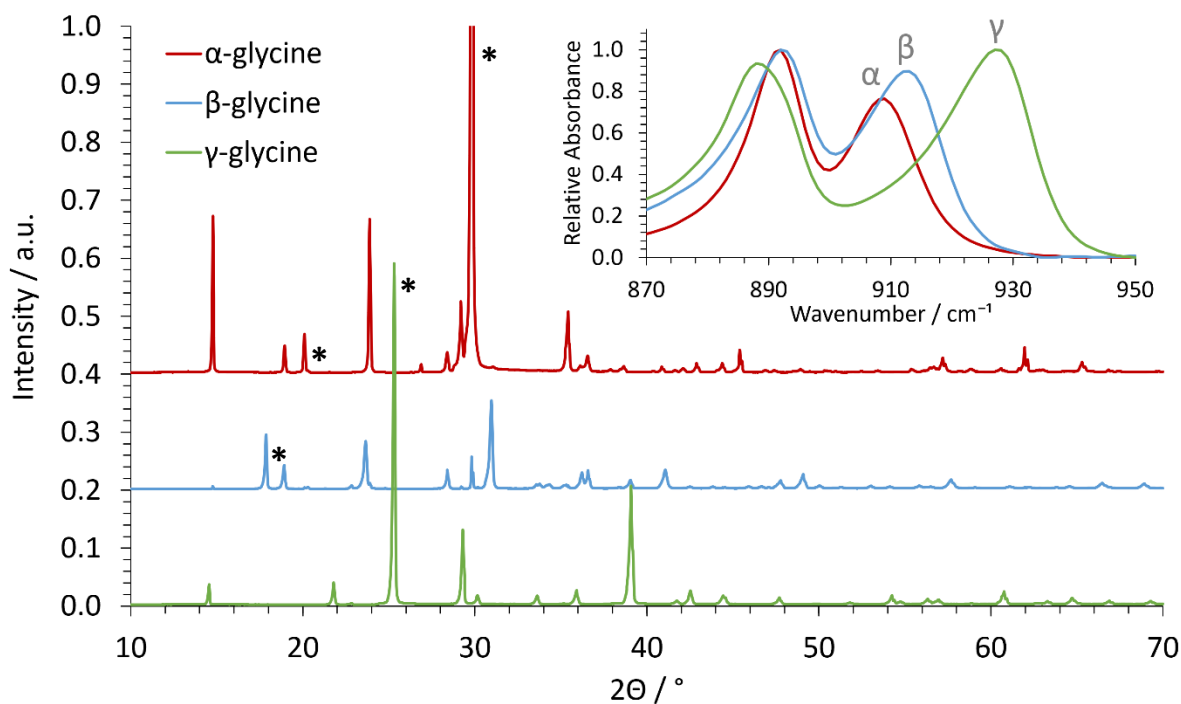
Figure 4.16: Representative powder X-ray diffraction (PXRD) spectra of glycine polymorphs obtained from a water-in-oil STF with $\frac{c}{c_{sat}}$ = 1.30 STF (γ-glycine), an oil-in-water STF with $\frac{c}{c_{sat}}$ = 1.30 STF (α-glycine) and a bicontinuous STF with $\frac{c}{c_{sat}}$ = 2.20 STF (β-glycine). The corresponding ATR-FT-IR spectra are shown in the inset.

Virtually 100% β-glycine could be crystallised, as verified by PXRD (Figure 4.16), by simply scaling up the STF with 0.25 mass fraction of water and $\frac{c}{c_{sat}}$ of 2.2 from 25 ml to 100 ml. It is suspected that the greater β-glycine proportion in the larger 100 ml crystallisation, was because the hydrophilic glass walls are wetted more by the aqueous phase of the STF, thereby reducing the nanoconfinement in the vicinity of these walls so that local α-glycine crystallisation is more likely here. Accordingly, crystallisation from larger volumes that have smaller surface area to volume ratios minimizes this container wall effect. The formation of α-glycine crystals adhered to the vertical glass sides supports this hypothesis.

Evidently, in the STF system with 0.25 mass fraction of water, and a relative concentration of 1.9, β-glycine emerged as one of the polymorphic products, existing for extended periods even with α-glycine present in the same solution. To assess the growth profiles of both polymorphs in this system, crystals were observed growing *in situ* using an optical microscope. The dimensions of the crystals were measured periodically, and the growth rate plotted against time elapsed, shown in Figure 4.17.

This demonstrates that for both the α- and β-crystals, there was initially (t ≈ 0 s) a relatively fast growth rate which slowed rapidly over the first 2 x 10^3 s (approximately 30 minutes). This relates to the faster initial growth until depletion of the local supersaturation around each crystal occurs, the growth becomes hindered and the rate of growth will slow until it reaches a plateau. At this point, the growth rate drops to 0 μm s^{-1}, i.e. the crystals stop growing due to a lack of solute. For α-glycine, the growth rate remains faster than that of β-glycine throughout the course of the investigation. This reflects the relative solubilities of each polymorph as α-glycine is more stable and therefore less soluble than the β polymorph. Consequently, the c_{sat} for α-glycine will be lower and the relative supersaturation level, $\frac{c}{c_{sat}}$, will be greater. The larger relative supersaturation of α-glycine compared with β-glycine means that, when grown at the same time, the α-polymorph will grow faster, and will continue to grow for longer as it effectively has more available solute to grow from before the saturation limit is reached. This is reflected in the growth rate profiles displayed in Figure 4.17.
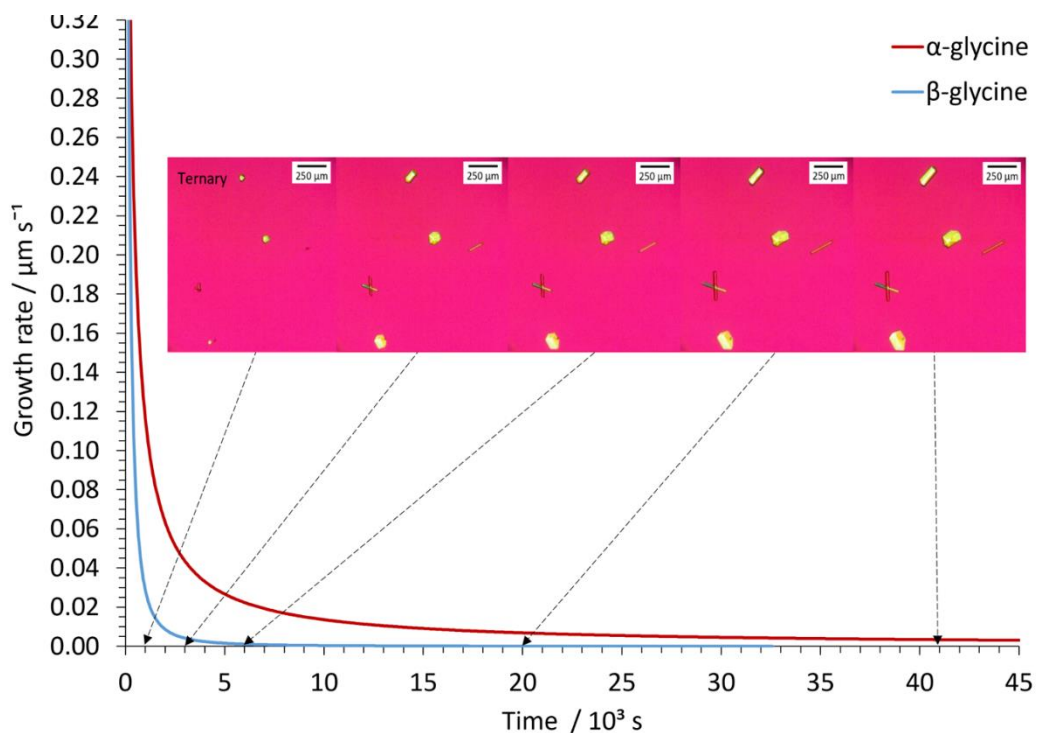
Figure 4.17: Optical micrographs showing three α-glycine crystals and three β-glycine needle crystals along with the average growth rate plot for the α- and β-glycine crystals during crystallisation in the $\frac{c}{c_{sat}}$ = 1.90 system.

It is significant here that growth rate of neither crystal became negative, which would indicate that the crystal was dissolving back into solution. Should Ostwald's ripening occur in this system, it would be expected that the β-polymorph would reach a growth rate of 0 μm s^{-1} faster than the α-polymorph (which is observed), but also that the crystal would then exhibit a negative growth rate as it dissolved due to this Ostwald's ripening. Equally, the profile of the α-polymorph would also either exhibit a corresponding increase in growth rate, or would sustain a faster growth rate for longer, over the period of β-polymorph dissolution. These features are not observed so it may be concluded that the crystals grow independently of each other and can persist despite the differences in stability.

This system was then compared to a binary, and therefore unconfined, ethanol/water system with the same mass fraction of ethanol (0.40) as in the STF. The results are summarised in Figure 4.18.
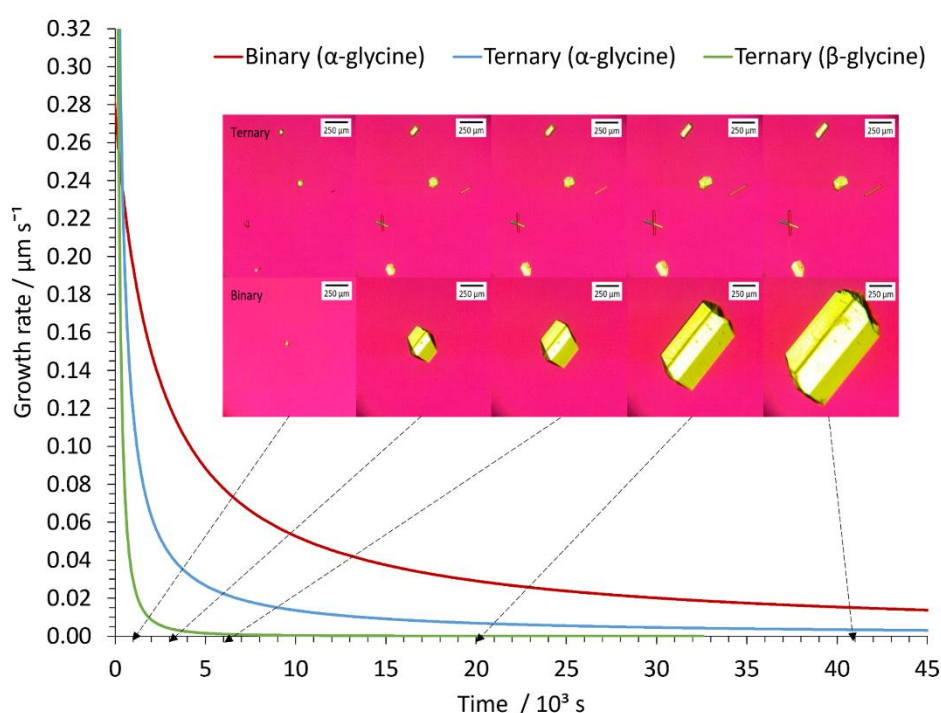
Figure 4.18: Comparative growth rate curves for α-glycine in the binary and ternary systems, and β-glycine in the ternary system, with corresponding optical microscope images. The systems contained an ethanol mass fraction of 0.40 and a glycine $\frac{c}{c_{sat}}$ = 1.90.

Here, a significantly faster growth rate was observed for the unconfined sample. This is reflected clearly in the optical microscope images taken over this period. For example, after 11 hours had elapsed, the confined and unconfined α-glycine crystals had grown to 0.17 mm and 1.1 mm in length,

respectively, and the measurable surface area from the microscope images was 43 times greater for the unconfined crystal (0.69 mm^2 compared to 0.016 mm^2 for the confined crystals). Alongside a significantly impeded growth rate, the STF system displays an enhanced nucleation rate. Here, six different crystals nucleated within the field of vision of the microscope, whereas only one crystal was found for the comparative binary system.

4.3.10 Crystallisation Mechanism in STFs

The crystallisation outcomes for the STFs containing 0.25 mass fraction of water are consistent with a mechanism that is markedly altered compared to crystallisation in normal, unstructured solutions. If a solute is soluble in only one of the immiscible liquids of an STF, and specifically the minor component one, the solute is largely confined to the nm-sized pools of that liquid and a degree of restricted diffusion arises, as shown using NMR diffusiometry (Figure 4.8). Then, as a crystal nucleus grows in a nm sized pool, there is a significant supersaturation depletion, both from the limited amount of solute in the nm-sized pool, and the restricted diffusion that impedes additional solute molecules entering the pool. This supersaturation depletion hinders the emergence of stable nuclei. Consequently, to achieve crystallisation a higher initial supersaturation is required, which in turn results in a higher nucleation rate. It is hypothesized that the higher nucleation rate will be further enhanced by two additional factors. Firstly, the large amount of interface, albeit diffuse, in the STF can help induce solute ordering. Secondly, the restricted diffusion of the immiscible liquids and the solute means that any locally high supersaturations will be prolonged, further facilitating nucleation.

Although the nucleation rate is higher in the STFs, crystal growth of the nuclei is quickly reduced due to the rapid supersaturation depletion as the nuclei grow in their nanoconfined regions. This reduced crystal growth continues until the nuclei or nanocrystals are surrounded by nm-sized pools of saturated solution. Further growth of the larger, more stable nanocrystals is then expected to occur predominantly via Ostwald's ripening through the dissolution of smaller, less stable nuclei or nanocrystals. However, this process is severely hampered by the restricted diffusion of the solute.

Hence, the crystallisation profile in the STFs is distinctly different to crystallisation in normal, unstructured solutions. In unstructured solutions, nucleation is usually the slow step, resulting in a limited population of nuclei that then grow rapidly past the nm-size range; in STFs, the higher nucleation rate and slower crystal growth create numerous nuclei that will then grow exceedingly slowly past the nm-size range once the local supersaturation has been depleted.

Essentially, this means that the STF can act an as an array of nanocrystal incubators when a suitable initial supersaturation is used. The higher nucleation rate and slower growth profile for glycine crystallisation within our STFs is readily apparent from simple visual observation, optical micrographs and turbidity measurements when supersaturations with $\frac{c}{c_{sat}}$ of 1.90 are employed in the 0.25 water mass fraction STF (Figure 4.17 – Figure 4.19).
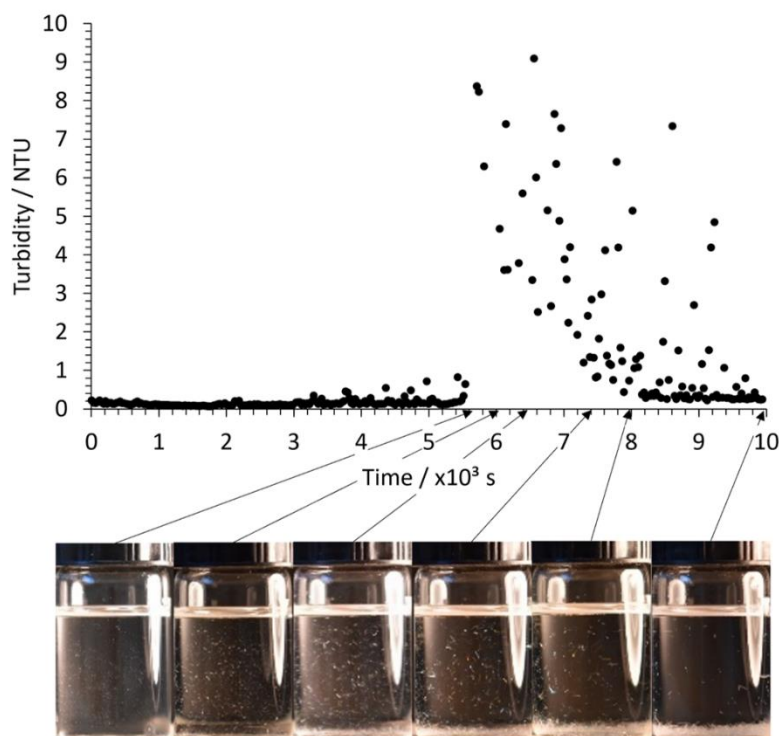
Figure 4.19: Turbidity measurements and visual observation of suspended crystals in the $\frac{c}{c_{sat}}$ = 1.90 system. The suspended crystals are particularly evident in the middle vials but have mostly sedimented in the far-right vial.

In contrast, for glycine crystallisation at the same 1.90 $\frac{c}{c_{sat}}$ value in the binary 0.60 water/0.40 ethanol mass fraction system, the samples had to be scanned in the optical microscope to locate the much

rarer crystals, which grew at a faster rate to produce larger crystals that rapidly sedimented; hence the crystals mainly just appeared at the base of the vial when taking turbidity readings (Figure 4.20).
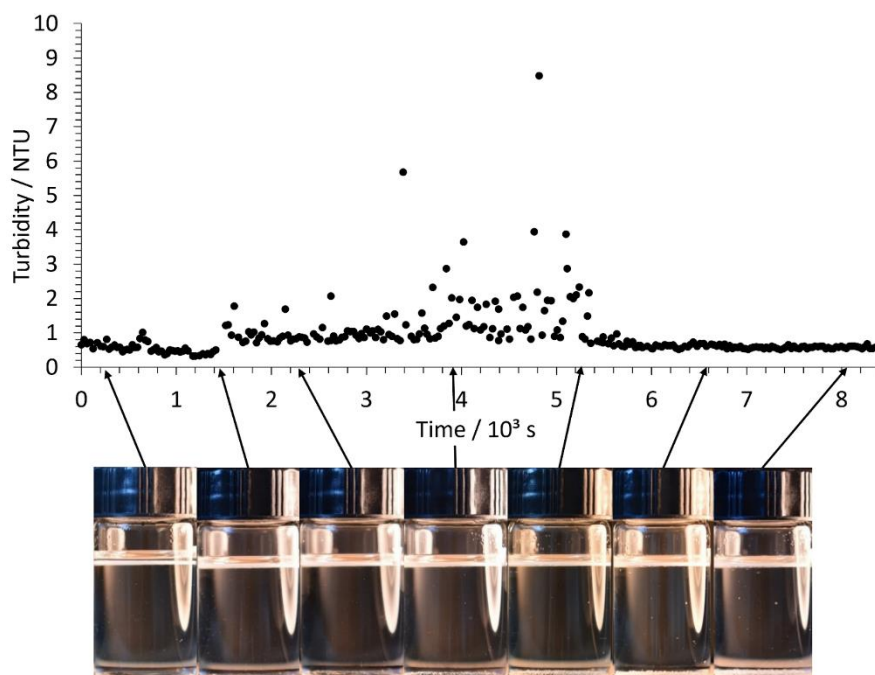
Figure 4.20: Turbidity measurements and visual observation of glycine crystallization in the binary system, showing glycine crystals growing at the base of the sample vial and not remaining suspended.

These findings confirm our premise that crystallisation in the STFs proceeds by a novel higher nucleation rate and slower growth pathway. At the lower $\frac{c}{c_{sat}}$ value of 1.30, the depletion of local supersaturation occurs in the nm crystal size range for the 0.25 water mass fraction STF, and hence the STF then acts as an array of nanocrystal incubators, with the slowly growing nanocrystals remaining suspended throughout the fluid for extended periods of 16 hours to over a day.

4.3.11 Seeding Experiments

Due to the intrinsic size restriction of the nanodomains in which crystals form, the overall yield of crystals formed is low relative to the yields achievable through bulk crystallisation. However, as nanocrystals were suspended in the STFs for extended periods, it was hypothesised that they could be used as seed nuclei for larger bulk crystallisations, thereby combining the benefits of both methodologies. Aliquots of the nanocrystal-containing STFs were used to seed metastable[203] supersaturated glycine solutions to induce crystallisation of the desired polymorph. The metastable

binary solutions contained 0.40 water and 0.60 ethanol mass fractions and had a relative glycine supersaturation, $\frac{c}{c_{sat}}$, of 1.30. If left undisturbed, or if an STF aliquot containing no glycine nanocrystals was added, these metastable binary solutions eventually produced α-glycine after ~1 day and ~2 hours, respectively (Figure 4.21). In agreement with previous studies[146,196,200] γ- and β-glycine crystallisation were never observed.
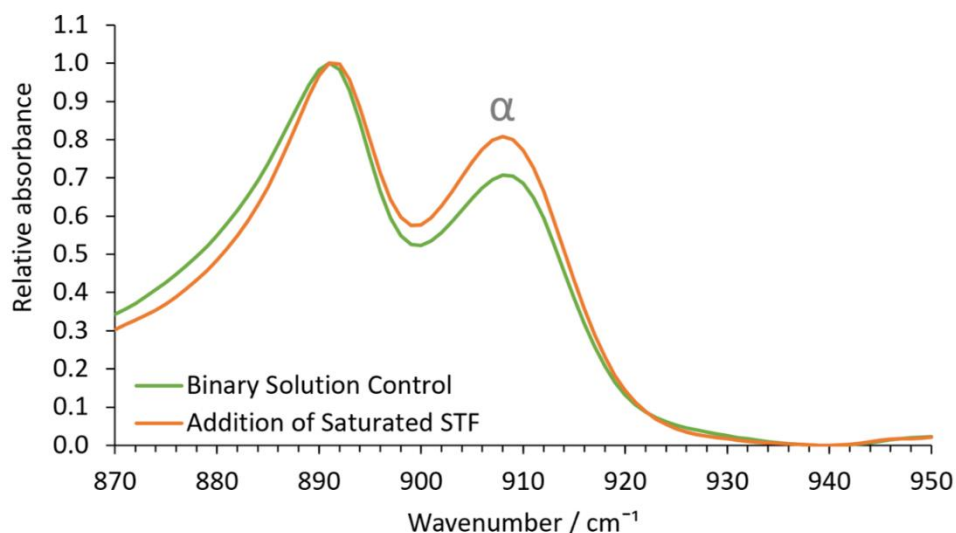
Figure 4.21: Representative control ATR-FT-IR spectra of extracted crystals after eventual ≈ 24-hour α-glycine crystallization in the $\frac{c}{c_{sat}}$ = 1.30 binary 0.40 water/0.60 ethanol mass fraction system and α-glycine crystallization after ≈ 2 hours when this system had a glycine-saturated STF aliquot added. Absorbance maxima at 909 cm^{-1} identify material as α-glycine.

Despite this, seeding these metastable binary solutions with aliquots of the γ-glycine nanocrystal-containing STFs resulted in visible γ-glycine crystals forming within a shortened timeframe of 1–2 hours. Similarly, seeding with higher glycine concentration STFs containing β-glycine nanocrystals produced β-glycine in the metastable binary solutions within 10 minutes, whilst seeding with STFs containing α-glycine nanocrystals produced α-glycine, again within a shorter timeframe of 1–2 hours (Figure 4.22). These initial tiny crystals then grew in solution for a total of 24 hours, where the difference between the seeded and unseeded samples became more evident (Figure 4.23).

Figure 4.22: Visible glycine crystallization in the seeded binary ethanol/water solutions containing 0.60 mass fraction ethanol and $\frac{c}{c_{sat}}$ = 1.30 after (a) 1 hour for γ-glycine crystallization due to seeding with the 0.25 water mass fraction STF with $\frac{c}{c_{sat}}$ = 1.30, (b) 10-20 minutes for β-glycine crystallization due to seeding with the 0.25 water mass fraction STF with $\frac{c}{c_{sat}}$ = 2.10 and (c) 1 hour for α-glycine crystallization due to seeding with the 0.40 water mass fraction STF with $\frac{c}{c_{sat}}$ = 1.30
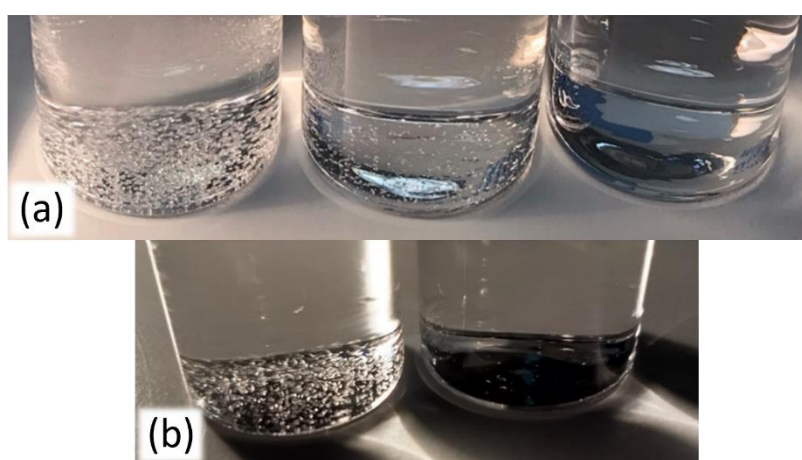
Figure 4.23: (a) Photographs taken 24 hours after seeding with the α-glycine (left) and γ-glycine (middle) nanocrystal-containing STFs compared to the control unseeded system (right). (b) Photographs taken 24 hours after seeding with the β-glycine nanocrystal-containing STF (right) compared to the control unseeded system (left).

Note there are far fewer visible crystals for the γ-glycine sample compared with the α-glycine sample even though the STF $\frac{c}{c_{sat}}$ = 1.30 value is the same. This is due primarily to the slower growth of γ-glycine compared to α-glycine. Furthermore, in the β-glycine sample there are more visible crystals than in the α-glycine sample due to the larger number of seeds in the higher supersaturation $\frac{c}{c_{sat}}$ = 2.10 STF. The polymorphic result of these tests was quantifiably measured using FT-IR spectroscopy for both the seeded samples and the STFs from which the seeds were extracted. The results are shown in Figure 4.24.
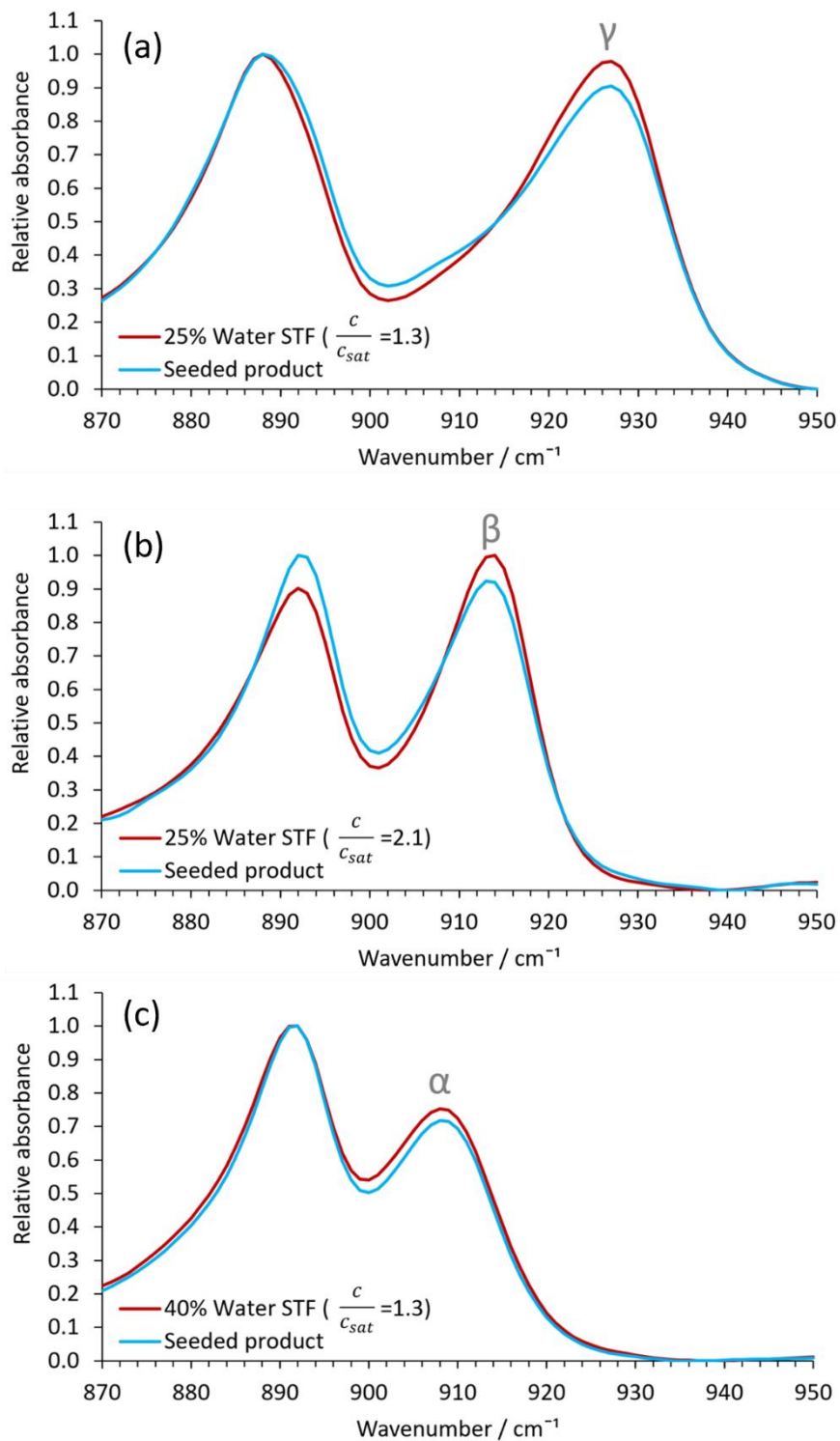
Figure 4.24: Representative ATR-FT-IR spectra showing (a) γ-glycine crystallization, (b) β-glycine crystallization and (c) α-glycine crystallization in the binary system after seeding with aliquots of the STFs containing seeds of these polymorphs. The ATR-FT-IR spectra from the same STFs once the glycine crystals had grown and sedimented are also shown. Absorbance maxima at 909 cm^{-1}, 914 cm^{-1} and 928 cm^{-1} identify material as containing α-glycine, β-glycine and γ-glycine, respectively.

There is an excellent correlation between the seed nanocrystal polymorphs and the macroscopic crystals produced in the metastable seeded binary solutions. This suspended nanocrystal seeding

method offers distinct advantages over traditional methods that frequently use grinding of macroscopic crystals to produce the seeds. Grinding is an energy-intensive process that often produces high energy defects on the seeds' surfaces, which can then act as sites for secondary nucleation of unwanted polymorphs. In contrast, the isolated suspended nanocrystals grow slowly under the restricted diffusion conditions in the STFs to produce well-formed single crystals that are bounded by low energy faces, even under high supersaturation conditions. This differs from crystallisation in unstructured fluids, where attempts to produce nanocrystals from a soluble component by inducing a high supersaturation through crash cooling invariably produce poorly crystalline colloidal particles that rapidly aggregate. Of course, seed suspensions in unstructured solutions can be obtained by antisolvent addition, reactive crystallisation, or the use of e.g. ultrasound or lasers.[204] However, these methods do not provide a generic capability for producing longer-lived nanocrystal suspensions of any desired polymorph. STFs may provide this generic capability.

4.4 Conclusions

In summary, we have revealed that a degree of restricted diffusion in STFs enables crystallisation to occur under higher nucleation rate and slower crystal growth regimes that are impossible to access in normal bulk solution crystallisation. This restricted diffusion prolongs the lifetime of locally high supersaturations and reduces the rate of Ostwald's ripening so that polymorphs that are difficult to nucleate, transitory and/or have slow growth can be targeted. In particular, under relatively low supersaturation conditions, crystallisation occurs under thermodynamic control and stable but slow-growing polymorphs, such as γ-glycine, can be obtained. Under higher supersaturation conditions, the even higher local supersaturations generated in STFs lower the nucleation energy barriers to all polymorphic forms, making them more accessible, whilst the restricted diffusion makes them less susceptible to dissolution in the presence of lower energy forms. Hence, metastable polymorphs that are hard to nucleate and often transient, such as β-glycine, can be readily extracted. The greater potential for multiple polymorph discovery within a single STF formulation means that STFs should

prove a potent and versatile tool for polymorph discovery, and selective crystallisation in general, particularly because they are able to target both stable and metastable polymorphs with vastly different stabilities and crystal growth rates. This could transform the current, scattergun approach to polymorph screening, which involves using many different solvents with different cooling profiles to hopefully obtain different polymorphs, but without any guarantee of success.

Furthermore, the STF can act as an array of nanocrystal incubators, with the nanocrystals remaining suspended in the fluid for extended periods of time. Accordingly, aliquots of the nanocrystal-containing STF can seed metastable solutions to induce crystallisation of the desired polymorph. Here, the longevity of these nanocrystal suspensions, the slow nanocrystal growth so that crystal perfection is maintained, and the ability to target specific polymorphs are key advantages over current seeding capabilities. Finally, the slow, restricted crystal growth rate in STFs should enable unprecedented study of early-stage crystallisation to provide new insights.

5 METHOD UBIQUITY

5.1 INTRODUCTION

Chapters 3 and 4 have established that the use of STFs can offer an opportunity to exercise control in the formation of polymorphic crystals. However, in this work so far only glycine has been used to demonstrate this. As discussed, glycine is an excellent proof-of-concept polymorphic compound due to the difficulty in nucleating any other polymorph in aqueous conditions besides α-glycine under ambient conditions. However, to further establish this methodology, STFs must be applied more widely to other chemicals. The two chemicals we chose for this initial proof of concept are ROY, a highly polymorphic organic molecule, and silica, which we use as a representative inorganic chemical that forms giant covalent structures. These are detailed further below.

5.1.1 5-methyl-2-[(2-nitrophenyl)amino]-3-thiophenecarbonitrile (ROY)

ROY (Figure 5.1), nicknamed for its distinctive red, orange and yellow crystals, currently holds the record for the largest number of fully characterised organic crystal polymorphs, with 12 different crystal forms discovered to date.[206] These are labelled R, Y, OP, ON, YN, ORP, Y04, YT04, R05, PO13, R18, and Y19. A 13th polymorph, RPL, has also been proposed, though it is highly unstable and has only been observed experimentally as deposits on β-succinic acid surfaces, making structural characterisation difficult and computationally derived structures controversial.[206-217] For this reason, it has not yet been confirmed on the Cambridge Structural Database (CSD) as a resolved structure of ROY. The crystal structures of each of the identified polymorphs are summarised in Table 5.1. Of all 13 proposed structures, the 6 highlighted in yellow are known to be grown from solution under ambient conditions.[208,209] Note that R18 and Y19 may also be crystallised from solution but required temperatures of 100 − 150 K.[216,217]

The difference in colour between the ROY polymorphs has been attributed to the change in the S−C−N−C dihedral angle, θ, highlighted in red in Figure 5.1, which is distinct for each observed polymorph.

In general, the lower the value of θ, the redder the crystals appear in colour, purportedly due to an increase in the π-conjugation between the thiophene and phenyl constituents.[206] This, however, is a simplistic view and there may be other effects that contribute to colour in some polymorphs such as intermolecular as well as intramolecular π-interactions.[218]
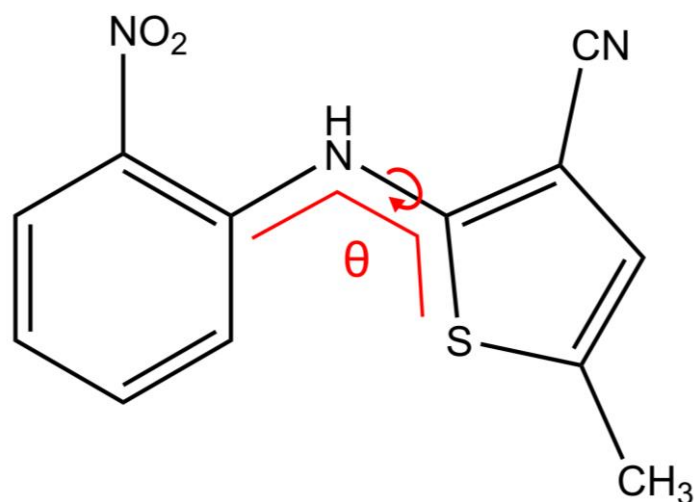
Figure 5.1: Structure of ROY with the S–C–N–C dihedral angle indicated by red lines.

Of the six yellow highlighted polymorphs, the order of stability was predicted by Beran *et al.*[206] to be Y > R > OP > ON > YN > ORP, where there is a small energy difference of ~4 kJ mol^{-1} between the most stable polymorph, Y, and the least stable, ORP. This makes polymorphic control difficult. Different methods have been employed to achieve this, e.g. by crystallising in methanol to produce Y and OP concomitantly,[219,220] by promoting epitaxial growth on substrates such as pimelic and succinic acid,[210] by crystallising inside supramolecular gels to template the growth of R,[221] or by introducing other specific additives such as polymer heteronuclei,[222] or FuROY pseudoseeds.[216]

Importantly for this work, nanoconfinement has been shown to demonstrate promising control over the crystallisation of ROY without the need for direct templating or seeding. Ha *et al.*[172] demonstrated that when ROY is crystallised in polycyclohexylethylene monoliths, selective crystallisation of Y may be achieved. This was later supported using microemulsions comprised of water/heptane, Igepal CA720 nonionic surfactant, and toluene as the ROY-containing confined phase, selectively nucleating the thermodynamically stable Y form.[66]

Table 5.1: Summary of ROY polymorphs to date, alongside their proposed crystal structures and growth technique(s).[2] *Structure proposed computationally but undetermined by SCXRD.

Polymorph	Colour	Morphology	Crystal Structure	Space Group	Dihedral angle / °	Growth Method	Year Discovery	Year Structure determined	Reference
R	Red	Prism	Triclinic	P$\bar{1}$	21.7	• Solution crystallisation • Melt crystallisation	1995	1995	[208]
Y	Yellow	Prism	Monoclinic	P2$_1$/n	104.7	• Solution crystallisation	1995	1995	[208]
ON	Orange	Needle	Monoclinic	P2$_1$/c	52.6	• Solution crystallisation • Melt crystallisation	1995	1995	[208]
OP	Orange	Plate	Monoclinic	P2$_1$/n	46.1	• Solution crystallisation	2000	2000	[209]
YN	Yellow	Needle	Triclinic	P$\bar{1}$	104.1	• Solution crystallisation • Melt crystallisation	2000	2000	[209]
ORP	Orange – Red	Plate	Orthorhombic	Pbca	39.4	• Solution crystallisation	2000	2000	[209]
RPL	Red	Plate	Orthorhombic	Pbca	22.6, 32.7	• Vapour deposition	2001	2019*	[210,211]
Y04	Yellow	Prism	Triclinic	P$\bar{1}$	76.9	• Melt crystallisation	2004	2020	[207,212]
YT04	Yellow	Prism	Monoclinic	P2$_1$/n	112.8	• Melt crystallisation and transformation	2004	2005	[212]
R05	Red	Prism	Monoclinic	P2$_1$	44.9, −34.0	• Melt crystallisation	2005	2018	[213,214]
PO13	Pumpkin – Orange	Needle	Monoclinic	P2$_1$/c	127.7	• Melt crystallisation	2013	2020	[215,216]
R18	Red	Block	Triclinic	P$\bar{1}$	10.3, 5.0	• Solution crystallisation	2018	2020	[217]
Y19	Yellow	Needle	Monoclinic	P2$_1$/c	60.7	• Solution crystallisation	2019	2020	[216]

5.1.2   Quartz

Under ambient conditions, silica (SiO_2) has three stable phases: quartz, cristobalite, and tridymite, which undergo interconversions at elevated temperatures. Additional polymorphs, coesite and stishovite, are known to exist at high pressures but are outside the scope of this work.[72,223]

The crystal structures of silica contain SiO_4 tetrahedra linked through shared oxygen atoms at their corners, and polymorphism arises when these tetrahedra arrange differently (Figure 5.2). The most stable polymorph under ambient conditions is α-quartz,[224] which requires temperatures and pressures of 200-300 °C and 15-100 bar, respectively, when nucleating in nature. This prohibits the generation of controlled, nm-sized quartz crystals because crystal growth proceeds rapidly after nucleation in these high temperature and pressure conditions to give larger sized crystals. Consequently, there is difficulty in producing nm-sized quartz crystals that can then seed milder hydrothermal syntheses, therefore requiring a lower energy input.[110]
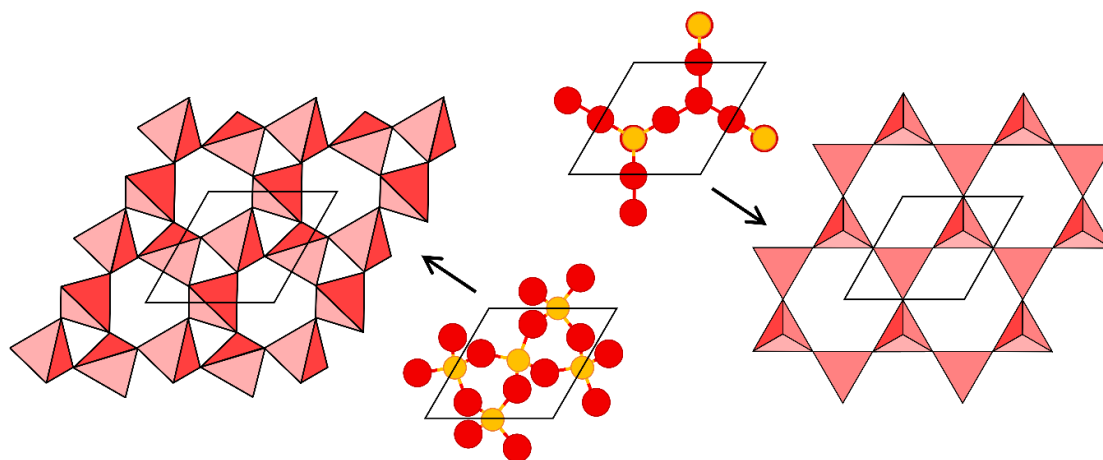
Figure 5.2: Atomic and polyhedral crystal structures of the silica polymorphs α-quartz (left) and tridymite (right).

The first chemical synthesis of nanoquartz was published in 2003 and detailed the dissolving of dry amorphous silica in NaOH, and then crystallisation at 300 °C and 8.58 MPa.[225] This method required dialysis to purify the product, where the pH had to be controlled (pH 8) to avoid amorphous product reforming. After this, more hydrothermal and solvothermal methods were tested, each using similarly high temperatures and pressures in basic aqueous NaCl solution and toluene/oleic acid/ethanol/TEOS/KOH emulsions, respectively. In the latter case, it was found that the emulsion

structures could template the crystal growth and aided in the controlled size distribution of the resultant crystals.

Currently, the primary route to nanoquartz synthesis is the sol-gel methodology[226-228] due to the narrow size distribution of the particles formed under milder conditions. Here, a dispersion of precursor material (a sol) is transformed through chemical reaction/thermal treatment into a gel, where the precursor reacts intermolecularly to form metal-oxygen bonded networks. These methodologies are often performed near room temperature and therefore it is common that the resultant silica is either amorphous or poorly crystalline, therefore a second heating step is typically employed to transform the product into crystalline silica.[226,227]

In 2018, Buckley *et al.* reported the formation of 1–5 nm α-quartz crystals formed under ambient conditions using w/o microemulsions, using sodium metasilicate (SMS) as the silica precursor. While this methodology has been successfully applied in organic structures such as glycine and ROY,[66] quartz is a giant covalent structure with much stronger covalent bonding present when compared to the intermolecular hydrogen bonding that determines the polymorphic structure in the organic solids. Therefore its occurrence, which likely required the breaking and reforming of Si-O bonds to produce the crystalline product rather than an amorphous one, was less expected. The successful formation of nanoquartz in the microemulsions was attributed to fluctuations in alkalinity in the droplet nanoreactors that facilitated the cleavage of the stronger Si-O covalent bonds. The resultant nanocrystals could then be used to seed hydrothermal syntheses under much milder conditions of 175 °C and 9 bar.[110]

5.1.3 Aims

The NMR diffusiometry studies performed in Chapters 3 and 4 indicate that solute must experience a degree of confinement within STF nanostructures, therefore restricting solute diffusion by more than 25% compared to an unconfined system, for polymorphic control to be achieved in these systems. Accordingly, this crystallisation method should not be limited to STFs comprised of only octanol,

ethanol, and water, but any STF in which the crystallising solute is soluble in one of the immiscible phases and is effectively insoluble in the other so that it may be confined.

ROY and quartz are ideal crystalline materials for testing the ubiquity of this methodology. ROY is insoluble in water and therefore a different STF comprised of toluene, IPA, and water was chosen, with toluene acting as the confined phase. Nanoquartz is an inorganic crystal and, as previously discussed, contains strong covalent bonds in its structure. In order to nucleate crystalline quartz under ambient conditions, it is vital that nanodroplet reactors be present in order to facilitate transiently high alkaline conditions that will hinder the rate of aggregation of the dissolved silica precursor into amorphous forms.

This chapter aims to investigate the ability of STF structures to crystallise ROY and nanoquartz, thereby demonstrating that this methodology is not limited to a single STF, and could produce a versatile assortment of crystalline materials.

5.1.4   Experimental

5.1.4.1   Materials

The chemicals used were as follows: octan-1-ol (99%, Fisher Scientific), ethanol (≥99.8%, Fisher Scientific), toluene (≥99.8%, Fisher Scientific), isopropyl alcohol (≥99.5%, Fisher Scientific), 5-methyl-2-[(2-nitrophenyl)amino]-3-thiophenecarbonitrile (ROY) (Sigma-Aldrich), sodium metasilicate nonahydrate (SMS) (≥98%, Sigma-Aldrich). Ultra-high purity water (18.2 MΩ cm) was obtained from a Sartorius arium® comfort water purifier.

5.1.4.2   ROY experiments

A binary system comprised of 0.475 mass fraction toluene and 0.525 mass fraction isopropanol (IPA), and an STF comprised of 0.100 mass fraction toluene, 0.375 mass fraction water and 0.525 mass fraction IPA, were made on a 20 g scale. ROY was then added to each sample to achieve a relative ROY concentration, $\frac{c}{c_{sat}}$, of 5.5 at 25 °C, with c_{sat} = 30 mg cm^{-3} and 3.5 mg cm^{-3} for the binary system and STF, respectively. The binary and STF samples were sealed with PTFE tape before being heated to 65

°C on a hot plate with stirring until all the ROY was dissolved. Samples were then placed in an oven at 70 °C to ensure full dissolution. After one hour, the samples were removed from the oven, placed in a water bath at 25 °C and left to crystallise undisturbed. The samples were monitored, and in the first trial, crystals were extracted ≈5-10 minutes after the first appearance of a mass of suspended ROY crystals in the STF. This gave the four ROY polymorphs Y, YN, ON and R in the STF. In subsequent tests on the STF system, crystals were extracted at different times to achieve the pure polymorphs. In particular, for the pure Y polymorph, crystals were extracted at earlier times, as the Y polymorph grew the fastest (it is both the thermodynamic and kinetic product in the toluene/IPA system). The YN and ON polymorphs appeared next as a mass of suspended needle crystals, and at later times the suspended needle mass sedimented and then disappeared as the R polymorph crystallised. In the binary system, only Y crystals were obtained irrespective of the extraction time, consistent with the Y-polymorph being both the kinetic and thermodynamic product.

5.1.4.3 Nanoquartz experiments

In these experiments, sodium metasilicate nonahydrate (SMS) was used as the precursor material for crystallisation of α-quartz. Initially, a stock solution was created by dissolving solid SMS in ultra-high purity (UHP) water, in such quantities that the solution contained 2.5 wt. % SMS, this was labelled solution A. This concentration was chosen, as above 2.5 wt%, the STFs began to destabilise. Then, a solution of ethanol and octanol was made, labelled solution B, directed by the desired final STF composition. Solution A was then added to solution B in such quantity as to achieve this final composition, which is outlined in Table 5.2. Similarly to the STFs used in Chapter 3, this system was made on a 200 ml scale.

Table 5.2: Composition of STF used for the crystallisation of α-quartz.

2.5 wt% SMS solution / wt%	Octanol / wt%	Ethanol / wt%
15	50	35

Next, the sample was sealed with PTFE tape and left at room temperature to crystallise. A typical nanoquartz synthesis using surfactant microemulsions took approximately two weeks before material

was extracted.[110] However, due to the COVID-19 pandemic, and to allow the system as long as possible to crystallise, this sample was allowed to grow for 2.5 years prior to an attempt at extraction.

Unfortunately, the yield of product was so low that extraction was not possible by typical centrifugation. Therefore, to analyse the product from this system, TEM grids were made up by depositing 20 drops of the STF directly onto holey carbon copper grids.

5.2 RESULTS AND DISCUSSION

5.2.1 ROY Crystallisation Studies

To gauge the likely polymorph screening capability of the STFs, we conducted trial experiments at high supersaturation of 5.5 on the highly polymorphic compound, ROY. ROY is extremely soluble in toluene and virtually insoluble in water, so a toluene/isopropanol/water STF was selected for these crystallisation studies. The phase diagram, adapted from Washburn *et al.*[229] is given by Figure 5.3.
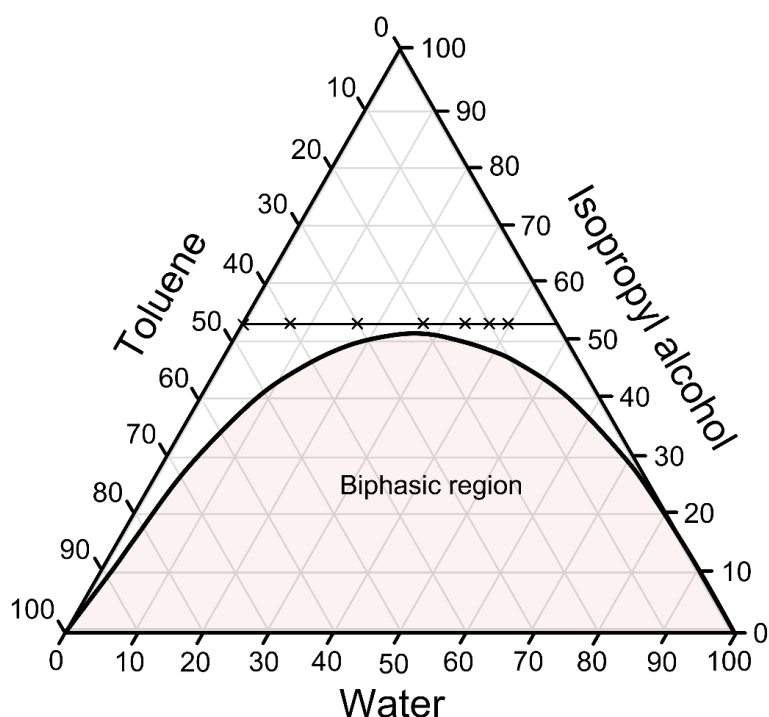
Figure 5.3: Ternary phase diagram for systems comprised of toluene, isopropyl alcohol, and water. STF compositions tested in the crystallisation of ROY are indicated by black crosses.

Here, different compositions along a line of constant 0.525 mass fraction of isopropyl alcohol (IPA) was chosen to test the ability of these STFs with respect to ROY crystallisation. This was in order to encapsulate the region directly bounding the biphasic region, but still maintaining a constant mass fraction of the hydrotrope, IPA, similar to the compositions tested in Chapter 4 for glycine. The distribution of compositions tested was weighted to the water-rich side of this line, so as to test the toluene-in-water compositions more thoroughly, given that they would likely lead to the nanoconfinement effects required for polymorphic control.

Three metastable polymorphs of ROY, the YN, ON and R forms, and the stable Y polymorph were formed within the same STF consisting of 0.100 toluene, 0.525 isopropyl alcohol and 0.375 water mass fractions (Figure 5.4), while only the stable Y form was obtained in the binary 0.475 toluene and 0.525 isopropanol mass fraction system at this same supersaturation level. This is noteworthy because the YN polymorph was not reported until five years after the Y, ON and R forms,[208,209] whereas here it appeared at the first attempt.
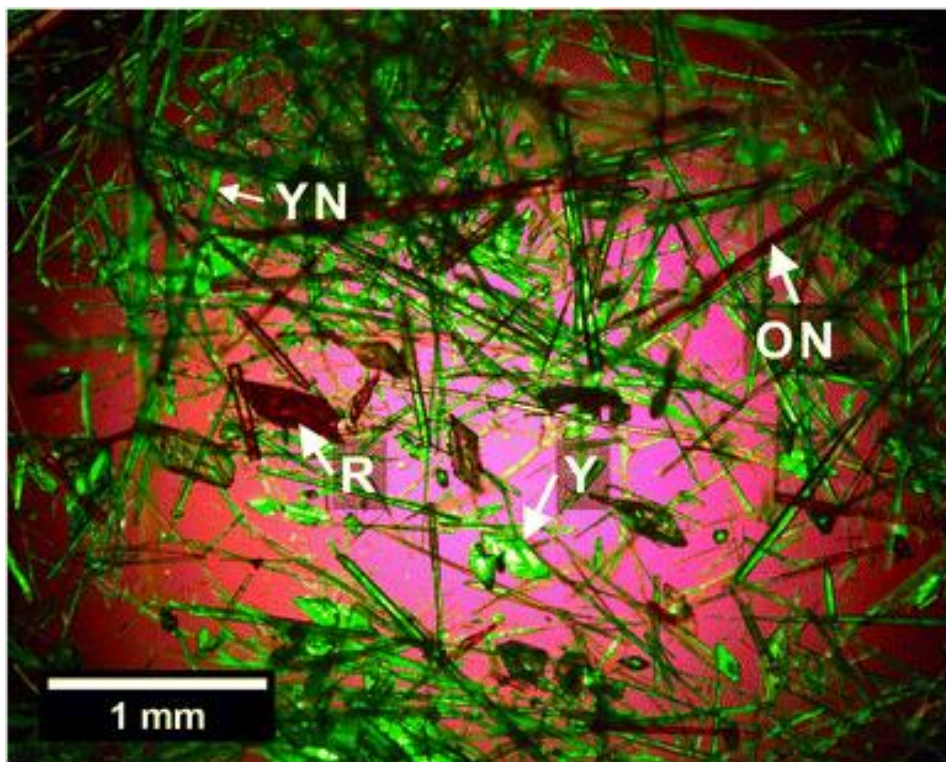
Figure 5.4: Optical micrograph showing four polymorphs of ROY (YN, ON, R and Y, with representative forms arrowed) from the polymorph screening trial on the toluene/isopropanol/water STF.

Subsequent crystallisations within this STF were then able to target a particular metastable form because the YN and ON forms appeared prior to R. Note that the melt-crystallised ROY polymorphs and the most unstable ROY polymorphs (obtained through high throughput methods and the use of specific additives) were not crystallised in this initial STF trial.[216,217,230] To induce their STF crystallisation, these would likely need, for example, switching to a different STF or inclusion of the specific additives. However, due to their instability, such polymorphs would not be suitable drug candidates. Consequently, these trials suggest that STFs can be used to rapidly identify polymorphs suitable for drug marketing by adopting the following strategy: performing a rapid screening test at high supersaturation to crystallise as many forms as possible, followed by an optimisation stage to target each polymorph using specific supersaturation ranges and crystallisation times. There is a growing library of STFs comprising several different oils,[21,43,47,52,57-61] and, whilst water is usually the other immiscible liquid with typically either ethanol or propanol as the amphisolvent, non-aqueous STFs have also been reported.[53,54] This should enable a suitable STF to be rapidly identified for a particular drug given the key requirement that the crystallising compound is soluble in one of the immiscible liquids and virtually insoluble in the other. Hence, the method should be generally applicable.

5.2.2 Quartz Crystallisation Studies

As a promising system in gaining thermodynamic control over the crystallisation of glycine in Chapter 3, a water/octanol/ethanol STF with mass fractions of 0.15/0.50/0.35, respectively, was chosen in an attempt to crystallise nanoquartz. Initially, the stability of the STF was tested using an aqueous phase ranging from 1.25 – 25 wt.% SMS solution. It was found that at concentrations above 5 wt.% SMS, the STF phase separated, presumably due to the increased presence of Na^+ ions, which are known to induce the salting out effect described by Marcus *et al.*[26] Consequently, a solution of 2.5 wt% SMS in water was chosen to scale up. This ensured that the STF would not be close to phase separation, but also, importantly, it would not be supersaturated with respect to amorphous silica and so wouldn't precipitate amorphous silica. In this way, it would mirror a setup that was successfully used to

synthesise nanoquartz in the surfactant microemulsion studies undertaken by Buckley *et al.*.[110] TEM images showing the nanocrystalline product are given in Figure 5.5.
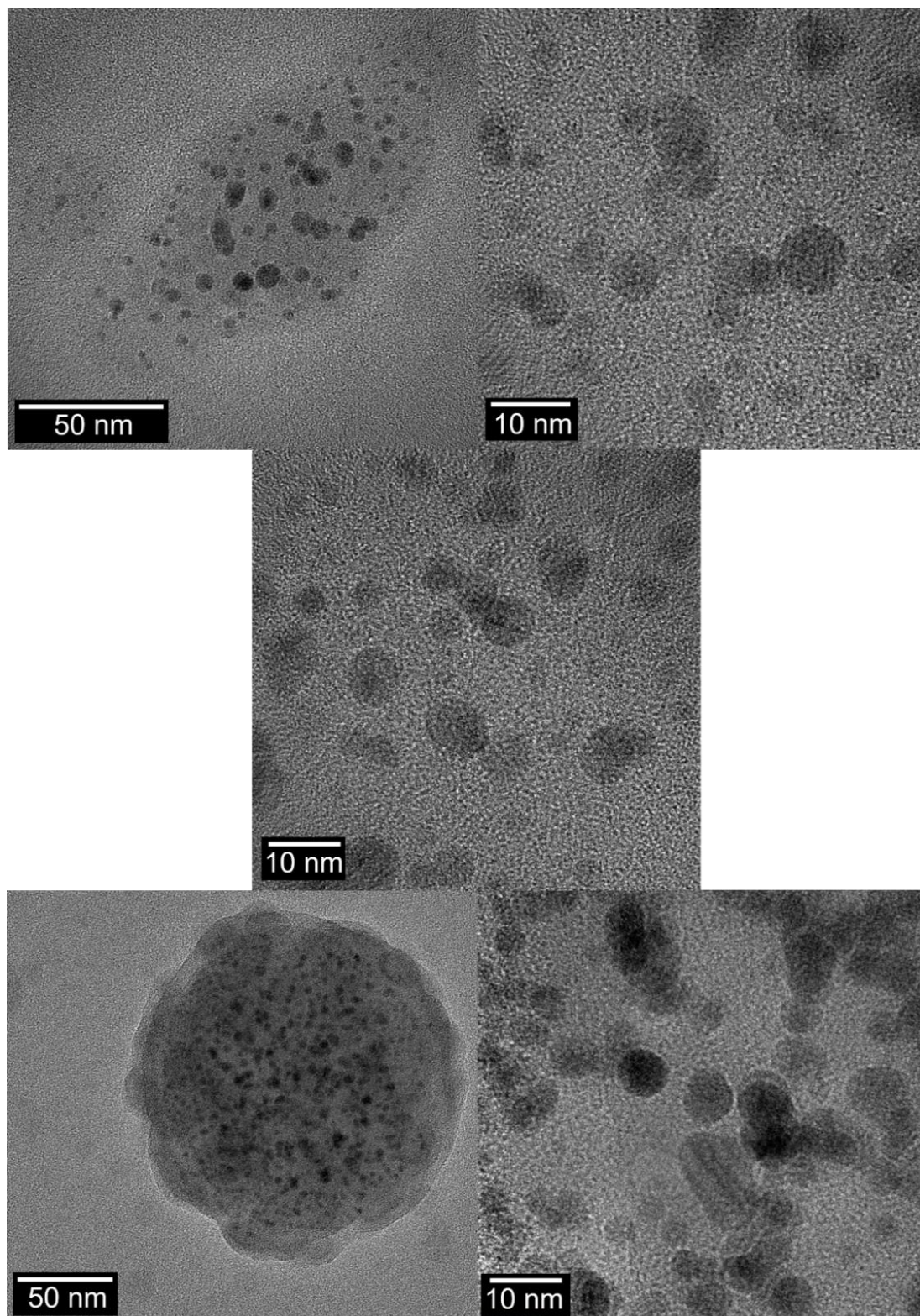
Figure 5.5: TEM images revealing crystalline silica nanoparticles from an STF comprised of 0.15, 0.35 and 0.50 mass fractions of water, ethanol and octanol, respectively.

A representative EDX spectrum of the silica crystals observed is shown in Figure 5.6, whereby, apart from the signals for copper and carbon which are attributed to the holey carbon copper grid, the only peaks observed were for silicon and oxygen, indicating that the crystals contained only silica, and no other impurities.
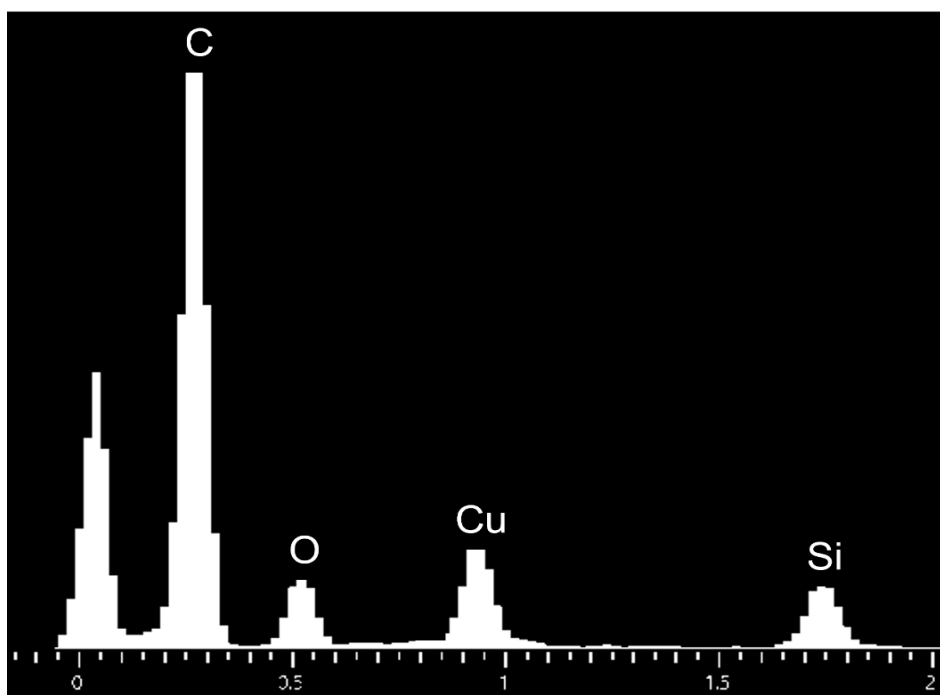
Figure 5.6: Representative EDX spectrum of a nanocrystal from the images displayed in Figure 5.5.

The diameter of 126 of the spherical crystals observed were measured and the results summarised in Figure 5.7. This shows a range from 2.1 – 9.0 nm with a mean crystal diameter of 5.1 nm. The polydispersity (PD) in this sample was 0.47. Typically, a PD value of <0.05 is regarded as a monodisperse sample, whereas a PD value of >0.7 is regarded as a broad, or polydisperse, distribution of particle sizes.[231] Consequently, the nanoquartz crystals synthesised in the STF cannot be considered monodisperse, though the polydispersity is likely to have been exasperated by the excessively long timescale available for crystal growth and Ostwald's ripening. The nm-size range indicates that this methodology can control the particle size to this length scale, likely due to the similar dimensions of the aqueous nano-domains present in the STF formulations, as well as the faster nucleation rate compared to slow growth rate observed in these systems.
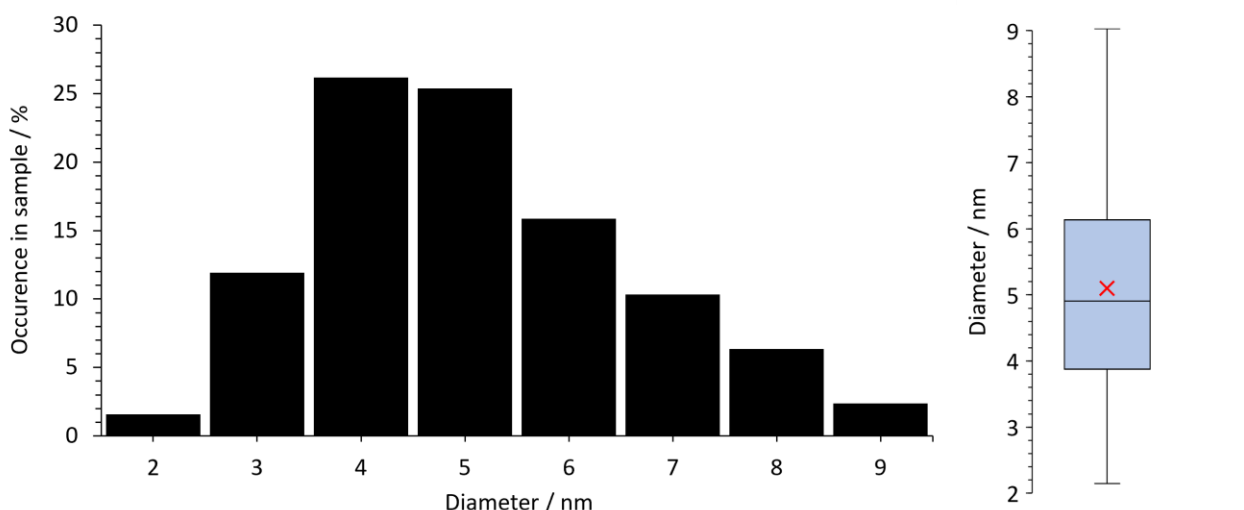
Figure 5.7: Size distribution of a sample of 126 nanocrystals observed using TEM.

FFT was performed on the TEM images recorded in Figure 5.5 to elucidate diffraction patterns that could be indexed (Figure 5.8). Analysis of these diffraction patterns revealed lattice parameters that are consistent with the ⟨212⟩ zone axes of α-quartz (Table 5.3 and Table 5.4). It should be noted that some measured d-spacings were slightly larger than those of bulk α-quartz, but align near-identically with the findings of Buckley *et al.*. It was posited that these deviations in the diffraction spacings were likely due to a perturbed α-quartz structure and surface defects, which become more significant when crystals are nm-sized compared to in bulk material due to their large surface-area-to-volume ratio.[110] The ⟨212⟩ zone axes revealed by the FFT are also the dominant zone axes observed in the microemulsion nanoquartz synthesis, where these zones were rationalised as occurring due to the quartz nanocrystals lying on, or close to, the low energy rhombohedral {101} faces. The {101} faces have a large proportion of Q3 Si–OH silanol surface sites, i.e. a silicon atom bonded to three bridging oxygen atoms and one Si–OH surface bond, rather than Q2 Si–(OH)2 sites. This aids their thermodynamic stability and so is consistent with the proposed model of the crystallisation occurring under thermodynamic control.[110] Due to the similarities in the microemulsion and STF methodologies, it follows that this is the likely cause of the deviations observed in the results summarised in Table 5.4.
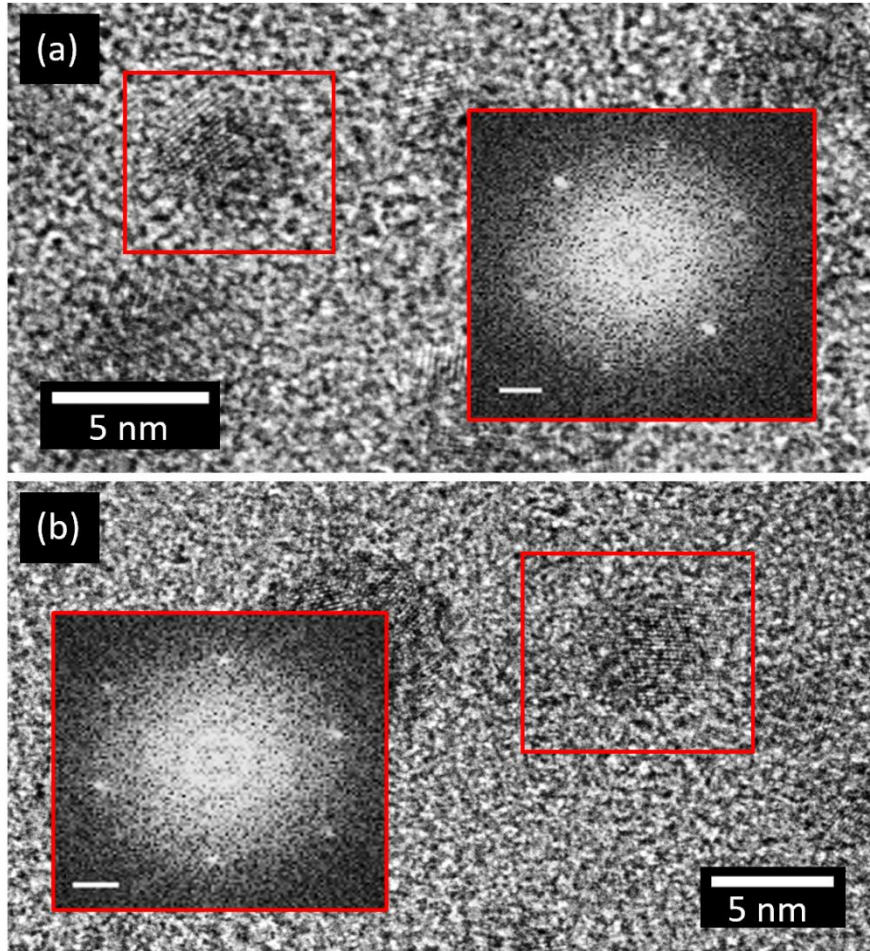
Figure 5.8: HREM images of ~5 nm α-quartz nanocrystals, with insets showing the FFT of the highlighted region. Inset scales bars represent 2 nm⁻¹.

Table 5.3: Assignments of crystal planes in the ⟨212⟩ zone axes of quartz.[110]

Zone axis	d-spacing / nm			Angle / °		
	$\{02\bar{1}\}$	$\{\bar{2}21\}$	$\{\bar{2}02\}$	$\{02\bar{1}\} - \{\bar{2}21\}$	$\{\bar{2}21\} - \{\bar{2}02\}$	$\{02\bar{1}\} - \{\bar{2}02\}$
⟨212⟩	0.198	0.198	0.167	72.6	53.7	53.7

Table 5.4: Diffraction spacings and angles of crystal planes measured from FFTs in Figure 5.8.

Figure	d-spacing / nm			Angle / °		
	$\{02\bar{1}\}$	$\{\bar{2}21\}$	$\{\bar{2}02\}$	$\{02\bar{1}\} - \{\bar{2}21\}$	$\{\bar{2}21\} - \{\bar{2}02\}$	$\{02\bar{1}\} - \{\bar{2}02\}$
5.9(a)	0.201	0.197	0.171	72.7	53.8	53.6
5.9(b)	0.198	0.198	0.171	72.6	53.6	53.7

Under ambient temperature and pressure, amorphous silica will usually precipitate from bulk aqueous solution.[232,233] Crystalline silica polymorphs typically only nucleate and grow under hydrothermal or

solvothermal conditions.[225,234,235] Currently, only the surfactant microemulsion method, which used a system of Span80 and Brij30 surfactants, alongside sodium metasilicate solution (<10 wt%) and heptane, has been successful in achieving the primary nucleation of quartz under ambient conditions.[110] Though the yield in the STF was exceedingly low, TEM images show evidence of $2-9$ nm sized nanoquartz crystals suspended in the STF. This provides additional evidence of the thermodynamic control achieved for glycine reported in Chapter 3 and strengthens the analogy between STF and surfactant microemulsions in being able to promote the crystallisation of both organic and inorganic nanomaterials.

5.3 CONCLUSIONS

In summary, through the crystallisation of ROY and α-quartz, this work shows the potential ubiquity of STFs for polymorphic control.

Using ROY, a highly polymorphic organic material, this work demonstrates the polymorph screening capability of an STF comprised of toluene, isopropanol and water. Polymorphic screening ability was previously shown in Chapter 4 using an STF of water, octanol and ethanol, with all three ambient temperature polymorphs of glycine being selectively targeted in a single composition, by tuning the supersaturation of the system. Here, the four clinically relevant polymorphs of ROY were crystallised concomitantly in a single STF formulation (Figure 5.4), again through tuning the supersaturation of the solute. This demonstrates that STFs may be a powerful tool in the polymorph screening of drug candidates. A relevant STF at high supersaturation could be used to crystallise as many polymorphs as possible, and then the supersaturation, crystallisation time, and STF composition may be altered to target specific forms. This work also demonstrates that this is not only valid for water confined domains in an STF of water, octanol and ethanol, but can be extended to any STF in which the crystallising solute is confined to one of the two immiscible phases, in this case, toluene.

Furthermore, through the crystallisation of $2-9$ nm sized quartz in the water, octanol, ethanol STF that has been the primary focus of this PhD work, the proposed mechanism of thermodynamic control

and the analogy to surfactant systems has been strengthened. This STF system was used in Chapter 3 to produce crystallisation of γ-glycine, the most stable glycine polymorph, revealing that despite the less rigid and more dynamic nature of the confined domains in STFs compared to surfactant microemulsions, thermodynamic control of crystallisation is still possible. While the yield of nanoquartz in this same STF was low, and could only be identified through TEM analysis, its presence is significant. α-quartz crystals have a giant lattice structure, comprised of covalently bonded SiO_2 tetrahedra (Figure 5.2). This differs from organic molecules, such as glycine and ROY, where polymorphism typically arises through variations in weaker intermolecular interactions such as hydrogen bonding and π-stacking, which are much more easily overcome than the covalent bonds. As a result, nanoquartz typically only nucleates under hydrothermal or solvothermal conditions, and has only been successfully nucleated under ambient conditions using surfactant microemulsions to elicit thermodynamic control.[110] Now, this has been achieved again using an STF system of 15/50/35 wt.% water/octanol/ethanol, respectively. This means that the same STF may be applied ubiquitously to nucleate the thermodynamically stable polymorph of a wide array of materials, ranging from simple organic molecules such as γ-glycine, to large inorganic materials such as α-quartz.

6 COMPUTATIONAL STUDIES

6.1 INTRODUCTION

Molecular dynamics (MD) was first used in the late 1950s to investigate the dynamics of liquids by Alder and Wainright, and later by Rahman in 1964.[236-241] Since, the use of MD has become widespread for simulating complex systems at the atomic scale. Through Newton's laws of motion, the time evolution of a system may be simulated, and kinetic and thermodynamic properties may be extracted.[236]

The MD simulations performed by Schöttl *et al.* of the water-octanol-ethanol STFs were successful in helping to elucidate a phase diagram for the system (Figure 1.8) and model the nanostructuring present (Figure 1.9).[28,242] While some research has been performed to investigate the impact of additives to this system, glycine has not been specifically considered. It has been observed that adding salts to the STF can either increase or decrease the size of the nanostructures by altering the interfacial ethanol-rich regions. In the former case, a salting out effect is observed, driving ethanol molecules to the interface, or into the octanol-rich phase. This would increase the size of the nanostructures, pushing the system closer towards phase separation. In the latter case, the antagonistic ion effect may occur, charging the interface which leads to an electrostatic repulsion effect, decreasing the size of the nanostructures and pushing the system towards a more highly mixed, molecular solution.[26]

To ensure that glycine does not significantly interfere with the nanostructures predicted by Marcus *et al.*,[26] experimental studies were performed as discussed in Chapters 3 and 4. It was observed that at high concentrations of glycine ($\frac{c}{c_{sat}}$ > 2.2), the STFs began to cloud and phase separate. This could be due to the increases in temperature, required to dissolve higher glycine concentrations, evaporating some of the more volatile ethanol component and destabilising the nanostructures, though care was taken to seal all systems during any crystallisation experiments. This could indicate that a salting-out effect does take place within the system, or else a combination of both factors. Experimentally, below

$\frac{c}{c_{sat}}$ = 2.2, any such effect seemed to have little impact on the outcome of the crystallisations. Polymorphic control was demonstrated thoroughly in the STFs, indicating the persistence of nanodroplet reactors capable of restricting diffusion of solute, and nucleating even the most thermodynamically stable polymorphs of glycine, silica and ROY.

In response to the COVID-19 pandemic, during which time experimental work could not be completed, computational studies were undertaken to mitigate the impact of the national lockdowns on the work in this thesis. This provided the opportunity to complete some MD simulations to allow the visualisation of these structures, confirm where glycine zwitterions reside, and if they had significant impacts on STF nanostructuring. Finally, diffusion constants were extracted from simulations for STFs containing an ethanol mass fraction of 0.40, to compare to the results recorded in Chapter 4.

6.2 EXPERIMENTAL

6.2.1 Molecular Dynamics

The simulations performed in this work used the Gromacs 2018.3 software package.[243,244] The systems were sampled as cubic boxes with periodic boundary conditions applied in all directions.

6.2.2 System Compilation

Firstly, octanol, ethanol, and glycine molecules were randomly inserted into cubic boxes with 10 − 11 nm edge lengths. The boxes were then solvated with water. The STF system used contained 2241, 4434, and 4859 molecules of octanol, ethanol, and water, respectively, with 0–20 glycine molecules depending on the simulation. Table 6.1 summarises the calculations used to determine the molecular setup of the systems. The amount of each material was based on a sample used during the synthetic component of this work, and the number of molecules was chosen to establish a total number of atoms of 120,000.

Table 6.1: Summary of a molecular setup for an example system.

	Water	Octanol	Ethanol
Number of atoms per molecule	4	27	9
Percentage (by mass) used in study / %	15	50	35
Molar ratio	0.42	0.19	0.38
Number of molecules	4866	2244	4440
Total number of molecules			11,549
Total number of atoms			120,000

6.2.3   Simulation Parameters

The OPLS all-atom force field[245] was employed for octanol, ethanol, and glycine molecules, with   L-OPLS dihedral potential corrections[246] in place for the octanol molecules to account for the relatively long hydrocarbon chain. Water was described by the TIP4P model,[247] and hence use four atoms in the system setup described in Table 6.1, where the fourth atom represents a virtual site. The energy of each configuration was minimised using a steepest descent algorithm. The simulation box was then equilibrated at a pressure and temperature of 1 bar and 300 K, respectively, for 150 ps with a time step of Δt = 2 fs. Equilibration used the Parrinello-Rahman barostat[248] and a velocity rescaling thermostat with a stochastic term (V-rescale). 21 Electrostatics and van der Waals interactions were described by a Particle Mesh Ewald summation[249] (PME) and a Lennard-Jones potential, respectively, each with a cut-off of 1 nm. Upon convergence, the cubic simulation boxes had edge lengths of approximately 10.6 nm. The production runs maintained identical simulation parameters; however, systems were sampled for 10 ns.

6.3   Results and Discussion

To visualise how glycine behaves when added to an STF a cubic simulation box with approximately 10.6 nm edge lengths was set up containing octanol, ethanol, water, and glycine in the composition outlined in Table 6.1. This composition was chosen to represent an STF with the most restricted

diffusion, and consequently the highest degree of nanoconfinement through NMR diffusiometry when assessing thermodynamic control in Chapter 3 (Figure 3.9). Snapshots generated from the MD trajectories are displayed in Figure 6.1. Here, partitioning and micro-structuring is clearly visible between the three components of the STF. Octanol, represented by the purple molecules, form into large, continuous structures, bordered predominantly by ethanol molecules (light blue). Then, within the ethanolic regions, the water molecules (dark blue) can be seen to form clusters in which the glycine molecules (yellow) are confined. This corroborates the theory that the crystallisation process behaves analogously to a surfactant-based microemulsion, whereby the glycine molecules are confined into aqueous pockets.
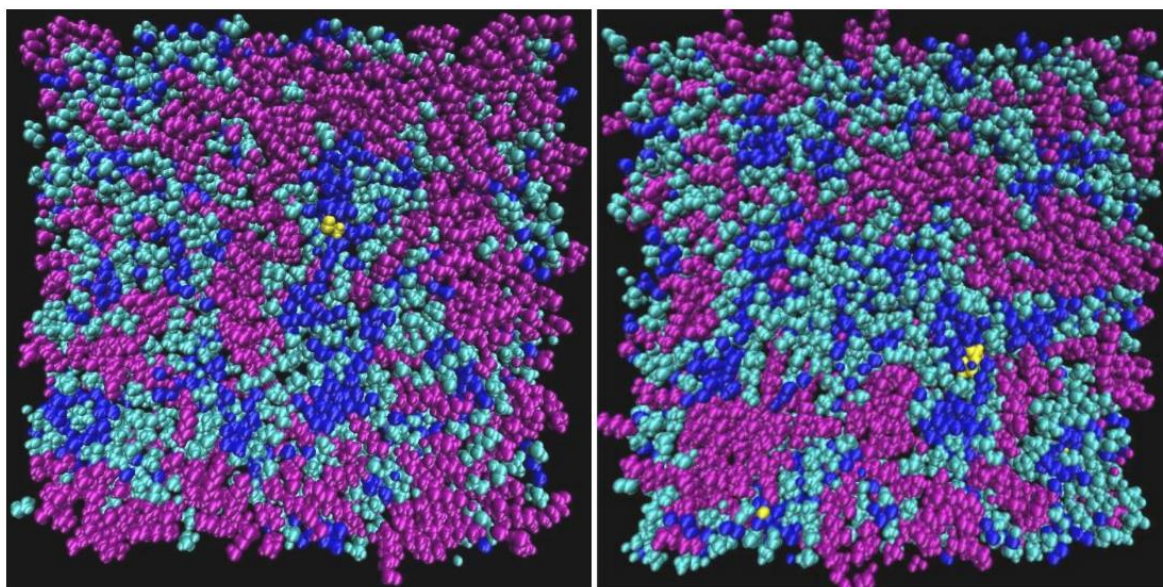
Figure 6.1: Snapshots of 1 nm thick slices taken from an STF simulation box containing octanol, ethanol, water and glycine – coloured purple, light blue, dark blue, and yellow, respectively.

In pure water, solute molecules may diffuse freely as shown by the highlighted trajectory in Figure 6.2. As there would be nothing other than supersaturation to limit the glycine crystallisation, the polymorph with the lowest free energy barrier will form first, persist, and grow (Figure 1.22(a)). This is kinetic control over crystallisation.
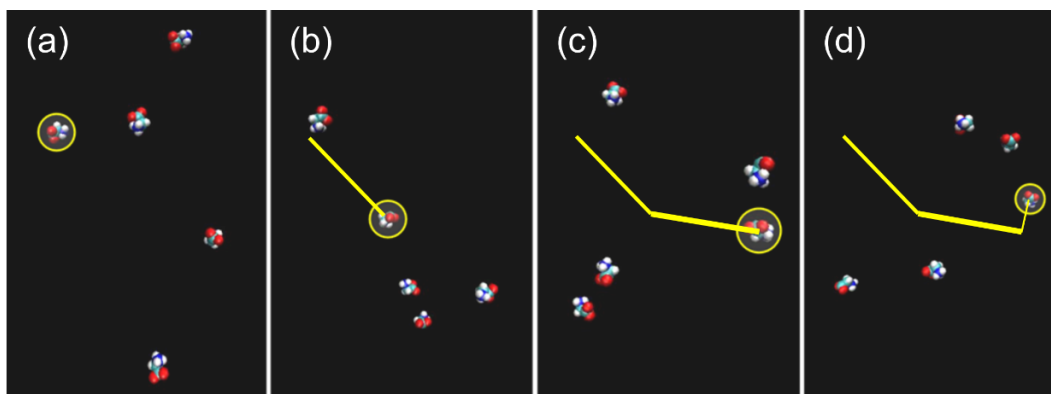
Figure 6.2: Snapshots from a simulation for bulk diffusion of glycine in water. (a), (b), (c), and (d) were captured after 0 ns, 0.5 ns, 1.0 ns, and 1.5 ns, respectively. A molecule has been highlighted to show its trajectory.

Unlike glycine in water, diffusion in STFs is restricted by confinement in aqueous pockets as shown by the highlighted trajectory in Figure 6.3 for a simulation of a comparable box size and duration with the same composition as seen in Table 6.1. Molecules may move freely within the aqueous pockets, or else may only pass to another pocket as they merge and break apart. Consequently, thermodynamic control may be achieved over crystallisation. If this were the case, then only the most stable polymorphs may persist long enough in the confined phase without dissolving back into solution before they can contact other solute molecules and grow.

Figure 6.3: Snapshots from a simulation displaying diffusion in an STF containing water, octanol and ethanol mass fractions of 0.15, 0.50 and 0.35, respectively. (a), (b), and (c) were captured after 0 ns, 1 ns, and 2 ns, respectively. A molecule has been highlighted to show its trajectory.

Figure 6.2 and Figure 6.3 demonstrate qualitatively how glycine molecules may be restricted by the nanostructuring present in an STF system. In order to make a more quantitative assessment, the computed diffusion coefficients of the glycine molecules were extracted from the trajectory files produced from the simulations. Figure 6.4 demonstrates how the diffusion constant of glycine varied

with water mass fraction in simulated STFs containing a constant ethanol mass fraction of 0.4, to mirror the tests performed in Chapter 4.
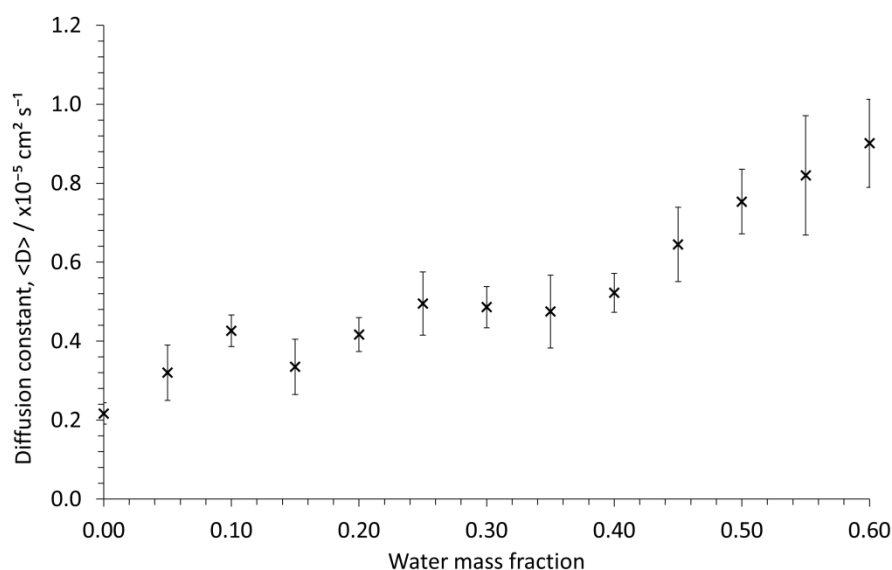
Figure 6.4: Diffusion constant of glycine zwitterions in STFs containing a constant mass fraction of 0.40 ethanol extracted from molecular dynamics simulation.

Firstly, it can be observed that there is a decrease in diffusion with decreasing water content. This mirrors the qualitative snapshots recorded. Additionally, this decrease is not linear, but there appears to be three regions, with transitions at water mass fractions (m_w) of 0.10 and 0.40. This closely follows the results of the experimental conductivity measurements taken for the same STF systems (Figure 4.6). Here, it was justified that below m_w = 0.10 aqueous nanodroplets began forming, increasing in number, allowing mobility, albeit restricted to the aqueous domains. Between m_w = 0.10 and m_w = 0.40, conductivity increased at a reduced rate, indicating the existing aqueous nanodomains swelling in volume. Then, when above m_w = 0.40, the diffusion increased rapidly, suggesting a drastic change in behaviour, where glycine is no longer restricted to confined nanodroplets, but instead is contained in the growing continuous water phase of the o/w microemulsion-like systems.

The diffusion constants extracted computationally cannot be directly compared to those determined experimentally as the computationally derived constants are roughly 10^4 orders of magnitude larger. This difference may be affected by the size of the simulation box which contained only 1.2 x 10^5 atoms. To place this in context, just 1 cm³ of water contains approximately 1 x 10^{23} atoms. Within

this, there were only 10 molecules of glycine, and by scaling up, the average diffusion of each glycine molecule would have a smaller uncertainty. However, for these initial experiments, the computational expense of modelling a more realistically sized system would have been unfeasibly high. More likely, this difference reflects the timescale of the simulation and the model used to simulate the glycine molecules. The simulations were run for 10 ns, which is 3.5×10^{12} times faster than the shortest experiment by NMR diffusiometry. Over longer timescales, molecules may travel further, and the impact of boundaries may be considered more effectively. If not given enough time, diffusing molecules may not encounter a boundary, and diffusion will appear less restricted. In this study, the simulation parameters were selected to imitate the simulations undertaken by Schöttl *et al.*[28,242] to model the behaviour of the water, octanol and ethanol STFs. This study did not consider however, the behaviour of glycine as a solute in such systems. In solution, glycine will exist in its zwitterionic form. The OPLS all-atom force field[245,246] was chosen for glycine to align with the parameters chosen for the octanol and ethanol molecules. Nonetheless, there are numerous models[250-255] that aim to model the glycine zwitterion and predict the crystallisation behaviour of glycine in solution, which give different atomic partial charges, and therefore it is unclear which most accurately account for the zwitterionic nature of glycine. It would therefore be prudent to investigate which glycine model would be most effective in modelling crystallisation dynamics in STFs.

Despite the difficulty in comparing the computational and experimental absolute diffusion constants, D, by using the viscosity of each system determined experimentally, the relative $D\eta$ values (as calculated in chapters 2 and 3) could be directly compared. This is because it is no longer the absolute values that are concerning, but the trends in the values compared to that of the unconfined system recorded using the same methodology. Therefore, both sets of data can be transformed to an arbitrary scale between $0 - 1$ in order to compare the trends in diffusion (Figure 6.5).
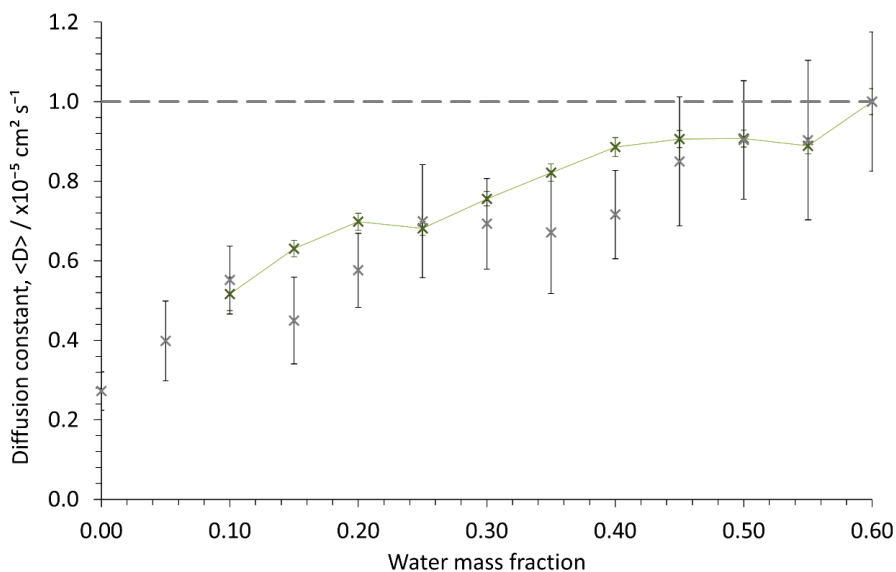
Figure 6.5: Relative Dη values (compared with the binary ethanol/water system) derived from computational methods (black) and experimental methods (green) for glycine in STF mixtures containing a constant ethanol mass fraction of 0.40.

Here, a similar decrease in the relative $D\eta$ for glycine with decreasing water content was observed, where only three of the twelve data points that can compared lie outside of the calculated uncertainty. It should be noted that the computationally calculated data points have a larger uncertainty than those calculated through NMR diffusiometry. This is due to the size and duration of the simulation, in which the diffusion constant was recorded for 10 glycine molecules over 10 ns. Ideally, this should be repeated with larger simulation boxes and for longer durations, though this was not feasible through this early study.

Overall, even with the lack of model optimisation for the glycine zwitterions, the OPLS all-atom force field was sufficient in modelling the degree of restricted diffusion in the STFs. This is likely due to glycine confinement being an outcome of fluid structuring rather than the glycine itself, and more significant complications may arise when attempting to model crystallisation, because this depends on the intermolecular interactions between the glycine molecules.

6.3.1 Crystallisation in STFs

Figure 6.6 shows snapshots from an MD simulation, where the glycine molecules have been isolated for clarity. Here, two molecules diffuse together, bind, and therefore may lead to a nucleation event (Figure 6.6(a)). Subsequently, the molecules continue to rearrange and break apart, eventually

diffusing away from each other. If the glycine molecules can break apart during crystallisation, then thermodynamic control can theoretically be achieved. This is because the metastable crystals may dissolve and recrystallise until the most stable polymorph forms and persists. This directly corroborates the experimental findings in Chapter 3 whereby γ-glycine was selectively nucleated in STFs in which glycine diffusion was restricted.
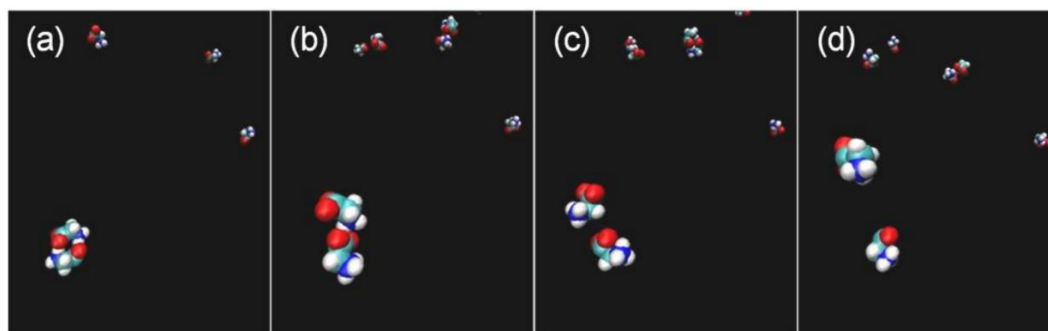
Figure 6.6: Snapshots from a simulation of an STF containing water, octanol and ethanol mass fractions of 0.15, 0.50 and 0.35, respectively. This displays a crystallising structure breaking apart. (a), (b), (c), and (d) were captured after 4.3 ns, 4.9 ns, 5.1 ns, and 5.5 ns, respectively.

By increasing the concentration of glycine within the simulation box, the supersaturation level may be increased. Therefore, the system can be altered from one that will not crystallise, i.e. it is stabilised due to nanoconfinement, to one in which the largest and most supersaturated droplets can form (near) stable nuclei. This is because the most stable polymorph typically has the lowest solubility and, therefore, compared with other polymorphs, can grow into larger nuclei, r_{min}^*, prior to the depletion of supersaturation. Moving further, the system will crystallise under kinetic control as, like in bulk systems, it becomes the lowest free energy barrier that determines the polymorphic outcome. This can be seen in Figure 6.6 – Figure 6.8 depicting systems containing 10, 5, and 20 molecules of glycine, respectively. In Figure 6.7, the glycine molecules stay spatially separated in the confined domains whereas in Figure 6.8, the glycine molecules aggregate quickly and irreversibly over 10 ns.
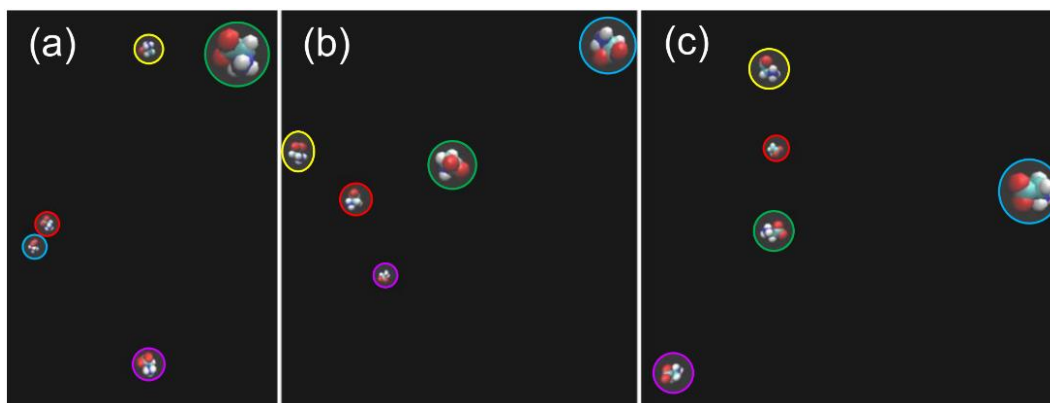
Figure 6.7: Snapshots from a simulation of an STF containing water, octanol and ethanol mass fractions of 0.15, 0.50 and 0.35, respectively. This demonstrates a non-crystallising solution. (a), (b), and (c) were captured after 0 ns, 5 ns, and 10 ns, respectively. Molecules have been highlighted to follow their trajectory.
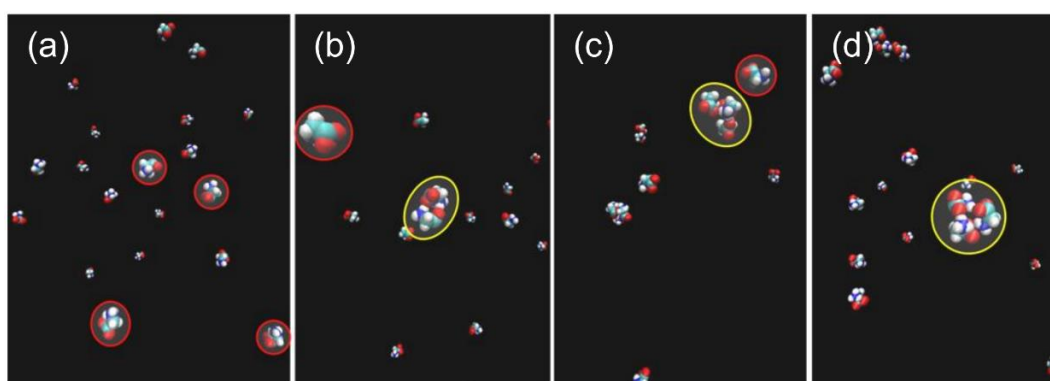
Figure 6.8: Snapshots from a simulation of an STF containing water, octanol and ethanol mass fractions of 0.15, 0.50 and 0.35, respectively. This demonstrates a crystallising solution. (a), (b), (c), and (d) were captured after 0 ns, 0.8 ns, 3.2 ns, and 8.7 ns, respectively. Molecules have been highlighted to follow their trajectory, where yellow and red represent the aggregated and free molecules of interest, respectively.

While it is not possible to accurately assess the polymorphic outcome of this early nucleation due to the lack of model optimisation for the glycine zwitterions, the clustering of individual glycine molecules is evident. It would be of interest in future work to assess the behaviour of these larger clusters (Figure 6.8(d)) over longer periods, to gauge whether they persist, grow, or dissolve back into solution by breaking apart. It would also be useful to assess the behaviour of the aqueous nanodomains as the clusters grow. This would determine if the additional size of the glycine structures affects the hydration of the water around the molecules and has any impact on the size of the water domains in the corresponding STF.

6.4 CONCLUSIONS

In summary, simulations were designed that would model STF formulations containing an ethanol mass fraction of 0.40, described experimentally in Chapter 4. The simulation parameters were chosen to mirror those of Schöttl *et al.,*[28,242] who first showed evidence of the nanostructuring found in an STF system containing water, octanol and ethanol. Additionally to the fluids, glycine molecules were added to the simulation boxes and simulations were run to assess their behaviour. It was found that the glycine did indeed reside in the aqueous nanodomains found in the STF, and were excluded from the continuous octanol phase, as indicated in the experimental work. Furthermore, the diffusion constant of glycine could be extracted from the trajectory output of the simulations, which showed similar trends to those seen experimentally. The relative $D\eta$ value calculated from both simulation and experiment showed a decrease of comparable magnitude with decrease in water content, suggesting that the simulation was successful in modelling the degree of restricted diffusion. Despite this, the simulations did not produce absolute diffusion constant values that correlated well to the experimental values. This has been attributed to both the vast difference in sample size, the length of time over which the molecules were allowed to diffuse, and the lack of optimisation of the model used for glycine zwitterions.

The computational work described in this chapter was primarily performed as a response to the COVID-19 pandemic, whereby access to laboratories was limited, and at times altogether restricted. Despite this, the computational studies performed in this chapter did show promising indication of the glycine confinement effects that have been observed experimentally. While the studies were not extensive, this will provide a good starting point for future exploration into the theoretical understanding of crystallisation in STF formulations.

7 CONCLUSIONS AND FUTURE WORK

7.1 CONCLUSIONS

Crystallisation is a process that is exploited widely in industry and in nature. As such, the ability to control the outcome of crystallisation is of great interest. This thesis aimed to assess the ability of STFs to replace surfactant microemulsions in tailoring the polymorphic outcome of crystallisation.

STFs are sometimes known as surfactant-free, or ultra-flexible microemulsions, as they can contain structuring similar to that of surfactant-based microemulsions. They are complex mixtures of two immiscible fluids and a hydrotrope, capable of solubilising both other phases equally. The hydrotrope uses this balanced solubility to accumulate into diffuse boundaries between the immiscible domains as it has an equal affinity for both.

Surfactant microemulsions have proven to be effective systems to nucleate the most stable polymorphs of various organic and inorganic materials. Here, the established mechanism of control is reliant on confining the crystallising solute in the nanostructures within the microemulsions. Due to the analogy of STF nanostructures with that of these traditional microemulsions, it was theorised that the same thermodynamic control of crystallisation may be achieved.

Under ambient conditions, glycine may exist as one of three polymorphs, α-, β-, and γ-glycine, where the order of stability is as follows: γ > α > β. However, while γ-glycine is the most stable, it is difficult to nucleate in aqueous solutions as the α form grows approximately 500 times quicker, and therefore dominates in bulk crystallisations. β-glycine is also difficult to grow, as it is so metastable that it will quickly transform to more stable forms in aqueous solution. Glycine was therefore selected as a proof-of-concept polymorphic system, as control must be demonstrated in order to preferentially nucleate and grow each form.

The first aim of this PhD study was to confirm whether or not glycine could be confined to the aqueous regions of an STF comprised of water, octanol and ethanol sufficiently to likely impact and control the crystallisation. To achieve this, UV-vis spectroscopy, conductivity measurement and NMR diffusiometry were used in conjunction. It was found that conductivity measurement was effective in indicating the compositions in which w/o, bicontinuous, and o/w nanostructures were found, and UV-vis spectroscopy could be used to indicate the regions in which thermodynamic control dominated and was lost. However, this only gave information on the structure of the STF. To understand the behaviour of each phase, and how glycine behaved when dissolved in these systems, NMR diffusiometry proved most effective. This showed that glycine remained confined to the aqueous phase, and its diffusion became most restricted when the water mass fraction of the STF was low and therefore the system was in the w/o nanostructured region of the ternary phase diagram (Figure 4.1).

Subsequently, these systems were used to crystallise glycine and the polymorphic outcome was determined. Initially, STFs with a constant water mass fraction of 0.15 were used to gauge the difference between the fluids that displayed w/o nanostructuring and those that behaved as a molecular solution. It was discovered that, as predicted, thermodynamic control was achieved when the glycine was confined within the nanostructured water domains, and was lost in favour of crystallising the kinetic product, α-glycine, when the nanostructuring disappeared.

To take this further, the nanostructured region of the phase diagram was investigated to understand how the different nanostructures impacted the outcome of crystallisation. It was concluded that three behaviours were exhibited at relatively low supersaturation, $\frac{c}{c_{sat}}$ = 1.30. In the w/o and o/w regions of the phase diagram, γ-glycine and α-glycine were grown selectively. In the bicontinuous section, a mixture of the two polymorphs was achieved. When the supersaturation was increased to $\frac{c}{c_{sat}} \geq 1.90$ in an STF with a water mass fraction of 0.25 (in the bicontinuous region), the metastable β-polymorph was selectively targeted. This persisted in solution for approximately 3.5 hours before transforming into α-glycine, which is remarkable compared with bulk solutions where β-glycine only persisted for

30 minutes. This indicated that the nuclei grew more independently from one another than in unstructured solutions, slowing down crystal growth and Ostwald's ripening, and allowing less stable forms that do nucleate to survive, even if there are more stable, faster growing polymorphs elsewhere in other aqueous pockets.

The key to these results was the growth rate evidence in which a high nucleation rate and relatively slow crystal growth was observed in STFs used for crystallisation control. This contrasts with bulk solution where a low nucleation rate and fast crystal growth is typically seen.

In Chapter 5 of this thesis, it was shown that this method is not limited to an STF of water, octanol and ethanol, nor to glycine. The same control was witnessed in the crystallisation of ROY from an STF of toluene, IPA and water, where toluene was the confined phase in which ROY was dissolved. It was found that at high supersaturation of $\frac{c}{c_{sat}} = 5.5$, the four clinically relevant polymorphs of ROY were crystallised concomitantly in a single STF formulation. STFs may therefore be a powerful tool in the polymorph screening of drug candidates. A relevant STF at high supersaturation could be used to crystallise as many polymorphs as possible, and then the supersaturation, crystallisation time, and STF composition may be altered to target specific forms.

Furthermore, it has been demonstrated that inorganic species as well as organic materials, structured through intermolecular hydrogen bonding may be crystallised. Despite low yields, giant covalent α-quartz was also nucleated through confinement of SMS in an STF of water, octanol and ethanol.

Finally, computational studies were undertaken to model the STFs used in the glycine crystallisation studies to observe the morphology of the nanostructures contained within, as well as to confirm the confinement of glycine to the water "pockets", and therefore its exclusion from the octanol domains. This showed agreement with the NMR diffusiometry experiments, though the computational studies were not extensive and had a lack of model optimisation.

The principal conclusion of this work is that STFs may provide a novel route to polymorph screening and crystallisation control in the future. The methodology appears to be ubiquitous and may be applied to other materials outside of those examined in this work.

7.2   FUTURE WORK

In future work, more computational studies on the structures of STFs should be performed. This should focus on different structures across the phase diagram and assess the radial distribution functions of the different components of the STFs, to establish more quantitative results. Furthermore, while some quantitative data have been extracted towards accurately modelling the diffusion of glycine zwitterions within the STF systems, this work relied on experimentally derived viscosity data in the analysis. To take this further, the viscosity of the systems should be derived through simulation and used to calculate appropriate $D\eta$ values, which may then be compared with the experimental results. This may also allow further insight into the experimentally observed viscosity profiles and the deviations from ideality and give a more rigorous evaluation of $D\eta$, as viscosities of individual components may be extracted and used, rather than the viscosity of the entire STF system.

An obstacle encountered in this simulation work was the production of a model suitable for simulating glycine zwitterions in this system. The simulation parameters outlined in Chapter 6 were selected to mirror work done on simulating the empty STFs. However, these were selected in order to simulate uncharged solvents. Nonetheless, there are numerous models[250-255] that aim to model the glycine zwitterion and predict the crystallisation behaviour of glycine in solution, which give different atomic partial charges, and therefore it is unclear which most accurately account for the zwitterionic nature of glycine. It would therefore be prudent to investigate which glycine model would be most effective in modelling crystallisation dynamics in STFs.

To perform any meaningful study into the crystallisation dynamics of glycine, or any other molecule in STFs, there must first be a thorough investigation into optimisation of the model used to describe the components of the system, and specifically of the solute. For glycine, this may first be assessed by

studying the lattice energies of the three polymorphs. This relates to the stability of the polymorphs, which has been well-documented experimentally to be β < α < γ in order of increasing stability. If this result can be achieved computationally by tuning the glycine force field parameters, further behaviours in solution such as diffusion coefficients may then be assessed and compared to experimental results to corroborate the model. Once an adequate glycine model has been produced, simulations should be re-run to more accurately describe the systems, expanding the scope to more of the phase diagram to widen our understanding. Furthermore, the dynamics of glycine crystallisation in STFs may be investigated, studying not only the clustering dynamics of glycine zwitterions to form crystal nuclei, but also to assess the polymorphic outcome of the resulting nuclei. This will provide more meaningful comparisons to the experimental results collected, which can be used to assess the impact of different STF nanostructures, as well as supersaturation, on the polymorphic outcomes.

These future studies should initially be directed at glycine crystallisation as a proof of concept to complement the work achieved in this thesis. However, from there, the theory may be applied to ROY, silica, or any other desirable crystalline material, as well as to simulate other STF systems, particularly those with less extensive characterisation in the literature compared with the water/octanol/ethanol system focussed on in this work.

Aside from the computational studies describe in this chapter, more work should be directed towards different STF systems, and different crystalline materials. While ROY and quartz were both successfully investigated, results were not extensive, and further investigations should be completed.

For ROY, a better understanding of the applicability of STFs in polymorph screening could be examined. For example, it would be of use to know if the ability to obtain different polymorphs in the same STF is limited to a narrow window of supersaturations. It would also be of interest to investigate the effect of experimental scale on the outcomes, as to be industrially applicable, the experiments would require scaling up from the 20 – 100 g investigations used in this work. It was found that for the glycine studies, scaling down below 100 g, the same high degree of polymorphic control was not

achieved. This was believed to be caused by wetting of the glass container surfaces, disrupting the nanostructuring at the solution-glass interfaces. This issue was exacerbated as the surface area-to-volume ratio of the solutions increased for smaller STF volumes in smaller containers. Consequently, industrial-sized scale ups should increase, rather than decrease, the polymorphic control exercised by the STFs used in this work. Furthermore, more rigorous characterisation studies on ROY in the STF of water, toluene and isopropanol should be performed, including UV-vis and conductivity measurements, as well as NMR diffusiometry to confirm the extent of restricted diffusion.

For quartz, the timescale over which nanoquartz could be nucleated should be investigated. These studies have shown that nanoquartz had been nucleated from the STF solution, but it is unlikely that it took the entire 2.5 years of growth time to achieve this. Indeed, for surfactant microemulsions, formation of nanoquartz was first shown after only two days. Additionally, no nanoquartz could be sedimented and then extracted from the STF solutions; it could only be detected in very limited quantities by TEM analysis from STF aliquots placed directly on the TEM grids. Investigations should be performed to try to extract solid nanoquartz from the STFs so further corroborating analysis, such as Si^{29} solid-state NMR and powder XRD, may be undertaken. This will likely involve scaling up the synthesis, using non-glass containers to reduce the wetting effects on the STF to increase the efficiency of the STF at smaller volumes, or experimenting with the precursor material. If the concentration of SMS was increased, this would theoretically increase the amount of potential product, though care would need to be taken not to encourage the formation of amorphous phases. Alternatives to SMS may also be investigated, as the SMS used in these investigations had a purity of only 98.5 wt.%. For example, fumed silica may be dissolved in basic conditions, and used in these systems as a comparison, to rule out any impact of other impurities in the system. It should be noted here that care was taken to remove impurities through centrifugation of the SMS solutions at 9000 rpm for 10 minutes prior to their use.

7.3 FINAL REMARKS

This thesis has presented a novel synthetic method for the crystallisation of organic and inorganic materials using structured ternary fluids as nanocrystal incubators. They can either be used to grow crystals to larger dimensions, or on the nanoscale where they may be used to seed larger bulk syntheses without the need to first extract the nanocrystals or mill larger crystals to use as seeds. Through this process, it has been demonstrated that both stable and metastable polymorphs may be selectively targeted by simply tuning the composition and/or supersaturation of the system.

This work should not be limited to the STFs and molecules/zwitterions herein described. As demonstrated in Chapter 5, this methodology should be ubiquitous, where the following conditions can be met:

1. The precursor solute is soluble only in one of the immiscible phases of the STF.

2. The STF can contain nanostructures that restrict the diffusion of the solute by more than 25% compared to an unconfined system.

Furthermore, if an STF can be identified as a suitable candidate for a target material, simple UV-vis and conductivity measurements may be performed as an early and inexpensive indication of the system's potential, followed by more rigorous NMR diffusiometry. If the above conditions are met, the system may be tailored through scale, and primarily supersaturation, to achieve polymorph control.

8 REFERENCES

1. T. Tadros, *Surfactants*, Academic Press, London, 1984.

2. M. Kappl H. Butt and K. Graf, *Physics and Chemistry of Interfaces*, John Wiley and Sons, Inc., 2003.

3. R. Nagarajan, *Langmuir*, 18:31-38, 2002.

4. M. Rosen, *Surfactants and Interfacial Phenomena*, John Wiley and Sons, Inc., 2006.

5. A. D. Haymet, N. T. Southall and K. A. Dill, *J. Phys. Chem. B*, 2002, **106(3)**, 521-533.

6. R. Silveston, B. Kronberg, M. Costas, *J. Dispers. Sci.*, 1994, **15(3)**, 333-351.

7. R. Woollam, W. Durnie Y. Zhu and M. L. Free, *Prog. Mater. Sci.*, 2017, **90**, 159-223.

8. E. Ruckenstein and R. Nagarajan, *Langmuir*, 1991, **7**, 2934-2969.

9. T. Tadros, *Emulsions: Formation, Stability, Industrial Applications*. Walter de Gruyter, 2016.

10. J. Sjoblom, *Encyclopedic Handbook of Emulsion Technology*, Marcel Dekker, 2001.

11. T. Cosgrove, *Colloid Science: Principles, Methods and Applications*. John Wiley and Sons, Inc., 2010.

12. P. Voorhees, *J. Stat. Phys.*, 1985, **38**, 231-252.

13. E. Dickinson and D. J. McClements, *Advances in food colloids*, Blackie Academic & Professional, London, 1995.

14. M. R. Patel, R. B. Patel and S. D. Thakore, in *Applications of nanocomposite materials in drug delivery*, Elsevier Woodhead Publishing, Duxford, 2018, pp. 667–700.

15. P. Winsor, *Trans. Faraday Soc.*, 1948, **44**, 376-398.

16. H. Hoffmann and D. Grabner, *Cosmet. Sci. Technol.*, 2017, 471-488.

17. G. D. Smith, C. E. Donelan and R. E. Barden, *J. Colloid Interface Sci.*, 1977, **60**, 488–496.

18. M. Klossek, D. Touraud, T. Zemb and W. Kunz, *ChemPhysChem*, 2012, **13**, 4116-4119.

19. O.Diat, M. Klossek, D. Touraud, B. Deme, I. Grillo, W. Kunz and T. Zemb, *J. Appl. Cryst.*, 2013, **46**, 1665-1669.

20. S. Schöttl, J. Marcus, O. Diat, D. Touraud, W. Kunz, T. Zemb and D. Horinek, *Chem. Sci.*, 2014, **5**, 2949-2954.

21. S. Schöttl and D. Horinek, *Curr. Opin. Colloid. Interface. Sci.*, 2016, **22**, 8-13.

22. T. Zemb, M. Klossek, T. Lopian, J. Marcus, S. Schöttl, D. Horinek, S. Prévost, D. Touraud, O. Diat, S. Marčelja and W. Kunz, *PNAS*, 2016, **113**, 4260-4265.

23. T. Lopian, S. Schöttl, S. Prévost, S. Pellet-Rostaing, D. Horinek, W. Kunz and T. Zemb, *ACS Cent. Sci.,* 2016, **2**, 467-475.

24. S. Prevost, T. Lopian, M. Pleines, O. Diat and T. Zemb, *J. Appl. Cryst.*, 2016, **49**, 2063-2072.

25. S. Prévost, M. Gradzielski and T. Zemb, *Adv. Colloid Interface Sci.*, 2017, **247**, 374-396.

26. J. Marcus, D. Touraud, S. Prévost, O. Diat, T. Zemb and W. Kunz, *Phys. Chem. Chem. Phys.*, 2015, **17**, 32528-32538.

27. S. Prévost, S. Krickl, S. Marčelja, W. Kunz, T. Zemb and I. Grillo, *Langmuir*, 2021, **37**, 3817–3827.

28. S. Schöttl, T. Lopian, S. Prévost, D. Touraud, I. Grillo, O. Diat, T. Zemb and D. Horinek, *J. Colloid Interface Sci.*, 2019, **540**, 623-633.

29. K. Roger, U. Olsson, R. Schweins and B. Cabane, *Angew. Chem. Int. Ed.,* 2015, **54**, 1452-1455.

30. S. A. Vitale and J. L. Katz, *Langmuir*, 2003, **19**, 4105–4110.

31. Y. Zhang, X. Chen and X. Liu., *Langmuir,* 2019, **35**, 14358-14363.

32. A. Lucia, P. G. Argudo, E. Guzmán, R. G. Rubio and F. Ortega, *Colloids Surf. A Physicochem. Eng. Asp.*, 2017, **521**, 133–140.

33. J. Marcus, M. Müller, J. Nistler, D. Touraud and W. Kunz, *Colloids Surf. A Physicochem. Eng. Asp.*, 2014, **458**, 3–9.

34. P. Bošković, V. Sokol, M. Dujmović, M. Gudelj and A. Prkić, *J. Cosmet. Sci.,* 2021, **72(3)**, 292-297.

35. P. Bošković, V. Sokol, D. Touraud, A. Prkić and J. Giljanović, *Acta Chim. Slov.*, 2016, **63**, 138–143.

36. M. Zoumpanioti, M. Karali, A. Xenakis and H. Stamatis., *Enzyme Microb. Technol.,* 2006, **39**, 531-539.

37. Y. L. Khmelnitsky, A. K. Gladilin, I. N. Neverova, A. V. Levashov and K. Martinek, *Collect. Czechoslov. Chem. Commun.*, 1990, **55**, 555–563.

38. N. Pan, S. Liu, Y. Han, D. Li and J. Chai, *J. Materiomics*, 2022, **8**, 781–789.

39. B. A. Keiser, David. Varie, R. E. Barden and S. L. Holt, *J. Phys. Chem.*, 1979, **83**, 1276–1280.

40. G. Lund and S. L. Holt, *J. Am. Oil Chem. Soc.*, 1980, **57**, 264–267.

41. D. Liu, H. Lu, Y. Zhang, P. Zhu and Z. Huang, *Soft Matter*, 2019, **15**, 462–469.

42. J. Xu, A. Yin, J. Zhao, D. Li and W. Hou, *J. Phys. Chem. B*, 2012, **117**, 450–456.

43. Y. Liu, J. Xu, H. Deng, J. Song and W. Hou, *RSC Adv.*, 2018, **8**, 1371–1377.

44. J. Jing, X. Li, Y. Zhang, Y. Liu, H. Lu, J. Wang and Y. Wu, *Langmuir*, 2022, **38**, 7898–7905.

45. X. Cui, J. Wang, X. Zhang, Q. Wang, M. Song and J. Chai, *Langmuir*, 2019, **35**, 9255–9263.

46. J.-D. Wang, Z.-H. Cai, Y.-H. Chang, Y.-Q. Wang, L.-N. Fu, X.-Y. Yan, P.-Q. Zhao, L. Liu, Y.-H. Liu and Y.-J. Fu, *Ind. Crops Prod.*, 2022, **186**, 115216.

47. B. Sun , J. Chai , Z. Chai , X. Zhang , X. Cui and J. Lu , *J. Colloid Interface Sci.*, 2018, **526** , 9 —17.

48. Y. Wu, L. Tang, Q. Zhang, F. Kong and Y. Bi, *Mater. Lett.*, 2021, **285**, 129053.

49. X. Li, H. Lu, L. Wang, S. Dai, B. Wang and Y. Wu, *J. Clean. Prod.*, 2022, **345**, 130990.

50. M. Song, W. Liu, Q. Wang, J. Wang and J. Chai, *J. Ind. Eng. Chem.*, 2020, **83**, 81–89.

51. Y. Wu, J. Jing, X. Li, W. Yue, J. Qi, N. Wang and H. Lu, *Langmuir*, 2023, **39**, 1181–1189.

52. B. S. Mirhoseini and A. Salabat , *J. Mol. Liq.*, 2021, **342**, 117555.

53. Z. Li, Z. Fan and Z. Chen, *Colloids Surf. A Physicochem. Eng. Asp.*, 2022, **649**, 129482.

54. V. Fischer, J. Marcus, D. Touraud, O. Diat and W. Kunz, *J. Colloid Interface Sci.*, 2015, **453**, 186–193.

55. J. Xu, L. Zhang, A. Yin, W. Hou and Y. Yang, *Soft Matter*, 2013, **9**, 6497.

56. J. Xu, L. Zhang, C. Li, T. Zhan and W. Hou, *RSC Adv.*, 2013, **3**, 21494.

57. W. Hou and J. Xu, *Curr. Opin. Colloid Interface Sci.*, 2016, **25**, 67–74.

58. M. E. EL-Hefnawy, *Mod. Appl. Sci.*, 2012, **6**, 101 —105.

59. J. Xu , L. Zhang , D. Li , J. Zhao and W. Hou, *Colloid Polym. Sci.*, 2013, **291**, 2515 —2521.

60. J. Xu , H. Deng , J. Song , J. Zhao , L. Zhang and W. Hou , *J. Colloid Interface Sci.*, 2017, **505**, 816 —823.

61. M. Jehannin , S. Charton , B. Corso , H. Mohwald , H. Riegler and T. Zemb, *Colloid Polym. Sci.*, 2017, **295**, 1817 —1826.

62. J. W. Gibbs, *Am. J. Sci.*, 1878, **s3-16**, 441–458.

63. M. Volmer and A. Weber, *Z. Phys. Chem.*, 1926, **119U**, 277–301.

64. R. Becker and W. Döring, *Ann. Phys.*, 1935, **416**, 719–752.

65. J. Frenkel, *J. Chem. Phys.*, 1939, **7**, 538–547.

66. C. E. Nicholson, C. Chen, B. Mendis and S. J. Cooper, *Cryst. Growth Des.*, 2011, **11**, 363–366.

67. Y.-S. Jun, Y. Zhu, Y. Wang, D. Ghim, X. Wu, D. Kim and H. Jung, *Annu. Rev. Phys. Chem.*, 2022, **73**, 453–477.

68. S. Karthika, T. K. Radhakrishnan and P. Kalaichelvi, *Cryst. Growth Des.*, 2016, **16**, 6663–6681.

69. J. Polte, *CrystEngComm*, 2015, **17**, 6809–6830.

70. S. J. Cooper, C. E. Nicholson and J. Liu, *J. Chem. Phys.*, 2008, **129**.

71. S. Teychené and B. Biscans, *Cryst. Growth Des.*, 2008, **8**, 1133–1139.

72. P. Buckley, *Ph.D. thesis*, Durham University, 2021.

73. P. M. Winkler and P. E. Wagner, *J. Aerosol Sci.*, 2022, **159**, 105875.

74. N. H. Fletcher, *J. Chem. Phys.*, 1958, **29**, 572–576.

75. M. Niederberger and H. Cölfen, *Phys. Chem. Chem. Phys.*, 2006, **8**, 3271–3287.

76. P. R. Wolde and D. Frenkel, *Science*, 1997, **277**, 1975–1978.

77. A. Sauter, F. Roosen-Runge, F. Zhang, G. Lotze, R. M. Jacobs and F. Schreiber, *J. Am. Chem. Soc.*, 2015, **137**, 1485–1491.

78. D. Maes, M. A. Vorontsova, M. A. Potenza, T. Sanvito, M. Sleutel, M. Giglio and P. G. Vekilov, *Acta Crystallogr. F:Struct. Biol.*, 2015, **71**, 815–822.

79. V. J. Anderson and H. N. Lekkerkerker, *Nature*, 2002, **416**, 811–815.

80. T. H. Zhang and X. Y. Liu, *J. Am. Chem. Soc.*, 2007, **129**, 13520–13526.

81. F. Ito, Y. Suzuki, J. Fujimori, T. Sagawa, M. Hara, T. Seki, R. Yasukuni and M. L. Chapelle, *Sci. Rep.*, 2016, **6**.

82. Z. Liao and K. Wynne, *J. Am. Chem. Soc.*, 2022, **144**, 6727–6733.

83. S. Lee, H. S. Wi, W. Jo, Y. C. Cho, H. H. Lee, S.-Y. Jeong, Y.-I. Kim and G. W. Lee, *PNAS*, 2016, **113**, 13618–13623.

84. M. Kaltenegger, S. Hofer, R. Resel, O. Werzer, H. Riegler, J. Simbrunner, C. Winkler, Y. Geerts and J. Liu, *CrystEngComm*, 2022, **24**, 4921–4931.

85. W. Kossel, *Ann. Phys.*, 1934, **413**, 457–480.

86. L. Derdour, E. J. Chan and D. Skliar, *Processes*, 2019, **7**, 611.

87. E. Hadjittofis, M. A. Isbell, V. Karde, S. Varghese, C. Ghoroi and J. Y. Heng, *Pharm. Res.*, 2018, **35**.

88. P. Cubillas and M. W. Anderson, *Zeolites and Catalysis*, 2010, 1–55.

89. D. P. Woodruff, *Philos. Trans. Royal Soc. A*, 2015, **373**, 20140230.

90. M. A. Lovette and M. F. Doherty, *Phys. Rev. E*, 2012, **85**.

91. A. E. Flood, *CrystEngComm*, 2010, **12**, 313–323.

92. M. K. Choudhary, R. Jain and J. D. Rimer, *PNAS*, 2020, **117**, 28632–28639.

93. L. Li and N. Rodríguez-Hornedo, *J. Cryst. Growth*, 1992, **121**, 33–38.

94. F. C. Frank, *Discuss. Faraday Soc.*, 1949, **5**, 48.

95. D. Le Pevelen and G. 95, in *Encyclopedia of Spectroscopy and Spectrometry*, Elsevier, New York, 2016, pp. 750–761.

96. E. H. Lee, *Asian J. Pharm. Sci.,* 2014, **9**(4), 163-175.

97. J. S. Aronhime, S. Sarig and N. Garti, *J. Am. Oil Chem. Soc.*, 1988, **65**, 1144–1150.

98. A. Dupont, M. Guerain, F. Danède, L. Paccou, Y. Guinet, A. Hédoux and J.-F. Willart, *Int. J. Pharm.*, 2020, **590**, 119902.

99. Y. Suwa and M. Inagaki, S. Naka, *J. Mater. Sci.*, 1984, **19**, 1397–1405.

100. E. C. Dybeck, N. S. Abraham, N. P. Schieber and M. R. Shirts, *Cryst. Growth Des.*, 2017, **17**, 1775–1787.

101. Y.-B. Hu, M. Wolthers, D. A. Wolf-Gladrow and G. Nehrke, *Cryst. Growth Des.*, 2015, **15**, 1596–1601.

102. J. Bauer, S. Spanton, R. Henry, J. Quick, W. Dziki, W. Porter and J. Morris, *Pharm. Res.*, 2001, **18**, 859–866.

103. W. A. Ostwald, *Phys. Chem.*, 1897, 289-330.

104. C. Chen, O. Cook, C. E. Nicholson and S. J. Cooper*, Cryst. Growth Des.*, 2011, **11**, 2228–2237.

105. O. Cook, *Ph.D thesis*, Durham University, 2012.

106. C. Chen, *Ph.D. thesis*, Durham University, 2013.

107. C. E. Nicholson and S. J. Cooper, *Crystals*, 2011, **1**, 195–205.

108. C. Chen, C. E. Nicholson, H. E. Ramsey and S. J. Cooper, *Cryst. Growth Des.*, 2015, **15**, 1060–1066.

109. N. J. Hargreaves and S. J. Cooper, *Cryst. Growth Des.*, 2016, **16**, 3133–3142.

110. P. Buckley, N. Hargreaves and S. J. Cooper, *Comm. Chem.*, 2018, **1**, 49.

111. S. Guerin, A. Stapleton, D. Chovan, R. Mouras, M. Gleeson, C. McKeown, M. Noor, C. Silien, F. Rhen, A. Kholkin, N. Liu, T. Soulimane, S. Tofail and D. Thompson, *Nat. Mater.*, 2017, **17(2)**, 180-186.

112. O. Kratky and O. Glatter, *Small angle X-ray scattering*. Academic Press, 1982.

113. K. Trueblood and J. Glusker, *Crystal structure analysis.,* Oxford University Press, 1985.

114. W. L. Bragg, *The diffraction of X-rays by crystals*., Nobel Lecture, 1922.

115. A. Bulakh and H. Wenk, *Minerals: Their constitution and origin*., Cambridge University Press, 2004.

116. A. Botana, J. A. Aguilar, M. Nilsson and G. A. Morris*, J. Magn. Reson*. 2011, **208**, 270-278.

117. D. Wu, A. Chen and C. S. Johnson, *J. Magn. Reson. Ser. A*, 1995, **115**, 260-264.

118. A. Jerschow and N. Müller, *J. Magn. Reson*., 1997, **125**, 372-375.

119. I. Krieger and K. Tanaka, *Pediatr. Res*., 1976, **10**, 25–29.

120. J.-C. Pei, D.-Z. Luo, S.-S. Gau, C.-Y. Chang and W.-S. Lai, *Front. Psychiatry*, 2021, **12**.

121. M. Bannai and N. Kawai, *J. Pharm. Sci*., 2012, **118**, 145–148.

122. Z. Zhong, M. D. Wheeler, X. Li, M. Froh, P. Schemmer, M. Yin, H. Bunzendaul, B. Bradford and J. J. Lemasters, *Curr. Opin. Clin. Nutr. Metab. Care*, 2003, **6**, 229–240.

123. E. Martínez, A. García, A. Saenz, L. Garduño, M. Salazar and G. Chamorro, *Pharm. Biol*., 2003, **41**, 449–453.

124. U. Heresco-Levy, D. C. Javitt, M. Ermilov, C. Mordel, A. Horowitz and D. Kelly, *Br. J. Psychiatry*., 1996, **169**, 610–617.

125. O. Rom, Y. Liu, Z. Liu, Y. Zhao, J. Wu, A. Ghrayeb, L. Villacorta, Y. Fan, L. Chang, L. Wang, C. Liu, D. Yang, J. Song, J. C. Rech, Y. Guo, H. Wang, G. Zhao, W. Liang, Y. Koike, H. Lu, T. Koike, T. Hayek, S. Pennathur, C. Xi, B. Wen, D. Sun, M. T. Garcia-Barrio, M. Aviram, E. Gottlieb, I. Mor, W. Liu, J. Zhang and Y. E. Chen, *Sci. Transl. Med*., 2020, **12**.

126. O. Rom, L. Villacorta, J. Zhang, Y. E. Chen and M. Aviram, *Curr. Opin. Lipidol.*, 2018, **29**, 428–432.

127. D. O. Akinde, *Poult. Sci. J*., 2014, **70**, 575–584.

128. E. Meléndez-Hevia, P. de Paz-Lugo, A. Cornish-Bowden and M. L. Cárdenas, *J. Biosci*., 2009, **34**, 853–872.

129. J. Chen, Y. Yang, Y. Yang, Z. Dai, I. H. Kim, G. Wu and Z. Wu, *J. Nutr*., 2021, **151**, 1769–1778.

130. S. Liu, H. Sun, G. Ma, T. Zhang, L. Wang, H. Pei, X. Li and L. Gao, *Front. Nutr*., 2022, **9**.

131. M. K. Souri, *Open Agric.*, 2016, **1**, 118–123.

132. J. Ohlund and T. Nasholm, *Tree Physiol*., 2001, **21**, 1319–1326.

133. S. Ghasemi, A. H. Khoshgoftarmanesh, M. Afyuni and H. Hadadzadeh, *Eur. J. Agron*., 2013, **45**, 68–74.

134. T. C. Streeter, R. Bol and R. D. Bardgett, *Rapid Commun. Mass Spectrom.*, 2000, **14**, 1351–1355.

135. P. Li and G. Wu, *Amino Acids*, 2017, **50**, 29–38.

136. M. Ashraf and M. R. Foolad, *Environ. Exp. Bot*., 2007, **59**, 206–216.

137. E. E. Benarroch, *Neurology*, 2011, **77**, 677–683.

138. R. H. Dunstan, M. M. Macdonald, G. R. Murphy, B. Thorn and T. K. Roberts, *Amino Acids*, 2019, **51**, 945–959.

139. A. Alves, A. Bassot, A.-L. Bulteau, L. Pirola and B. Morio, *Nutrients*, 2019, **11**, 1356.

140. E. V. Boldyreva, V. A. Drebushchak, T. N. Drebushchak, I. E. Paukov, Y. A. Kovalevskaya and E. S. Shutova, *J. Therm. Anal. Calorim*., 2003, **73**, 409–418.

141. M. Anbu Arasi, M. Alagar and M. Raja Pugalenthi, *Chem. Phys. Lett*., 2021, **765**, 138301.

142. R. J. Davey, R. J. Dowling and A. J. Cruz-Cabeza, *Isr. J. Chem*., 2021, **61**, 573–582.

143. A. Dawson, D. R. Allan, S. A. Belmonte, S. J. Clark, W. I. David, P. A. McGregor, S. Parsons, C. R. Pulham and L. Sawyer, *Cryst. Growth Des*., 2005, **5**, 1415–1427.

144. K. Srinivasan, *J. Cryst. Growth*, 2008, **311**, 156–162.

145. J. S. Rodríguez, G. Costa, M. B. da Silva, B. P. Silva, L. J. Honório, P. de Lima-Neto, R. C. Santos, E. W. Caetano, H. W. Alves and V. N. Freire, *Cryst. Growth Des*., 2019, **19**, 5204–5217.

146. I. Weissbuch, V. Y. Torbeev, L. Leiserowitz and M. Lahav, *Angew. Chem., Int. Ed*., 2005, **44**, 3226–3229.

147. Y. Liu, J. F. Black, K. F. Boon, A. J. Cruz-Cabeza, R. J. Davey, R. J. Dowling, N. George, A. Hutchinson and R. Montis, *Cryst. Growth Des*., 2019, **19**, 4579–4587.

148. V. Yu. Torbeev, E. Shavit, I. Weissbuch, L. Leiserowitz and M. Lahav, *Cryst. Growth Des*., 2005, **5**, 2190–2196.

149. J. W. Chew, S. N. Black, P. S. Chow, R. B. H. Tan and K. J. Carpenter, *CrystEngComm*, 2007, **9**, 128-130.

150. A. Manson, J. Sefcik and L. Lue, *Cryst. Growth Des*., 2022, **22**, 1691–1706.

151. K. Renuka Devi and K. Srinivasan, *Cryst. Res. Technol*., 2015, **50**, 389–394.

152. J. E. Aber, S. Arnold, B. A. Garetz and A. S. Myerson, *Phys. Rev. Lett*., 2005, **94**.

153. J. Zaccaro, J. Matic, A. S. Myerson and B. A. Garetz, *Cryst. Growth Des*., 2000, **1**, 5–8.

154. R. Dowling, R. J. Davey, R. A. Curtis, G. Han, S. K. Poornachary, P. Shan Chow and R. B. H. Tan, *Chem. Comm*., 2010, **46**, 5924–5926.

155. X. Yang, X. Wang and C. B. Ching, *J. Chem. Eng. Data*., 2008, **53**, 1133–1137.

156. S. A. Azhagan, V. S. Kathiravan and N. S. Priya, *Mater. Sci.-Pol*., 2018, **36**, 483–493.

157. L. J. Little, A. A. King, R. P. Sear and J. L. Keddie, *J. Chem. Phys*., 2017, **147**.

158. G. B. Chernobai, Y. A. Chesalov, E. B. Burgina, T. N. Drebushchak and E. V. Boldyreva, *J. Struct. Chem*., 2007, **48**, 332-339.

159. E. S. Ferrari, R. J. Davey, W. I. Cross, A. L. Gillon and C. S. Towler, *Cryst. Growth Des*., 2003, **3**, 53–60.

160. A. Y. Lee, I. S. Lee and A. S. Myerson, *Chem. Eng. Technol*., 2006, **29**, 281-285.

161. S. Z. Ali Ahamed, G. R. Dillip, P. Raghavaiah, K. Mallikarjuna and B. Deva Prasad Raju, *Arab. J. Chem.*, 2013, **6**, 429–433.

162. A. Airinei, M. Homocianu and D. O. Dorohoi, *J. Mol. Liq.*, 2010, **157**, 13–17.

163. M. A. Rauf and S. Hisaindee, *J. Mol. Struct.*, 2013, **1042**, 45–56.

164. İ. Sıdır, Y. Gülseven Sıdır, H. Berber and E. Taşal, *J. Mol. Liq.*, 2013, **178**, 127–136.

165. S. Smith and F. B. Abdallah, *J. Thermodyn. Catal.*, 2017, **8(1)**.

166. M. J. Kamlet, J. L. Abboud, M. H. Abraham and R. W. Taft, *J. Org. Chem.*, 1983, **48**, 2877–2887.

167. M. A. Rauf, S. Hisaindee, J. P. Graham and M. Nawaz, *J. Mol. Liq.*, 2012, **168**, 102–109.

168. M. Juramy, R. Chevre, P. C. Vioglio, F. Ziarelli, E. Besson, S. Gastaldi, S. Viel, P. Thureau, K. D. M. Harris and G. Mollica, *J. Am. Chem. Soc.*, 2021, **143**, 6095–6103.

169. H. Bishara and S. Berger, *J. Mater. Sci.*, 2019, **54**, 4619.

170. Q. Jiang, H. Hu and M. D. Ward, *J. Am. Chem. Soc.*, 2013, **135**, 2144.

171. B. D. Hamilton, M. A. Hillmyer and M. D. Ward, *Cryst. Growth Des.*, 2008, **8**, 3368.

172. J. M. Ha, J. H. Wolf, M. A. Hillmyer and M. D. Ward, *J. Am. Chem. Soc.*, 2004, **126**, 3382-3383.

173. F. C. Meldrum and C. O'Shaughnessy, *Adv. Mater.*, 2020, **32**, 2001068.

174. H. K. Christenson, *J. Condens. Matter Phys.*, 2001, **13**.

175. M. Liu and R. Y. Wang, *Sci. Rep.*, 2015, **5**.

176. B. Jin, S. Liu, Y. Du, G. Kaptay and T. Fu, *Phys. Chem. Chem. Phys.*, 2022, **24**, 22278–22288.

177. A. van Teijlingen, S. A. Davis and S. R. Hall, *Nanoscale Adv.*, 2020, **2**, 2347–2351.

178. D. Jin and J. Zhong, *J. Phys. Chem. B*, 2023, **127**, 5295–5307.

179. J. M. Ha, B. D. Hamilton, M. A. Hillmyer and M. D. Ward, *Cryst. Growth Des.*, 2009, **9**, 4766–4777.

180. M. Beiner, Rengarajan, S. Pankaj, D. Enke and M. Steinhart, *Nano Lett.*, 2007, **7**, 1381–1385.

181. G. T. Rengarajan, D. Enke, M. Steinhart and M. Beiner, *Phys. Chem. Chem. Phys.*, 2011, **13**, 21367.

182. C. L. Jackson and G. B. McKenna, *Chem. Mater.*, 1996, **8**, 2128–2137.

183. Y. Diao, K. E. Whaley, M. E. Helgeson, M. A. Woldeyes, P. S. Doyle, A. S. Myerson, T. A. Hatton and B. L. Trout, *J. Am. Chem. Soc.*, 2011, **134**, 673–684.

184. P. C. Vioglio, P. Thureau, M. Juramy, F. Ziarelli, S. Viel, P. A. Williams, C. E. Hughes, K. D. Harris and G. Mollica, *J. Phys. Chem. Lett.*, 2019, **10**, 1505–1510.

185. A. B. Buanz and S. Gaisford, *Cryst. Growth Des.*, 2017, **17**, 1245–1250.

186. S. E. Wolf, J. Leiterer, M. Kappl, F. Emmerling and W. Tremel, *J. Am. Chem. Soc.*, 2008, **130**, 12342–12347.

187. A. Alieva, M. Boyes, T. Vetter and C. Casiraghi, *CrystEngComm*, 2020, **22**, 7075–7081.

188. L. Li, D. Mustafi, Q. Fu, V. Tereshko, D. L. Chen, J. D. Tice and R. F. Ismagilov, *PNAS*, 2006, **103**, 19243–19248.

189. A. Yashina, F. Meldrum and A. deMello, *Biomicrofluidics*, 2012, **6**, 022001.

190. A. Parkes, A. Ziaee, G. Walker and E. O'Reilly, *CrystEngComm*, 2022, **24**, 6825–6829.

191. V. Slabov, D. Vasileva, K. Keller, S. Vasilev, P. Zelenovskiy, S. Kopyl, V. Ya. Shur, A. Vinogradov and A. L. Kholkin, *Cryst. Growth Des*., 2019, **19**, 3869–3875.

192. D.-K. Buˇcar, R. W. Lancaster and J. Bernstein, *Angew. Chem., Int. Ed*., 2015, **54**, 6972–6993.

193. Y. Liu, B. Gabriele, R. J. Davey and A. J. Cruz-Cabeza, *J. Am. Chem. Soc*., 2020, **142**, 6682–6689.

194. L. J. Little, R. P. Sear and J. L. Keddie, *Cryst. Growth Des*., 2015, **15**, 5345–5354.

195. C. S. Towler, R. J. Davey, R. W. Lancaster and C. J. Price, *J. Am. Chem. Soc*., 2004, **126**, 13347.

196. L. Dang, H. Yang, S. Black and H. Wei, *Org. Process Res. Dev.*, 2009, **13**, 1301–1306.

197. S. Hwang and J. Karger, *Magn. Reson. Imag.*, 2019, **56**, 3–13.

198. S. P. Moulik and B. K. Paul, *Adv. Colloid Interface Sci*., 1998, **78**, 99–195.

199. K. Shinoda, M. Araki, A. Sadaghiani, A. Khan and B. Lindman, *J. Phys. Chem*., 1991, **95**, 989–993.

200. I. Weissbuch, L. Leisorowitz and M. Lahav, *Adv. Mater*., 1994, **6**, 952–956.

201. G. Han, S. Thirunahari, P. S. Chow and R. B. H. Tan, *CrystEngComm*, 2013, **15**, 1218–1224.

202. G. Han, S. Thirunahari, P. S. Chow and R. B. H. Tan, *Pharmaceutics*, 2021, **13**, 262.

203. L. A. I. Ramakers, J. McGinty, W. Beckmann, G. Levilain, M. Lee, H. Wheatcroft, L. Houson and J. Sefcik, *Cryst. Growth Des*., 2020, **20**, 4935–4944.

204. J. McGinty, N. Yazdanpanah, C. Price, J. H. ter Horst and J. Sefcik, in *The Handbook of Continuous Crystallization*, Royal Society of Chemistry, London, 2020, ch. 1, pp. 1–50.

205. K. Renuka Devi, V. Gnanakamatchi and K. Srinivasan, *J. Cryst. Growth*, 2014, 400, 34-42.

206. G. J. Beran, I. J. Sugden, C. Greenwell, D. H. Bowskill, C. C. Pantelides and C. S. Adjiman, *Chem. Sci.*, 2022, **13**, 1288–1297.

207. X. Li, X. Ou, H. Rong, S. Huang, J. Nyman, L. Yu and M. Lu, *Cryst. Growth Des*., 2020, **20**, 7093–7097.

208. G. Stephenson, T. Borchardt, S. Byrn, J. Bowyer, C. Bunnell, S. Snorek and L. Yu, *J. Pharm. Sci*., 1995, **84**, 1385–1386.

209. L. Yu, G. A. Stephenson, C. A. Mitchell, C. A. Bunnell, S. V. Snorek, J. J. Bowyer, T. B. Borchardt, J. G. Stowell and S. R. Byrn, *J. Am. Chem. Soc*., 2000, **122**, 585–591.

210. C. A. Mitchell, L. Yu and M. D. Ward, *J. Am. Chem. Soc*., 2001, **123**, 10830–10839.

211. J. Nyman, L. Yu and S. M. Reutzel-Edens, *CrystEngComm*, 2019, **21**, 2080–2088

212. S. Chen, I. A. Guzei and L. Yu, *J. Am. Chem. Soc*., 2005, **127**, 9881–9885.

213. S. Chen, H. Xi and L. Yu, *J. Am. Chem. Soc*., 2005, **127**, 17439–17444.

214. M. Tan, A. G. Shtukenberg, S. Zhu, W. Xu, E. Dooryhee, S. M. Nichols, M. D. Ward, B. Kahr and Q. Zhu, *Faraday Discuss*., 2018, **211**, 477–491.

215. K. S. Gushurst, J. Nyman and S. X. M. Boerrigter, *CrystEngComm*., 2019, **21**, 1363–1368.

216. A. L´evesque, T. Maris and J. D. Wuest, *J. Am. Chem. Soc*., 2020, **142**, 11873–11883.

217. A. R. Tyler, R. Ragbirsingh, C. J. McMonagle, P. G. Waddell, S. E. Heaps, J. W. Steed, P. Thaw, M. J. Hall and M. R. Probert, *Chem*., 2020, **6**, 1755–1765.

218. L. R. Warren, E. McGowan, M. Renton, C. A. Morrison and N. P. Funnell, *Chem. Sci*., 2021, **12**, 12711–12718.

219. J. Falk, D. Hofmann and K. Merz, *IUCrJ*, 2018, **5**, 569–573.

220. T. Y. Nguyen, E. A. Roessler, K. Rademann and F. Emmerling, *Z. fur Krist. - Cryst. Mater*., 2016, **232**, 15–24.

221. J. A. Foster, K. K. Damodaran, A. Maurin, G. M. Day, H. P. Thompson, G. J. Cameron, J. C. Bernal and J. W. Steed, *Chem. Sci*., 2017, **8**, 78–84.

222. C. P. Price, A. L. Grzesiak and A. J. Matzger, *J. Am. Chem. Soc*., 2005, **127**, 5512–5517.

223. V. Swamy, S. K. Saxena, B. Sundman and J. Zhang, *J. Geophys. Res. Solid*., 1994, **99**, 11787–11794.

224. R. Di Febo, L. Casas, Á. A. del Campo, J. Rius, O. Vallcorba, J. C. Melgarejo and C. Capelli, *J. Eur. Ceram*., 2020, **40**, 6188–6199.

225. J. Bertone, J. Cizeron, R. Wahi, J. Bosworth and V. Colvin, *Nano Lett*., 2003, **3**, 655-659.

226. M. Cargnello, T. Gordon and C. Murray, *Chem. Rev*., 2014, **114**, 9319-9345.

227. I. Rahman and V. Padavettan, *J. Nanomater*., 2012, 1-15.

228. T. Matsuno, Y. Kuroda, M. Kitahara, A. Shimojima, H. Wada and K. Kuroda, *Angew. Chem., Int. Ed*., 2016, **55**, 6008–6012.

229. R. E. Washburn and A. Beguin, *J. Am. Chem. Soc*., 1940, **62**, 579-581.

230. A. Singh, I. Lee and A. Myerson, *Cryst. Growth Des*., 2009, **9**, 1182–1185.

231. T. Mudalige, H. Qu, D. Van Haute, S. M. Ansar, A. Paredes and T. Ingle, in *Nanomaterials for Food Applications*, Elsevier, 2019, pp. 313–353.

232. W. Stöber, A. Fink and E. Bohn, *J. Colloid Interface Sci*., 1968, **26**, 62–69.

233. X.-D. Wang, Z.-X. Shen, T. Sang, X.-B. Cheng, M.-F. Li, L.-Y. Chen and Z.-S. Wang, *J. Colloid Interface Sci*., 2010, **341**, 23–29.

234. X. Jiang, Y.-B. Jiang and C. J. Brinker, *Chem. Comm*., 2011, **47**, 7524– 7526.

235. L. M. Sochalski-Kolbus, H.-W. Wang, A. J. Rondinone, L. M. Anovitz, D. J. Wesolowski and P. S. Whitfield, *Cryst. Growth Des*., 2015, **15**, 5327–5331.

236. R. Petrenko and J. Meller, *eLS*, 2010.

237. B.J. Alder and T.E. Wainwright, in *Prigogine, I., Ed., International Symposium on Transport Processes in Statistical Mechanics*, John Wiley Int., New York, 1957, 97-131.

238. B.J. Alder and T.E. Wainwright, *J. Chem. Phys*., 1959, **31**, 459.

239. A. Rahman, *Phys. Rev.*, 1964, **136(2A)**, A405–11.

240. G. Battimelli and G. Ciccotti, *Eur. Phys. J. H.*, 2018, **43**, 303–335.

241. A. K. Padhi, M. Janežič and K. Y. J. Zhang, *Adv. Protein Chem. Struct. Biol*., 2022, 439–454.

242. S. Schöttl, D. Touraud, W. Kunz, T. Zemb and D. Horinek, *Colloids Surf. A Physicochem. Eng. Asp.*, 2015, **480**, 222–227.

243. D. Van der Spoel, E. Lindahl, B. Hess, G. Groenhof, A. Mark and H. Berendsen, *J. Comp. Chem.*, 2005, **26**, 1701-1718.

244. M. Abraham, T. Murtola, R. Schulz, S. Páll, J. Smith, B. Hess and E. Lindahl, *SoftwareX*, **1**, 2015, 19-25.

245. W. Jorgensen, D. Maxwell and J. Tirado-Rives, *J. Am. Chem. Soc.*, 1996, **118**, 11225–11236.

246. S. Siu, K. Pluhackova and R. Böckmann, *J. Chem. Theory Comput.*, 2012, **8**, 1459–1470.

247. J. Abascal and C. Vega, *J. Chem. Phys.*, 2005, **123**, 234505.

248. M. Parrinello and A. Rahman, *J. Appl. Phys.*, 1981, **52**, 7182–7190.

249. U. Essmann, L. Perera, M.L. Berkowitz, T. Darden, H. Lee and L.G. Pedersen, *J. Chem. Phys.*, 1995, **103**, 8577–8593.

250. D. W. Cheong and Y. D. Boon, *Cryst. Growth Des.*, 2010, **10**, 5146–5158.

251. J. L. Derissen, P. H. Smith and J. Voogd, *J. Phys. Chem.*, 1977, **81**, 1474–1476.

252. S. Gnanasambandam, Z. Hu, J. Jiang and R. Rajagopalan, *J. Phys. Chem. B*, 2008, **113**, 752–758.

253. J. Voogd, J. L. Derissen and F. B. Van Duijneveldt, *J. Am. Chem. Soc.*, 1981, **103**, 7701–7706.

254. K. T. No, J. A. Grant, M. S. Jhon and H. A. Scheraga, *J. Phys. Chem.*, 1990, **94**, 4740–4746.

255. J. A. Chisholm, S. Motherwell, P. R. Tulip, S. Parsons and S. J. Clark, *Cryst. Growth Des.*, 2005, **5**, 1437–1442.

256. H. Zhang and O. Annunziata, *Langmuir*, 2008, **24**, 10680–10687.

257. M. A. Malik, M. Y. Wani and M. A. Hashim, *Arab. J. Chem.*, 2012, 5, 397–417.

258. R. Bandyopadhyaya, R. Kumar and K. S. Gandhi, *Langmuir*, 2000, 16, 7139–7149.

259. P. D. Fletcher, A. M. Howe and B. H. Robinson, *J. Chem. Soc.*, 1987, **83**, 985.

260. M. da Graça Miguel, H. D. Burrows, M. A. Escaroupa Pereira and A. P. Varela, Colloids Surf. A: Physicochem. Eng. Asp., 2001, **176**, 85–99.

261. Z. Cao, Y. Hu, J. Li, Y. Kai and W. Yang, Fluid Ph. Equilib., 2013, **360**, 156-160.

When considering microemulsion-based crystallisations, it is common that a Poisson distribution is used to approximate the distribution of solute molecules within the array of microemulsion droplets.[108,256–260] This is assumed because, after the STF has been formed, the probability that a crystallisable molecule is added to a particular droplet is rare, owing to the restricted diffusion between droplets and at equilibrium the solute molecules will be randomly distributed. As the STF systems has this far proven analogous to the surfactant microemulsion systems, the same approximation has been used in this work.

Table A.1: Composition of each fluid component of the STF used for the following calculation of solute distribution.

	Mass fraction	Volume in 100 ml STF / ml	Solubility of glycine in STF / g ml^{-1}
Water	0.25	21	
Octanol	0.35	36	0.415
Ethanol	0.40	43	

Assuming spherical droplets with a mean diameter of 4 nm, the volume of a single droplet is 33.5 nm^3. Consequently, in the 100 ml STF sample there will be approximately 6×10^{20} droplets. When $\frac{c}{c_{sat}} = 2$, the mass of glycine in the STF is 0.830 g which equates to 6.7×10^{21} molecules of glycine.

For a single droplet, the mean number of solute molecules per droplet is 11.

The probability that a droplet contains n number of crystallisable molecules assuming a Poisson distribution is as follows:

$$f(n; \lambda) = \frac{\lambda^n e^{-\lambda}}{n!}$$

where, λ is the mean number of crystallisable molecules per droplet.
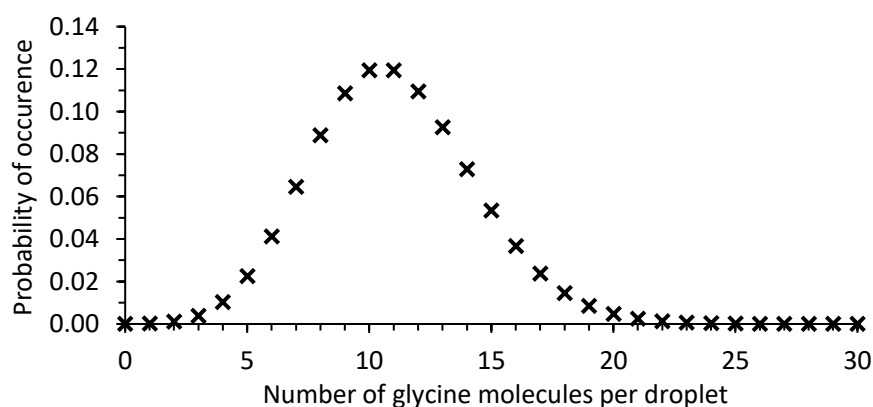

Figure A.1: Poisson distribution of glycine molecules across water droplets in an STF containing water, octanol and ethanol mass fractions of 0.25, 0.35 and 0.40, respectively, and a relative concentration of glycine in the total STF of $\frac{c}{c_{sat}}$ = 2.

The distribution plotted in figure A.1 leads to a probability that droplets contain supersaturations with $\frac{c}{c_{sat}}$ in excess of 4 of ~0.1 %, or approximately 10^{17} droplets. This value assumes that all water in the system is bound in discrete pockets with no miscibility with either ethanol or octanol, which is inaccurate. Factors that must be considered are the miscibility of water in ethanol and octanol and the solubility of glycine in the mixed ethanol/water and ethanol/octanol domains.[261] This would lead to a decrease in the number of droplets with $\frac{c}{c_{sat}} > 4$ which has been approximated as >10^{16} droplets.